University of Southampton

Damage Identification in Beam-like Structures by Vibration-based Analysis and Artificial Neural Networks

by

Melin Şahin

A thesis submitted for the degree of
Doctor of Philosophy

in the
Faculty of Engineering, Science and Mathematics
School of Engineering Sciences
Ship Science

March, 2004

Dedicated to my mother,

For her endless and unconditional support, encouragement, patience, understanding and love. My gratitude and my love to her are beyond words.

UNIVERSITY OF SOUTHAMPTON

ABSTRACT

FACULTY OF ENGINEERING, SCIENCE AND MATHEMATICS
SCHOOL OF ENGINEERING SCIENCES
SHIP SCIENCE
Doctor of Philosophy

Damage Identification in Beam-like Structures by Vibration-based Analysis and Artificial Neural Networks

by
Melin Şahin

Laminated composites and sandwich structures are increasingly being used in different engineering applications such as in aeronautical, marine and offshore structures where high stiffness, light weight, good corrosion resistance and temperature stability are the primary issues. During their service life, these structures experience extreme loadings and harsh environmental conditions potentially leading to structural damage. This could significantly reduce mechanical strength and result in performance degradation of the structure.

Therefore, in order to maintain the performance of the structure, localisation and quantification of the damage is a promising research area. Since the determination of the severity and the location of the damage is an inverse and non-unique problem, an intelligent algorithm is needed to perform the damage detection analysis.

This study presents a damage detection algorithm, which uses vibration-based analysis data obtained from beam-like structures to locate and quantify the damage by using artificial neural networks. The inputs and the corresponding outputs required to train the neural networks are obtained from the finite element analyses for different vibration modes of the beams. Multi-layer feedforward backpropogation neural networks have been designed and trained by using different damage scenarios. After validation of the neural networks, new damage cases obtained from finite element and experimental analyses have been introduced and neural networks have been tested for location and severity predictions.

The results from the neural networks depict that severity and location of the damage can be predicted by using as input the global (natural frequencies) and the local (strain or curvature mode shapes) dynamic behaviour of the beam-like structures.

Acknowledgements

I would like to thank my supervisor Professor R. A. Shenoi for his supervision, support, guidance, encouragement and patience throughout this research.

I would like to extend my warmest thanks to Dr. J. M. Dulieu-Barton for her advice and valuable suggestions during my research.

I would like to thank Prof. P. Temarel and Prof. M. J. Brennan for valuable suggestions during the MPhil transfer viva.

I am thankful to Prof. K. Worden for valuable and helpful academic discussions and recommendations during the initial stage of my research.

I am grateful to the teaching and technical staff in the School of Engineering Sciences and I also wish to thank Dr. P. Cunningham and Dr. G. Aglietti for their help during the experimental work. The financial assistance of EPSRC is also gratefully acknowledged since part of the experiment has been carried out using dynamic test equipment purchased from EPSRC grant.

I am also thankful to Dr. M. Gunning, Dr. G. Brambilla and Mr. Y. Cho from Optoelectronics Research Centre for providing fibre optic sensors and valuable technical support.

I am indebted to Prof. Y. Yaman and Prof. P. A. Wilson who were the first to open the gateway for my PhD studies.

My thanks go to my colleagues and friends; Tariq, Mirza, Ajaya, Marion, Nick, Elli, Simon, Ana, Stella and many more for their encouragement.

Finally, I would like to thank my mother, my sister and my father for their constant encouragement, moral support and endless love. Without them, this work could not have been achieved.

Table of Contents

List of Symbols

E	Elastic modus
f	Natural frequency
$f(net)$	Activation function
G	Shear modus
g	Acceleration of gravity
h	Distance between two collocation points
L	Length of the beam
m	Number of nodes in hidden layer
n	Number of nodes in input layer
N	Number of random entries
o_i	Input values
o_j	Activation values for hidden layer nodes
o_k	Activation values for output layer nodes
p	Number of nodes in output layer
t	Total thickness of the beam
t_k	Target values
v_i	Normalised displacement
v_i''	Curvature
w_{ji}	Weights between input and hidden layer
w_{kj}	Weights between hidden and output layer
Δw_{ji}	Error in weights between input and hidden nodes
Δw_{kj}	Error in weights between hidden and output nodes
x_i	Data in vector form
$\bar{x}_i$	Normalised data

ρ	Density
v	Poisson's ratio
Δ	Percentage noise
ω	Circular frequency
ζ	Damping ratio
η	Learning parameter

[Other symbols are defined when they appear in the text]

List of Abbreviations

ANN	Artificial neural network
BPNN	Backpropagation neural network
CFRP	Carbon fibre reinforced plastic
CLPT	Classical laminated plate theory
CPT	Classical thin plate theory
DFT	Discrete Fourier transform
DL	Location of the damage
DS	Severity of the damage
FBG	Fibre Bragg grating
FBGIS	Fibre optic Bragg grating interrogation system
FEA	Finite element analysis
FEM	Finite element model
FFT	Fast Fourier transform
FOS	Fibre optic sensor
FRF	Frequency response function
FRP	Fibre reinforced plastic
FSDT	First order shear deformation theory
GFRP	Glass fibre reinforced plastic
HSDT	Higher order shear deformation theory
LOC	Location where the maximum absolute difference in curvature mode occurs
MAC	Modal assurance criterion
MADC	Maximum absolute difference in curvature mode shape
MLP	Multilayer perceptron
MSE	Mean square error
NDI	Non-destructive inspection
ODS	Operational deflection mode shape
PSD	Power spectral density

PVDF	Polyvinlydine fluoride
PZT	Lead zirconate titanate piezoelectrics
RNF	Reduction in natural frequency
SMA	Shape memory alloy
UD	Unidirectional

List of Tables

List of Figures

PART A

BACKGROUND

Chapter One INTRODUCTION

Non-Destructive Inspection (NDI) techniques **[1-1]** are generally used to investigate the critical changes in structural parameters so that an unexpected failure can be prevented before it can occur. These so called local and visual methods concentrate on a part of the structure and in order to perform the inspection, the structure may need to be taken out of service. In order to apply these techniques, the location of the damage needs to be known and it should be accessible for inspection. Since these damage identification techniques also require a large amount of human involvement that affects the accuracy of the testing, they prove to be expensive to implement. The main challenge in NDI applications is to design a structural health monitoring system that is capable of detecting the damage signature in service life of the structure without *a priori* information about the location of the damage. This is accomplished via integrated sensors and employing an intelligent algorithm having pattern recognition capabilities which are capable of analysing the damage characteristics. Moreover, by using these kinds of early warning systems, the risk of more serious failure of the structure and the overall maintenance cost can be reduced by excluding unnecessary inspection activities.

1.1 Damage Identification in Structures

Damage identification can be divided into four hierarchical levels **[1-2]** as follows:

Level#1: Determination that damage exists in the structure

Level#2: Investigation of the location of the damage

Level#3: Quantification of the severity of the damage

Level#4: Prediction of the remaining service life (i.e. residual life) of the structure

Vibration-based analysis data indicates the existence of the damage (Level#1) when it is used as an input pattern to the analysis. Localisation (Level#2) and quantification (Level#3) of the damage can only be obtained if vibration-based input is provided with a structural model and an identification algorithm. A prediction of residual life of the structure (Level#4) requires

further analysis including fracture mechanics, structural design assessment and fatigue-life analysis.

Another way of classification in damage identification is that Level#1 is considered as a forward problem since the damage can be modelled mathematically and vibration response of the structure provides the necessary information about the existence of damage. On the other hand, Level#2 and Level#3 damage identifications are in the inverse problem category. This is because the damage signature might be the same for different extents of damage occurring at different geometrical locations of the structure, making the problem non-unique. Therefore, Artificial Neural Networks (ANNs) can be designed and trained through a learning process by non-linear parameterised mapping between the input and the output sets via their highly interconnected processing elements to extract features. They can also be used to classify and describe the patterns from the possible damage scenarios in the damage assessment applications.

1.2 Objectives

The primary aim of this work is to develop a technique which is applicable in quantification and localisation of the damage (Level#1, 2 and 3) by using vibration-based analysis features as an input to artificial neural networks via distributed strain sensors bonded to surface or embedded into structure. The technique starts from the basic assumption that damage can be directly related to a decrease of stiffness in the structure and identifies the structural damage with limited amount of distributed sensors.

The specific objectives of the present work can be summarised as follows:

- To identify damage in structures from changes in their vibration responses
- To measure patterns providing global and local information about damage characteristics
- To investigate the effectiveness of the features introduced to different ANN architectures as various input-output pairs for damage quantification and localisation
- To achieve better understanding about simulation of a damage and its effect on structural dynamic behaviour
- To validate the technique by numerical (finite element) and experimental means
- To demonstrate the feasibility of using embedded fibre Bragg grating (FBG) sensors for strain measurements especially in sandwich structures

1.3 Overview of the Proposed Approach

In order to achieve the main objectives of this research mentioned in the previous section, a deep knowledge should be gained in various areas. **Figure 1.1** summarises these areas by highlighting the novelty and main contributions to knowledge in italics.

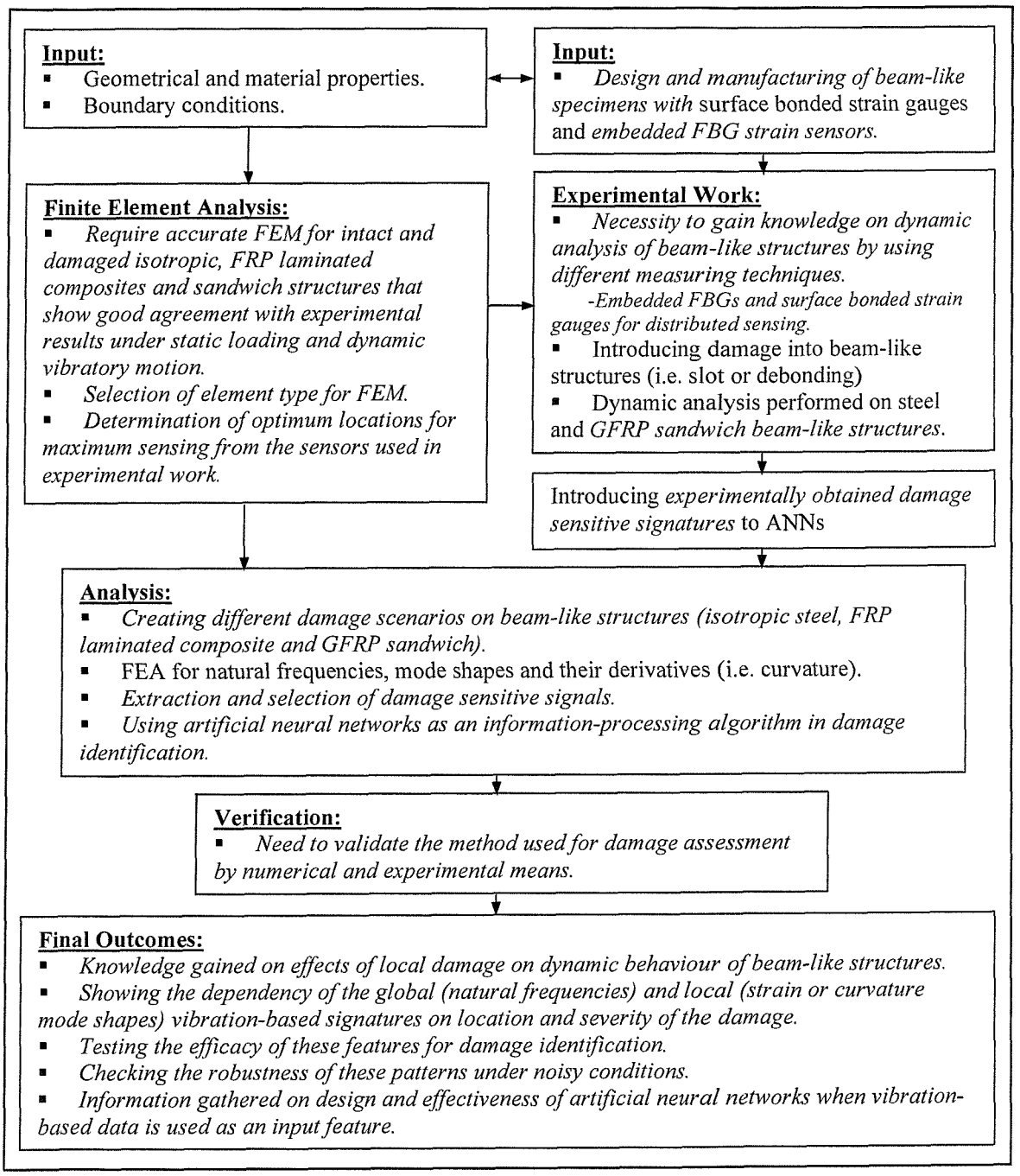

Figure 1.1 General overview of the proposed approach

Chapter Two LITERATURE REVIEW

2.1 Introduction

Any kind of damage adversely affects the current and future performance of the structure and therefore it must be carefully investigated before it results in a catastrophic failure. There are different methods available for structural inspection and performance monitoring. These methods can be categorised as local and global. The former which concentrates on specific part of the structure is categorised as NDI technique **[2-1]**. In order to perform an NDI, structure should be taken out of service on a regular basis without having a priori information about the damage; that is a costly procedure. On the other hand, the latter is independent from the location of the damage and can be performed by measuring changes in the structural dynamic characteristics. Therefore, these global damage detection techniques are becoming more popular recently and, therefore, have been reviewed by several researchers **[2-2], [2-3], [2-4], [2-5], [2-6]**.

2.2 Features and Methods in Vibration–based Damage Identification

Previous investigators have utilised vibration-based analyses to generate features that can be used to predict severity as well as location of the damage and this can be helpful to ascertain which feature will be most efficient and practical in predicting damage characteristics. In the following section, detection methods will be categorised and briefly explained considering the data obtained from the experimental and numerical analyses and the technique used to post process the data for damage assessment will be outlined.

2.2.1 Natural Frequency Changes

There is a large amount of literature on damage detection by using changes in frequencies. In this section, methods using natural frequency changes as a damage signature are

reviewed. All types of structural damage reduce the stiffness of the structure locally and any changes of stiffness cause change in the natural frequencies and structural damping. Since the measurement of natural frequencies is easier than that of changes in damping of a structure, damage can be detected from dynamic analysis aiming at natural frequencies. Additionally, determination of the damage from frequency measurements is quite convenient since an arbitrarily chosen single point is enough to perform the modal analysis to obtain dynamic characteristics of the structure.

One of the earliest research has been done by Cawley and Adams **[2-7]**. The authors used frequency measurement method via finite element analysis (FEA) for various types of damage in composite materials. Structural damage was numerically modelled either by reducing the stiffness of the element or setting it to zero that leads to reduction in natural frequencies. Since frequency changes tended to be small, large number of mode pairs was used. It can be concluded from the numerical analyses that reduction in frequencies shows the existence of the damage. Inada *et al.* **[2-8]** proposed a damage identification method using natural frequency change and response surfaces in order to localise and quantify the damage. In this approach, natural frequencies were used for damage identification and response surfaces were used to obtain approximate expressions indicating damage location and length. First, damage identification of a carbon fibre reinforced plastic (CFRP) cantilever beam was conducted. Then, same analysis was also performed with CFRP cantilever plate to show the applicability of the proposed method. Finally, good agreement between actual and predicted damage parameters (stiffness degradation, location and size of the damage) was achieved.

Zak *et al.* **[2-9]** applied finite element method to find the effects of closing delamination on vibrating laminated composite plate. Eight-layer graphite/epoxy cantilever composite plate was used for numerical calculations to investigate the influence of the location and the length of delamination on natural frequencies. In order to verify the accuracy of the model and the numerical results, an experiment with impulse excitation was performed on composite plate with mid-plane delamination. Authors concluded that if the length of the delamination grows and its position changes, the natural frequencies decrease and vibration modes are also affected. Valdes and Soutis **[2-10]** also investigated the effect of delamination on the modal frequencies of laminated composite beams and examined the performance of piezoelectric materials as sensor/actuator pair. In the analysis, the authors used eight-ply carbon/epoxy prepreg cantilever laminated beam having a small Teflon film inserted during the manufacturing. A sharp thin scalpel blade introduced into the mid-plane and two piezoelectric elements were used for self-sensing and actuating applications. They extended the effect of damage by repeatedly pushing

the blade against the delamination front and observed that the delamination area was gradually extended from the free edge until it covered almost all of the specimen width. The changes of the modal frequencies of the specimen compared to those of the non-delaminated one showed a good indication of the degree of damage, especially at high frequency levels.

Lakshmi and Jebaraj **[2-11]** proposed a new technique based on the percentage change in natural frequencies in the first five modes to identify the presence of through thickness cracks and their locations along a cantilever aluminium beam. They also performed sensitivity analyses on bending, torsional and strain mode shapes by considering the effects on local modal parameters due to crack for different crack depths at different locations. It was observed from the analyses that the absolute percentage change in frequencies increases as the depth of the crack increases. Additionally, this change is maximum if the crack is located at the peak/trough of the strain mode and it is minimum if the crack is located at the node of strain mode. In Hu *et al.* **[2-12]**, the authors developed two different algorithms to assess structural damage using modal test data. The first algorithm avoided the employment of the analytical global stiffness and mass matrices that led to approximate estimation of the damage extent; on the other hand, in the second algorithm, analytical mass matrix was employed, which gave completely accurate prediction for the damage extent. A 10-bay planar truss structure was used for FEA and the multiple damage cases were simulated with reduction in the stiffness of the selected elements in the bays. In experimental work, a clamped-clamped aluminium beam with saw cut was used as a test specimen on which modal analysis was performed to obtain natural frequencies and mode shapes. The authors concluded that with the increase of the number of the frequencies and modes, the accuracy in the detection of damage location and prediction of damage extent become better and the selection of modes is also critical for the successful multiple damage identification.

2.2.2 Displacement and Curvature (Strain) Mode Shape Changes

As mode shapes can be obtained both experimentally and by numerical means, damage detection techniques which use this concept have been studied by several researchers.

Ren and De Roeck **[2-13]** proposed a technique to predict the damage location and severity based on changes in frequencies and mode shapes of vibration of simple and continuous beams with number of different damage scenarios. Structural characteristics before and after the damage that was simulated by reducing the stiffness of assumed elements including multiple damage cases were calculated with FEA. The technique was also tested with the existence of

numerically generated noise. The authors (Ren and De Roeck **[2-14]**) applied this algorithm on reinforced concrete beams and performed an experiment to establish the relation between damage and changes of the structural dynamic characteristics. Static tests were aimed to produce the successive damage on the central zone of the beam with almost uniform damage intensity. On the other hand, dynamic tests were aimed at finding natural frequencies and modes with the help of impact hammer and accelerometers. The authors finally concluded that the proposed method could be applicable to simple structures for damage localisation. Ahmadian *et al.* **[2-15]** examined a method which uses measured displacement data and a finite element model (FEM) to locate damage in uniform beam structures. Damage was modelled by either changing the flexural rigidity of the selected elements or creating a discretisation error by varying the length of the elements. Since the method uses a combination of measured displacements, it is capable of locating the damage correctly.

Friswell *et al.* **[2-16]** applied a genetic algorithm by using vibration data based on changes in frequency and mode shapes to identify the position of one or more damage sites in a uniform cantilever beam and to estimate the extent of the damage at these sites. The theory is based on the optimisation of objective (error) function obtained from analytical and measured data with the genetic algorithm. The simulation results showed that the algorithm is robust to systematic errors in the measured data and powerful in damage localisation for single damage site compared to multiple one. Fox **[2-17]** applied the Modal Assurance Criterion (MAC) on natural frequency data obtained from finite element analyses of intact and damaged beams. Although changes in natural frequency indicated that damage might be present in the structure and MAC gave useful indication of the relative extend to which modes were affected by the damage, these two approaches were not sufficient to locate the damage. Therefore, the author used a relative difference function based on intact and damaged mode shapes to assess the damage. It was concluded from the analyses that mode shape information was required to determine the location of the damage. Pandey *et al.* **[2-18]** performed modal analyses with cantilever and simply supported beams and used curvature mode shape parameter for damage detection. In this method, curvature mode shapes were obtained numerically from the displacement mode shapes by using a central difference approximation. Damage was modelled as a percentage reduction in stiffness of one of the elements in the finite element model. The results demonstrated that the absolute difference between the curvature mode shape of the intact and that of the damaged beam was a good indicator to detect and locate the damage, since the maximum absolute difference occurred in the damage zone.

Yuen **[2-19]** developed a numerical method using finite element modelling technique to establish the fundamental relationship between damage location, damage size and eigenparameters (i.e. displacement and rotation). A cantilever beam having damage zone with reduced stiffness was used as a model and eigenparameters were estimated by using each eigenvalue as a normalisation factor. Since the rotation eigenparameter took a step jump in a value when crossing over the damage zone and the displacement eigenparameter changed its slope at the same location, the proposed method showed that definitive characteristics were related to the location and extent of damage. Ratcliffe **[2-20]** extended the research and used one-dimensional Laplacian operator on the discrete first bending mode shape of a finite element free-free beam with 50% damage on one of its elements in FEM. Since the damage was severe, this operator indicated the location of the damage. But, for less severe damage, the Laplacian was not that powerful to indicate the damage and it retained its characteristic shape. For this reason, a method calculating the difference between the cubic polynomial and Laplacian was developed. It was observed that this modified Laplacian method provided the necessary information to identify the location of the damage from mode shape data although damage was less severe compared to one used for Laplacian operator. Ho and Ewins **[2-21]** presented a numerical analysis, so called damage index, comparing the curvatures of the in-service structure and those of the baseline at every measurement location. In the analysis, first three transverse vibration mode shapes were considered and different damage configurations were used by reducing the thickness at a particular location. Damage index was performed for four different numerical studies, namely measurement noise, spatial resolution of the mode shapes, damage severity and changes to boundary conditions to investigate the effects of these parameters on the accuracy of predicting the location of the damage. It was observed from the numerical results that noise level constraints and higher resolution of mode shapes increase the sensitivity of the damage index to damage.

Pai and Young **[2-22]** used the boundary effect detection method **[2-23]** for location detection of damage by using structural operational deflection mode shapes via scanning laser vibrometer measurements. Experiments were performed using single frequency excitation at the chosen frequency on cantilever and simply supported beams with different damage types, including cracks and internal holes at different locations. The experimental results showed that high frequency operational deflection mode shapes are better than low frequency ones for locating the damage. The authors also concluded that the proposed method provides damage indicators with different levels of accuracy for different levels of inspection but a clear damage signal is always needed for extraction of the data. Cornwell *et al.* **[2-24]** generalised this

method, which is based on strain energy and developed for beam-like structures, to plate-like structures having two-dimensional curvature. The modified method uses mode shape information of the structure before and after the damage to detect and locate the damage. It was assumed during the analyses that mode shapes were known exactly on a very fine grid of sensors but in actual practice this is not the case. Therefore, calculation of derivatives and integrals when the mode shapes were known at relatively small number discrete locations was the main drawback of the study. Researchers also focussed on curvature mode shapes by considering higher and multiple modes.

Wahab and Roeck **[2-25]** proposed a curvature damage factor by performing an averaging over absolute differences in curvature mode shapes of a continuous beam for the first five modes and applied this technique to a real bridge to evaluate and locate the damage. Damage was simulated as a percentage reduction in stiffness of one of the elements of the beam FEM. They concluded that modal curvatures of lower modes are more accurate than those of higher ones and extensive measurement grid throughout the structure is needed to get a good estimation for the modal curvatures. Waldron *et al.* **[2-26]** aimed at quantifying the damage from operational deflection mode shapes (ODSs) by scanning laser doppler vibrometer. The angle between healthy and damaged normalised ODS was used as a damage signature in the analysis. Aluminium beams having fatigue crack grown in a tension machine was used in experimental work and the damage was simulated as stiffness reduction in FEA. The authors investigated the effects of loading, frequency range of excitation and the boundary conditions on detection of damage and performed sensitivity analyses of translational and rotational ODSs. Experimental work and FEA denoted that rotational ODSs give better accuracy in lower and higher modes although they are difficult to measure compared to translational ODSs. Additionally, it was perceived that visibility of the damage effect on ODS considerably increases when the damage is near or at an anti-nodal point for the higher frequency modes. The authors also concluded that higher frequencies are better indicator for damage detection and location prediction.

2.2.3 Frequency and Time–Frequency Analyses

The following researchers concentrated on obtaining frequency response function (FRF) of structures and in this way they investigated additional features that could be used for damage identification. In this section, research areas including wavelet analysis and electrical impedance methods are also reviewed.

Jian *et al.* **[2-27]** used Polyvinlydine Fluoride (PVDF) piezoelectric patches for damage detection in composite material. Unidirectional, four-ply laminated cantilever plates with surface bonded and embedded piezoelectric patches were used as test specimens under mechanical pulse delivered by a marble rolling down an inclined through and striking the plate. During the experiment, changes in frequency response spectrum of the delaminated composite plates were monitoried. The spectra showed distinct shifts in the vibrational frequencies to lower as delamination size increased. The analyses also showed that very little change in the frequencies occurred until the delamination became very large and ,therefore, it was concluded from the observations that a full-width delamination is required to significantly reduce the frequencies of the lower modes. Lee and Shin **[2-28]** presented a new algorithm, which requires natural frequencies and mode shapes of the intact structure and FRF of the damaged structure to predict the location and the magnitude of the damage. The structures used in the analyses were cantilever and simply supported Euler Bernoulli beams. Damage was modelled as change in stiffness by degradation of the elastic modulus at various extents along the beam span. FRFs were obtained by varying excitation frequency as well as measurement point to obtain sufficient number of equations. Then the algorithm reduced the domain of the problem by searching for damaged free zones and removing them from the spatial domain of the problem to leave damaged zones only. The effect of noise on the algorithm was also considered. The authors concluded that FRF provides more information on damage in a desired frequency range than modal data and better accuracy can be achieved by including higher modes.

Sampaio *et al.* **[2-29]** extended the theory **[2-18]** to all frequencies in the measurement range and used FRF data rather than just mode shape data in the calculation of curvatures to predict the existence, location and the extent of the damage. The authors performed a numerical study on ten degrees of freedom lumped mass model for four different levels of damage and applied the same theory on a real bridge structure. Damage was modelled as change in stiffness in the numerical analyses and as cuts in the web and flange of the girder of the bridge in the experiment. The influence of the frequency, input force location and the noise effect were also investigated in the study. The results indicated that for wider frequency ranges the difference in

the curvatures of the damaged and intact model become less significant due to frequency shift. The method worked better in the range before the first anti-resonance or resonance, whichever comes first. The authors also observed that the method is quite insensitive to noise and the effect of the position of the exciting force is not important from the damage detection performance point of view.

Castellini and Revel **[2-30]** demonstrated the measurement capabilities of laser doppler vibrometer in damage detection and characterisation technique. FEM was used to produce the data related to large variety of delaminations with reduced level of noise with ideal excitation conditions and to test the algorithm before its final application to real experimental case. FEM of the delamination was represented by a cavity obtained with two pyramids with same square bases and opposite vertices. Then, vibration information in each node of the mesh was obtained from FEA. Parallel to FEA, laser doppler vibrometer was used to measure vibration data from experiments. Finally, the proposed algorithm, which was based on the root mean square values and standard deviation of the FRFs was tested with both numerical and experimental data for damage characterisation. Sunders *et al.* **[2-31]** developed a theory to detect, locate and quantify damage in composite structures from changes in the measured modal response of the structure. Internal-state variable theory, which relates the current values of the stress to the current value of the strain through elastic moduli, was used to describe the constitutive behaviour of the cantilever composite beam. The authors also derived damage detection equations that can be solved to provide the unknown damage parameters (location and magnitude of the damage) by using combined experimental and analytical methods. Their numerical and experimental work on a laminated beam in the intact state and in three additional states of progressive damage showed that the proposed method is feasible for damage detection in viscously damped composite beams with transverse cracking.

Fukunaga *et al.* **[2-32]** used first order approximation technique for numerical prediction of transient response of electrical potential changes on sensors for location prediction and an iterative estimation scheme for solving non-linear optimisation problems based on quadratic programming technique to predict damage extent. Numerical studies were performed on carbon epoxy cantilever composite beam. Reduction in the elastic moduli by the same portion in all directions of one of the element in FEM model was used to simulate the damage. Since electrical potential change in time domain does not provide any distinguishable features for the location and the extent of the damage, all data was transferred to frequency domain by using fast Fourier transform technique. The authors also investigated the robustness of the technique by enlarging the response and adding white noise in the time domain. It can be

concluded from their analysis that the accuracy of the approach strongly depends on reliable modal data of the intact structure. Kessler *et al.* **[2-33]** used FRF method for the in situ detection of damage in composite materials. They concentrated on structural health monitoring aspects of the frequency response method and used it as a candidate to predict the existence of the damage in graphite/epoxy panels. They introduced different types of damage including delamination, fatigue induced damage and a drilled hole to specimens. Finite element simulations for modal response and frequency response analyses by using scanning laser vibrometer were also performed and the effect of the damage on frequency response was investigated by obtaining the first six natural frequencies of the damaged specimens. The results demonstrated that the method could not extract damage type, size, location and orientation information since several combinations of these features could yield identical responses. On the other hand, it can provide good insight as to the global condition of the system and can be implemented cheaply.

In addition to frequency-based analyses, time-frequency analysis (i.e. wavelets) is also used as a tool to extract features that can provide additional information about the damage characteristics. Wavelet decomposition is a successive approximation method that adds more and more projections onto detail spaces spanned by wavelets and their shifts at different scales. Wavelet decomposition divides up the time scale plane in such a way that high-frequency activity is described with very sharp time resolution. These capabilities of wavelet make it popular in signal processing applications.

The approach and solution procedure of damage identification by intelligent signal processing was outlined by Staszewski **[2-34]**. The author also referred to data pre-processing, feature extraction and selection, pattern recognition and data/information fusion by giving examples from wavelet and neural network applications on composite materials. Wu *et al.* **[2-35]** performed an experimental work on different composite beams having different damage types (i.e. cracks and delamination) with surface bonded piezoelectric (lead zirconate titanate PZT) patches by stimulating them at the third modal frequency. After obtaining amplitude-frequency of the output sampling signals from PZT sensors, wavelet packets were used to obtain eight auto regression spectra on these signals to extract and recognise the characteristic signal, which can be used as an input for neural network for the characterisation of the damage on composite beams. The authors concluded that this method is effective for damage characterisations but it should be generalised and implemented to identify the location and magnitude of the damage as well. Okafor and Dutta **[2-36]** used wavelet transforms to detect structural damage on an aluminium cantilever beam. Damage was simulated as a stiffness reduction in FEA and created by machining a notch on the specimen. The displacement data

corresponding to the first three modes were obtained by scanning laser vibrometer and analysed with the wavelet transform. The authors concluded that single damage was accurately located by using wavelet decomposition of the finite element test beam and the experimental beam mode shapes. It was also pointed out that the magnitude of the wavelet coefficient at the location of the damage increased linearly with the increase in the amount of damage.

Electrical impedance technique (Lopes *et al.* **[2-37]**), which utilises the electromechanical coupling property of PZT material based on high frequency structural excitation, is also used as an effective method for structural health monitoring because of its easy implementation and simple structural evaluation. The authors used model-based damage detection procedure by modelling damage as a reduction of stiffness in FEM and two cuts with different depths in the real test structure with surface bonded PZT patches. The damage metric, a function of the severity and the distance between the damage and the PZTs, indicated that damage can be localised by impedance technique and quantified by model-based detection algorithm using model generation by optimisation scheme. The same approach was also used on an aluminium cubic frame structure **[2-38]** to identify structural damage.

2.3 Artificial Neural Network Applications

It can be seen from the previous researches that change in natural frequencies helps to characterise the severity of the damage. However, locating the damage from the changes in natural frequencies alone is difficult as modal frequencies are global properties of the structure and hence cannot provide spatial information about structural changes. In order to overcome this drawback additional features, such as displacement or curvature mode shapes, which provide spatial information about the damage, can be used. In addition to these parameters, other methods including frequency, time-frequency and impedance methods are also available to obtain extra features related to damage characteristics and to detect structural damage. The analyses performed on structures under dynamic loading showed that for better estimation of severity and location of the damage, multiple modes should also be considered. Since each natural frequency and the corresponding mode are affected to different extents depending on the location of the damage, analyses become too complicated to be handled. Therefore, Artificial Neural Networks (ANNs) can be used in the post processing of vibration-based data to extract the features and to solve this inverse and non-unique pattern recognition problem.

Waszczyszyn and Ziemianski **[2-39]** summarised the application areas of back-propagation neural networks (BPNNs) and discussed some problems where ANN can be used in the analyses. They mainly concentrated on data selection and processing, design of BPNNs and the accuracy of neuro-computing. The conclusion drawn from their numerical and experimental work is that ANNs are suitable to the analysis of problems with noisy or incomplete data and they can be efficiently applied to process the experimental data where there are not known mathematical models or given a priori relationship between the input and the output data. Worden and Tomlinson **[2-40]** also used BPNN to identify (i.e. locate and quantify) the damage in a cantilever aluminium beam and plate structures. Damage was modelled with local stiffness reduction by deleting groups of elements from FEM. The authors used four different sets of data (first and second mode shapes and Yuen function for the first mode shape and curvature of the first mode) to train the ANN. The finite element simulation and ANN results showed that the curvature of the first mode of vibration appears to provide the best data for damage identification. However, the Yuen functions did not supply any useful information and proved to be unsuitable for training of BPNN. In Worden and Burrows **[2-41]**, the authors developed an algorithm using iterative insertion/detection method, genetic algorithm and simulated annealing to optimise the location and the number of the sensors for the fault detection. Optimal sensor distributions obtained from each method were used in ANN. Three different damage severities at different locations on a cantilever plate were simulated by removing small groups of elements in the FEM or setting their Young's modulus to zero. Mode shapes and curvature values were supplied to multi-layer perceptron (MLP) model in the training and location predictions were performed for the simulated damage.

Mukherjee and Ravindra **[2-42]** investigated the power of ANNs in early damage detection. A cantilever aluminium beam with different crack intensities at different locations was used in the analysis and strain time histories were obtained by performing a transient dynamic analysis with impulse excitation. Since strain time histories contain a very large number of data points which are difficult to handle, a compression tool was used to convert time histories to Haar values and these values are used as input to ANN for location and extent estimation of the damage. They observed from the time histories that the damage at the root region has more severe effect on the natural period of the structure, stiffness loss due to damage at the root is higher and the strains generally increase with the increasing damage intensity. Zang and Imregun **[2-43]** presented a method for an efficient and accurate reduction of the FRF data so that ANN technique can be applied routinely to structural damage detection. They performed principal component analysis on FRF data obtained from railway wheels subjected to

random dynamic loads during their operation. An ANN was trained with this dimensionally reduced and noise filtered data. The experimental results indicated that although the extension of the methodology to damage location is somewhat more difficult, the use of ANN with FRF data which is reduced via principal component analysis provides necessary information about the existence of the damage.

Another research (Zapico e*t al.* **[2-44]**) aimed at assessing the damage from measured modal parameters by using ANNs. The authors modelled two-storey steel frame and steel-concrete floor structures by using FEM and performed modal testing on real structures to obtain natural frequencies and mode shapes. MLP type ANN was trained to localise and find the amount of damage in the structures by using different combinations of natural frequencies and mode shapes as input. The FEA and experimental results showed that both input and output parameters should be correctly selected since too many parameters could affect the generalisation of MLP network by creating different combinations of damage leading to similar modal results. In Xu *et al.* **[2-45]**, an adaptive MLP technique was used for the detection of horizontal cracks hiding inside the carbon and glass epoxy anisotropic laminated plate. The excited surface displacement response and the crack parameters (crack size and location) were used as input and output pair for the ANN respectively. The results of the numerical study indicated that the longer and shallower the crack is, the more significant the distortion would be in the surface displacement response. They also concluded that MLP technique is very effective for the damage detection in the presence of the noise in response data.

Ball and Worden **[2-46]** concentrated on the application of ANN as a low-pass filter on vibration data to reduce its noise content. By using auto-associative training, an ANN is trained to replicate the given input at the output layer with a smaller number of nodes in the intermediate or hidden layers than in the input/output layers. By this algorithm, ANN is forced to perform some sort of data compression or filtering of the signals as they propagate from the input layer to the output layer. The case study testing the filter capabilities of ANN indicated that the use of ANN as a filter is severely restricted since there are so many limitations on the topology and the parameters affecting the performance of the network. In their other study, Worden and Ball **[2-47]** applied ANN as a tool for the condition monitoring of a simple two-dimensional cantilever framework structure. The eigenvectors (horizontal and vertical modal deflections in FEM) of the structure with ten different fault severities in the first, second and third modes were used to train an ANN with and without added random noise. It was shown that the use of modal quantities instead of using strain pattern allows the use of a more compact ANN architecture resulting in less computational work. Worden *et al.* **[2-48]** used auto-

associative neural network for the detection and classification of damage in machines (gearbox and a ball bearing) by using experimental vibration data. Four (progressive removal of 25%, 50%, 75% and 100% of one of tooth face width) and five different damage scenarios (new ball-bearing, completely broken outer race, broken cage with one loose element, damaged cage with four loose elements and badly worn ball-bearing) were created on gearbox and ball bearing respectively. The results showed that spectral information alone is inadequate for unambiguous classification and further post-processing is needed for more accurate and better condition monitoring. A static load application (Worden *et al.* **[2-49]**) was also performed to predict the position of a fault in a framework structure using ANN. The damage was created by removing a member of the framework in the experiment and simulated by giving a very low Young's modulus for that member in the FEM. Sets of strain data were obtained from strain gauges attached to the framework under different static loading and these data sets were presented to the network which was trained with finite element simulation data in order to locate the fault in the structure. The study showed that ANN trained with noise-corrupted data could successfully locate faults in the structures.

Sensburg *et al.* **[2-50]** performed three different case studies on aluminium cantilever beam, plate and a carbon fibre composite fin with a rudder. For each case, different damage scenarios were created both experimentally and simulated by using finite element software. The proposed method requires measured mode shapes and modal frequencies of the damaged structure from undamped normal modes of vibration. Structural defects are found and located by an iterative optimisation procedure minimising the structural changes to match the modes and frequencies of the damaged structure. Both FEA and test results indicated that damage could be detected from dynamic test data by using ANN. Kudva *et al.* **[2-51]** presented a damage detection scheme to estimate the size and location of the damage by using strain values at discrete locations on an aluminium stiffened panel under uniaxial compression. They used ANN as a pattern recogniser and trained it with strain values obtained from distributed set of sensors located on the damaged structure. The authors also determined the strain pattern corresponding to the intact structure by using FEA. The results showed that location detection is easier than size estimation and use of hierarchical ANN (i.e. a network trained and simulated in two steps: first step for size and approximate location of the damage and second step for exact location prediction of the damage) is more efficient than using one big network. Islam and Craig **[2-52]** modelled various length delaminations in Kevlar-epoxy composite beam by using FEM and performed modal analysis for the first five natural frequencies of cantilever composite test specimens with surface bonded piezoelectric sensors and actuators. The authors trained an ANN

using numerical model and tested for location and size prediction of delamination by using data having natural frequencies of the beam obtained from both experiment and by FEA. The simulation results showed that predicted and actual values of the size and the location of delamination were quite close to each other. Okafor *et al.* **[2-53]** presented experimental and theoretical work to investigate the effect of delaminations on modal frequencies of glass epoxy composite beam. They inserted a Teflon film into the mid-plane of the laminate to create delamination and performed modal testing to obtain natural frequencies. The first four normalised modal frequencies were used as an input to ANN for the prediction of non-dimensional delamination length. It is observed from the analyses that modal frequencies degrade with the increasing delamination size and this can be used as a signature to assess the delamination.

Roberts *et al.* **[2-54]** used ANN to find the correlations between the local forging conditions (temperature, strain rate and local strain, as input) and extent of damage (as output) that occurred on the surface of aluminium metal matrix composite brakes. This particular application of ANN showed that although three parameters are not sufficient to describe damage evolution in composite forging, ANN is able to make sensible predictions of the damage locations. Yun and Bahng **[2-55]** proposed an approach for the estimation of parameters of two-span planar truss and multi-storey frame using BPNN particularly for the case with noisy and incomplete measurement of the modal data. The data supplied as an input pattern to ANN in the training was the natural frequencies and mode shapes of the structure. The numerical analyses indicated that the accuracy of the estimation for the stiffness matrix of the system could be improved by imposing noise during the training with intensity similar to the measurement noise level and by including additional measurement information (i.e. rotational degrees of freedom).

Pandey and Barai **[2-56]** used MLP with backpropagation learning algorithm to identify damage in a twenty-one-bar truss structure simulating a bridge. The authors used ANN to identify the damage zone from vertical displacements under static load of five nodal forces. Damage was modelled by stiffness reduction, which is a function of cross-sectional area of the members. All patterns were generated with the help of finite element software and used for the training of two different ANN architectures. The authors mentioned how difficult it is to design an ANN by choosing a proper topology and all other parameters (learning rate, momentum, error tolerance, etc.) which are directly affecting the performance of the ANN. From the numerical simulation results, it was concluded that MLP model is quite appropriate for structural damage identification. By considering different architectures of ANNs used in the analysis, the one having two hidden layers showed better performance compared to that with

single layer. Barai and Pandey **[2-57]** also investigated the performance of the generalised delta rule used as a separate case in the training of ANNs for damage identification. The authors used strain data in the training and simulation of ANN and observed that strain measurement taken together with displacement measurement significantly improved the performance of the ANN. Seo and Lee **[2-58]** used the electrical resistance change as a damage parameter in fatigue damage of CFRP laminates. ANN was also used as a tool to investigate the electrical resistance damage parameter, fatigue life and stiffness reduction. In the designed ANN, electrical resistance was used as input and either stiffness or fatigue cycle was used as a separate output. It was observed during the fatigue test that measured stiffness and electrical resistance change showed similar trends of change and good agreement was achieved between the predicted values obtained from ANN and experimental study.

2.4 Sensors for Vibration Analysis and Damage Detection

2.4.1 Smart Materials

The following researchers used smart materials such as piezoelectrics (PZT), shape memory alloys (SMA) etc. as sensory material to record dynamic responses and detect the damage occurred in structures.

Chiu *et al.* **[2-59]** performed a set of numerical analyses to investigate whether the concept of smart structures can be used to detect damage in the repair itself as well as monitor damage growth in the parent structure. An array of piezoceramic elements was used to detect disbonds of adhesive layer between the repair boron/epoxy doubler and an aluminium plate structure. Two different signal analysis techniques (mechanical impedance and transfer function) were assessed to determine the presence of any disbond in the adhesive layer. In the mechanical impedance technique, the piezoceramic sensors/actuators distributed over the structure were actuated in turn and the mechanical impedance at the drive point was determined. On the other hand, in the transfer function technique, the piezoceramic actuators were actuated individually and the transfer function between the actuator and the rest of the sensors was calculated. The information obtained from the piezoceramic showed that the magnitude of the impedance and that of the transfer function decrease with increasing disbond size. Chattopadhyay *et al.* **[2-60]** investigated the effects of delamination on the dynamic response of smart composite plate by using root mean square values of the plate response to an impulsive

disturbance. The FEM used in the analysis was delaminated cantilever composite plate with five pairs of surface bonded piezoelectric actuators. The results showed that in the presence of the delamination, natural frequencies of the plate changed since there was a small reduction in the structural stiffness due to delamination. Additionally, root mean square values of the response of the delaminated plate turned out to be higher than that of the non-delaminated one and the dramatic jumps in these values in the delamination boundaries were observed.

Wang and Chang **[2-61]** proposed an active structural health monitoring system for impact damage detection in composite structures by using a built-in network of PZTs. The system used was capable of analysing the difference in sensor signals recorded in two different times (reference and damaged state), detecting the presence of damage and also identifying the location and extent of it. The authors performed experiments with graphite/epoxy composite plates on which damage was introduced by quasi-static impact. Then, in order to find the spectral components of time domain signals, swept frequency method and joint time-frequency analysis were used. The authors concluded that input energy, input frequencies, size of the damage and size of the piezoceremic patch were the major factors affecting the results during the experiment. Ogisu *et al.* **[2-62]** investigated an integrated health monitoring system with embedded SMA foil sensor and actuator in CFRP laminated panel to suppress transverse crack propagation and delamination. They performed adhesive property, tensile, compressive, and interlaminar shear strength tests on different panels with embedded SMA foils. It was experimentally found that the interlaminar adhesive strength must be improved in order to avoid failure initiating at the interface between the SMA foil and CFRP smart panel. Further investigations on the relationship between electrical resistance and strain of SMA showed that SMA foils are possible candidates for sensor application for health monitoring in composite structures.

Since the determination of the location, size and the number of sensors on the structure is one of the most important stages in the design which directly affects the performance of the algorithm using these sensors, several researchers focused on the optimisation problem to find the best location and size for smart materials used as sensors to achieve better vibration sensing and actuators for more effective vibration control of beam-like structures **[2-63]**, **[2-64]**, **[2-65]**, **[2-66]**, **[2-67]**.

2.4.2 Fibre Optic Strain Sensors

In fibre optic sensing, the response to external influence is deliberately enhanced so that the resulting change in optical radiation can be used as a measure of the external perturbation. Fibre optic sensors (FOS) serve as transducers and convert measurands like temperature, strain, rotation or electric and magnetic currents into corresponding change in the optical radiation.

FOSs have a number of advantages with respect to conventional strain sensors when they are applied to smart structure on-line health monitoring applications. Since these sensors are very light in weight, large number of them can be used without greatly increasing the mass of the structure and without significantly modifying the passive mechanical and dynamic properties of the host structure. A single fibre may have many sensors and this reduces the number of connections and increases reliability. Because of their small size, chemical and physical compatibility with materials, they can also easily be embedded in composite materials in a non-obtrusive manner that does not degrade structural integrity.

They can be used either as localised sensors that determine the measurand over a specific segment of the optical fibre and similar in the sense of conventional strain sensors or as distributed sensors, each element of which is used both for measurement and data transmission. These sensors can simultaneously sense more than one parameter (strain, temperature, etc.) with high bandwidth and the outputs can be multiplexed for high-speed data transmission resulting in a fast response time. Since FOSs are insensitive to electromagnetic interference and can withstand harsh environments, they are one of the best candidates for marine and aeronautical applications.

Considering the numerous advantages mentioned above, several investigators have opted for FOSs over other smart materials for damage detection and long time structural health monitoring.

Okabe *et al.* **[2-68]** performed an experiment on CFRP composite beam with embedded Fibre Bragg grating (FBG) sensors to detect the transverse cracks from the change in the form of the reflection spectrum. In the analysis, uncoated FBG sensors were embedded between 0-degree ply in order not to deteriorate the strength and the stiffness of the CFRP and also located on the border of 90-degree ply where the transverse cracks appeared. During the experiment, quasi-static tensile load was applied to the specimen at room temperature. Reflection spectra were measured and change in the spectrum caused by the occurrence of the transverse cracks was investigated. Since FBG sensors are very sensitive to non-uniform strain distribution influencing the reflection spectrum along the entire length of the gratings, these

types of sensors have a potential for detecting damage. The results showed that the occurrence of transverse cracks could be detected from the change in the reflection spectrum and the FBG sensors used in the experiment could detect only transverse cracks around the sensors. Therefore, as a design criterion, FOSs should be embedded in the points where cracks are expected to occur earlier than other points. Green *et al.* **[2-69]** worked on the embedded FOSs in composite materials to produce self-monitoring components for aerospace and marine applications. They concentrated on the local disturbances to the composite structure caused by embedded sensors since sensors themselves cause perturbations in the strain field within the material and this causes localised strain indication errors. The theoretical and experimental works showed that a suitable coating, good adhesion between the optical fibre and the laminated matrix, a precision contact between the sensor system and the input circuitry of the monitoring instrumentation are required in order to minimise the effect of the embedded fibre on the overall mechanical performance of a part and decrease the strain reading inaccuracy.

Dakai *et al.* **[2-70]** performed an experiment to investigate the curing effect on optical parameters of FOSs. Tests on composite structures with FOSs before and after the curing process showed that since the fibre optic coating became softened and the total length of the fibre optic became shortened after curing, great additional loss was generated. The authors also created new idea of a self-repairing network with hollow optic fibres filled with transparent glue, double ingredient epoxy resin, so as to repair the damage effectively and automatically. When the structure is damaged, the liquid core optic fibre will be damaged and the glue will flow out changing the output light signal. Then, damage location, type and extent will be shown by data acquisition system and controlled by exciting the array of SMAs, which can restore their previous shape. Additionally, if the transparency of the composite material is good, untouched measurement method can be used to detect the damage as well. Johnson *et al.* **[2-71]** employed multi-channel distributed strain measurement system with FBG sensors to monitor the structural dynamical response of a high-speed air cushion surface effect catamaran. The structure was constructed from sandwich material of a porous core and fibre-reinforced polymers and experienced normal ship vibrations, bending motions and wave slamming that may cause large scale damage. Two different techniques, scanning Fabry-Perot filter technique (suitable up to several hundred Hz with relatively high strain levels) and interferomatric technique (typically used for signals in the tens of kHz range to capture low amplitude and high frequency impact induced strains in the structure) were used to detect the strain-induced shifts in the Bragg wavelengths. The analysis of the data obtained from a group of sensors bounded to the surface of the structure in various locations with epoxy showed that FBGs are suitable measuring

system for low frequency, high amplitude strains due to bending of the hull as well as small amplitude, high frequency vibrations originating from the propulsion system.

Rippert *et al.* **[2-72]** used multi-mode based FOSs embedded into CFRP prepreg composites to measure the microbendings. The optical signal obtained from the sensor contains information not only on the strains in the structure due to loading but also on the elastic energy. This means, strain releases whenever damage occurs on the base structure. During the experiment, time and time-frequency analyses of the signal were performed using the short time Fourier transform. Acoustic waves, which were produced by the damage initiation, were also identified by modal acoustic emission. An adaptive filter was used to remove excessive noise and spectral subtraction techniques were applied to see the expected optical events more clearly. The experimental results indicated that the sensor could detect the initiation of the damage and characterise its frequency content. Han *et al.* **[2-73]** performed an experimental study with polarimetric optical fibres, which were specially integrated into the structure for vibration monitoring. The test specimen used in the experiment was a clamped-clamped sandwich plate with electro-rheological material inside. Two different types of sensor were attached to the structure by an adhesive. One of the fibre optic sensors was of integrated type and the other was of localised type. In order to determine the optimal location for these sensors, mode shapes, slopes and curvature distributions were obtained. Specimens were excited in a frequency range covering their first natural frequency. The experimental results indicated that integrated FOS is better than a localised sensor since the integrated one provides a relatively clear signal in spectral analysis.

Bhatia *et al.* **[2-74]** developed a technique for detection of edge induced and local internal delamination caused by cyclic loading of graphite-epoxy prepreg composite panel with $[90/0/0/\pm45]_s$ ply orientation. They used two extrinsic Fabry-perot interforemetric sensor pairs, one bonded at each face of the structure and the other embedded between the two pairs of adjacent [0/0] plies and parallel to graphite fibre direction of the plies. Such a configuration minimises the size of the local resin-rich region surrounding embedded elements. During the experiment, output from two embedded sensors was used to determine whether delamination occurred at any interface. Then, in order to determine the survivability of the sensors during the composite lay-up and curing, ultrasonic detection test was performed. Finally, the authors proposed that several multiplexed sensors could be used to determine the delamination locations in multi-layered composites. Davis *et al.* **[2-75]** investigated the dynamic strain characteristics of a cantilever beam with wavelength division multiplexed FBGs. Three surface bounded sensors were oriented to obtain strain information at different locations. During the experiments,

the first three vibration modes were considered. The first sensor was placed at the root of the beam to read strain from all vibration modes and the second sensor was placed at a node point of the third vibration mode and the third was mounted at a node point of the second vibration mode. This provides different sensitivities to the modes for each grating. After exciting the beam in its first three vibration modes, three peaks corresponding to natural frequencies of the beam were obtained from the FOSs. They also performed static deformation tests on this beam to obtain shape functions. Comparison between experimental and measured beam mode shapes showed good agreement with each other.

2.5 Summary

In this section, references in the literature review (i.e. numbers in brackets) are classified by considering numerical and experimental studies on various structures (**Table 2.1**), features extracted from vibration-based analysis (**Table 2.2**) and different levels of damage assessment (**Table 2.3**). After giving an introductory information about simulation of damage in finite element and experimental analysis (**Table 2.4**), different types of vibration sensors (**Table 2.5**) are compared between each other on the basis of application areas, their advantages and their main drawbacks.

Table 2.1 Damage detection on different structures

			Studies on Damage Detection		
			Numerical Simulations		**Experimental Work**
			Analytical Models	***Finite Element Models***	
Structures	**Beam**	***Isotropic***	[11] [12] [16] [17] [22] [23] [26] [28] [39] [53] [29]*	[11] [12] [13] [15] [17] [18] [19] [20] [21] [25] [26] [40]	[12] [17] [20] [22] [23] [26] [36] [42] [58]
		Composite	[32] [60]	[8] [27] [30] [31] [33] [59]	[8] [14] [27] [30] [32] [33] [35] [52] [53]
	Plate	***Isotropic***	-	[7] [24] [41] [50] [51]	[24]
		Composite	[45]	[7] [9] [30] [52]	[7] [9] [10] [30] [61]
	Truss and Frame	***Isotropic***	[37] [38]	[44] [48] [49] [55] [56] [57]	[37] [38] [48] [49]
		Composite	-	[12]	[12] [44]
	Large Structure	***Isotropic***	-	-	[25] [29] [43] [47]
		Composite	-	-	[14] [50] [54]

* Lumped mass discrete system

Table 2.2 Features and tools in damage detection

			Damage Detection Methods and Tools	
			Direct Application of Features	***Neural Network Applications***
Vibration Based Analysis [2]* [3]* [4]* [5]* [6]*	**Frequency Changes**		[7] [8] [9] [10] [11] [12] [13] [14] [17] [18] [19] [20] [27] [28] [31] [33] [60]	[16]§ [44] [46]** [50] [52] [53] [55]
	Mode Shape	***Displacement***	[12] [13] [14] [15] [17] [18] [22] [23] [24] [25] [26]	[16]§ [41] [44] [50] [55]
		Rotation	[19] [26]	-
	Mode Shape Derivatives	***Curvature***	[18] [19] [20] [21] [22] [23] [24] [25]	[40] [41] [50]
		Strain Measurement	-	[42] [44] [49] [54]
	Frequency and Time-Frequency Analysis		[27] [28] [29] [30] [31] [32] [33] [34] [35] [36] [37] [38] [59] [61]	[34] [35] [39] [43] [45] [47]
	Static Applications and Fatigue Analysis		-	[48] [51] [56] [57] [58]

*Reviews and classifications, ** Noise filtering and data compression, §Genetic Algorithm

Table 2.3 Features for different levels of damage assessment

			Levels of Damage Assessment			
			Existence	***Location***	***Severity***	***Type***
Vibration Based Analysis	**Frequency Changes**		[7] [11] [12] [13] [17] [18] [19] [20] [27] [28] [31] [33] [44] [50] [60]	[7] [8] [9] [11] [12] [17] [31] [44] [50] [52] [60]	[8] [9] [10] [13] [16] [17] [31] [44] [52] [53]	[7]*
	Mode Shape	***Displacement***	[12] [18] [24] [26] [41] [44] [50]	[12] [14] [15] [16] [17] [22] [23] [26] [44]	[22] [23] [44]	-
		Rotation	[26]	[19] [26]	[19]	-
	Mode Shape Derivatives	***Curvature***	[24] [25] [41] [50]	[18] [19] [20] [21] [24] [25] [40]	[18] [19] [21] [40]	-
		Strain Measurement	[42] [49]	[42] [49]	[42] [44] [54]	-
	Frequency and Time-Frequency Analysis		[27] [29] [30] [31] [33] [34] [37] [43] [47] [59]	[28] [29] [30] [31] [32] [34] [37] [38] [39] [45] [47] [61]	[28] [29] [30] [31] [32] [33] [34] [35] [36] [37] [38] [45] [61]	[35]
	Static Applications and Fatigue Analysis		-	[48] [51] [56] [57]	[51] [56] [57]	-

* Rough estimation

Table 2.4 Damage types and modelling

		Simulation of Different Damage Types	
		Finite Element Analysis	**Experimentally**
Damage Types	**Hole**	• Setting stiffness of the elements to zero • Removing area or deleting elements from the model	Drilling
	Saw cut, Notch and Slot	• Percentage reduction in stiffness of the elements • Percentage reduction in thickness • Percentage reduction in cross-section of the model	• Cutting with jewellers saw • Removing material from the surface
	Delamination	• Additional boundary conditions by using spring elements • Creating a cavity in the model	• Introducing a thin Teflon foil or Fluorinate Ethylene Propylene into structure • Pushing with a sharp and thin scalpel against the delamination front and forcing it to grow
	Fatigue, Transverse and Matrix Cracks	Percentage reduction in stiffness of the elements	Using tensile test machine under cyclic load
	Crush Damage	Percentage reduction in stiffness of the elements	Pressing with steel ball into structure by using hydraulic press
	Impact Damage	Impulse loading in very short time	• Impact with mallet • A marble rolling down an inclined through and striking the structure

Table 2.5 Comparison of sensory equipment

		Sensors for Vibration Analysis and Damage Detection		
		Application Areas	**Advantages**	**Drawbacks**
Sensors	***Accelerometer***	Acceleration history, Frequency and FRF measurements	Simple, easy to use, suitable for high frequency applications	Not suitable for light weight structures and online applications, interference with electro-magnetic fields
	Vibrometer	Velocity history, Frequency and FRF measurements	Non-contacting measurement, accurate	Not suitable for online applications
	Strain Gauges	Dynamic strain history and static strain measurements	Inexpensive, easy and simple procedure for bonding	Heavy and massive wiring, sensitive to temperature changes, interference with electro-magnetic fields
	PVDF* and PZT**	By covering the structure, an active surface can be obtained. Suitable for impact damage detection and it is also used as an actuator	Inexpensive, suitable for online, distributing and embedding applications, short response time and light in weight	Create a gap between layers of composite laminate in embedding applications
	SMA§	To control low frequency vibrations of flexible bodies and to achieve an active damage control as a sensor and an actuator	Suitable for online applications, available as thin wires, mesh can be obtained by embedding into structure (distributing) and light in weight	Modelling difficulties, not well known material and physical properties
	FOS§§	Dynamic strain history, frequency and FRF measurements, static strain and shape function measurements, curvature modes, load history measurements, cure monitoring in composite structures and long term structural health monitoring	High accuracy and high speed data transmission, suitable for online and embedding applications, immunity to electro-magnetic interference, multiplexing capabilities, wide bandwidth, light in weight, it responds only strain if temperature compensation is applied, linear response, it can withstand high temperatures and other harsh environments	Delicate and expensive, requires laser source

*Polyvinlydine Fluoride, ** Lead Zirconate Titanate Piezoelectrics,

§Shape Memory Alloy, §§Fibre Optic Sensor

2.6 Conclusions

A brief literature review on features obtained from vibration-based analyses, damage detection methods, tools and sensors used for vibration analyses and damage detection was presented in this chapter. The following conclusions can be drawn from this review:

- Natural frequency shift is extensively used to predict the existence of damage. Since the measurements of natural frequencies are independent from the location of the excitation and the measurement point, they can easily be obtained by using frequency response functions methods. As the changes in frequencies provide only global information about the dynamic characteristics of the structure, one is not able to relate these changes to the location, severity and type of damage. Therefore, in order to perform a complete damage assessment in the structures, other parameters giving local information about damage such as displacement or curvature (strain) mode shapes should also be included in the analyses. As this involves measurement of strains, one has to use electrical strain gauges, piezoelectric materials, shape memory alloys or fibre optic strain sensors.

- Since strain mode shapes are more effective in prediction of location and severity of damage than displacement ones, it is convenient to obtain them from distributed strain sensing systems. Considering their superiorities (**Table 2.5**) to conventional strain gauges, fibre optic strain sensors are quite promising in strain sensing applications especially in composite material applications. Moreover, in order to have cost effective solutions in strain sensing for maximum efficiency, the number and the location of the sensors should be optimised.

- Various researchers have suggested that in order to achieve better accuracy in the damage detection, multiple and higher modes should be considered. The difficulty here is that damage detection is an inverse and non-unique problem since different damage types could be responsible for the same changes in the dynamic behaviour of the structure depending on their location and extent. Therefore, an intelligent algorithm capable of dealing with noisy and incomplete data should be adapted to system for damage detection. Artificial neural networks are the best candidates for these applications because of their suitability for self-adaptiveness and applicability to problems that do not have an algorithmic solution or for which an algorithmic solution is too complicated to be found. Additionally, ANNs can serve as a data reduction tool when long time or frequency histories are available.

➢ Designing an ANN is in itself an important subject since selection of features extracted from vibration-based analyses and used as input-output pairs for training, topology of the neural network and internal parameters in the simulation are crucial from the performance point of view. Experiments have shown that strain sensors away from the damage are not effective and do not supply relevant information about damage. But use of ANN can solve this problem by using the information coming from the other sensors as well. The majority of damage detection methods require modelling either mathematically or by using finite element analysis.

Therefore, most researchers concentrate on isotropic beam or plate-like structures in their studies since modelling of both main structure itself and damage is easier compared to laminated composite and sandwich structures. Laminated composite and sandwich structures are extensively used in aeronautical, marine and civil engineering applications. Hence, one of the aims of this study is to impart the existing methods, based on vibration-based analyses, using fibre optic strain sensors and artificial neural networks, and implement them in real practical use for structural health monitoring and damage detection, especially on composite and sandwich structures.

PART B

MODELLING and ANALYSES

Chapter Three **RESEARCH PROBLEM**

3.1 Introduction

In model-dependent vibration-based damage detection approach, it is essential to have an accurate numerical model of the intact structure. Based on this model, a damaged structure is created by considering different damage scenarios; the effects of the damage on the structural response and dynamic characteristics are investigated. Then, parameters providing necessary information about the damage characteristics are extracted and compared with the undamaged reference model. Thus, the first step in damage identification is monitoring of these parameters during in-service life of the structure. In order to monitor dynamic behaviour of the structure, vibration sensors are required. After considering various application dependent criteria about type, number and location of these sensors, a data management scheme needs to be implemented. This procedure includes obtaining and processing of the data by extracting features, filtering and compressing them and storing the necessary information that can be used as input for the detection algorithm. Finally, the designed intelligent algorithm is used to detect, locate and quantify the damage in the structure.

3.2 Solution Methodology

The procedure can be divided into three main parts: numerical analysis based on finite element modelling, experimental analysis and verification of the method. This is illustrated in **Fig. 3.1**.

In the numerical analysis part, fixed-free beam-like models (steel, fibre reinforced plastic laminated composite and sandwich beams) were generated by using finite element software (ANSYS 6.1®) and the damaged models were created from these undamaged models by using different damage scenarios. After obtaining the models, static and dynamic finite element analyses are performed. The aim of the static analyses on the steel and sandwich beams is to find the strain values at particular locations where strain gauges and FBG strain sensors are

located. These numerical strain data obtained from undamaged finite element models are then compared to experimental analysis results in order to calibrate gauges and FBG strain sensor and to check structural coupling between the beam and the sensors. The dynamic analyses are aimed to find global (natural frequencies) and local (curvature and strain mode shapes) vibration characteristics of the structures. After performing sensitivity analysis on these vibration data, some features such as, reduction in natural frequencies due to damage and maximum absolute differences in curvature mode shapes between the undamaged and damaged structures, are extracted. An artificial noise has been added to these features in order to simulate experimental uncertainties. Finally, all data are normalised before introducing them to ANNs. After designing different ANNs for damage localisation and quantification, the input-output pairs obtained from FRP laminated beam model are introduced to these neural networks for training and validation of the algorithm. A set of test cases is also used for severity and location prediction of the damage.

In the second part, cantilever steel and sandwich beams with real structural damage are used in experimental static and dynamic analyses. Static analyses are performed by using surface bonded strain gauges and FBG strain sensors on an intact steel beam for calibration purposes. In the dynamic analyses, miniature piezoelectric accelerometers are used to obtain frequency response amplitudes, from which resonant frequencies and damping ratios can be extracted. Having found the resonant frequencies, intact and damaged beam specimens have been excited at those particular frequencies to obtain dynamic strain mode shapes via the distributed strain gauges. Finally, all theoretical, finite element and experimental analysis results are compared with each other.

In the final part, an experimentally validated damage detection algorithm, which uses combination of global and local vibration-based analysis data as input to ANNs for location and severity prediction of damage in isotropic beam structures, is presented before generalising it for damage assessment of sandwich beam structures with embedded FBG strain sensors.

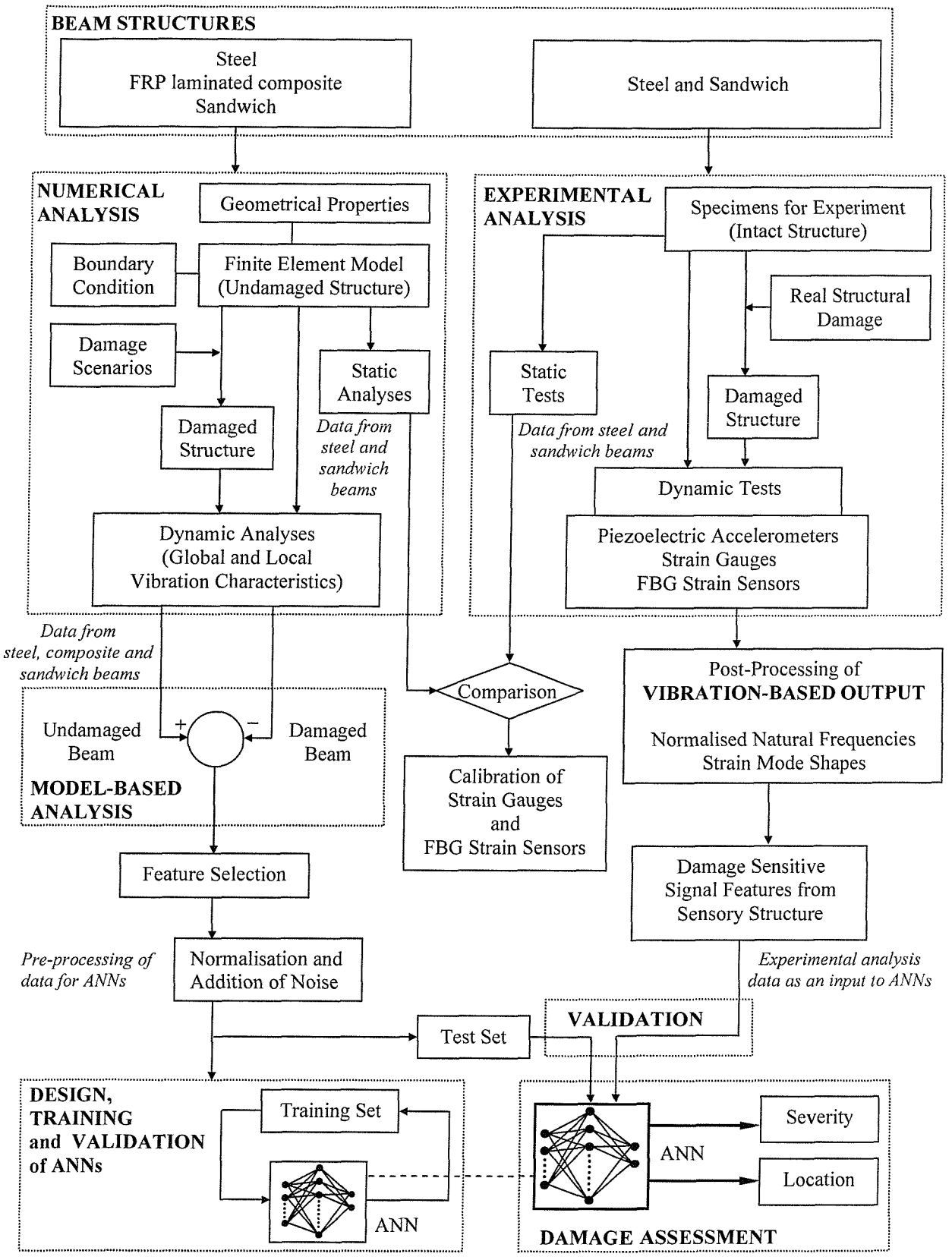

Figure 3.1 Outline of the method and procedure

Chapter Four THEORETICAL MODELLING

4.1 Introduction

In order to investigate the dynamic behaviour of the structure, free vibration characteristics are of primary importance. Hence, in this chapter, equations of motion for transverse vibration of a beam-like structure are derived with corresponding boundary conditions. Solution for natural frequencies, displacement and curvature mode shapes are presented by following a successive set of simplifications from introduced theoretical background for laminated composite and sandwich plates. After presenting an overview about possible damage types and mechanisms in structures, the analysis tool selected for damage detection is reviewed reflecting its application areas, capabilities and design criteria.

4.2 Dynamic Characteristics of Structures

There are two main composite panel topologies namely; single-skin fibre-reinforced composites and sandwich panels. FRP laminated materials are composed of two distinct phases. One phase (fibre) acts as reinforcement of a second phase, so called matrix. These two phases of composite must be carefully chosen so as to obtain a material which is structurally efficient. Since the choice of materials (fibre and matrix), volume fraction, layer orientation, number of layers in the specified direction, thickness of the individual layers, type of the layer and the stacking sequence of the layers are the primary parameters in the designing process, composites can be fabricated for particular application to achieve a specific demand. Additionally, their low weight, high stiffness, high strength, low thermal expansion, low (or high) rate of heat transfer, electrical conductivity (or non-conductivity), corrosion resistance and longer fatigue life make them one of the strongest candidate and most commonly used material in aerospace, marine and offshore, civil, automotive, medical and military applications **[4-1], [4-2], [4-3]**. On the other hand, a sandwich structure which consists of three distinct layers (i.e. the bottom face, top face and the core) is a special form of laminated composite structure. The thin stiff faces act together

to form an efficient stress couple that counteracts the external bending moment and thick, light and considerably weak core (i.e. relative to the skin) resists shear and stabilises the faces against buckling or wrinkling. The main advantage of sandwich construction is that the strength and stiffness can be increased without a corresponding increase in the weight **[4-4]**. **Figure 4.1** shows schematic drawing of laminated composite and sandwich structures.

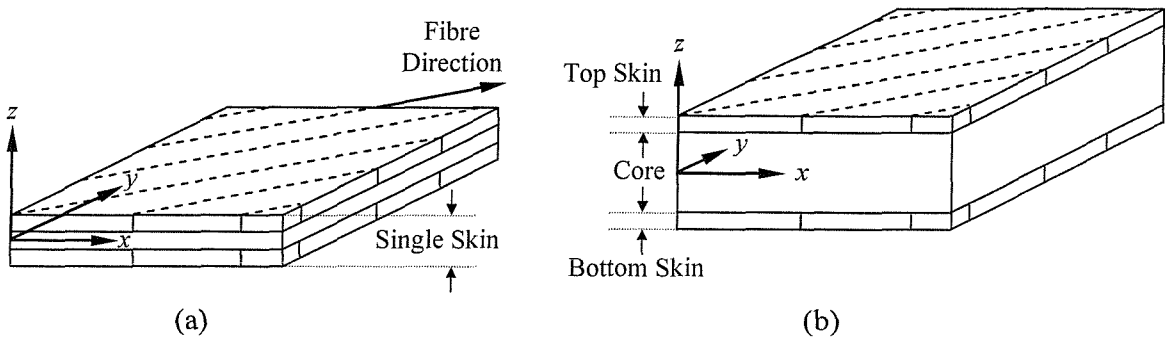

(a) (b)

Figure 4.1 Schematic drawing of structures (a) Laminated composite (b) Sandwich

In this section, in order to investigate the behaviour of composite (**[4-5]**, **[4-6]**) and sandwich structures, basic theories of plates are briefly reviewed by presenting the formulation and the assumptions considering different geometrical and material criteria in the calculations. These theories can be found in four main categories:

i) Classical thin plate theory (CPT)
ii) First order shear deformation theory (FSDT)
iii) Higher order shear deformation theory (HSDT)
iv) Theory of three-dimensional elasticity (3-D)

In most applications, the thickness of the plate is small compared to the planar dimensions and hence two-dimensional theories (i, ii, and iii) are frequently used.

In classical thin plate theory (CPT, **[4-7]**, **[4-8]**) the transverse shear effects are neglected according to Kirchhoff assumption assuming that the lines perpendicular to the mid-plane before deformation remain perpendicular after deformation. This means the in-plane displacements are assumed to vary linearly through thickness and the transverse displacement is

assumed to be constant through the thickness of the plate. Displacement components in CPT are defined as follows:

$$\begin{aligned} u_1(x,y,z) &= u(x,y) - \frac{\partial w}{\partial x} \cdot z \\ u_2(x,y,z) &= v(x,y) - \frac{\partial w}{\partial y} \cdot z \\ u_3(x,y,z) &= w(x,y) \end{aligned} \tag{4.1}$$

where u_1 and u_2 are in-plane displacements in x and y direction respectively and u_3 is the displacement in the thickness direction (z direction). u and v are mid-plane translation components and the partial derivative of w with respect to x and y are the rotation angles. This theory is adequate for analysis of thin plates, especially when transverse deformation is negligible. If the structure in the analysis is fibre reinforced composite laminate, the extension of CPT, which is classical laminated plate theory (CLPT), is used for the analysis of thin plates. In this case since the total number of displacement variables does not depend on the number of layers in the laminate, it is suitable for the analysis of thinner laminates. However, the weakness in the theory is that fibre reinforced composites where elastic modulus along the fibre direction is significantly higher than the effective transverse shear moduli are susceptible to thickness failures and therefore CLPT is not recommended to be used for composites that are likely to fail in transverse shear or delamination.

The more general form of the displacement field (Eq. 4.2) considers the effect of transverse shear on the bending of elastic plates that leads to the development of the first order shear deformation theory (FSDT, **[4-9]**, **[4-10]**). The FSDT is more commonly known as "the Mindlin plate theory".

$$\begin{aligned} u_1(x,y,z) &= u(x,y) - \phi_1 \cdot z \\ u_2(x,y,z) &= v(x,y) - \phi_2 \cdot z \\ u_3(x,y,z) &= w(x,y) \end{aligned} \tag{4.2}$$

where rotational angles are replaced with more general form of variables (ϕ_1, ϕ_2) including shear. FSDT yields a constant value of transverse shear strain through the thickness of the plate and thus requires shear correction factors. For composite laminates these factors generally depend on ply orientation, lamination scheme, geometry and boundary conditions. This theory

does not consider the effects of cross-sectional warping, which plays an important role in sandwich structures with stiff face and weak core and results in an unrealistic variation of the transverse shear stress through thickness of the laminate.

The higher order shear deformation theories (HSDT, **[4-11]**, **[4-12]**, **[4-13]** **[4-14]**, **[4-15]**) are based on assumed higher order expressions of the displacement field. The most general form (up to and including third order) for HSDT is "Reddy's strain consistent third order theory" **[4-7]** and defined as:

$$\begin{aligned} u_1(x,y,z) &= u(x,y) + \alpha \cdot z \cdot \frac{\partial w}{\partial x} + \beta \cdot z \cdot \phi_1 + \lambda \cdot z^2 \cdot \psi_1 + \gamma \cdot z^{3\cdot} \cdot \theta_1 \\ u_2(x,y,z) &= v(x,y) + \alpha \cdot z \cdot \frac{\partial w}{\partial y} + \beta \cdot z \cdot \phi_2 + \lambda \cdot z^2 \cdot \psi_2 + \gamma \cdot z^{3\cdot} \cdot \theta_2 \\ u_3(x,y,z) &= w(x,y) + \lambda_1 \cdot z \cdot \psi_3 + \gamma_1 \cdot z^{2\cdot} \cdot \theta_3 \end{aligned} \tag{4.3}$$

where ϕ_1 and ϕ_2 are rotations of a transverse normal about y and x axes, respectively and ψ_i and θ_i are undetermined functions. Depending on the constants (i.e. tracers, $\alpha, \beta, \lambda, \lambda_1, \gamma$ and γ_1), classical, first, second and third order theories can be obtained. For example,

$\alpha = 0, \beta = 1, \lambda = 1, \gamma = \lambda_1 = \gamma_1 = 0$ gives second-order theory and

$\alpha = 0, \beta = 1, \lambda = 0, \gamma = 1, \lambda_1 = \gamma_1 = 0$, $\theta_1 = -\frac{4}{3h^2}(\phi_1 + \frac{\partial w}{\partial x})$ and $\theta_2 = -\frac{4}{3h^2}(\phi_2 + \frac{\partial w}{\partial x})$ gives

third-order theory of Reddy. The major drawback of the conventional HSDT lies in that it is unable to satisfy the interlaminar continuity from layer to layer and stress equilibrium over the lateral surfaces without regard to the transverse normal stress.

Three-dimensional theories (3-D, **[4-16]**, **[4-17]**, **[4-18]**) use three-dimensional displacement fields with various edge boundary conditions in terms of double Fourier series in x, y in-plane and polynomials in z out-of-plane coordinates as follows:

$$
\begin{aligned}
u_1^k(x,y,z) &= \sum_{j,m,n}\left[U_{jmn}Z_j(z)U_m(x)U_n(y)\right]^k \\
u_2^k(x,y,z) &= \sum_{j,m,n}\left[V_{jmn}Z_j(z)V_m(x)V_n(y)\right]^k \\
u_3^k(x,y,z) &= \sum_{j,m,n}\left[W_{jmn}Z_j(z)W_m(x)W_n(y)\right]^k
\end{aligned}
\tag{4.4}
$$

where k is the layer number.

By using energy variational approach, small strains are expressed in terms of displacements as:

$$
\begin{aligned}
&\varepsilon_{xx} = \frac{\partial u_1}{\partial x}, \quad \varepsilon_{yy} = \frac{\partial u_2}{\partial y}, \quad \varepsilon_{zz} = \frac{\partial u_3}{\partial z}, \\
&\gamma_{yz} = \frac{\partial u_3}{\partial y} + \frac{\partial u_2}{\partial z}, \quad \gamma_{xz} = \frac{\partial u_3}{\partial x} + \frac{\partial u_1}{\partial z}, \quad \gamma_{xy} = \frac{\partial u_2}{\partial x} + \frac{\partial u_1}{\partial y}
\end{aligned}
\tag{4.5}
$$

where ε's and γ's are normal and shear strains respectively. The relation between strain and stress (σ_{ij}) for general anisotropic material is

$$
\sigma_{ij} = C_{ijkl} \cdot \varepsilon_{kl} \quad \text{where} \quad \varepsilon_{kl} = \frac{1}{2}\gamma_{kl}
\tag{4.6}
$$

having 21 independent stiffness constants. For more special cases such as, orthotropic (9 constants), orthotropic material with transverse isotropy (5 constants) and isotropic material (2 constants), the number of independent stiffness constants reduces. The generalised equations of motion can be derived by using following energy equations (Eq. 4.7) considering each layer and the boundary conditions.

$$
\begin{aligned}
V &= \sum_{p=1}^{P}\int_{v_p}\left\{\frac{1}{2}\sigma_{ij}\varepsilon_{kl}\right\}_p dx\,dy\,dz, \qquad i,j,k,l = x,\ y,\ z, \\
T &= \sum_{p=1}^{P}\int_{v_p}\left\{\frac{1}{2}\rho\left(u_{1,t}^2 + u_{2,t}^2 + u_{3,t}^2\right)\right\}_p dx\,dy\,dz
\end{aligned}
\tag{4.7}
$$

where V and T are the strain and kinetic energy components respectively and subscript t and variable P indicate time derivative of the terms in the equation and the total number of layers respectively.

Since the solution of Eq. 4.7 is beyond the scope of this study, the solution for natural vibration of special case (cantilever isotropic beam) is given by considering further simplifications from vibration of plate structures.

The governing equation for natural vibration of an isotropic plate can be expressed with the following homogenous equation:

$$D\left[\frac{\partial^4 w}{\partial x^4}+\frac{\partial^4 w}{\partial x^2 \partial y^2}+\frac{\partial^4 w}{\partial y^4}\right]+\rho \cdot h\frac{\partial^2 w}{\partial t^2}=0 \quad \text{where} \quad D=\frac{Eh^3}{12(1-\nu^2)} \tag{4.8}$$

where E, h, ρ and ν are the modulus of elasticity, thickness, density and Poisson's ratio of the beam respectively. Since beams have variation only in one direction, fourth-order differential equation of motion can be simplified considering an elemental length of beam undergoing vibratory motion so as to find the lateral vibration characteristics of the uniform beam structures **[4-19], [4-20], [4-21], [4-22]**. Hence, Eq. 4.8 can be simplified by using following relations:

$$EI\left[\frac{\partial^4 w}{\partial x^4}\right]+\rho \cdot A\frac{\partial^2 w}{\partial t^2}=0 \quad \text{where} \quad E \cdot I = D \cdot b \ , \ \nu = 0 \tag{4.9}$$

where b, A and I are the width, cross-sectional area and second moment of area of the beam respectively. A new variable can be assigned for w as $Y(x,t)$ having spatial variable in x direction only. For free vibration solution, separation of variables can be used as:

$$Y(x,t)=\tilde{y}(x)y(t) \tag{4.10}$$

or it can be in the form of

$$Y(x,t)=\sum_{i}^{N}\tilde{y}_i(x)y_i(t) \tag{4.11}$$

if the structure vibrates in a number of modes. Considering equations (4.10) and (4.11), $\tilde{y}$, $y(t)$, i and N are mode shape, a function of time, mode number and the total number of modes respectively. In free vibration case equation (4.12) defines the total transverse deformation of the structure.

$$Y(x,t) = \sum_{i}^{N} A_i \tilde{y}_i(x) \sin(\omega_i t + \phi_i) . \tag{4.12}$$

Substituting equation (4.12) into (4.9) gives

$$\frac{\mathrm{d}^4 \tilde{y}}{\mathrm{d}x^4} - \beta^4 \tilde{y} = 0 \quad \text{where } \beta^4 = \frac{\rho A \omega^2}{EI} \text{ and } \omega = 2\pi f \tag{4.13}$$

where ω and f are the natural frequencies of the beam measured in rad/s and Hz, respectively. The general solution for equation (4.13) is in the form of

$$\tilde{y}(x) = C_1\cos(\beta x) + C_2\sin(\beta x) + C_3\cosh(\beta x) + C_4\sinh(\beta x) \tag{4.14}$$

where C_1, C_2, C_3 and C_4 are the constants to be determined from boundary conditions. For fixed-free beam (Eq. 4.15) having a length of L

$$\text{at } x = 0, \quad \tilde{y}(0) = 0 = \left.\frac{\partial \tilde{y}}{\partial x}\right|_{x=0} \text{ and at } x = L, \quad \left.\frac{\partial^2 \tilde{y}}{\partial x^2}\right|_{x=L} = 0 = \left.\frac{\partial^3 \tilde{y}}{\partial x^3}\right|_{x=L} . \tag{4.15}$$

Applying equation (4.15) on (4.14), the transcendental equation for λ can be expressed as:

$$\cos(\lambda)\cosh(\lambda) + 1 = 0 \quad \text{where } \lambda = \beta L . \tag{4.16}$$

The solution of this equation gives the natural frequencies of the fixed-free beam as,

$$f_i = \frac{\lambda_i^2}{2\pi L^2}\left(\frac{EI}{m}\right)^{1/2} \qquad m = \rho A \tag{4.17}$$

and for the first three modes; $\lambda_1 = 1.87510407$ $\lambda_2 = 4.69409113$ $\lambda_3 = 7.8547574$

where f_i, λ_i and m are the natural frequency (in Hertz), dimensionless parameter which is a function of the boundary conditions and mass per unit length of the beam respectively.

The shape of the natural modes is calculated from following equation:

$$\tilde{y}\left(\frac{x}{L}\right) = \cosh(\frac{\lambda_i}{L}x) - \cos(\frac{\lambda_i}{L}x) - \kappa_i\left[\sinh(\frac{\lambda_i}{L}x) - \sin(\frac{\lambda_i}{L}x)\right] \tag{4.18}$$

$$\kappa_1 = 0.73409514, \quad \kappa_2 = 1.018467319 \quad \kappa_3 = 0.999224497$$

where κ 's are the constants depending on the boundary conditions.

Figure 4.2 shows the first three normalised displacement mode shapes of the fixed-free beam plotted using Eq. 4.18.

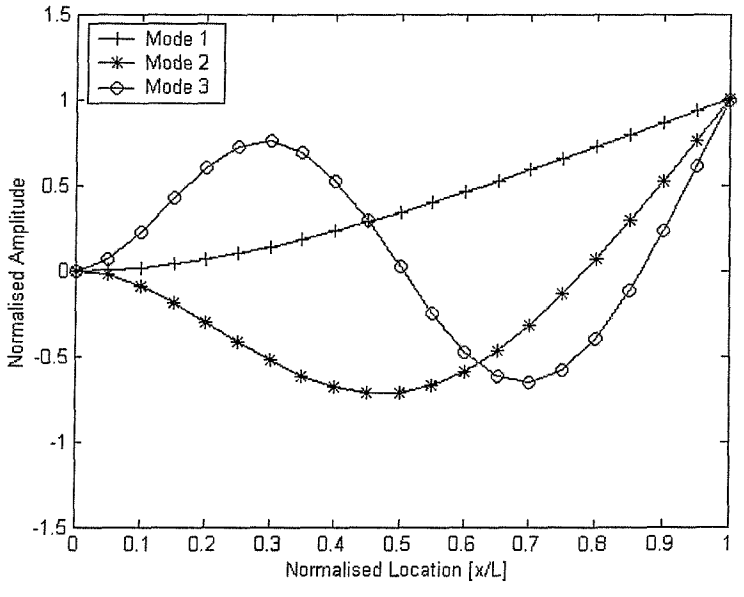

Figure 4.2 Normalised displacement mode shapes of fixed-free beam

The curvature mode shapes (Eq. 4.19) can be obtained by taking the second spatial derivative of the non-dimensional displacement mode shape equation (Eq. 4.18).

$$\frac{d^2\tilde{y}\left(\frac{x}{L}\right)}{dx^2} = \frac{\lambda_i^2}{L^2}\left[\cosh(\frac{\lambda_i}{L}x) + \cos(\frac{\lambda_i}{L}x) - \kappa_i\left(\sinh(\frac{\lambda_i}{L}x) + \sin(\frac{\lambda_i}{L}x)\right)\right] \tag{4.19}$$

The first three normalised curvature mode shapes ($\tilde{y}'' = \frac{L^2}{\lambda_i^2}\frac{d^2\tilde{y}}{dx^2}$) of the fixed-free beam are shown in **Fig. 4.3**.

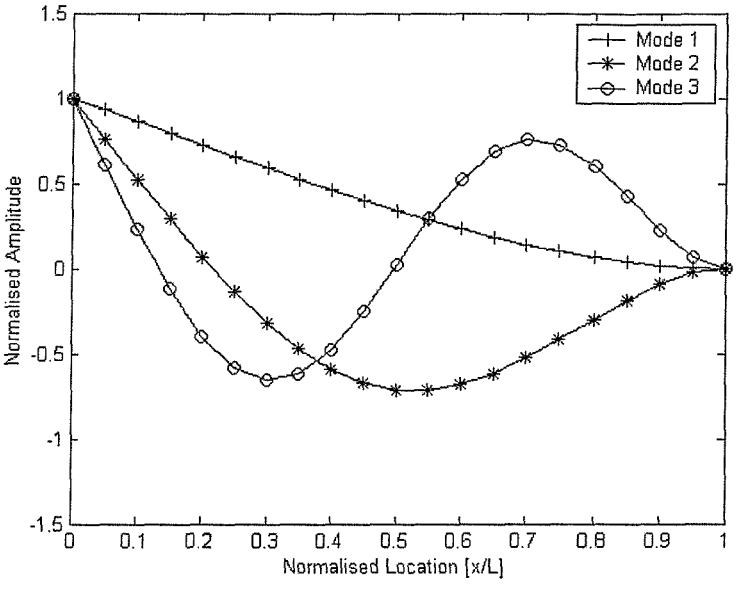

Figure 4.3 Normalised curvature mode shapes of fixed-free beam

4.3 Damage Mechanisms in Structures

Damage may be in different forms in various structures resulting from a number of causes. Considering isotropic structures, the type of the damage mostly observed is a crack that changes the dynamic characteristics of the structure under vibratory motion. On the other hand in composite structures, there are two main types of failure mechanisms in a single lamina: micromechanical and macromechanical.

Micromechanical failures take the forms of transverse matrix cracking due to a brittle matrix and a relatively strong interface, fibre-matrix debonding due to weak interface, shear fractures caused by relatively ductile matrix and strong interface and fibre failures such as, fibre breakage, fibre pullout and fibre buckling (i.e. kinking) **[4-1]**.

Macromechanical failures can be implemented by four widely used failure theories valid for individual homogeneous laminae with orthotropic material properties, namely: Maximum stress, maximum strain, Tsai-Hill and Tsai-Wu **[4-2]**. Failure analysis of a laminate is much more difficult than that of a single lamina. The main three definitions of failure used in

this case are initial (first-ply) failure, ultimate laminate failure and interlaminar failure. In sandwich structures, delamination between the face and the core material is one of the most common types of damage since this is the interface where two different materials meet and generally they have the tendency of separation from each other under vibration.

Definition of the damage is one of the most important criteria to be considered during the designing stage of a detection algorithm. The term damage detection used in this thesis is to express the use of measured or simulated structural dynamic responses (or their derivatives) in detecting changes in the condition of the structure.

Throughout the thesis, different types of local structural damage are created experimentally and simulated numerically by using finite element analysis tool. In order to detect these damage, model-dependent vibration-based analyses are performed on different beam-like structures considering the effect of the damage on vibration characteristics of the structure. Depending on the size of the structure and the damage and the number of parameters monitored during in-service life of the structure, large number of sensors may be required. This brings the necessity of a damage detection algorithm that can handle large number of sensors and the complex signals generated from these sensors by using analytically generated data simulating possible damage scenarios.

4.4 Damage Detection Algorithm

Investigation of structural damage is a pattern recognition problem. This is an important component of both data pre-processing and decision making and it can be categorised in three different groups. These are namely: Statistical (or decision theoretic), syntactic (or structural) and neural network based approaches. Statistical approaches are on the basis of probability and probability density functions for characterisation. On the other hand, syntactic pattern recognition approach uses interrelationship or interconnections of features providing structural information for classification and description. Finally, neural network based approaches including hierarchical structures, clustering, pattern association and learning are the black-box implementation of pattern recognition algorithms **[4-23]**.

The algorithm adopted here is based on ANN, an information-processing algorithm that is inspired by the way which brain processes information. As the brain has multiple neurons working together in parallel to process information, similarly an ANN can be configured and

trained through a learning process by non-linear parameterised mapping between the input and the output sets via their highly interconnected processing elements **[4-24], [4-25], [4-26], [4-27]**.

The main advantages of ANNs are their applicability to problems that do not have an algorithmic solution or for which an algorithmic solution is too complicated to be found. Besides this, ANN offers other capabilities like self-adaptiveness, generalisation and abstraction capabilities. In recent years, they have been widely used to investigate the estimate damage in isotropic and composites structures. In the following sections, brief theoretical background about ANN will be given.

4.4.1 General Neuron Model

Since ANNs have been inspired and influenced by the human biological nervous system, the best way to understand the structures of a general artificial neuron is to make an analogy with a typical biological neuron. Neuron, the basic computing element of the biological system, is a small cell composed of a nucleus, soma (cell body of the neuron), axon (neurons' output channel), dendrites (neurons' input receptors for coming signals) and synapses (interconnection points between neurons which couple the axon with the dendrite of another cell). Neurons receive electrochemical stimuli from multiple sources and respond by generating electric pulses transmitted to other neurons via their dendrites' synapses. The magnitude of the signal received by a neuron from another depends on the efficiency of the synaptic transmission and if enough active inputs are received at once then the neuron will be activated and fired by propagating a sequence of action potential spikes down the axon to either excite or inhibit other neurons; if not, then the neuron will remain in its interactive, quiet state. **Figure 4.4** shows a biological neuron.

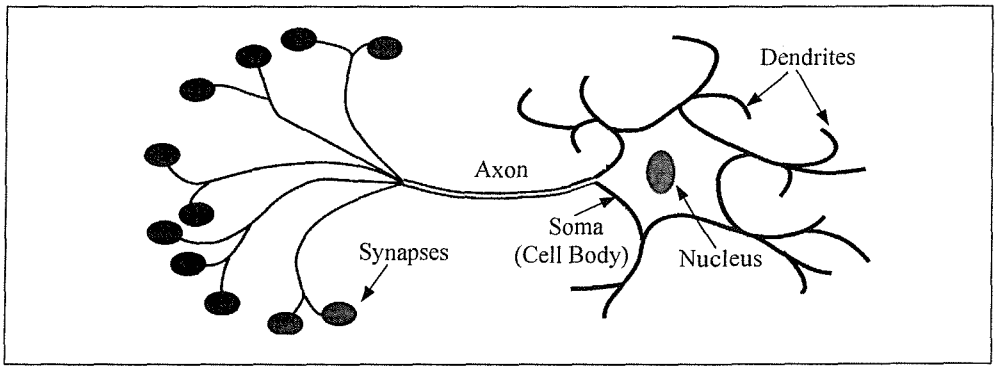

Figure 4.4 A biological neuron

On the other hand, the corresponding artificial neuron has a set of inputs ($x_1, x_2, ...x_n$) with associated weights ($w_1, w_2, ...w_n$). These inputs applied to artificial neurons are summed in the next level providing a neuron output ($net = \sum_i^n w_i x_i$). Then, a threshold operation by using activation functions (such as, step, linear, ramp, hyperbolic tangent, sigmoid, etc.) is performed on the net signal and the final output signal transferred to other neurons is calculated. An artificial neuron model is shown in **Fig. 4.5**.

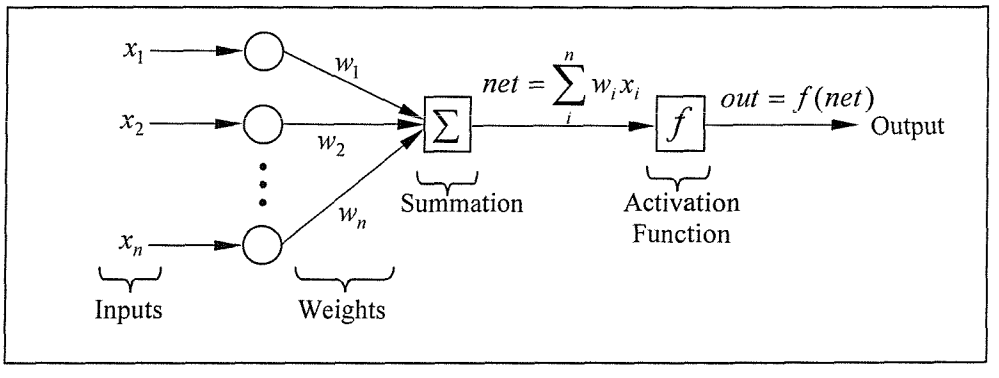

Figure 4.5 An artificial neuron

4.4.2 Design of ANNs

ANNs can be categorised in different subgroups considering their architecture, direction and type of connection, learning strategies and methods. Single-layer network is the simplest ANN, which is a group of neurons providing a simple output from a weighted sum of the inputs. By connecting neurons of single-layers in series, multi-layer ANN is obtained. ANNs may have a type of connection between the neurons either within the same layer (intralayer networks) or between different layers (interlayer networks). If the information is fed in one direction (from input to output) by using weights then it is called feedforward (nonrecurrent) network. On the other hand in feedback (recurrent) networks, the final output is calculated by using connections extending from output layer to layer of inputs. Since ANNs have the ability of learning, which is achieved via training, they can be categorised as supervised and unsupervised by considering training methods. The main aim of training the network is to adjust the weights so that introducing a set of inputs produces the desired set of outputs. Supervised training requires a pair of input and desired output (target) vectors sequentially applied by calculating the

difference (error) and feeding back through the network and changing the weights according to an algorithm that minimises the error. In contrast with supervised training, unsupervised training does not need any target vectors and it uses an algorithm that modifies the network weights in such a way that similar vectors are clustered into same classes as an output pattern. In those types of training methods, learning is achieved by examining different sample data or the environment.

As multi-layer neural networks are quite powerful in solving pattern recognition problems and can be trained to approximate any function arbitrarily well, they are selected and used in this study. The reason for adopting supervised type of learning with feedforward backpropagation is from the fact that the inputs and desired outputs (i.e. targets) are known for samples in the training data, which is generated using FEA from different damage scenarios. Since backpropagation algorithm adjusts the connections only between the layers, the designed ANNs have interlayer type of connection. **Figure 4.6** shows the classification of ANNs with most popular learning methods.

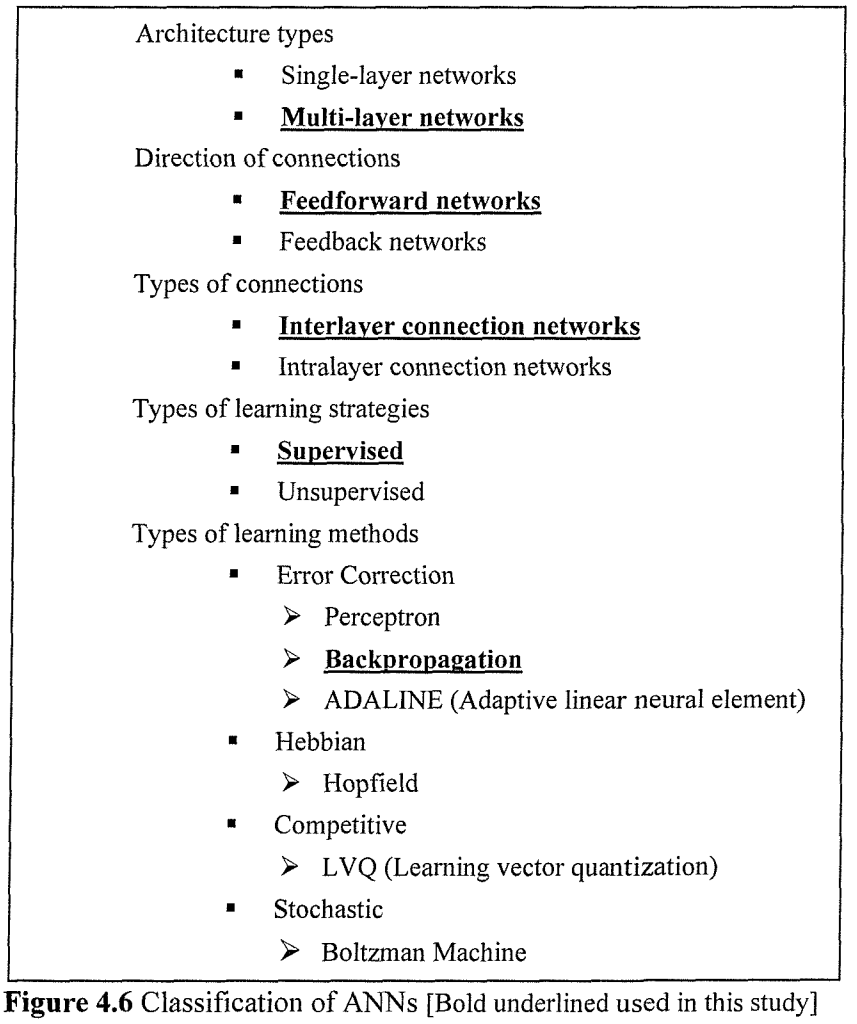

Figure 4.6 Classification of ANNs [Bold underlined used in this study]

4.4.3 Multi-layer Feedforward BPNNs

Multi-layer feedforward ANN with backpropagation (so called pattern associator) **[4-28], [4-29]** used in this thesis is one of the most common neural network having supervised learning strategy and error correction learning method (generalised delta rule) with applicability in classification, pattern recognition, prediction and optimisation applications.

Multi-layer networks have three layers: an input layer, output layer and a layer in between which is not connected directly to the input or the output so called the hidden layer if more than three-layers are used. There is always one input and one output layer but there might be more than one hidden layers in multi-layer networks. Each layer has its own nodes depending on the number of input-output pairs and the topology of the network. The learning rule in multi-layer perceptrons is called the "generalised delta rule" or generally "backpropagation rule". **Figure 4.7** shows the schematic representation of the variables and the architecture of the multi-layer neural network.

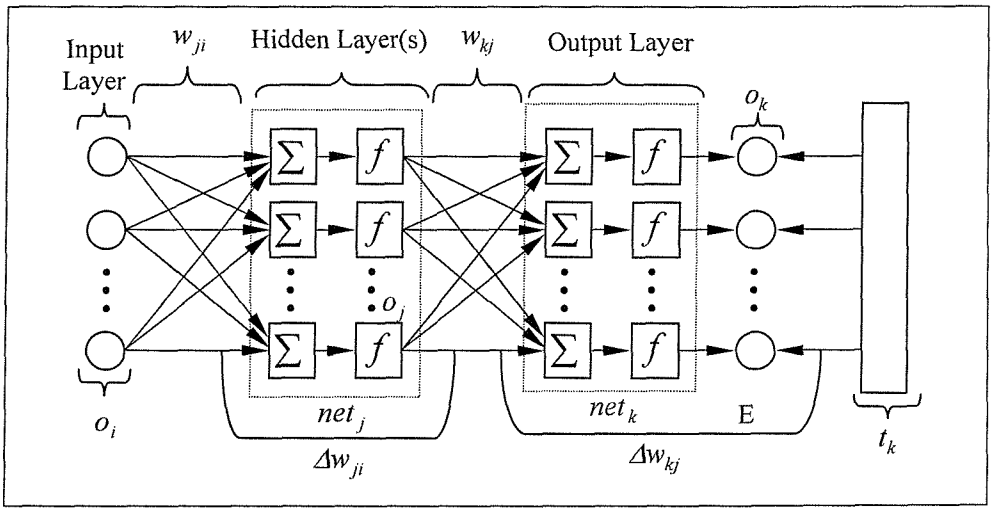

Figure 4.7 Multilayer neural network architecture

The theoretical calculations and the implementation of the algorithm are given by considering the optimisation procedure based on gradient descent that adjusts the weights in order to reduce the system error. During the learning phase, input and output pairs are introduced to the network and the training pattern propagates from input layer to output layer (i.e. feedforward). The computed output is compared with the desired output (target) values and the error values are calculated. When the process is repeated a number of times (i.e. training),

those error values are fed in the backward direction from output to input layer (i.e. backpropagation) to modify the weights until the total output error converges to a minimum or until some limit is reached in the number of training iterations (i.e. epochs).

As can be seen from **Fig. 4.7**, the very first step in the calculations is selecting input data, o_i ($i = 1,2,\ldots,n$), for training and initialising the weights randomly. Then, net input at the node in layer j ($j = 1,2,\ldots,m$) and k ($k = 1,2,\ldots,r$) are calculated as,

$$net_j = \sum_{i=1}^{n} w_{ji} o_i \text{ and } net_k = \sum_{j=1}^{m} w_{kj} o_j \tag{4.20}$$

and the respective outputs of node j and k after performing the calculations by using activation function are

$$o_j = f(net_j) \text{ and } o_k = f(net_k). \tag{4.21}$$

In this analysis, the threshold non-linear node function used is sigmoid activation (**Fig. 4.8**) which is continuous and differentiable everywhere and it is mathematically expressed as:

$$f(net) = \frac{1}{1+e^{-net}}. \tag{4.22}$$

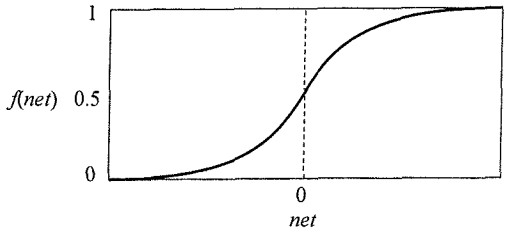

Figure 4.8 Sigmoid activation function

The training is processed by introducing input-output pairs and stabilising the weights in such a way that the square of the error, E_{tot}, in the system (Eq. 4.23) is minimised and hence the outputs, o_k, converged to desired target values, t_k.

$$E_{tot} = \frac{1}{P}\sum_{p=1}^{P} E^p \quad \text{where } E^p = \frac{1}{2}\sum_{k=1}^{r}\left(t_k^p - o_k^p\right)^2 \tag{4.23}$$

where p denotes the number of training patterns. The minimum error between the output and the target values is computed by taking the derivative of the function E^p and introducing the learning parameter, η (note that the superscript p is dropped for simplicity, i.e. $E^p = E$). The error in weights between input and the hidden nodes and between hidden and the output nodes are calculated respectively as:

$$\Delta w_{ji} = -\eta\frac{\partial E}{\partial w_{ji}} \text{ and } \Delta w_{kj} = -\eta\frac{\partial E}{\partial w_{kj}}. \tag{4.24}$$

Using the chain rule for the partial derivative calculation

$$\frac{\partial E}{\partial w_{kj}} = \frac{\partial E}{\partial net_k}\frac{\partial net_k}{\partial w_{kj}} = \frac{\partial E}{\partial net_k}\frac{\partial}{\partial w_{kj}}\left(\sum_{j=1}^{m} w_{kj} o_j\right) = \frac{\partial E}{\partial net_k} o_j \text{ where } \delta_k = \frac{-\partial E}{\partial net_k} \tag{4.25}$$

therefore equation (4.24) can be rewritten as

$$\Delta w_{ji} = \eta\delta_j o_i \text{ and } \Delta w_{kj} = \eta\delta_k o_j \ . \tag{4.26}$$

Here, the calculation of δ is a recursive process and obtained by using chain rule and equation (4.26).

$$\delta_k = -\frac{\partial E}{\partial net_k} = -\frac{\partial E}{\partial o_k}\frac{\partial o_k}{\partial net_k} \text{ where } \frac{\partial E}{\partial o_k} = -\left(t_k - o_k\right) \text{and } \frac{\partial o_k}{\partial net_k} = f_k'(net_k) \tag{4.27}$$

hence

$$\delta_k = -\left(t_k - o_k\right) f_k'(net_k) \tag{4.28}$$

and following similar procedure for the internal nodes

$$\delta_j = f_j'(net_j)\sum_{k=1}^{r}\delta_k w_{kj} \tag{4.29}$$

All weights are modified accordingly by using equation (4.30) in the training process introducing each input-output set to ANN.

$$\begin{aligned} w_{ji}^{new} &= w_{ji}^{old} + \Delta w_{ji} = w_{ji}^{old} + \eta\delta_j o_i \\ w_{kj}^{new} &= w_{kj}^{old} + \Delta w_{kj} = w_{kj}^{old} + \eta\delta_k o_j \end{aligned} \tag{4.30}$$

Parallel to training, another set of data is also used to monitor the error during the validation. Finally, new test cases are introduced to ANNs for further predictions.

The design and application of the proposed multi-layer feedforward backpropagation ANNs used for damage detection in FRP laminated beams, validation of the method on steel beams and application to sandwich beams are extensively explained in Chapter 7, Chapter 8, and Chapter 9, respectively.

Chapter Five EXPERIMENTAL DESIGN

5.1 Introduction

The dynamic characteristics of the structures are investigated by performing three different experiments. The first one used a digital vibration controller to measure and record the acceleration response of the structure under different excitations covering a certain range of frequencies, which can then be used to obtain resonant frequencies and damping ratios of the beams. In the second experiment, a signal-conditioning amplifier is used to measure dynamic strains at eight different locations from which strain mode shapes of the structure can be obtained. The third test uses fibre optic Bragg grating interrogation system (FBGIS) to record strain from surface bonded and embedded fibre Bragg grating (FBG) strain sensors. The following sections will also outline the experimental set-up considering individual units and the characteristics of the transducers used during the experiments by describing different excitation types and the specimens used in the analyses.

5.2 Experimental Set-up for Vibration Testing

Three main units are used during the vibration testing performed on intact and damaged beams via electro-dynamic vibration generator **[5-1]**. These are namely:

(a) Digital vibration controller with data acquisition unit for acceleration measurements **[5-2]**
(b) Signal-conditioning amplifier with data acquisition system for strain measurements with electrical resistance strain gauges.
(c) Fibre optic Bragg grating interrogation system with fibre Bragg grating strain sensors.

Figure 5.1 shows the experimental set-up for vibration testing. This experimental set-up is used to determine frequency response functions, resonant frequencies, dynamic strain histories and strain mode shapes of the cantilever intact and damaged beams.

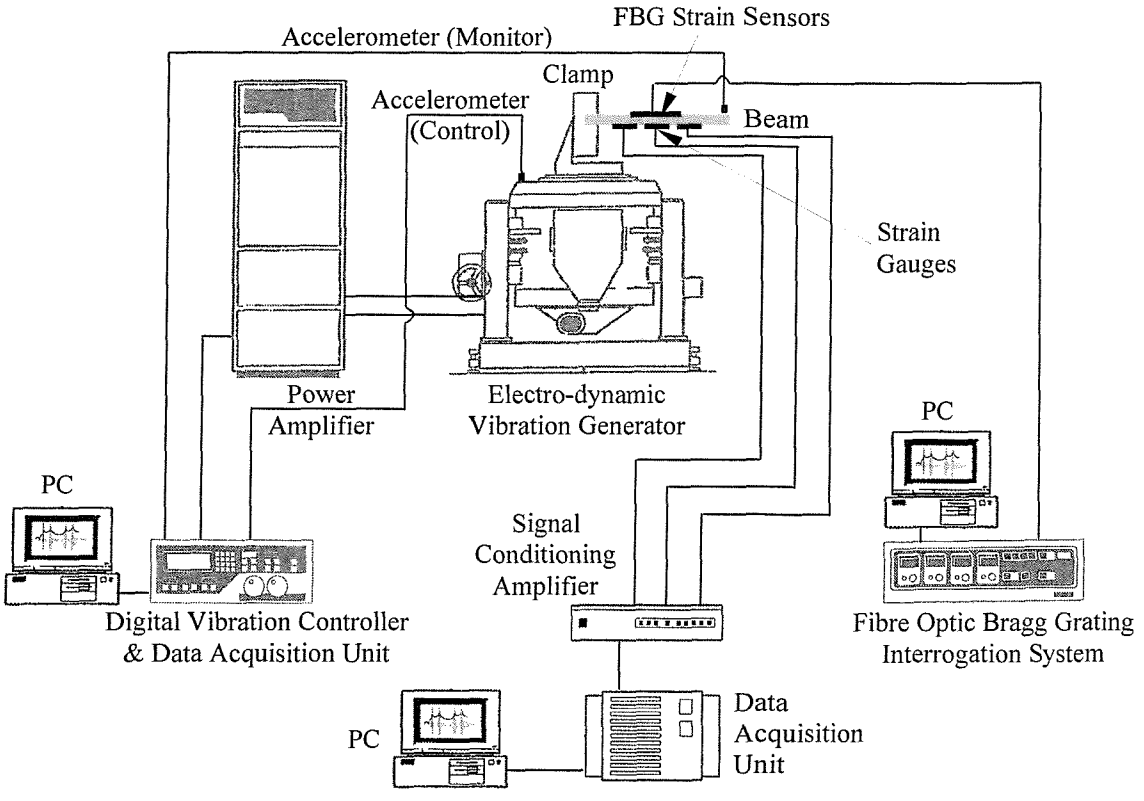

Figure 5.1 Experimental set-up for vibration testing

5.2.1 Acceleration Measurement

A four-channel (one input channel for controlling and three output channels for monitoring) digital vibration controller with data acquisition unit is used to measure acceleration amplitude histories from two channels including both input (control excitation) and output (dynamic behaviour of the specimen). The software has the capabilities of post-processing the data, plotting the amplitude of input and output signals in frequency domain and zooming to peak values for more accurate prediction of the resonant frequencies.

5.2.2 Strain Measurement with Strain Gauges

A Measurements Group Model 2000 signal-conditioning amplifier having 10 channels is used to amplify the signals from strain gauges. The strain readings are recorded by using National Instruments VXI A/D acquisition system as change in voltage. The excitation level is

set to 2 V that is equivalent to $1000\,\mu\varepsilon$ and then the bridge is balanced. In order to find calibrated and measured strain values, the following equations **[5-3]** are used:

$$\mu\varepsilon_{cal} = \frac{R_g \cdot 10^6}{K \cdot (R_c + (R_g/2))} \quad \text{where } R_c = 59.94\,\text{k}\Omega,\ R_g = 120\,\Omega,\ K = 2.11 \tag{5.1}$$

$$\mu\varepsilon_{measured} = \frac{V_{loaded}}{(V_{cal} - V_{unloaded})}\mu\varepsilon_{cal} \quad \text{where } V_{unloaded} = 0,\ V_{cal} = 2\text{V} \tag{5.2}$$

In these equations, $K, R_g, R_c, V_{cal}, V_{loaded}, \varepsilon_{cal}$ and $\varepsilon_{measured}$ are the gauge factor of strain gauge, strain gauge resistance, calibration resistor, calibration voltage, voltage reading from loaded strain gauge, calibrated strain and measured strain respectively.

5.2.3 Strain Measurement with FBG Strain Sensors

A Fibre Optic Bragg Grating Interrogation System is used with in-house software that provides simultaneous strain and temperature measurements under static and dynamic loading by using dual-wavelength superimposed FBG method **[5-4]**. Assuming that the strain and temperature are essentially independent and the wavelength shifts in strain and temperature are linear, Eq. 5.3 can be used in the calculation of strain and temperature from wavelength shifts.

$$\Delta\lambda_B = K_{\Delta\varepsilon} \cdot \Delta\varepsilon + K_{\Delta T} \cdot \Delta T \tag{5.3}$$

where $\Delta\lambda_B, K_{\Delta\varepsilon}, K_{\Delta T}, \Delta\varepsilon$ and ΔT are the Bragg wavelength shift, strain and temperature sensitivities of FBG and change in strain and temperature respectively. During the analysis, $K_{\Delta T}$ is assumed as zero (i.e. no temperature compensation) and $K_{\Delta\varepsilon}$ is taken as 1.24 **[5-4]** which is an average value for FBG sensors made from standard telecoms fibre. The verification of FBGIS and its limitations under dynamic and static loading conditions are given in Appendix A and partly in Appendix B respectively.

5.3 Transducers

The available sensors for vibration measurements were outlined in Chapter 2 by considering their effectiveness and application areas. In this section, experimental dynamic

analyses performed by using piezoelectric accelerometers **[5-5]**, surface bonded strain gauges and fibre optic strain sensors (FOS) are explained and brief technical information about their characteristics is also given.

5.3.1 Accelerometers

Two accelerometers are used during the experimental analysis. One of the accelerometers (ISOTRON® PE Accelerometer, LDS 2256-100) **[5-6]** is used to control the input excitation amplitude supplied to the electro-dynamic vibration generator and the other (PCB Piezotronics, 352 M119) **[5-7]** is used to monitor the output acceleration amplitude from the specimen. The sensitivities of the accelerometers are 99.2 mV/g and 9.90 mV/g respectively. The accelerometer monitoring the response of the beam is attached on the centre line at the free end of the beam using mounting wax. This location of the accelerometer is selected from among several locations considered because it gives sufficient responses for all first three modes.

5.3.2 Strain Gauges

Eight single element electrical resistance gauges (FLA 3-11) **[5-8]** with gauge length of 3mm, nominal resistance of 120 Ω ± 0.3 and a gauge factor of 2.11 are used to measure the direct strain on the surface of the beams. The distributed surface bonded strain gauges, which are numbered from the one closer to free end of the beam, can be seen from **Fig. 6.3**. The detail information about the spatial location of the gauges along the beam will be given in the finite element analysis for curvature mode shape section (Section 6.4.2).

5.3.3 Fibre Optic Sensors

The significant advantages of FOSs over conventional accelerometers and strain gauges were outlined in Section 2.4.2 and **Table 2.5**. There are varieties of FOSs available for strain sensing. In this particular application, FBGs **[5-4], [5-9], [5-10]** are used since they are able to perform absolute strain measurements with good linearity. FBG strain sensors are created in an optical fibre by periodically modulating the core refractive index over a short length along the fibre. When a section of fibre containing a grating is subjected to axial strain or to temperature change, the grating spacing and the refractive index change. This change affects the Bragg wavelength and it acts as sensor to detect strain (Eq. 5.3).

5.4 Excitation

There are several experimental techniques available in order to measure and estimate the dynamic characteristics of the structures. These techniques generally use an external excitation given to the structure to acquire a dynamic response. During the analyses, three different types of excitation (frequency sweep, constant frequency and random excitation) are applied via the electro-dynamic vibration generator controlled by the digital vibration control system. Impact excitation is also given to specimens using an instrumented hammer.

5.4.1 Frequency Sweep Excitation

The purpose of the frequency sweep (i.e. sine sweep) excitation is to identify the response of a test piece to vibration across a range of frequencies. In this way, resonant frequencies of the test specimen can be investigated. The sweep rate can be entered to the system as a time per complete frequency sweep or directly as a rate (Hz/s). Uni-directional type sine sweep with linear incremental sweep rate from low frequency limit to higher level of frequency is used as an excitation during the experimental modal analysis aiming to investigate the first three resonant frequencies of the beams.

5.4.2 Constant Frequency Excitation

This type of excitation can be applied with constant acceleration input operating at a single frequency. After obtaining resonant frequencies of the test specimen by using sine sweep, corresponding displacement or strain mode shapes can be extracted by applying constant frequency excitation at each resonant frequency of interest.

5.4.3 Random Excitation

During the random test, the test specimen is subjected to vibration consisting of constantly and randomly (i.e. continuous random noise with Gaussian distribution) varying levels of frequencies within a specified range. One of the most important parameters in random test is bandwidth value which is used to determine the highest frequency that can be displayed while the test is running. The "best fit" option in the software is used during the test since it automatically sets the bandwidth to the value that accommodates the entire profile. Broadband

excitation of 10 Hz to 710 Hz covering the first three modes of vibration is given to test structure. The output of random test is the power spectral density (PSD) of the signal, a measure of power within each 1Hz band of the test spectrum, in gn^2/Hz for that frequency point, gn denoting the acceleration due to gravity g.

5.4.4 Impact Excitation

Impact excitation with instrumented hammer can be used to excite the structures in different frequency and force levels. During the analysis, ENDEVCO Model 28981A modal hammer **[5-11]** set is used. The load cell in the head of the hammer detects the magnitude of the force felt by the impactor and this force is equal and opposite to that experienced by the structure. The stiffness of the hammer tip is very important from the frequency range point of view. Since the stiffer tip makes the duration of the pulse shorter, the higher frequency range can be covered by the impact. This instrumented hammer has three different tips (aluminium, rubber, plastic) to tailor the input force pulse and built-in signal conditioner/amplifier with switchable gain of 1 or 10. The gain for the instrumented hammer is used as 10 and the aluminium tip having a voltage sensitivity of 0.227 mV/N is chosen. The applied force can be calculated from the output by using equation 5.4. The details of the modal analysis performed on sandwich structures are given in Appendix B.

$$\text{Force} = \frac{\text{Peak Voltage}}{\text{Voltage Sensitivity}} \quad [\text{N}] \tag{5.4}$$

5.5 Test Specimens

5.5.1 Steel Beam Specimens

Intact (control) and damaged steel beams (**Figs. 6.3** and **6.4**) are used during the experimental dynamic analysis. These two specimens have identical geometrical and material properties shown in **Table 5.1**. The damage is created by removing the material from the surface of the specimen across the whole width at 205mm away from the fixed end in order to obtain a 2mm deep and 10mm wide slot on the lower part of the beam. Surface bonded

distributed strain gauges are used for measurement of both dynamic and static responses; on the other hand, static test for calibration of the system is performed by using FBG strain sensors.

Table 5.1 Geometrical and material properties of steel specimen

Length [m]	0.450
Width [m]	0.040
Thickness [m]	0.003
Elastic Modulus [Pa]	207.10^9
Density [kg/m^3]	7850
Poisson's ratio	0.33

5.5.2 Sandwich Beam Specimens

Another set of intact and damaged specimens used during the analysis comprises sandwich beams with GFRP skin and foam core cell. The manufacturing process, geometrical and material properties, embedding process of FBG strain sensors and dynamic analysis performed on these beams are explained in Chapter 9 in detail.

PART C

DAMAGE IDENTIFICATION

Chapter Six ISOTROPIC BEAM STRUCTURE

6.1 Introduction

In model-dependent vibration-based analyses, it is important to have an accurate numerical model before performing the experiments. Since closed-form solution is available for modal analysis of the intact isotropic beam-like structures, a uniform (450mm x 40mm x 3mm) steel beam ($E = 207.10^9$ Pa, $\rho = 7850\,\text{kg/m}^3$, $\nu = 0.33$) is a very good candidate for calibration of the experimental set-up and preliminary applications of the proposed damage detection method before applying it to different structures which are more complicated to model such as laminated composites or sandwich structures.

6.2 Frequency Analysis

Theoretical, numerical and experimental modal analyses are performed to find the first three natural frequencies of intact and damaged fixed-free steel beams. Theoretical calculation is only carried out for intact uniform beam. In numerical analysis, finite element models of intact and damaged steel beams are created by using commercial software package, ANSYS 6.1® **[6-1]**. In this section, not only modelling of the beam-like steel structure but also simulation of the damage introduced to this structure is addressed. After performing an experimental modal analysis, results are compared with those obtained from numerical calculations in order to verify the finite element beam models and to check the accuracy of the measuring instruments used during the experiment.

6.2.1 Theoretical Calculation

The first three bending natural frequencies of a cantilever steel beam can be calculated theoretically by using equation (4.17). The results are tabulated in **Table 6.1**.

Table 6.1 First three natural frequencies of intact cantilever beam (Theoretical Solution)

Mode No	Natural Frequency [Hz]
1st Bending	12.2893
2nd Bending	77.0156
3rd Bending	215.6461

6.2.2 Finite Element Modelling and Analysis

In the finite element modelling of the steel beam, three different element types (BEAM3, SHELL63 and SOLID45 **[6-2]**) are used. Shear deflection is not included in models using BEAM3 and SHELL63 type of elements. **Figure 6.1** shows finite element models of cantilever beam in isometric view. Due to the difficulties in showing finer mesh densities, 6x45 and 6x90x3 mesh densities are shown in **Fig. 6.1** for shell and solid elements models, respectively. SHELL63 type elements are selected for meshing and further analyses since local damage can be modelled by using these four-node quadrilateral two-dimensional elements either by changing their stiffness or thickness at particular locations. Since shell elements have six degrees of freedom (three translational and three rotational) at each node, cantilever boundary condition can also be modelled more realistically by constraining all degrees of freedoms of the nodes located at the root of the beam. The first three bending natural frequencies of the intact cantilever beam for different mesh densities are also obtained in order to check the mesh independency. Since the variation in natural frequencies is less than 1% between 12x180 (i.e. 12 and 180 element divisions along the width and the length of the beam respectively) and 24x260 mesh densities, the former having 2160 elements is used for all latter simulations. After performing modal analysis for the first three bending natural frequencies, results obtained from different models are compared with closed-form solution in **Table 6.2**.

Table 6.2 First three natural frequencies of intact cantilever beam (FEA)

	Natural Frequency [Hz]		
	Beam Elements	Shell Elements	Solid Elements
Mode No	90	12 x 180	6 x 90 x 3
1st Bending	12.289 (-0.0024)	12.382 (0.7543)	12.395 (0.8601)
2nd Bending	77.011 (-0.0060)	77.578 (0.7302)	77.668 (0.8471)
3rd Bending	215.62 (-0.0121)	217.390 (0.8087)	217.69 (0.9478)

[Number in parenthesis shows the percentage difference between theoretical and FEA results]

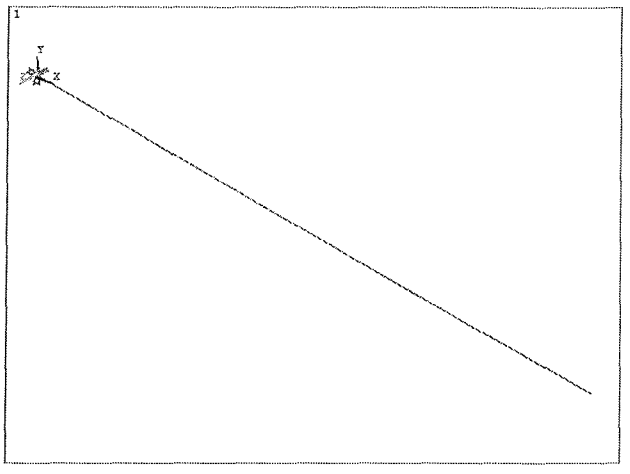

(a)

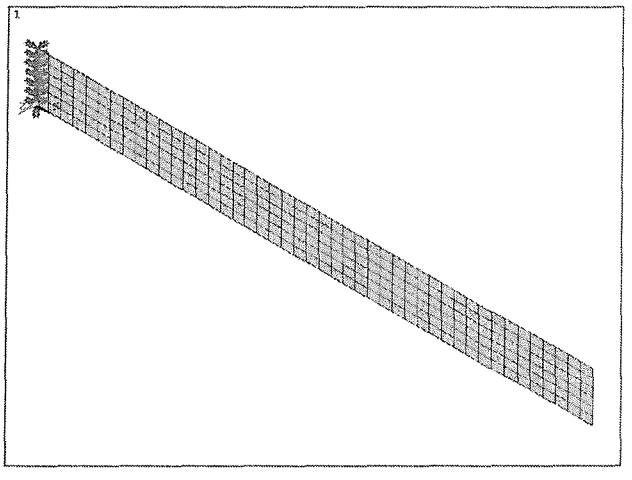

(b)

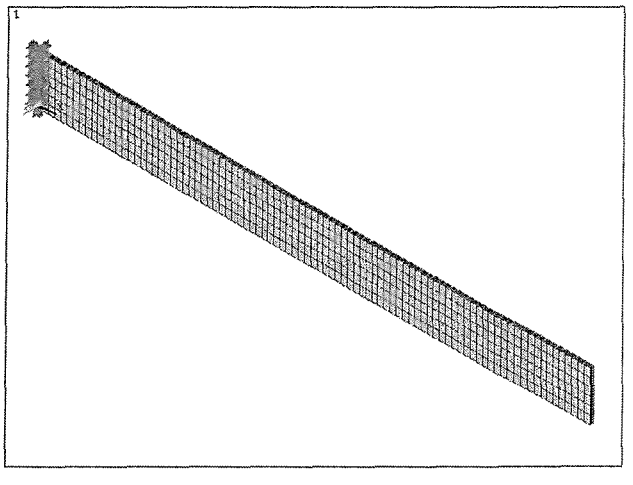

(c)

Figure 6.1 Finite element models of steel cantilever beam
(a) Beam elements (b) Shell elements (c) Solid elements

A structural damage of 2mm deep and 10mm wide slot along whole width of the beam located at 205mm away from the fixed end is simulated. This damage can be modelled in three different ways by using beam, shell and solid elements. Damage is introduced by changing thickness, cross-sectional area and second moment of area of the selected elements in the model where beam elements are used. In shell elements, the thickness of the beam is modified at the location of the damage and new reduced thickness information is given to finite element model (FEM) as 1 mm. Finally, same damage is modelled geometrically using three-dimensional solid elements. **Figure 6.2** shows the location and the zoom view of the damage in FEM of the beam with solid elements. A 6x45x3-mesh density is used for demonstration.

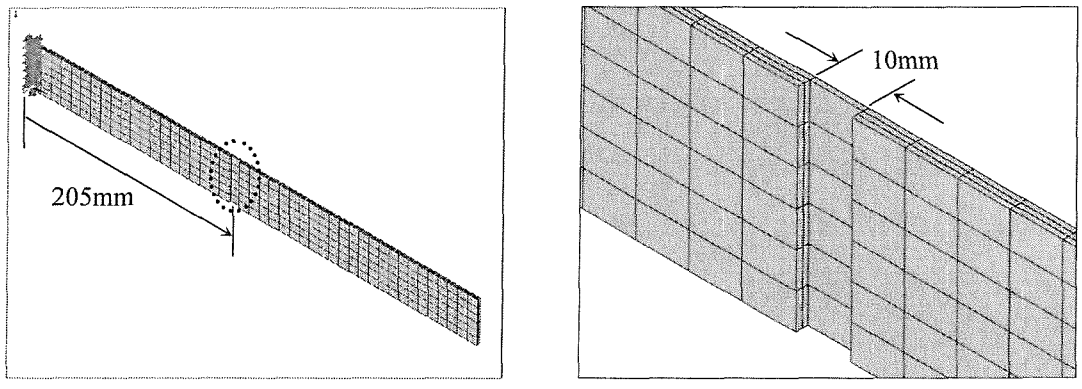

(a) (b)

Figure 6.2 Damaged beam with solid elements (a) Damage location (b) Zoom view

Modal analyses are also performed numerically on damaged beams modelled by beam, shell and solid elements and the results for the first three natural frequencies are tabulated in **Table 6.3**.

Table 6.3 First three natural frequencies of damaged cantilever beam (FEA)

	Natural Frequency [Hz]		
	Beam Elements	Shell Elements	Solid Elements
Mode No	90	12 x 180	6 x 90 x 3
1st Bending	10.538	10.738	10.683
2nd Bending	58.859	60.327	60.054
3rd Bending	210.80	212.369	213.470

6.2.3 Experimental Analysis

Two steel beams having same geometrical (450mm x 40mm x 3mm) and material properties are used during the experimental modal analysis. One of the beams is selected as control specimen (intact structure, **Fig. 6.3**) and the other is used as a damaged beam (**Fig. 6.4**) having a 2mm deep and 10mm wide slot which is created by removing the material from the surface of the specimen along whole width at 205mm away from the fixed end. The distributed surface bonded strain gauges are numbered starting from the one closer to free end of the beam (**Fig. 6.3**). The detailed information about the spatial location of the gauges along the beam is given in **Fig. 6.9**.

In order to find the first three resonant frequencies of the intact and damaged cantilever beams, frequency sweep excitation is applied in the range of 3 – 253 Hz with an increment of 0.5 Hz. This range is estimated from theoretical and finite element modal analysis results. The excitation amplitude is set to 0.5g throughout the sweep and controlled by an accelerometer mounted to electro-dynamic vibration generator. The output signal coming from the test specimen is also monitored with another accelerometer which is attached along the centre line at the free end of the beam. This location of the accelerometer is selected from among several locations considered because it gives sufficient responses for all three modes.

Figures 6.5 and **6.6** show half of the peak-to-peak values of the acceleration amplitude of intact and damaged specimens with increasing frequency respectively. The numbers near each peak response level indicate experimentally obtained resonant frequencies. All frequencies for the damaged and intact beam are also tabulated and compared with FEA results in **Table 6.4**.

Table 6.4 First three natural frequencies of intact and damaged beams [Hz]

	Finite Element Analysis (Shell Elements, 12x180)			Experimental Results		
Mode No	Intact Beam	Damaged Beam	$\frac{f_{damaged}}{f_{intact}}$	Intact Beam	Damaged Beam	$\frac{f_{damaged}}{f_{intact}}$
1st Bending	12.382	10.738	0.8672	11.8	9.2	0.7796
2nd Bending	77.578	60.327	0.7776	73.1	50.5	0.6908
3rd Bending	217.390	212.369	0.9769	205.6	200.8	0.9766

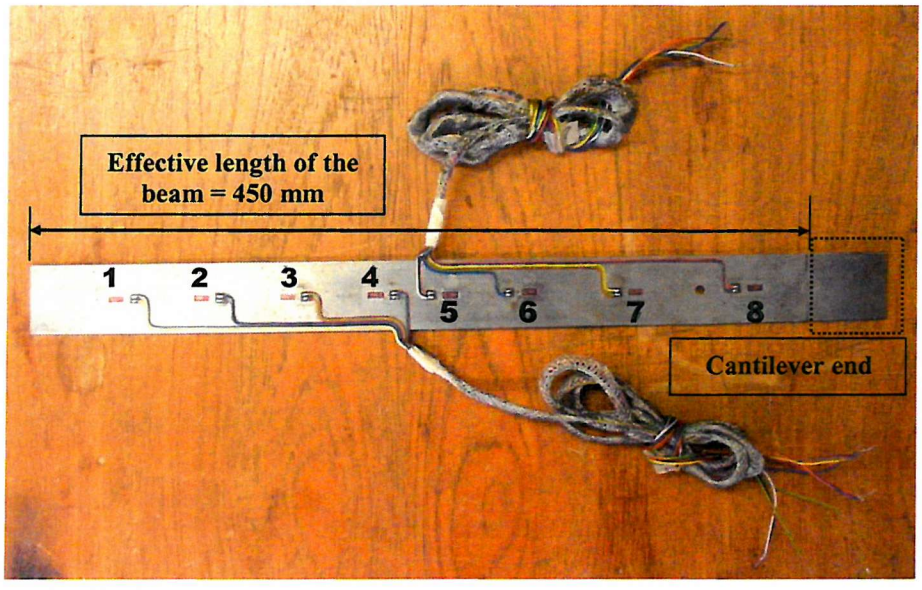

Figure 6.3 Intact steel beam specimen with distributed strain gauges

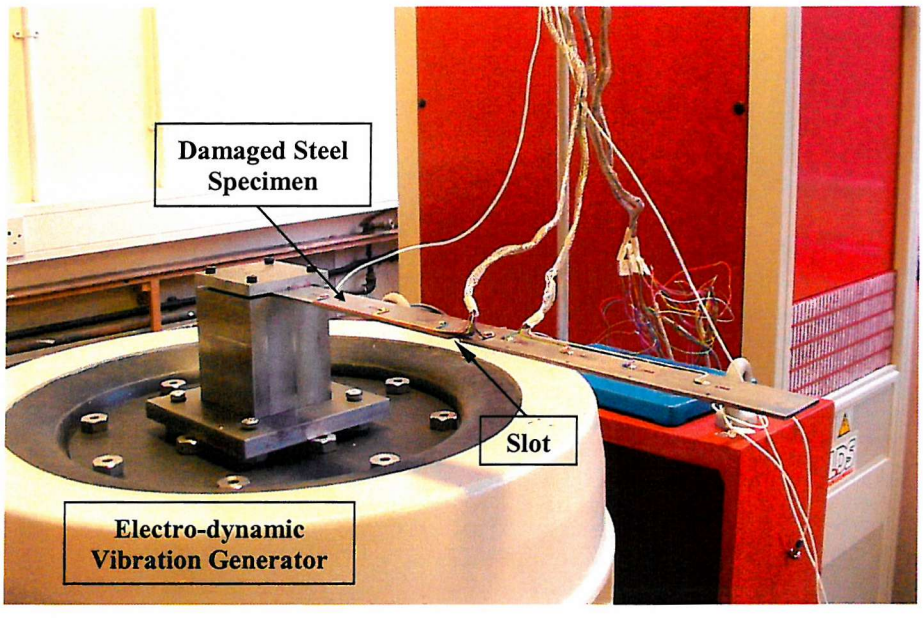

Figure 6.4 Damaged steel beam specimen on the test rig

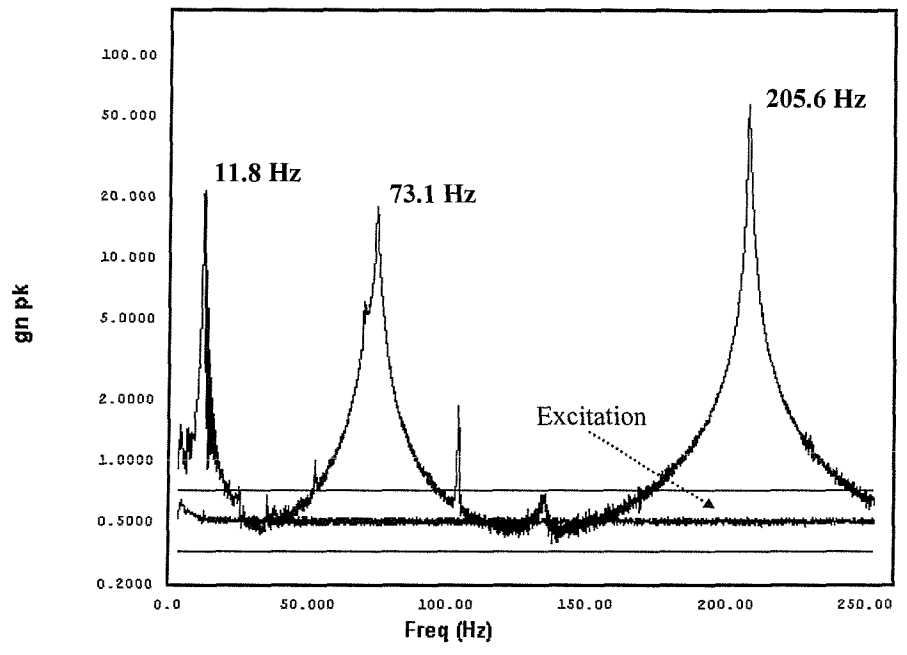

Figure 6.5 Frequency response of intact cantilever beam

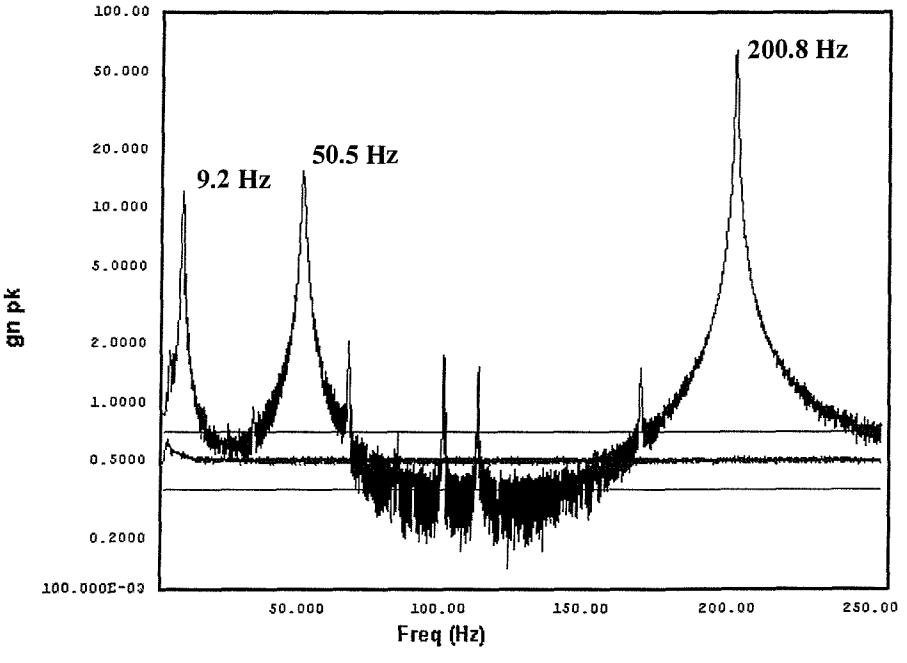

Figure 6.6 Frequency response of damaged cantilever beam

6.3 Damping Analysis

All structures have different amount of damping which brings the system to equilibrium at higher or lower amplitudes depending on the magnitudes of the damping forces. Damping ratio is especially important for forced vibration analysis. The aim of this section is to find the damping ratio (ζ) of the intact and damaged steel beams. The first three modes are of primary interest in damping analysis. Frequency response amplitude of each mode is taken and damping ratios are estimated from the half-power bandwidth method **[6-3]**. In order to find the damping ratios from the frequency response function (FRF), the resonant frequency (f_{res}) and two frequencies (f_1 and f_2) on either side of the resonant frequency for which the amplitude is $\frac{1}{\sqrt{2}}$ times the resonant amplitude should be found. **Figure 6.7** shows estimation of material damping by using half-power bandwidth method in the first bending mode.

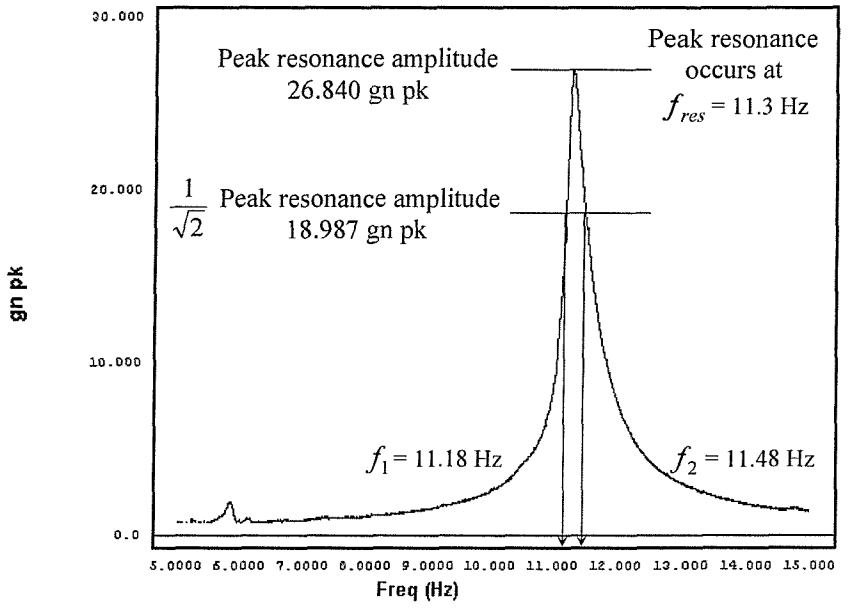

Figure 6.7 Estimation of material damping from half-power bandwidth method (Steel beam, 1st Bending Mode)

Damping ratios obtained using Eq. 6.1 in the range of the first three resonant frequencies for intact and damaged beams are tabulated in **Table 6.5**. These values are used in finite element harmonic analysis of the steel beam. (Section 6.4.2.2)

$$\zeta = \frac{BandWidth}{2f_{res}} = \frac{f_2 - f_1}{2f_{res}} \tag{6.1}$$

Table 6.5 Damping ratios of intact and damaged steel beams

Mode No	Intact Beam	Damaged Beam
1st Bending	0.01327	0.03591
2nd Bending	0.01273	0.01337
3rd Bending	0.00414	0.00373

6.4 Curvature (Strain) Mode Shape Analysis

During the analyses, curvature mode shapes are obtained in three different ways. The following flowchart (**Fig. 6.8**) shows the procedure followed and applied on steel beam in order to achieve curvature or strain mode shapes.

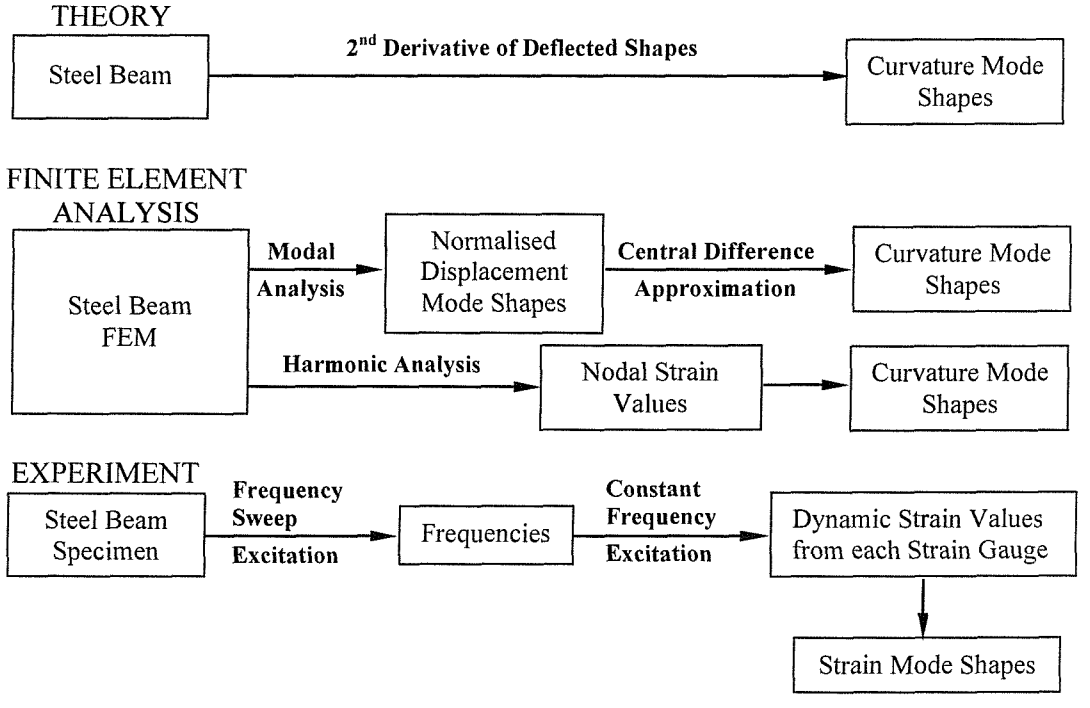

Figure 6.8 Methods to obtain curvature (strain) mode shapes

6.4.1 Theoretical Solution for Curvature Mode Shapes

As explained in Section 4.2, normalised curvature mode shapes can be obtained theoretically by using Eq. 4.19 for uniform, homogeneous, slender single-span beams having isotropic elastic material properties. Hence, the intact steel beam used in the analyses satisfies these conditions, the data plotted in **Fig. 4.3** is the solution for curvature mode shapes of this cantilever beam. The theoretical results are also shown in **Fig. 6.13** for comparison purposes.

6.4.2 Finite Element Analysis for Curvature Mode Shapes

The curvature mode shapes of the steel beam are obtained by using two different FEA approaches. The first approach is free vibration modal analysis from which normalised displacement mode shapes are calculated. Then, central difference approximation **[2-18]** is applied on normalised displacement mode shapes by using equation (6.2) in the calculation of curvature mode shapes.

$$v_i'' = \frac{(v_{i+1} - 2v_i + v_{i-1})}{h^2} \tag{6.2}$$

where v_i'', v_i, h and i are the curvature, normalised transverse displacement, the distance between two collocation points in the FEM and the number of collocation points along the beam model respectively. The second approach is harmonic analysis based on frequency sweep excitation. Since this is a forced vibration analysis, nodal strain values are available from FEA. This means that there is no need to use normalised displacement mode shapes and central difference approximation in the calculation of curvature mode shapes which can be obtained directly from finite element nodal strain data.

6.4.2.1 *Free Vibration*

In this part of the analysis, modal analysis is performed on finite element model of the steel beam in order to obtain displacement mode shapes for the first three natural modes. Normalised displacement mode shapes are used as an input data for Eq. 6.2 to calculate curvature mode shapes. Since this equation is valid for equally spaced collocation points, more number of nodes which are evenly distributed and located along the centre line of the beam are selected from FEM to increase the accuracy and smoothness of the curvature mode shapes.

Then, curvature values at eight different collocation points (**Fig. 6.9**) where strain gauges are located on the beam test specimen are selected and normalised with respect to curvature value at Location 8.

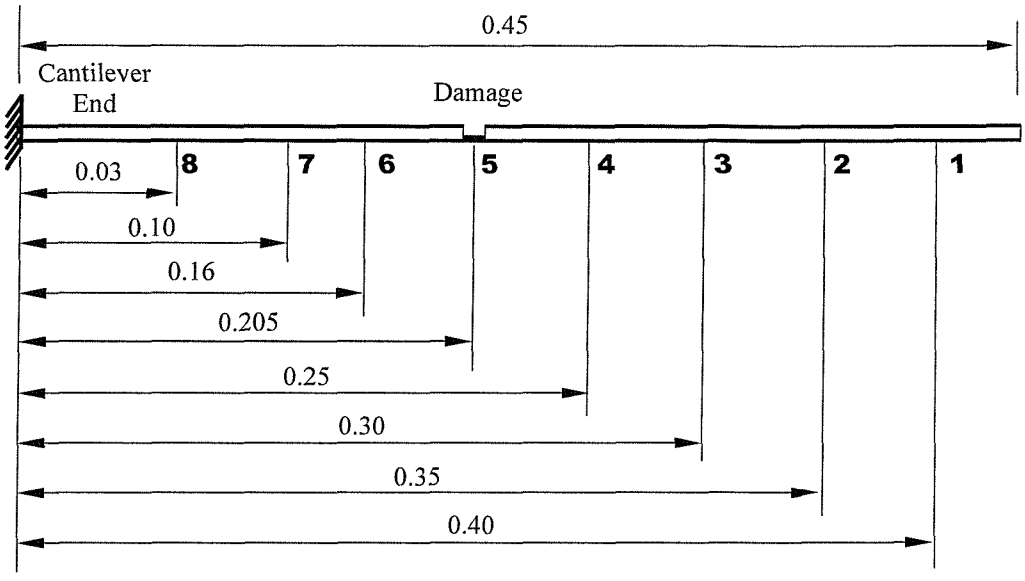

Figure 6.9 Collocation points on damaged beam [Not to scale, Dimensions in meter]

6.4.2.2 *Forced Vibration*

In this part of the analysis, harmonic analysis is performed by sweeping frequency with 0.5 Hz increment within different ranges of each mode of intact and damaged FEM of the steel beam structure. Mode superposition method in ANSYS® is used with constant modal damping ratio and stepped forcing frequency in a specified frequency range by superimposing the first 20 modes. The experimentally obtained damping ratio of each mode (**Table 6.5**) is specified accordingly during the analysis. Magnitude of the excitation force during the analysis is taken as $0.5g$ in the vicinity of the first mode resonance and $0.75g$ for the second and third mode resonance vicinities. **Figures 6.10** and **6.11** show elastic strain values from eight different locations (**Fig. 6.9**) obtained by sweeping the frequency across first, second and third bending resonant frequencies on intact and damaged beams respectively. Then, frequency range and sweep rate are reduced and strains corresponding to resonant frequencies are zoomed in order to achieve higher accuracy in the analysis. In order to obtain the normalised strain mode shapes from FRF, maximum strain values (i.e. peak values occurring at resonant frequencies) are selected, normalised with respect to nodal strain value at Location 8. These strains values are also plotted in **Figs. 6.13** and **6.14** for the intact and damaged beams respectively and compared with the results obtained from theory and experimental analysis in the results and comparison section (Section 6.4.4).

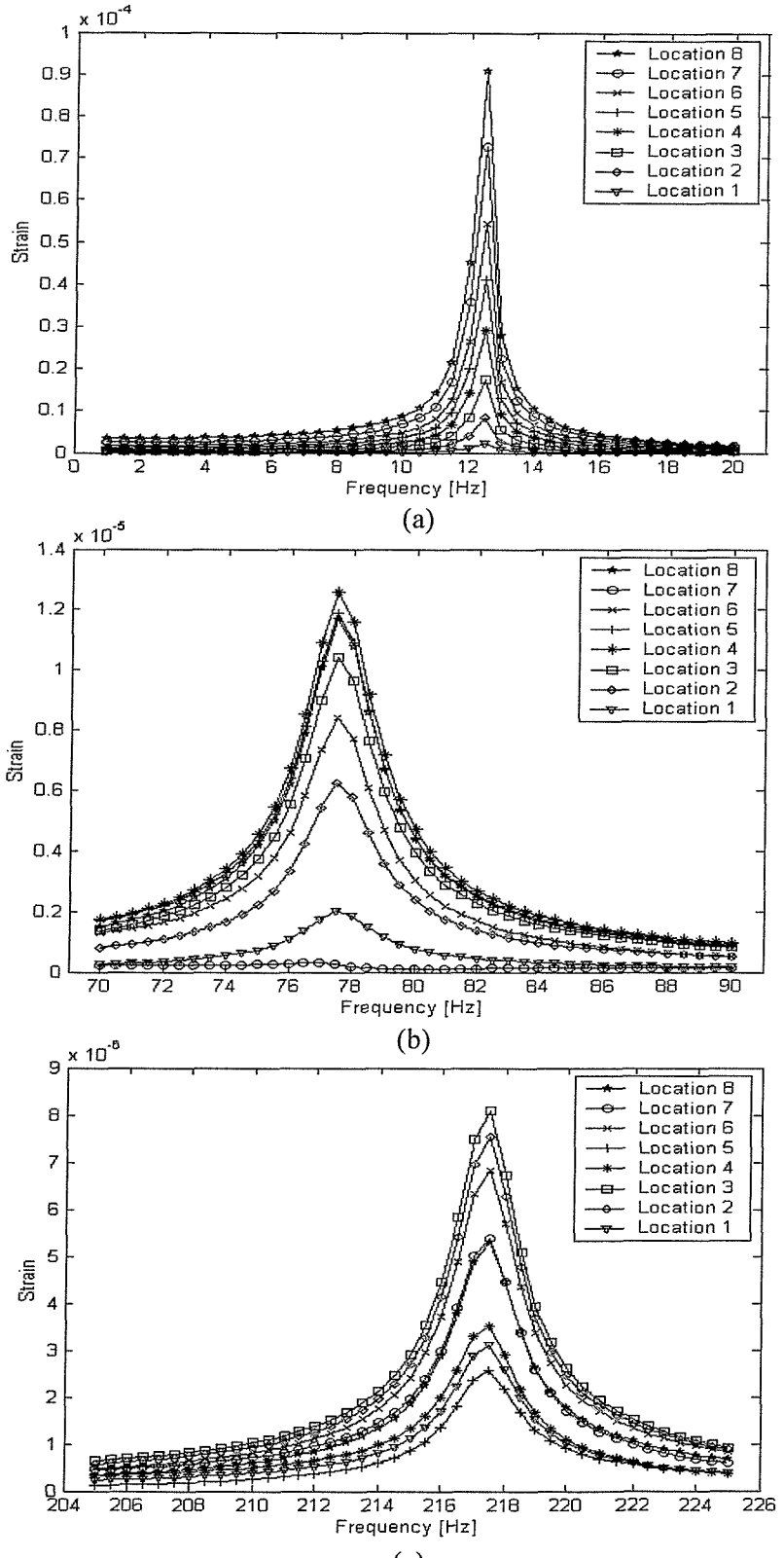

Figure 6.10 Strain values for intact steel beam for different frequency ranges (a) 1-20 Hz (b) 70-90 Hz (c) 205-225 Hz

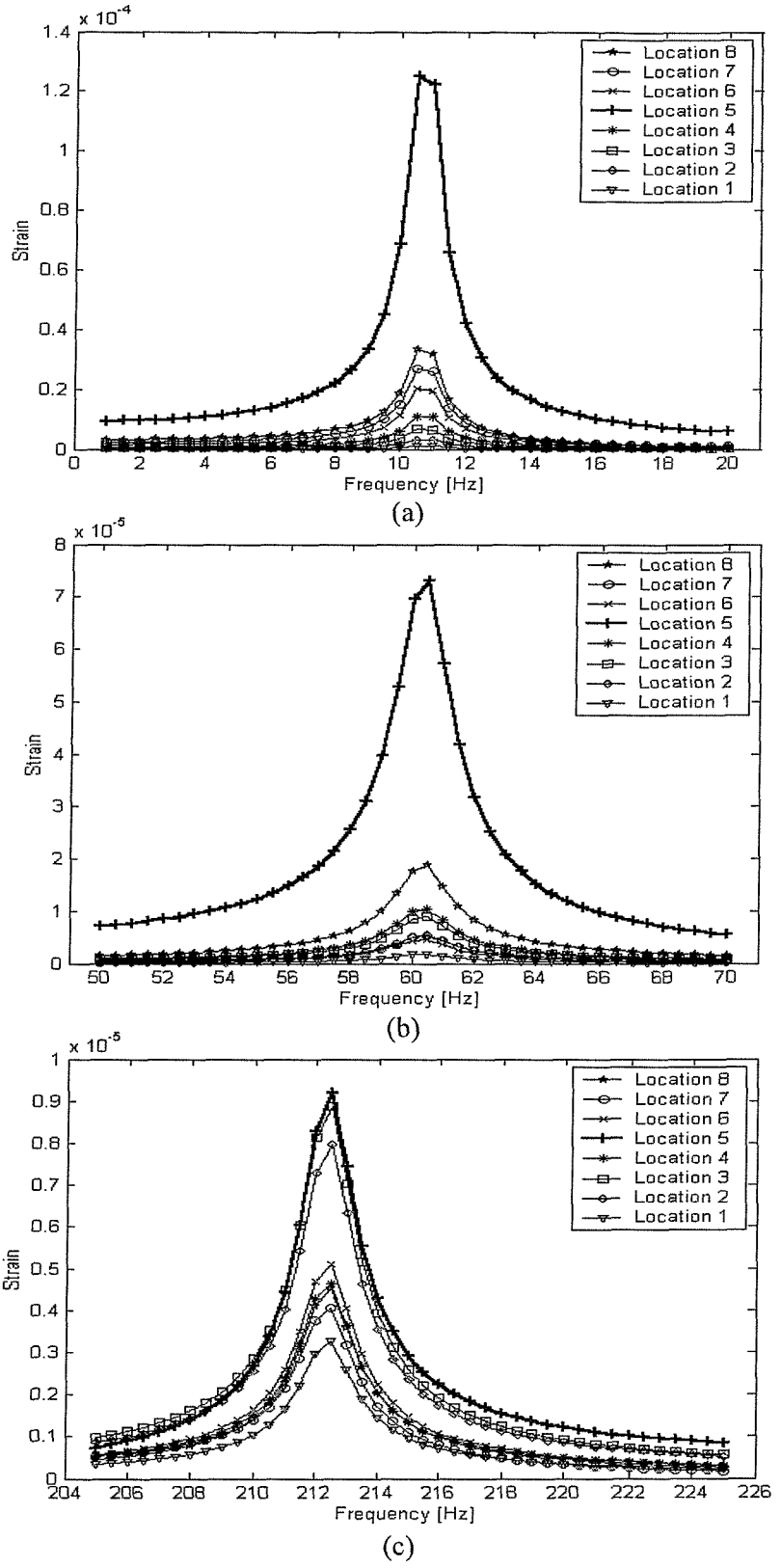

Figure 6.11 Strain values for damaged steel beam for different frequency ranges (a) 1-20 Hz (b) 50-70 Hz (c) 205-225 Hz

6.4.3 Experimental Analysis for Strain Mode Shapes

After obtaining the resonant frequencies numerically, experimental modal analysis (**[6-4], [6-5]**) is also performed so as to obtain the dynamic strain mode shapes of intact and damaged beams excited at those particular resonant frequencies. During the dynamic strain analysis, sampling rate and sample length are taken as of $800s^{-1}$ and 4000 respectively corresponding to 5s strain measurements. The amplitude of the constant acceleration input given to electro-dynamic vibration generator operating at fundamental resonant frequency is taken as $0.5g$ during the dynamic strain experiment. **Figure 6.12** shows the voltage output of eight strain gauges in the first mode of the intact beam. These voltage values are converted to strain and normalised with respect to strain gauge number 8, which is the closest strain gauge to the fixed end of the beam. Same procedure is followed for the second and third mode of the intact and the damaged beams with amplitude of $0.75g$ constant acceleration input. All normalised strain mode shapes of intact and damaged beams (**Figs. 8.12** and **8.13**) obtained from experimental strain time histories (**Figs. 8.6 – 8.11**) are plotted and shown in Chapter 8.

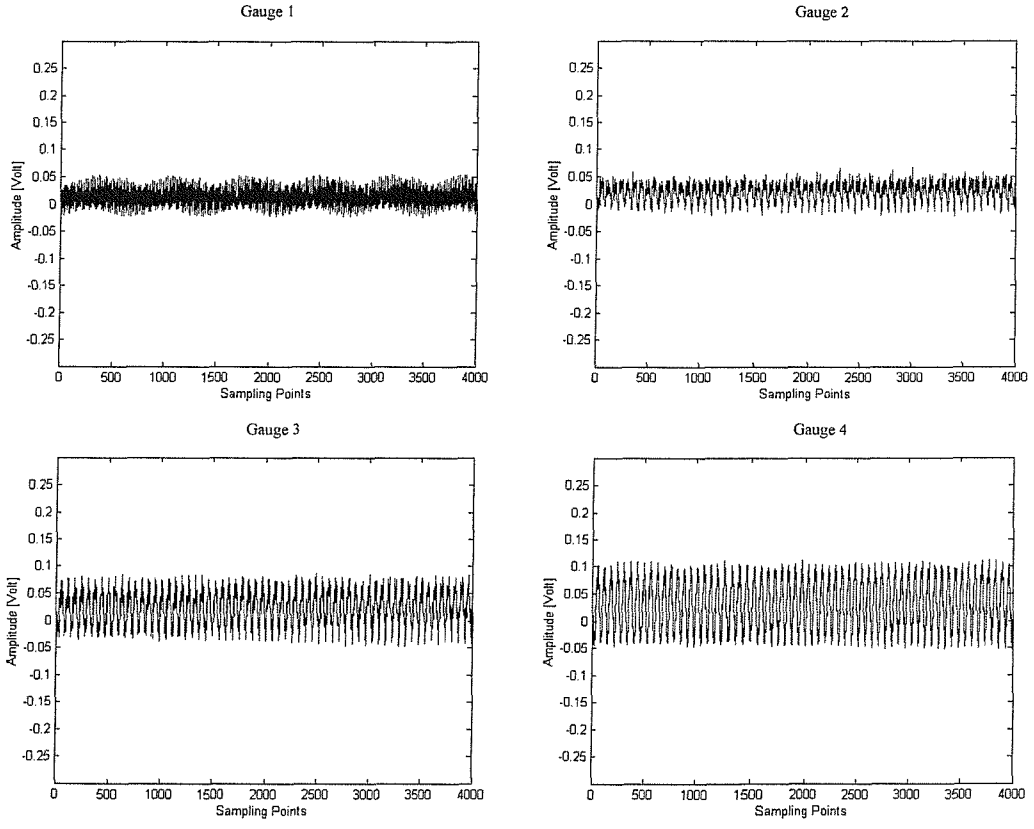

Fig. 6.12 (continued over)

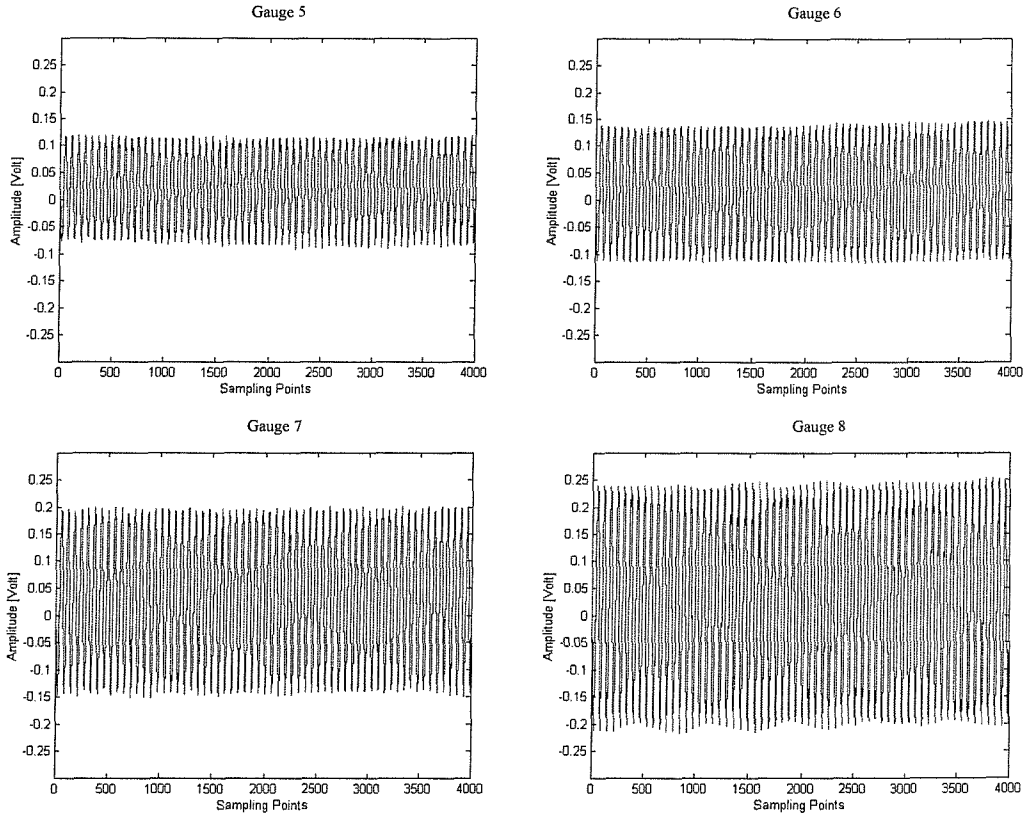

Figure 6.12 Voltage output of eight strain gauges in the first mode (Intact Beam)

6.4.4 Results and Comparisons

In this section, all theoretical and finite element (i.e. shell elements) analysis results are presented and compared to each other for the steel cantilever beam. Throughout the analyses, the first three natural modes are of primary interest for the calculation of curvature or strain mode shapes. **Figure 6.13** shows normalised absolute curvature mode shapes of the intact beam obtained considering eight different locations corresponding to locations of strain gauges along the beam specimen. Normalisation is performed with respect to location 8, which provides a reasonable finite amount of strain for all three modes, in order to investigate the relative change in curvature at eight different locations.

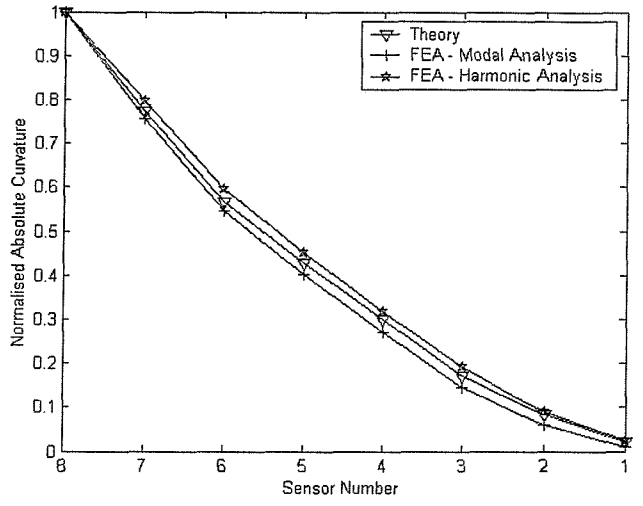

(a)

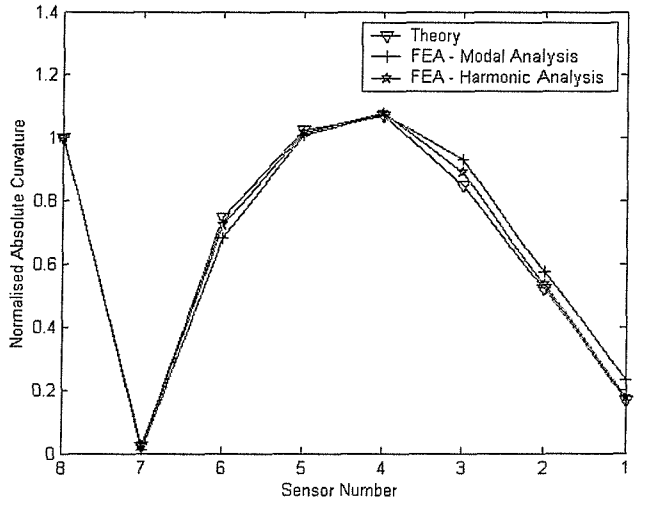

(b)

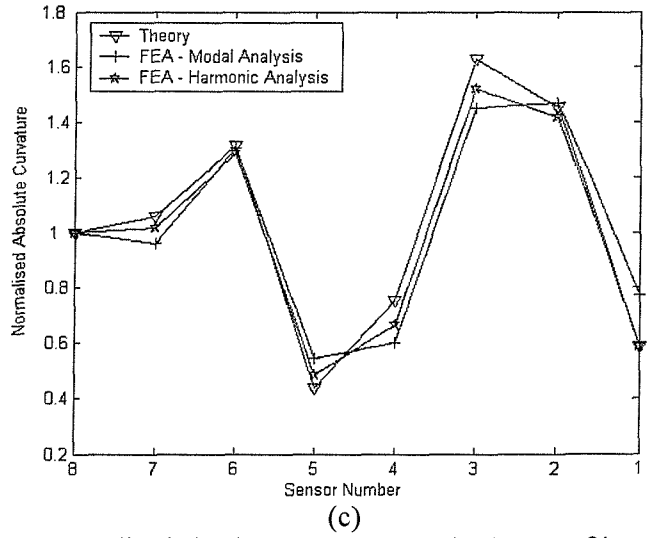

(c)

Figure 6.13 Normalised absolute curvature mode shapes of intact steel beam

(a) Mode 1 (b) Mode 2 (c) Mode 3

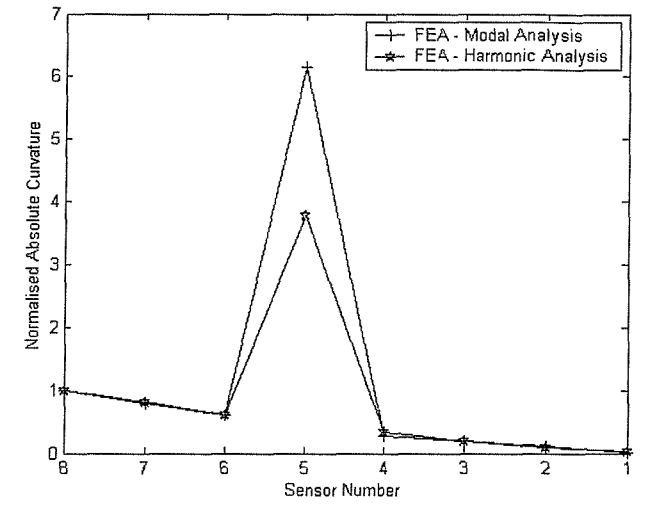

(a)

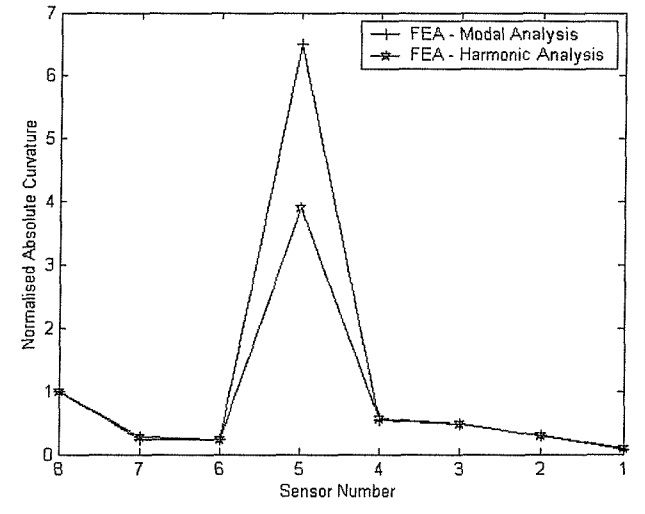

(b)

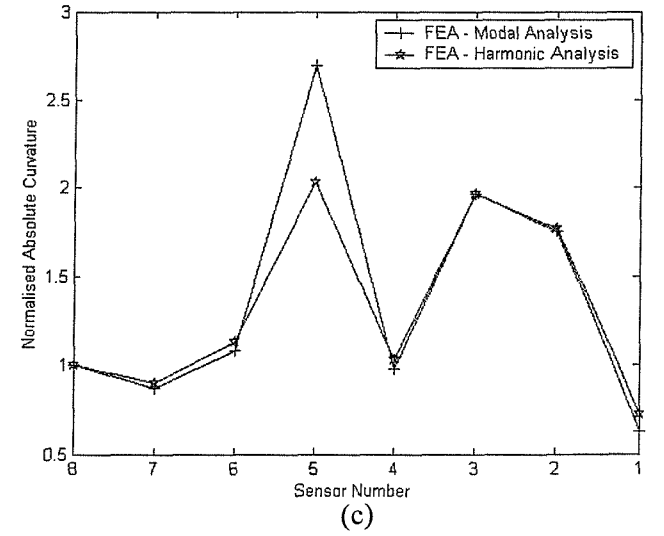

(c)

Figure 6.14 Normalised absolute curvature mode shapes of damaged steel beam

(a) Mode 1 (b) Mode 2 (c) Mode 3

It can be seen from **Fig. 6.13** that the curvature results are quite close to each other for the intact beam. Same approach and analyses performed on intact beam are also applied to damaged beam (**Fig. 6.14**). Although the general trend is similar in change in curvature along the beam, the values show slight differences at the damage location between the two different finite element analyses. On the other hand, the same point (location 5 or sensor number 5) shows a sudden change in the curvature making it discontinuous at that particular location where the damage is located. The effect of severity and location of the damage on absolute differences in curvature mode shapes between intact and damaged structures will be investigated in section 7.4 by performing sensitivity analysis on FEA data of laminated composite beams.

6.5 Static Strain Analysis

6.5.1 Strain Gauges

A Static strain experiment is performed on the steel beam specimen in order to calibrate the strain gauges. A mass of 200 gram is applied at the free end of the beam along the centre line and strain data are recorded from eight different gauges (**Fig. 6.3**). Since the output of the strain-conditioning unit is voltage, MATLAB® **[6-6]** program is used to post process the data for the calculation of the normal strains (Eqs. 5.1 and 5.2). In order to verify the strain measurements obtained from strain gauges, FEA is also performed with static load of 1.962N (equivalent to 200g mass). **Table 6.6** shows the FEA results (shell elements, 12x180 mesh density) obtained at eight different locations along the intact beam under static loading. The comparison of the finite element and experimental static strain analysis results can be seen from **Fig. 6.15**.

Table 6.6 Finite element static strain analysis results

Location	Strain [$10^{-6}\varepsilon$]
1	7.9421
2	15.799
3	23.696
4	31.594
5	38.703
6	45.811
7	55.261
8	63.708

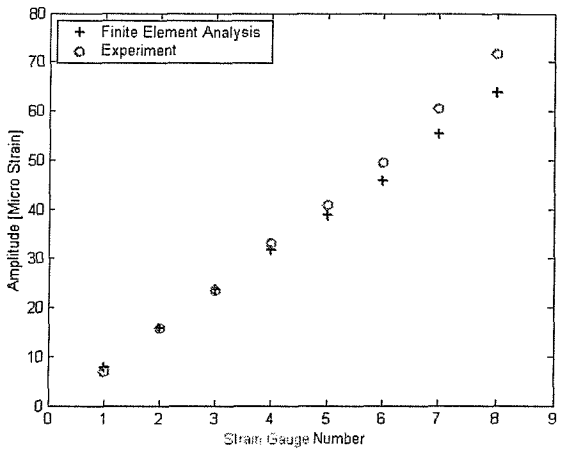

Figure 6.15 Static strain analysis results (FEA – Experimental)

6.5.2 FBG Strain Sensors

Another steel beam (450mm x 40mm x 3mm) having three surface bonded strain gauges and three FBG strain sensors located at lower and upper surface of the structure is used for calibration purpose. The accuracy and the linearity of the FBGIS, consistency and repeatability of the measurements with FBG strain sensors are also checked by performing static strain experiment. **Figure 6.16** shows the location of the strain gauges and the FBG strain sensors along the beam.

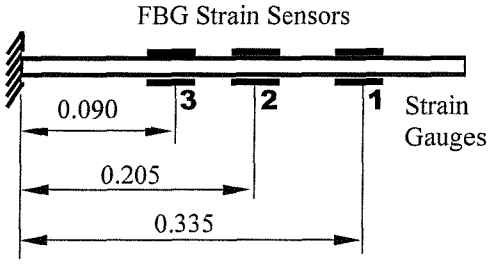

Figure 6.16 Location of strain gauges and FBG strain sensors

[Not to scale, dimensions in meter]

An incremental static load of 140, 240, 340 and 440 gram are applied along the centre line of the beam at the free end and strain variations in three FBG strain sensors are recorded. The changes in strain values of the FBG strain sensors due to static loads are shown in **Fig. 6.17**. The discontinuity in strain history occurs at the instant of application of the static load.

Finite element and experimental strain analysis by using electrical resistance gauges are also performed with 140-gram load. The tabulated form of the results can be seen in **Table 6.7**.

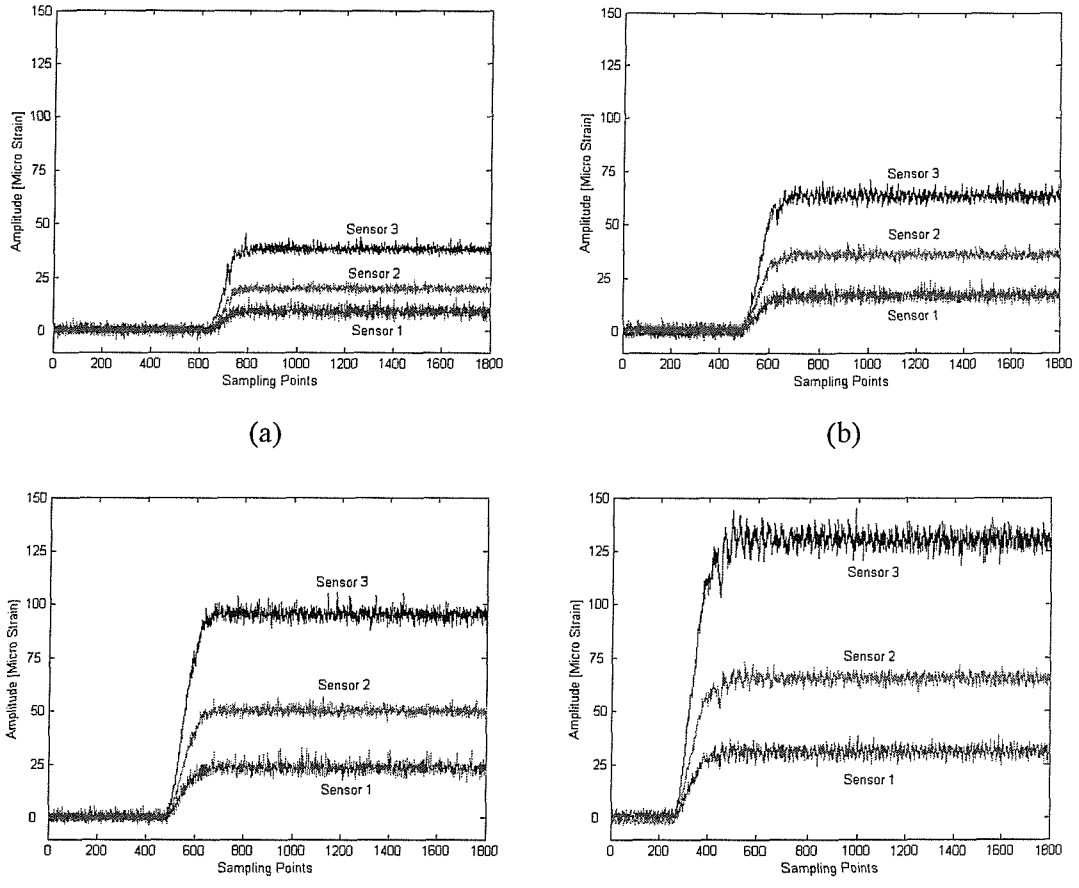

Figure 6.17 Strain measurement with FBGs

Static load of (a) 140 gram (b) 240 gram (c) 340 gram (d) 440 gram

Table 6.7 Strain analysis results with 140-gram static load

Location	FEA [$10^{-6}\varepsilon$]	Strain Gauges [$10^{-6}\varepsilon$]	FBG Strain Sensors [$10^{-6}\varepsilon$]
1	12.7170	11.5627	9.1231
2	27.0914	26.4292	23.1294
3	39.7584	36.6438	38.1370

6.6 Conclusions

In this chapter, vibration characteristics of intact and damaged isotropic beams were investigated. It can be seen from the summary section (**Table 2.1**) in the literature review chapter that there are numerous investigations concentrated on the calculation of natural frequencies and/or displacement modes shapes (or curvature mode shapes, Laplacian, etc.) in the determination of damage in isotropic structures. **Table 6.8** shows studies on isotropic beam structures and the features including both frequency changes and curvature mode shapes obtained from free vibration analysis.

Table 6.8 Studies on isotropic beam structures and features

Studies on Isotropic Beam Structures	[11] [12] [13] [15] [16] [17] [18] [19] [20] [21] [22] [23] [25] [26] [28] [36] [39] [40] [42] [53] [58]
Frequency Changes	[11] [12] [13] [17] [18] [19] [20] [28]
Curvature Mode Shapes or Strain History	[18] [19] [20] [21] [22] [23] [25]
Both Frequency Changes and Curvature (Strain) Mode Shapes	[18] [19] [20]

[Numbers in brackets are references from Chapter 2]

In this study, beams were modelled using finite element analysis and specimens were manufactured with surface bonded strain gauges and FBG strain sensors. Dynamic analyses were performed with different excitations aiming at natural frequencies and local dynamic strain histories. During the analysis, the first three natural modes of the beams were of primary interest. Both numerical and experimental results showed that there was a strong correspondence between the existence of the damage and reduction in frequencies depending on the natural mode of interest (**Table 6.4**).

Curvature modes were calculated numerically not only using second derivative of the deflected mode shape from continuous beam theory and modal analyses followed by central difference approximation in free vibration (in references **[2-18], [2-19], [2-20]**) but also by using forced vibration under harmonic excitation providing local (nodal) strain values. The results from numerical work were compared to strain mode shapes obtained experimentally using electro-dynamic vibration generator and eight distributed strain gauges along the span of the

beams. In order to compare curvature and strain variations along the beam span, the data was normalised with respect to the gauge, which is closest to root of the beam (i.e. at location eight). Change in curvature along intact beam obtained from experimental analysis (**Fig. 8.12**) showed good agreement with the ones obtained from numerical analyses (**Fig. 6.13**). On the other hand, in the damaged beam case, both numerical results (**Figs. 6.14)** showed some variations from the experimental one (**Fig. 8.13**) especially at the location of the damage due to the local change in thickness.

Considering the strain data (**Fig. 6.17**) from surface bonded FBG strain sensors, it can be concluded that filtering of the noise is an important issue for further analysis. Additionally, FBG strain data under static loading condition provides slightly different values although strain analysis results obtained from strain gauges and FEA are quite close to each other.

It can finally be concluded from numerical and experimental analyses that the modelling of the real damage in FEA, the method used in the calculation of the curvature mode shapes, structural coupling between the sensors (or gauges) and the host structure, the noise content in the data are the most important factors affecting the accuracy of the analysis results.

Chapter Seven LAMINATED COMPOSITE BEAM STRUCTURE

7.1 Introduction

This chapter investigates the effectiveness of the combination of global (changes in natural frequencies) and local (curvature mode shapes) vibration-based analysis data as input for ANNs for location and severity prediction of damage in FRP laminates **[7-1], [7-2]**. Since the dynamic behaviour of isotropic structure (steel beam) has already been analysed in Chapter 6, an FRP composite beam is selected as a base structure for further analyses before investigating the behaviour of sandwich structures. A finite element analysis tool has been used to obtain the dynamic characteristics of intact and damaged cantilever laminated composite beams for the first three natural modes. Different damage scenarios have been introduced by reducing the local stiffness of the selected elements at different locations along the finite element model of the beam structure. After performing the sensitivity analyses aimed at finding the necessary parameters for the damage detection, different input-output sets have been introduced to various ANNs. In order to check the robustness of the input used in the analysis, random noise has been generated numerically and added to noise-free data during the training of the ANNs. Finally, trained feed-forward backpropagation ANNs have been tested using new damage cases and checks have been made for severity and location prediction of the damage.

7.2 Frequency Analysis

An intact cantilever composite beam model used in the analysis is made up of four-layer, equal thickness, symmetric cross-ply [0°/90°/90°/0°] laminae with following normalised geometrical and dimensionless elastic orthotropic properties.

$$\frac{L}{w}=10,\quad \frac{L}{t}=100 \tag{7.1}$$

$$\frac{E_1}{E_2} = \frac{E_1}{E_3} = 40, \quad \frac{G_{12}}{E_2} = \frac{G_{13}}{E_3} = 0.6, \quad \frac{G_{23}}{E_3} = 0.5, \quad \nu_{12} = \nu_{23} = \nu_{13} = 0.25 \tag{7.2}$$

L, w and t are the length, width and total thickness of the beam and E's, G's and ν's are elastic moduli, shear moduli and the Poisson's ratio respectively. These elastic constants are selected to simulate high modulus FRP composites similar to those in the work of Mallikarjuna and Kant **[7-3]**.

7.2.1 Finite Element Modelling and Analysis

A three-dimensional linear layered structural shell element with eight nodes, SHELL99 **[6-2]**, is selected to model the layered composite beam. **Figure 7.1** shows the finite element mesh of the composite beam with shell elements (2x20-mesh density).

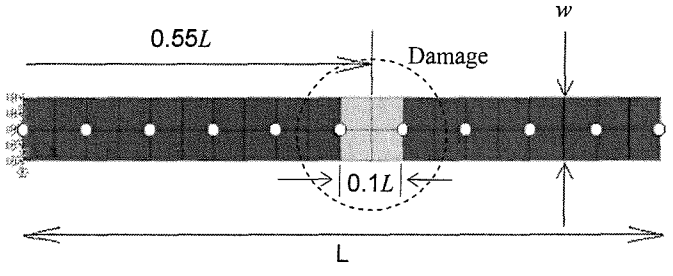

Figure 7.1 Finite element model of cantilever composite beam (Top view)

In order to validate the modelling approach with the results from **[7-3]** and **[7-4]**, geometry (square, simply supported, symmetric, cross-ply, equal thickness composite plate) similar to their case is used with the same material properties (Eq. 7.2). 100 elements (10x10) are used in the finite element model and the dynamic analysis is performed to find the first dimensionless natural frequency of the plate structure. **Table 7.1** shows the results of modal analysis performed with this plate and it can be seen that the present ANSYS model gives good agreement with the previous published work.

The composite cantilever beam model was thus derived by changing the geometry and boundary condition from the validated plate model outlined in the previous paragraph. Four different mesh densities having 40, 80, 200 and 800 elements are used to perform mesh

independence studies of the intact beam model by performing modal analysis aiming at the first three bending natural frequencies. The results obtained from these cases showed less than 0.1 per cent difference in the computed frequencies; hence the mesh density of 40 elements having 165 nodes is used for all subsequent simulations in order not to increase the computational time. Each element has six degrees of freedom corresponding to three translations and three rotations at each node. In order to satisfy the cantilever boundary condition at the root of the beam, all nodal displacements and rotations are made equal to zero.

Table 7.1 Dimensionless fundamental frequency of composite plate

	Dimensionless Frequency	% Difference from Closed Form Solution
Closed Form Solution **[7-4]**	15.270	-
Higher-Order Shear Theory **[7-3]**	15.090	-1.17
First-Order Shear Theory-FEA **[7-3]**	15.073	-1.29
Present ANSYS result	15.215	-0.360

7.2.2 Damage Scenarios

The main aim of modelling a non-dimensional FRP laminated composite beam is to create a vibration-based analysis data base having natural frequencies and curvature mode shapes from the first three modes of the intact and damaged beams when the local damage is introduced with twenty one different damage severities at six different spatial locations along the span of the beam.

7.2.2.1 *Severity of Damage*

Structural damage is modelled as local reduction in stiffness of the selected elements by changing the modulus of elasticity. In order to make the system sensitive enough to detect less severe damage, a 2.5 per cent incremental reduction is used between the intact and the damaged beam up to 25 per cent stiffness reduction (i.e. 10 different damage severities). For more severe damage, the incremental reduction in stiffness is chosen as 5 per cent from 25 per cent to 80 per cent local damage (i.e. 11 different damage severities). Therefore, totally 21 different damage

scenarios are created by local stiffness reduction in FEM. The assumption made here is that the effect of the damage results in a local reduction in the stiffness which is modelled by reducing the material properties of the selected elements in all directions by the same amount.

7.2.2.2 *Location of Damage*

Six different locations are selected along the span of the beam in order to introduce different damage severities. These locations are $0.2L$, $0.35L$, $0.45L$, $0.55L$, $0.65L$ and $0.8L$ away from the fixed end. The width and the length of the damage are kept constant during the analyses as $0.1L$ that corresponds to four elements in FEM. In **Fig. 7.1**, the location of the damage (grey area in circle) has been taken as $0.55L$ as an example.

After performing modal analysis, 126 different natural frequency reductions (21 different damage severities at 6 different locations) are obtained for each mode of the damaged beam with respect to that of intact one. All these variations in natural frequencies for different damage scenarios from the first three natural modes will be investigated in the sensitivity analysis and feature extraction section (Section 7.4).

7.3 Curvature Mode Shape Analysis

A finite element modal analysis has been performed in Section 7.2 to find the first three undamped natural frequencies and corresponding normalised displacement mode shapes of the cantilever laminated composite beam. Eleven points along the centre line of the beam are selected to obtain one-dimensional curvature mode shapes. In **Fig. 7.1**, the white dots show the locations of these collocation points along the beam. During the analysis, curvature mode shapes are calculated from displacement mode shapes by using equation (6.2) at these collocation points. Since the length of each element in the finite element model is constant along the beam and the absolute differences between the curvature mode shapes of the intact and the damaged structures are of primary interest, the h^2 term in equation (6.2) appears as a constant scaling factor and has been taken as unity for the sake of simplicity in the curvature calculations. Since 126 different damage scenarios are created for the composite beam, the curvature mode shapes corresponding to these cases are not shown here. All variations in absolute differences between intact and damaged curvature mode shapes along the beam with different stiffness reductions at various locations will be presented in the next section.

7.4 Sensitivity Analyses and Feature Extraction

7.4.1 Percentage Reduction in Natural Frequencies

By considering the variations of the percentage reduction in the frequencies for the first three natural modes, the effect of the severity and the location of the damage on natural frequencies are investigated. The percentage reduction in natural frequencies with twenty-one different severities of the damage at six different locations along the beam in three different modes can be seen in **Fig. 7.2.** From the variations and trends in this figure, it can be concluded that the reduction in natural frequencies increases with the increasing severity.

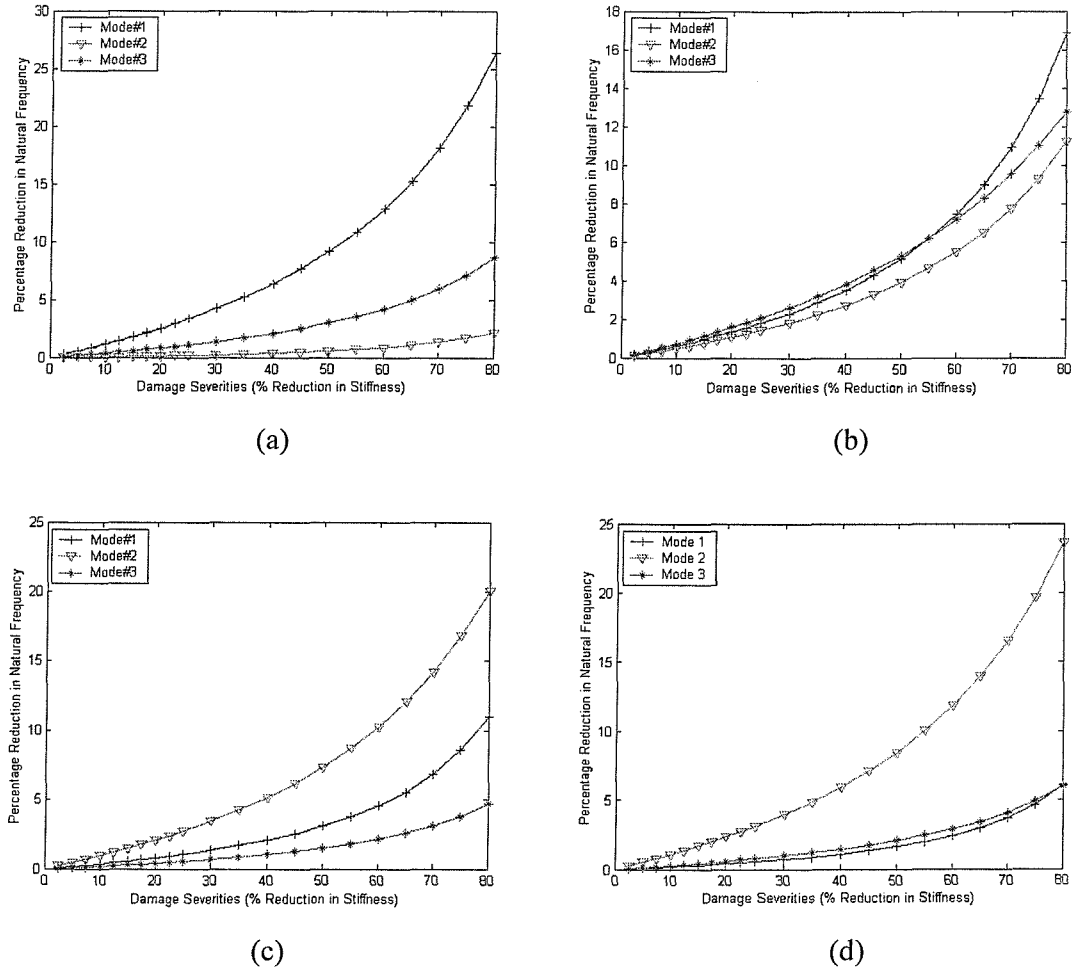

Fig. 7.2 (continued over)

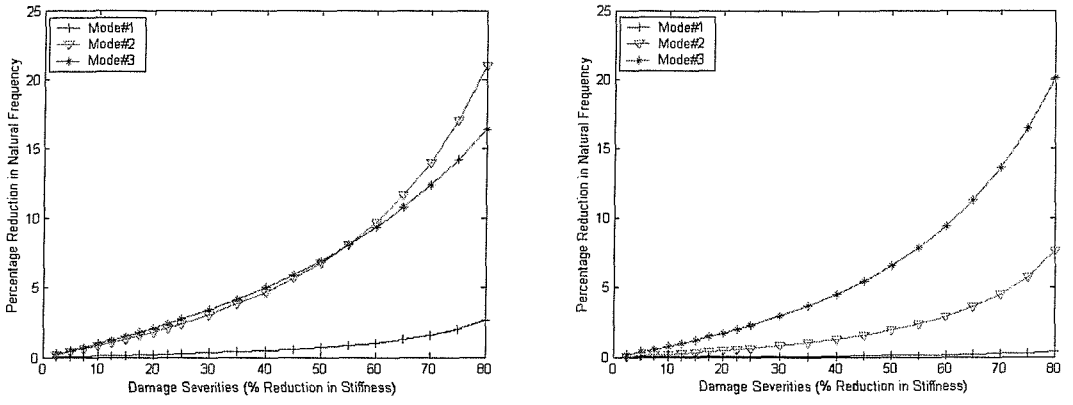

Figure 7.2 Percentage reduction in natural frequencies for different damage locations: Damage located at (a) 0.20*L* (b) 0.35*L* (c) 0.45*L* (d) 0.55*L* (e) 0.65*L* (f) 0.80*L*

As it can be seen in **Fig. 7.2a**, there is a higher reduction in natural frequency in Mode 1 when the damage is near the root of the beam (i.e. at 0.2*L*). On the other hand, in **Fig. 7.2b**, almost all modes are affected approximately up to same extent. **Figs. 7.2c** and **d** show that Mode 2 is much more influenced when the damage is located around mid-span (i.e. at 0.45*L* and 0.55*L*) of the beam. It can be seen from **Fig. 7.2e** that reduction in natural frequency in Mode 2 and Mode 3 are almost same when the damage located at 0.65*L*. Finally, when the damage is located at 0.80*L* (**Fig. 7.2f**), there is more reduction in frequency in Mode 3 than those in Mode 2 and Mode 1. This indicates that it is important to consider more than one mode of the beam since, depending on the location of the damage different natural modes of the beam are affected to different extents in the reduction of frequency.

7.4.2 Absolute Differences in Curvature Mode Shapes

After considering the effects of natural frequency reduction, the effectiveness of absolute differences in curvature mode shape between the intact and the damaged composite beams is investigated. Since three different modes of vibration and six different damage locations are considered during the analyses, totally eighteen different variations are obtained from absolute differences in curvature mode shapes between the intact and the damaged beams. These variations are shown from **Figs. 7.3** to **7.5** for six different locations of the damage at the first three natural modes.

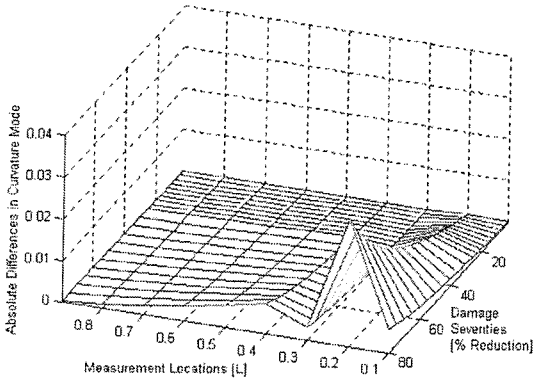

(a)

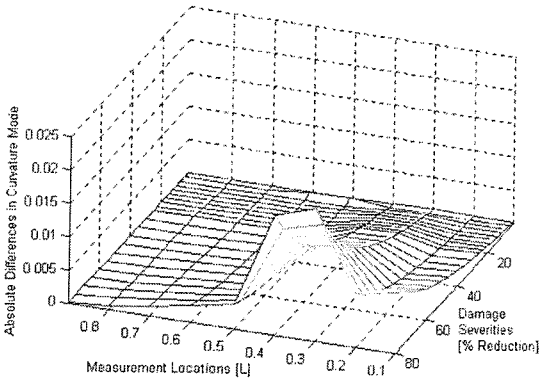

(b)

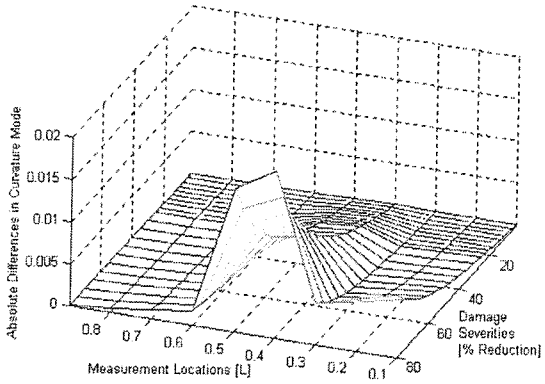

(c)

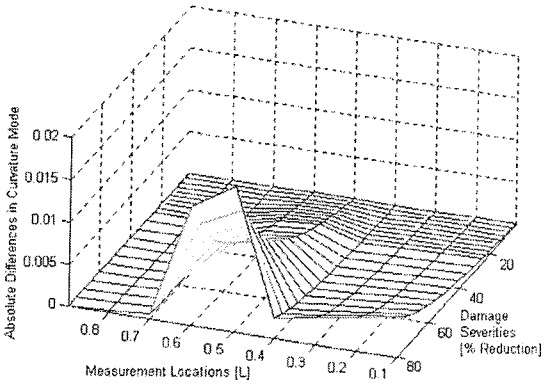

(d)

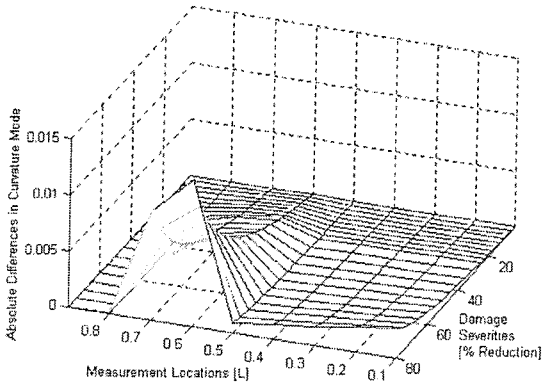

(e)

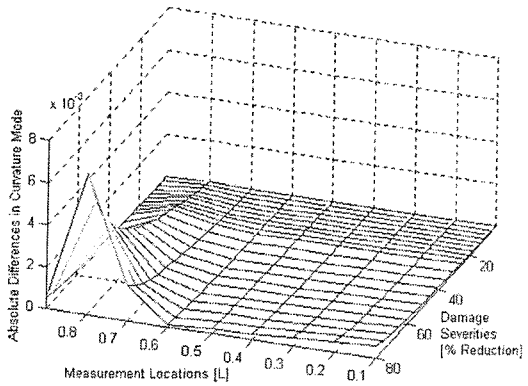

(f)

Figure 7.3 Variation of the magnitude of the absolute differences in curvature modes along the beam with different severities in Mode 1: Damage located at (a)0.20*L* (b)0.35*L* (c)0.45*L* (d)0.55*L* (e)0.60*L* (f)0.80*L*

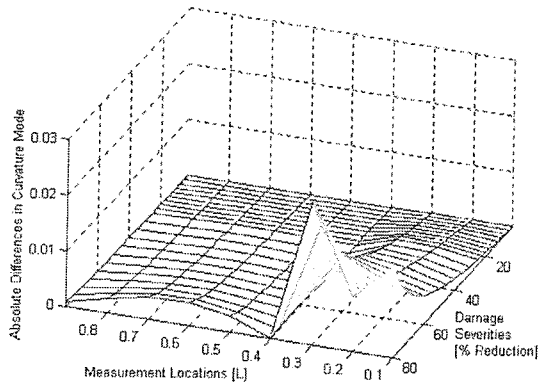

(a)

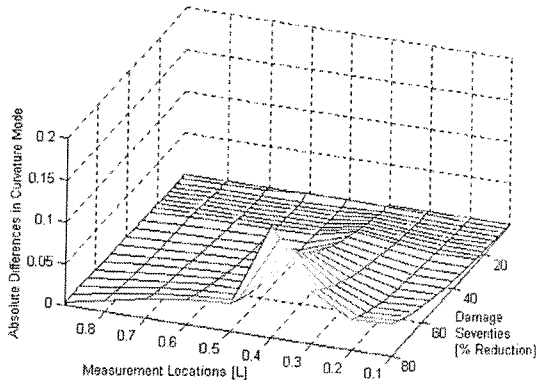

(b)

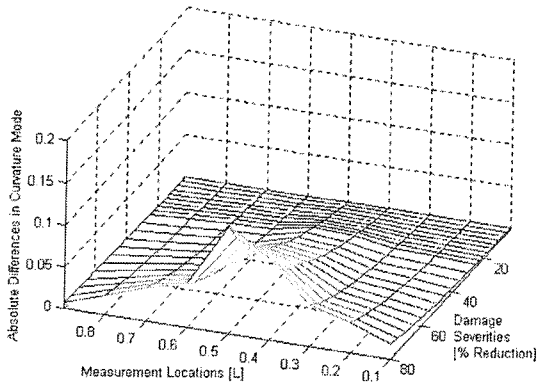

(c)

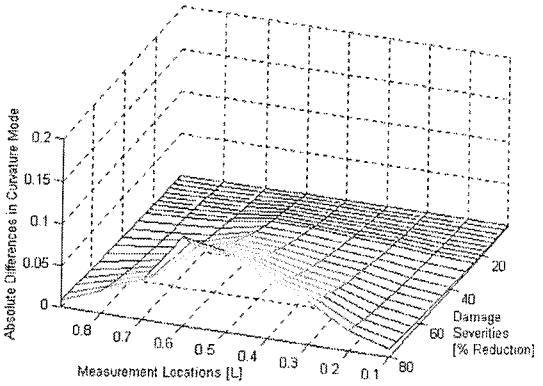

(d)

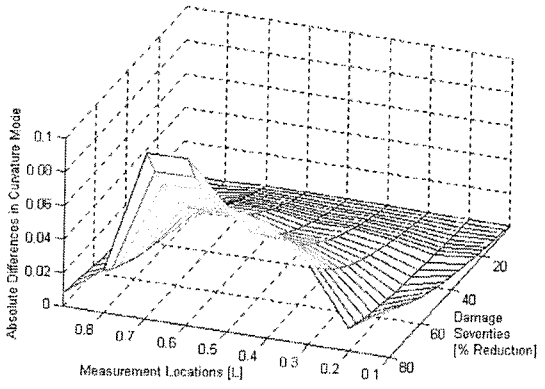

(e)

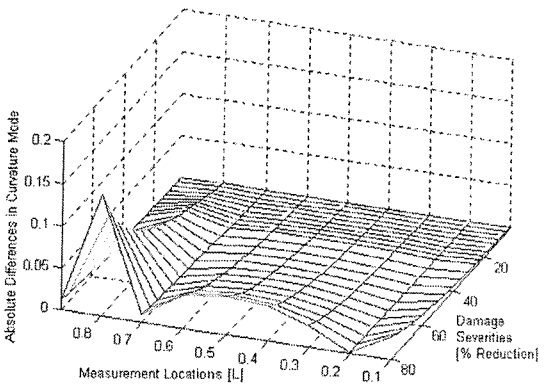

(f)

Figure 7.4 Variation of the magnitude of the absolute differences in curvature modes along the beam with different severities in Mode 2: Damage located at (a)0.20L (b)0.35L (c)0.45L (d)0.55L (e)0.60L (f)0.80L

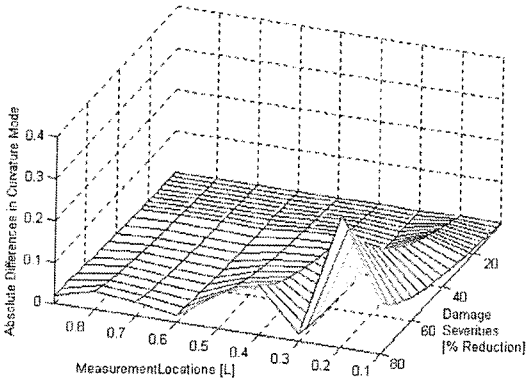

(a)

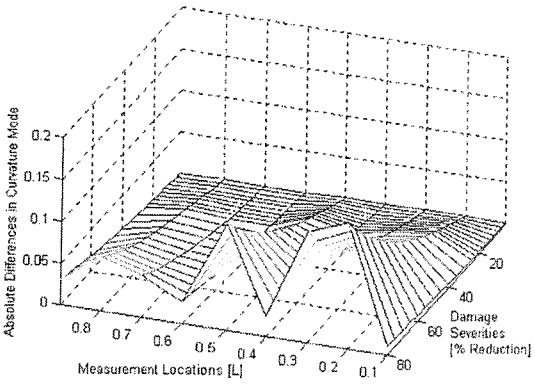

(b)

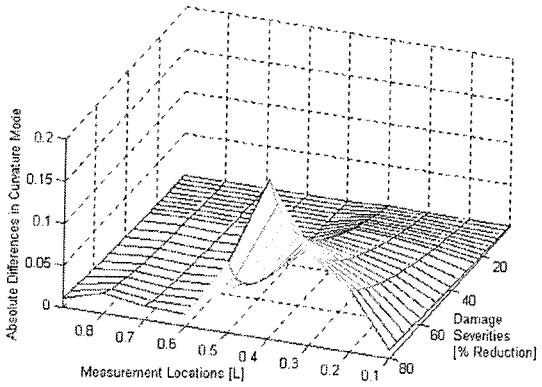

(c)

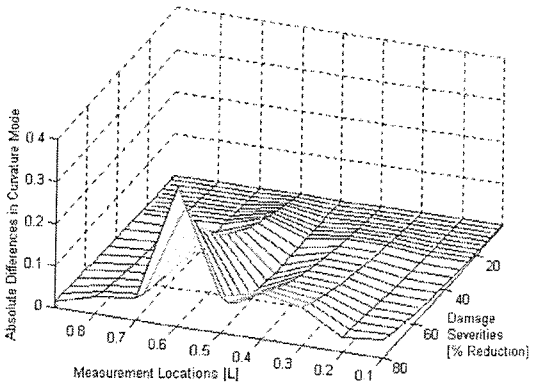

(d)

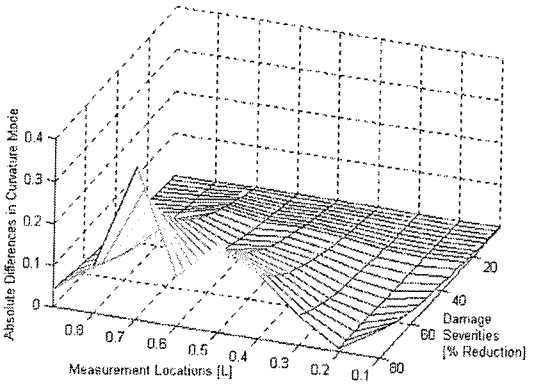

(e)

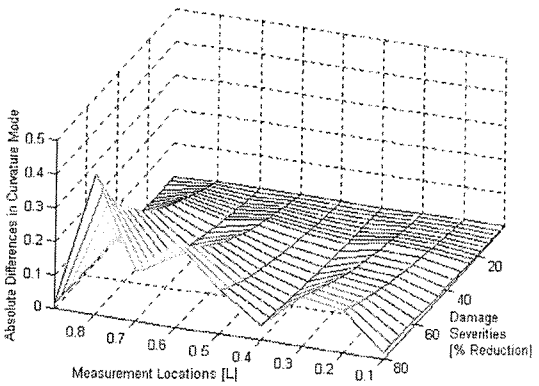

(f)

Figure 7.5 Variation of the magnitude of the absolute differences in curvature modes along the beam with different severities in Mode 3: Damage located at (a)0.20*L* (b)0.35*L* (c)0.45*L* (d)0.55*L* (e)0.60*L* (f)0.80*L*

It can be seen from **Figs 7.3** to **7.5** that the maximum absolute difference occurs near damage location. Therefore, the maximum value of the absolute difference in curvature and its corresponding location along the beam obtained from three different modes would be additional information serving as input to the ANN in the quantification and localisation of the damage.

7.4.3 Pre-Processing of Features

After deciding on the features extracted from the model-dependent vibration–based data, some necessary pre-processing is performed. Normalisation of the input-output pairs and addition of artificial noise to different input data are presented in this section. The main aim of the pre-processing is to arrange the data in such a way that it can easily be introduced to damage identification algorithm as input-output pairs.

7.4.3.1 *Normalisation of Data*

As input data should not be too close to 0 or 1 in order to avoid numerical difficulties, the first three natural frequencies of the beam are normalised by calculating the ratio of natural frequencies of the damaged beams to that of intact one. Since small reductions in stiffness lead to small changes in natural frequencies, thus giving values close to 1, an additional normalisation **[2-45]** is performed by using the following equation:

$$\bar{x}_i = \frac{x_i - \beta x_{i_{min}}}{\alpha x_{i_{max}} - \beta x_{i_{min}}} \quad \text{where } \alpha = 1.1\ ,\ \beta = 0.9,\quad i = 1,2..126 \tag{7.3}$$

Here, x_i is the data (reduction in natural frequencies) to be normalised, $\bar{x}_i$ is the normalised form of the data and α and β stand for the normalisation constants. Maximum absolute differences in the curvature mode shape data are also normalised using equation (7.3). There is no need to normalise the location data since it is readily available as percentage of the beam length, which is between 0 and 1 (**Fig. 7.1**).

7.4.3.2 *Addition of Artificial Noise*

Artificial noise is created by using a random number generator, *randn*, in MATLAB®. *Randn* generates random numbers with a normal distribution having zero mean, variance and standard deviation of one. Using equation (7.4), different percentages of noise are added to normalised frequency and maximum differences in curvature mode shape data.

$$Data_{With\ Noise} = Data_{Noise\ Free} \cdot \left[1 + \frac{\Delta}{100} randn(n)\right] \tag{7.4}$$

Here, n and Δ are the number of random entries in the noise-free data and the percentage noise added to noise-free data respectively. Since natural frequency measurements are more reliable and robust than strain (or curvature) mode shape measurements that require distributed sensors in real applications, higher level of percentage noise is added to maximum absolute differences to curvature mode shape data compared to normalised frequency data to simulate the experimental uncertainties.

7.5 Simulation of ANN for Damage Detection

In this study, a supervised feed-forward multi-layer backpropagation ANN in MATLAB® Neural Network Toolbox **[7-5]** is used to estimate the severity and location of the damage in beam-like laminated composite structures.

7.5.1 Designed ANNs for Damage Detection

Since the aim of the analysis is to investigate the effectiveness of the vibration-based analysis inputs in ANN applications for the severity and location prediction of the damage, different combinations of input data from the first three natural modes of the composite beam are introduced to ANNs. The effects of multiple modes on predictions of ANNs are also investigated in Appendix C justifying the use of three modes.

The size of the ANN is very important since small networks cannot represent the system while larger networks can be over-trained. Hence optimisation in the size of the network is crucial and this is generally obtained by a trial and error method. Therefore, different neural networks with one hidden layer are designed to maximise performance in the prediction of the

severity and location of the damage. The studies on using one and two hidden layers are discussed in Appendix D, justifying the use of one hidden layer ANN. **Table 7.2** shows all the ANNs designed and used in the analyses with a variety of input and output pairs. Values (separated with semicolon) used in the architecture column of **Table 7.2** show the total number neurons in the input, hidden and output layers respectively.

Table 7.2 ANNs used in the analyses

	Input	Output	Architecture
1.	RNF	DS	3:6:1
2.	RNF	DL	3:6:1
3.	RNF	DS&DL	3:8:2
4.	MADC	DS	3:6:1
5.	MADC	DL	3:6:1
6.	MADC	DS&DL	3:8:2
7.	RNF&MADC	DS	6:9:1
8.	RNF&MADC	DL	6:9:1
9.	RNF&MADC	DS&DL	6:12:2
10.	MADC&LOC	DS	6:9:1
11.	MADC&LOC	DL	6:9:1
12.	MADC&LOC	DS&DL	6:12:2
13.	RNF&MADC&LOC	DS	9:18:1
14.	RNF&MADC&LOC	DL	9:18:1
15.	RNF&MADC&LOC	DS&DL	9:18:2

7.5.2 Noise-free Input Data

The most important criterion in the selection of the training samples is to find the ideal set that can represent the total possible samples in the space. In this analysis, 126 different damage scenarios are generated by using 21 different reductions in stiffness at 6 different locations throughout the beam. 100 input-output pairs, chosen at random, are given to the ANN for training and the rest of the input-output pairs are used to check the generalisation of the learning during the validation process.

7.5.3 Input Data with Noise

One of the most important problems with the use of the backpropagation algorithm is the generalisation of learning capability. Therefore artificial random noise has been added to data used in the noise-free case in order to achieve a better generalisation during the training of ANNs and to simulate the experimental uncertainties numerically. **Table 7.3** shows the different percentages of noise combinations added to frequency and maximum absolute differences in curvature mode shape data.

Table 7.3 Addition of percentage noise to input data

Input Data	Percentage Noise (Δ) on	
	RNF	MADC
RNF	0.5	-
RNF	1	-
RNF	2	-
MADC&LOC	-	1
MADC&LOC	-	3
MADC&LOC	-	5
RNF&MADC&LOC	0.5	1
RNF&MADC&LOC	1	3
RNF&MADC&LOC	2	5

First, 100 copies of each input data from the first three natural modes are obtained and different noise histories having same percentage level are added. This process simulates the fact that each mode has its own energy level and can only be obtained separately from the others. Since totally 126 different damage scenarios are used in the analyses with 100 copies, final input data having 10000 and 2600 entries is introduced to selected ANNs (RNF, MADC&LOC, and RNF&MADC&LOC in **Table 7.3**) during the training and validation runs respectively.

7.5.4 Test cases for ANNs

Sixteen different cases are used to test the trained neural networks, as shown in **Table 7.4**. In the first eight cases, the damage locations are selected from training sets while in the

other eight cases, new locations are considered. In both cases, eight new reductions in stiffness are introduced to ANNs. After completing simulations with different ANN architectures, three networks (First, eleventh and fifteenth ANNs in **Table 7.2**) are selected on the basis of minimum mean square error and better convergence with the increase in number of epochs during the training. An additional set of three networks (second, fourth and fifth ANNs in **Table 7.2**) is also used for the prediction performance comparisons.

Table 7.4 Test cases for ANNs

Reduction in Stiffness [%]	Location [L]
8	0.55
14	0.20
21	0.80
37	0.45
42	0.35
53	0.65
62	0.20
73	0.65
8	0.50
14	0.60
21	0.30
37	0.75
42	0.25
53	0.40
62	0.30
73	0.40

7.6 Artificial Neural Network Predictions

7.6.1 Noise-free Case

7.6.1.1 Damage Severity Predictions

In the first ANN (RNF-DS), the reduction in natural frequencies is given as an input and severity of the damage is predicted as an output. In this training run, the mean square error is reduced to a value lower than 10^{-3} after 10000 epochs. Here, epoch denotes the number of times the same training input set introduced to the ANN. In **Fig. 7.6a**, the trend of the mean square error (MSE) can be seen with increasing number of epochs. Considering the error between the training (black solid line) and the validation sets (grey solid line) during the learning process, it can be concluded that the generalisation is almost achieved. The first test with three inputs

(reduction in natural frequencies from three natural modes) is performed on 16 different cases. **Figure 7.6b** shows the results of the neural network regarding prediction of the severity of the damage. The symbols, circles and crosses, indicate the first and the last eight test cases used in **Table 7.4** respectively. The dotted lines lying on both sides of the centre line indicate a 5 per cent deviation from the target values.

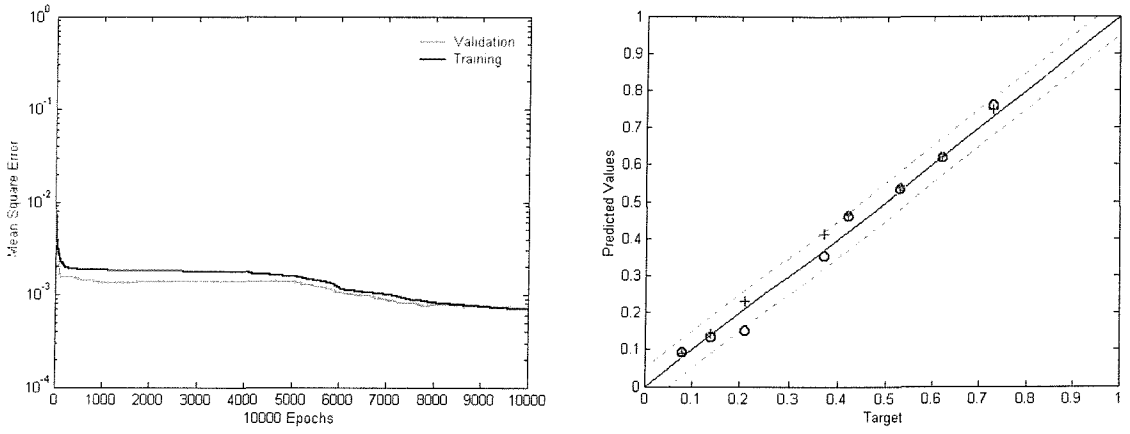

(a) (b)

Figure 7.6 ANN results for severity predictions (Input: RNF, Output: DS)
(a) Mean square error with number of epochs (b) Severity predictions

The fourth ANN test run (MADC-DS) is performed to predict the severity of the damage by using maximum absolute differences in curvature mode shape from the first three modes. Severity predictions for this particular test case can be seen in **Fig. 7.7**.

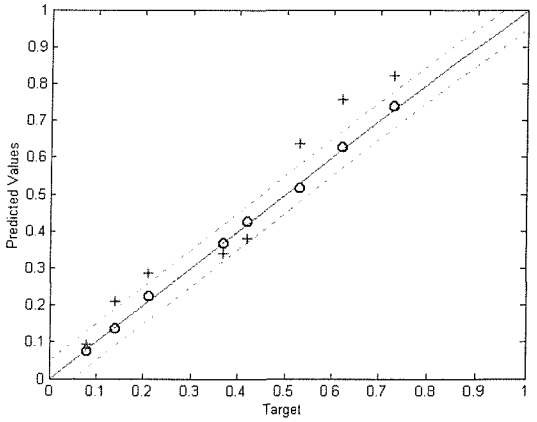

Figure 7.7 ANN results for severity predictions (Input: MADC, Output: DS)

7.6.1.2 Damage Location Predictions

In the second ANN (RNF-DL), the reduction in natural frequencies is given as an input and location of the damage is predicted as an output. Since the input introduced to the ANN is not directly related with the output to be predicted, the generalisation is not achieved. **Figures 7.8a** and **b** show the performance of the ANN during the learning and the location predictions for the test cases respectively.

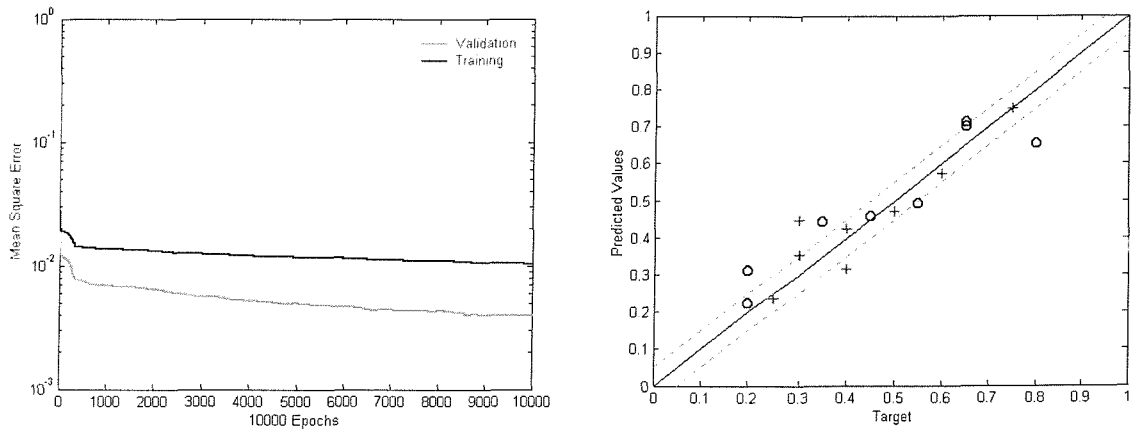

(a) (b)

Figure 7.8 ANN results for location predictions (Input: RNF, Output: DL)
(a) Mean square error with number of epochs (b) Location predictions

The fifth ANN test run (MADC-DL) is for the location prediction of the damage by using maximum absolute differences in curvature mode shape data as input. **Figure 7.9** shows the location predictions for this particular test case.

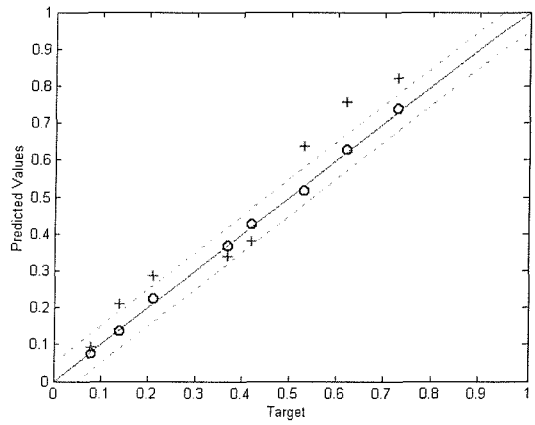

Figure 7.9 ANN results for location predictions (Input: MADC, Output: DL)

The eleventh ANN test run (MADC&LOC-DL) is for the prediction of location of damage. In this case, the maximum absolute differences in curvature mode shape and their corresponding locations along the beam are given as an input to the ANN. Since the input features, the maximum absolute differences and their corresponding locations, are good indicators for the location prediction of the damage, the mean square error is reduced to below 10^{-5}. A slight difference is observed in the error residual between the training and validation. The prediction of this ANN can be seen in **Fig. 7.10**. Although almost all the predictions are within 5 per cent limit, first eight predictions (shown with circles) are quite accurate compared to the last eight test case predictions. This means a better generalisation is needed for higher accuracy.

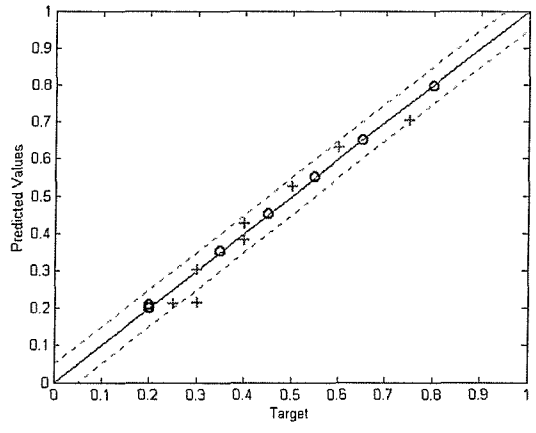

Figure 7.10 ANN results for location predictions (Input: MADC&LOC, Output: DL)

7.6.1.3 *Both Damage Severity and Location Predictions*

The fifteenth ANN test run (RNF&MADC&LOC-DS&DL) involved in training is performed with nine inputs namely: reduction in natural frequencies, maximum absolute differences in curvature mode shape and their corresponding locations along the beam from the first three natural modes. In this case, severity and the location of the damage are predicted. Since the input and output pairs are larger in size and the association between the features is much more complicated compared to previous runs, the mean square error values for both the training and validation reach a value between 10^{-4} and 10^{-5} after 10000 epochs. Due to the inherent complexity of the test, bigger difference between the training and the validation error values occurred at the end of the training. The results show that there is a slight overestimation in the prediction of severity (**Fig. 7.11a**). On the other hand, in the prediction of location of the damage, the outputs are closer to target values with acceptable deviations (**Fig. 7.11b**).

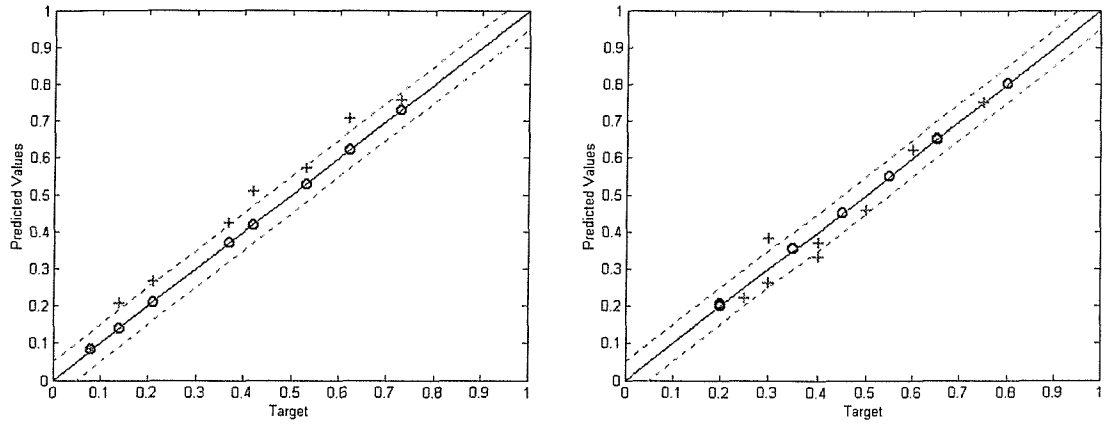

(a) (b)

Figure 7.11 ANN results for severity and location predictions (Input: RNF&MADC&LOC) (a) Severity predictions (Output: DS) (b) Location predictions (Output: DL)

7.6.2 Noise Polluted Data

In this section, only three ANNs having best performance in the prediction of severity and location of the damage in noise-free case (First, eleventh and fifteenth ANNs in **Table 7.2**) are selected and tested for new damage scenarios (**Table 7.4**) with addition of percentage noise (**Table 7.3**).

7.6.2.1 Damage Severity Predictions

Figure 7.12 shows the severity predictions of the first ANN (RNF-DS) with three different levels of added artificial noise. It can be seen from **Fig. 7.12** that increase in percentage noise level adversely affects the severity predictions.

7.6.2.2 Damage Location Predictions

Location predictions of the eleventh ANN (MADC&LOC-DL) with three different levels of added artificial noise is shown in **Fig. 7.13**. It can be seen from the figure that location predictions for the damage are more accurate than severity predictions when maximum absolute differences in curvature mode shape and location information are introduced to ANN as input although the noise levels are relatively higher than the ones used on the normalised frequency data.

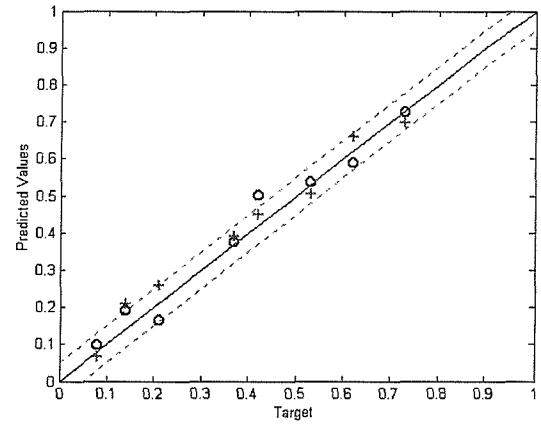

(a)

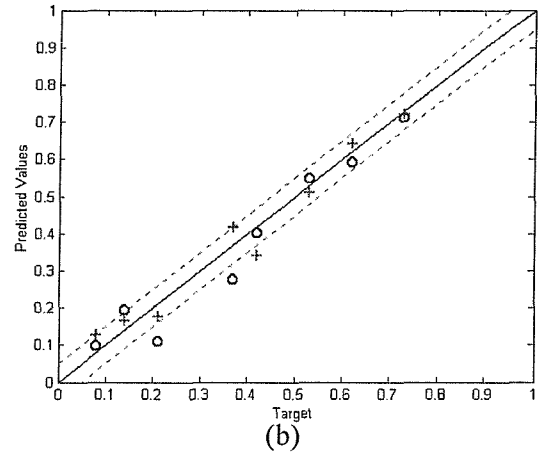

(b)

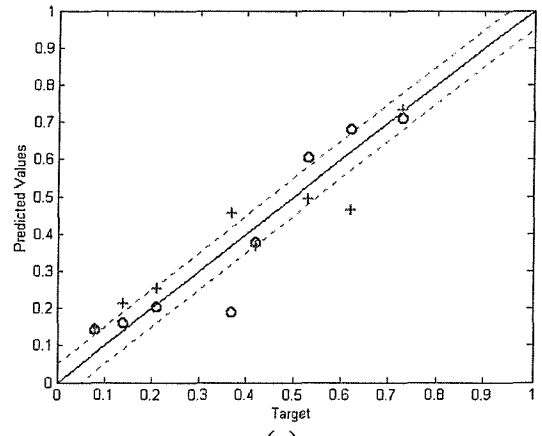

(c)

Figure 7.12 ANN results for severity predictions with an addition of noise (Input: RNF, Output: DS) (a) 0.5% Noise (b) 1% Noise (c) 2% Noise

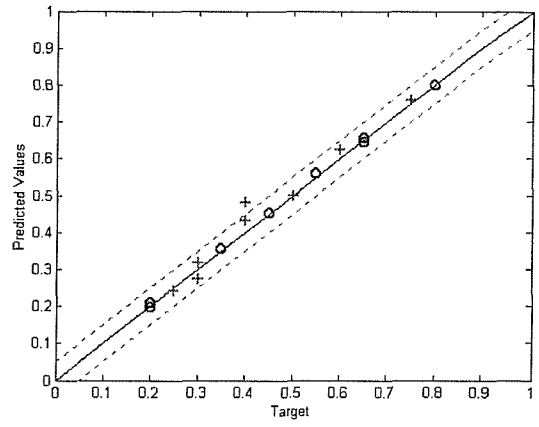

(a)

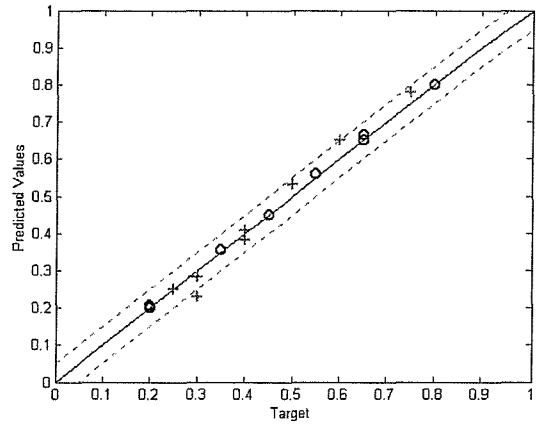

(b)

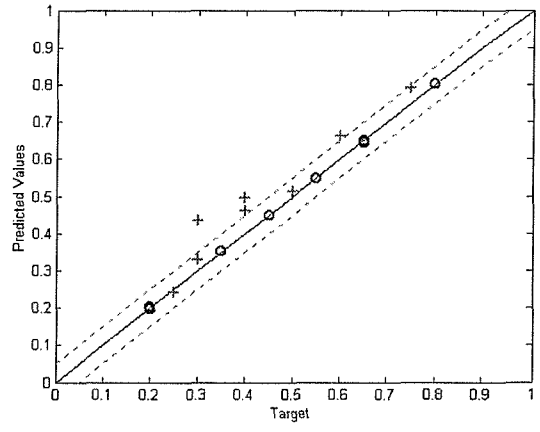

(c)

Figure 7.13 ANN results for location predictions with an addition of noise (Input: MADC&LOC, Output: DL) (a) 1% Noise (b) 3% Noise (c) 5% Noise

7.6.2.3 Both Damage Severity and Location Predictions

Further analyses concentrate on the effects of different noise combinations on frequency and maximum absolute differences in curvature mode shape data for the prediction of severity and location of the damage by single neural network (RNF&MADC&LOC-DS&DL) having all three inputs from first three natural modes of the beam as an input. ANN predictions with the noise-polluted data can be seen from **Figs. 7.14** to **7.16**. In these three figures, the noise combination is gradually increased on frequency and maximum absolute differences in curvature mode shape data. It can be concluded from the figures that although predictions are in the acceptable region with a couple of under and overestimations at lower noise level combinations, the location predictions are more accurate and robust than severity predictions using single ANN with all inputs at higher level of noise combinations.

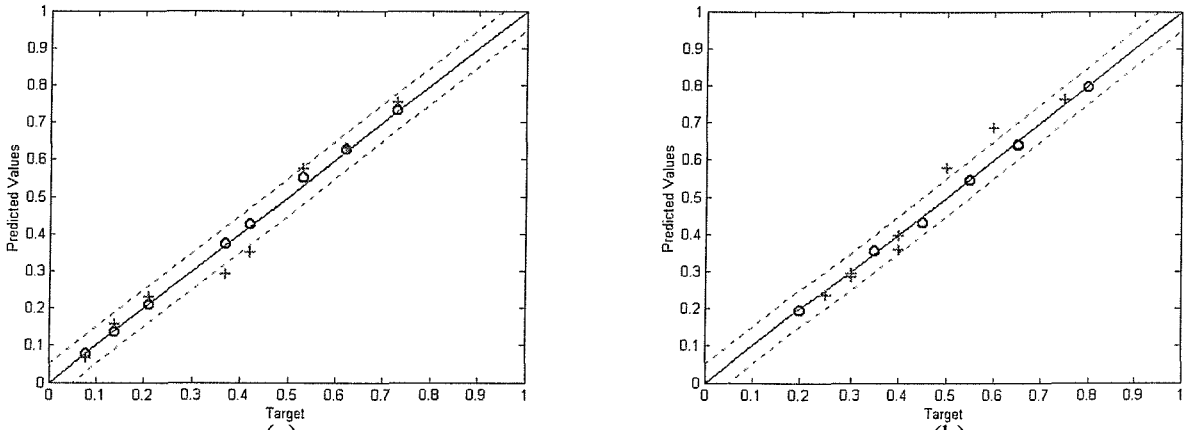

(a) (b)

Figure 7.14 ANN predictions with noise combination of 0.5% on RNF and 1% on MADC

(a) Severity predictions (b) Location predictions

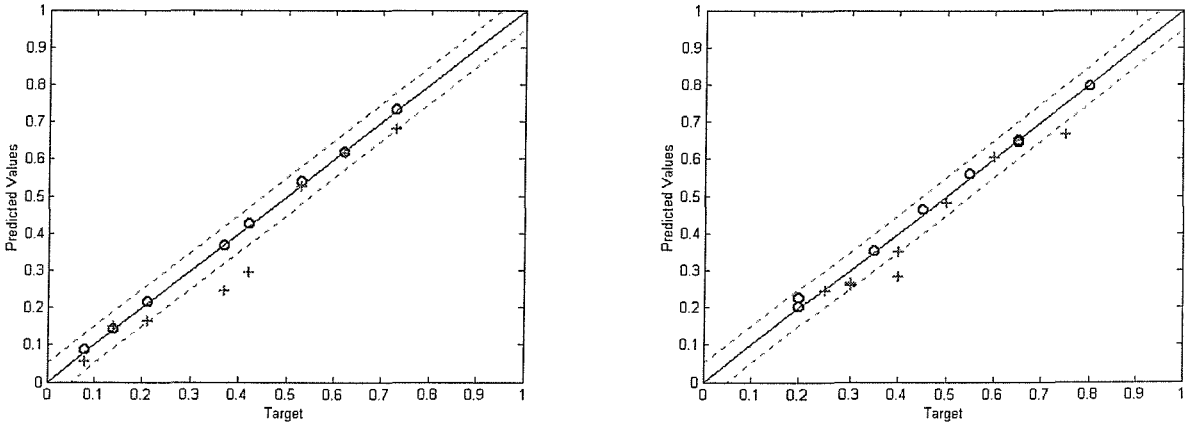

(a) (b)

Figure 7.15 ANN predictions with noise combination of 1% on RNF and 3% on MADC

(a) Severity predictions (b) Location predictions

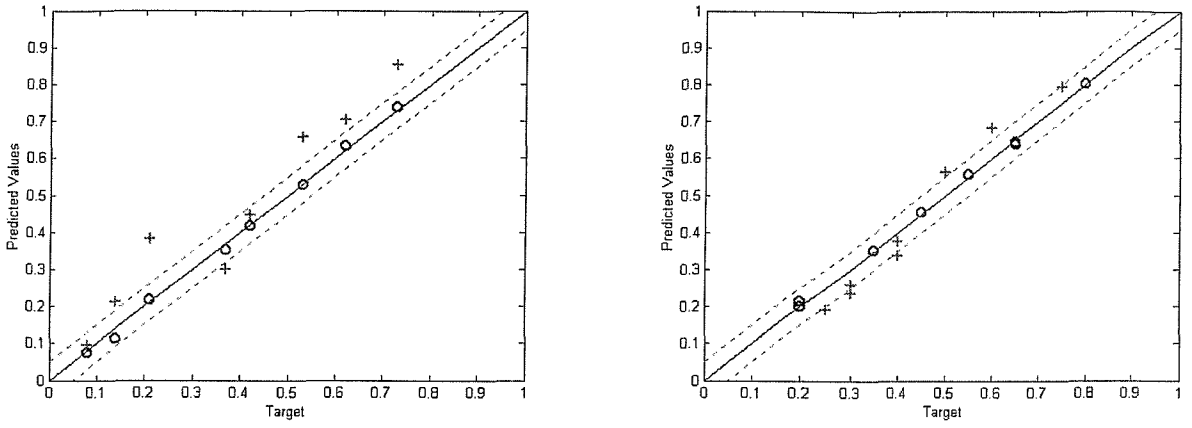

(a) (b)

Figure 7.16 ANN predictions with noise combination of 2% on RNF and 5% on MADC
(a) Severity predictions (b) Location predictions

7.7 Conclusions

In this chapter, features extracted from vibration-based analysis on beam-like composite laminate were used in order to predict the severity and location of the damage and to investigate the effectiveness of these features as input to feed-forward backpropagation neural networks.

In literature, local and global patterns (i.e. curvature mode shapes and natural frequencies) obtained either from experimental work or numerically simulated vibration analysis data were used in ANN applications (**Table 7.5**) in order to detect damage in composite beam structures. However, there is no particular study found in the literature considering different combinations of the vibration analysis data as input to ANN.

Table 7.5 Studies on composite beam structures and features for ANN applications

Studies on Composite Structures	[7] [8] [9] [10] [12] [14] [27] [30] [31] [32] [33] [35] [44] [45] [50] [52] [53] [54] [59] [60] [61]
Frequency Changes	[44] [50] [52] [53] [55]
Curvature Mode Shapes or Strain History	[44] [50] [54]
Both Frequency Changes and Curvature (Strain) Mode Shapes	[50]*

*In different case studies, [Numbers in brackets are references from Chapter 2]

In this chapter, different input-output pairs have been generated from various damage scenarios and used for the training and validation of different types of ANNs either noise-free or with an addition of percentage artificial noise to simulate the experimental uncertainties. The results obtained using new test cases show that selection of features considered as an input data is crucial in the accuracy of prediction of damage. In addition to the selected features, the level of the artificial noise added to input data is also very important from the generalisation and robustness point of view of the designed ANNs. It can be concluded that although reduction in natural frequencies is considered as an indicator for the existence of the damage and its severity, it did not provide any useful information about the location of the damage. On the other hand, maximum absolute differences in curvature mode shapes and their corresponding locations along the beam served as better indicators for the location of the damage. Therefore, these features were used as separate input for the ANNs.

When the combination of these three features (i.e. reduction in natural frequencies, maximum absolute differences in curvature mode shapes and their corresponding locations) are introduced to ANNs, the results regarding severity and location of the damage are not as promising as the ones obtained with individual inputs. Hence it can be concluded that two separate ANNs function more efficiently than one trained ANN using all the combined inputs in the noise-free case. On the other hand, when the increased level of noise-polluted data introduced as an input, whilst training, ANNs provided more accurate and robust predictions in the localisation of the damage compared to damage quantification.

Finally, the severity and location predictions of various ANNs trained with different combinations of vibration-based analysis data showed that the features extracted and used as an input and the level of noise on these features play an important role in the accuracy of the predictions of ANNs for structural damage detection.

Chapter Eight EXPERIMENTAL VALIDATION OF THE METHOD

8.1 Introduction

This chapter presents an experimentally validated damage detection algorithm using combination of global and local vibration-based analysis data as input to ANNs for location and severity prediction of damage in isotropic beam structures **[8-1]**. The global parameters refer to change in natural frequencies and the local parameters refer to change in curvature (in FEA) or strain (in experimental study) mode shapes of the structure in the first three natural modes. In FEA, different damage scenarios have been introduced by reducing the local thickness of the selected elements at different locations along the FEM of the beam structure. The necessary features for damage detection have been selected by performing sensitivity analyses and different input-output sets have been introduced to various ANNs. In order to check the robustness of the input data used in the analysis and simulate the experimental uncertainties, artificial random noise has been generated numerically and added to noise-free data during the training of the ANNs. In the experimental analysis, two steel beams with eight surface-bonded distributed electrical strain gauges and an accelerometer mounted at the tip have been used to obtain modal parameters such as resonant frequencies and strain mode shapes. Finally, experimentally obtained data has been introduced to trained ANNs in order to predict severity and location of the damage.

8.2 Finite Element Modelling

8.2.1 Frequency Analysis of Intact Beam

The steel beam (**Fig. 6.3**) is modelled by using four-node quadrilateral two-dimensional linear structural shell element, SHELL63, with ANSYS 6.1® commercial software. First three bending natural frequencies of the intact cantilever beam for different mesh densities are obtained in order to check mesh independency. Since the variation in natural frequencies is less

than 1% between 4x90 (i.e. 4 and 90 element divisions along the width and the length of the beam respectively) and 16x360 mesh densities, the former having 360 elements, is used for all later simulations by considering the computational efficiency. After performing modal analysis for the first three bending natural frequencies, results obtained from models having different mesh densities are compared to closed-form solution (Eq. 4.17) in **Table 8.1**. The number in parentheses shows the percentage difference between theoretical and FEA results.

Table 8.1 First three natural frequencies of intact beam [Hz]

		Shell Elements	
Mode No	Closed-form Solution	4x90	16x360
1st Bending	12.2893	12.3859 (0.7860)	12.3818 (0.7527)
2nd Bending	77.0156	77.6044 (0.7645)	77.5748 (0.7261)
3rd Bending	215.6461	217.5093 (0.8640)	217.3731 (0.8008)

8.2.2 Damage Scenarios

Local damage is introduced with 32 damage severities at 15 different spatial locations along the span of the beam i.e. 480 different damage scenarios. Structural damage is modelled as a local reduction in thickness of the selected elements. The incremental reduction in thickness is chosen as 2.5% up to 80% local damage. The locations of the damage are at different percentages away from the cantilever end, shown in **Table 8.2**. The width (10mm) and the length (40mm) of the damage are kept constant during the analysis corresponding to two elements in span wise and four elements in the width direction in FEM. In **Fig. 8.1**, the FEM of the damaged beam with a 2mm deep slot corresponding to 66.67% reduction in thickness at the location of $0.4556L$ is shown as occurs in the experimental analysis.

Table 8.2 Different damage locations

Normalised spatial location from root [L]		
0.044	0.30	0.54
0.10	0.34	0.60
0.14	0.40	0.64
0.20	0.44	0.70
0.24	0.50	0.74

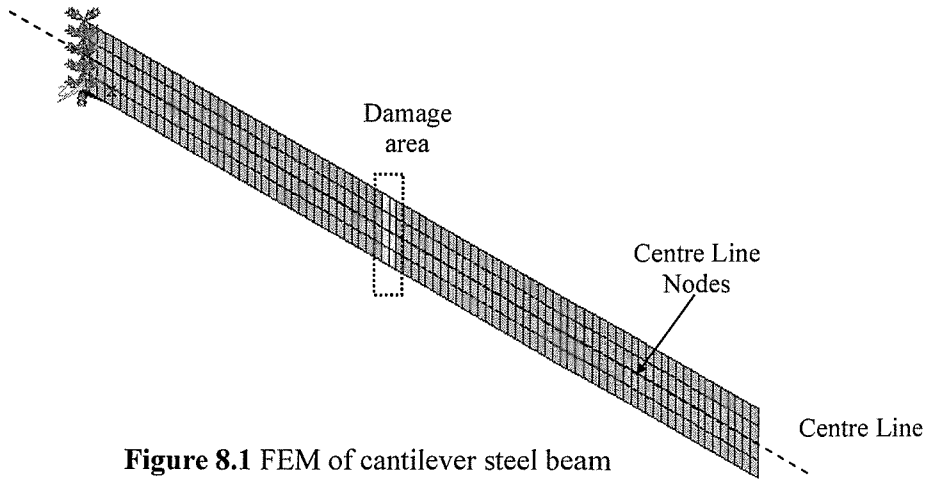

Figure 8.1 FEM of cantilever steel beam

8.2.3 Modal Analysis of Damaged Beam

A normal mode dynamic analysis is performed to find the first three undamped natural frequencies and their corresponding displacement mode shapes of the cantilever beam. **Table 8.3** shows the first three natural frequencies of the intact and the damaged beam (2mm deep slot at the location of 0.4556L), which is used in experimental study for comparison and validation. 91 points along the centre line of the beam are selected from FEM in order to obtain one-dimensional displacement mode shapes. During the analysis, curvature mode shapes are calculated by using central difference approximation (Eq. 6.2). All modal analysis data (natural frequencies and corresponding curvature mode shapes) is presented in the feature extraction section.

Table 8.3 First three natural frequencies of intact and damaged beam [Hz]

	Finite Element Analysis Results		
Mode No	Intact Beam	Damaged Beam	$\frac{f_{damaged}}{f_{intact}}$
1st Bending	12.3859	10.7415	0.8672
2nd Bending	77.6044	60.3581	0.7778
3rd Bending	217.5093	212.4555	0.9768

8.3 Feature Extraction

In the first part of this analysis, the effect of the severity and the location of the damage on the first three natural frequencies of the structure are investigated. **Figure 8.2** shows the

percentage reduction in natural frequencies with 32 different severities at selected 8 different locations. It can be seen from the **Fig. 8.2** that different vibration modes are affected to different extents due to the reduction in thickness, depending on the location of the damage. This illustrates the need to consider more than one vibration mode for improved damage prediction. In the second part, the variation of the magnitude of the absolute differences in curvature mode shapes between the intact and the damaged beam is considered at the same locations in mode 1, 2 and 3 respectively. **Figures 8.3-8.5** show these variations in the first, second and third modes respectively. In these figures, each collocation point corresponds to location of the strain gauges used in the experiment and they are numbered accordingly.

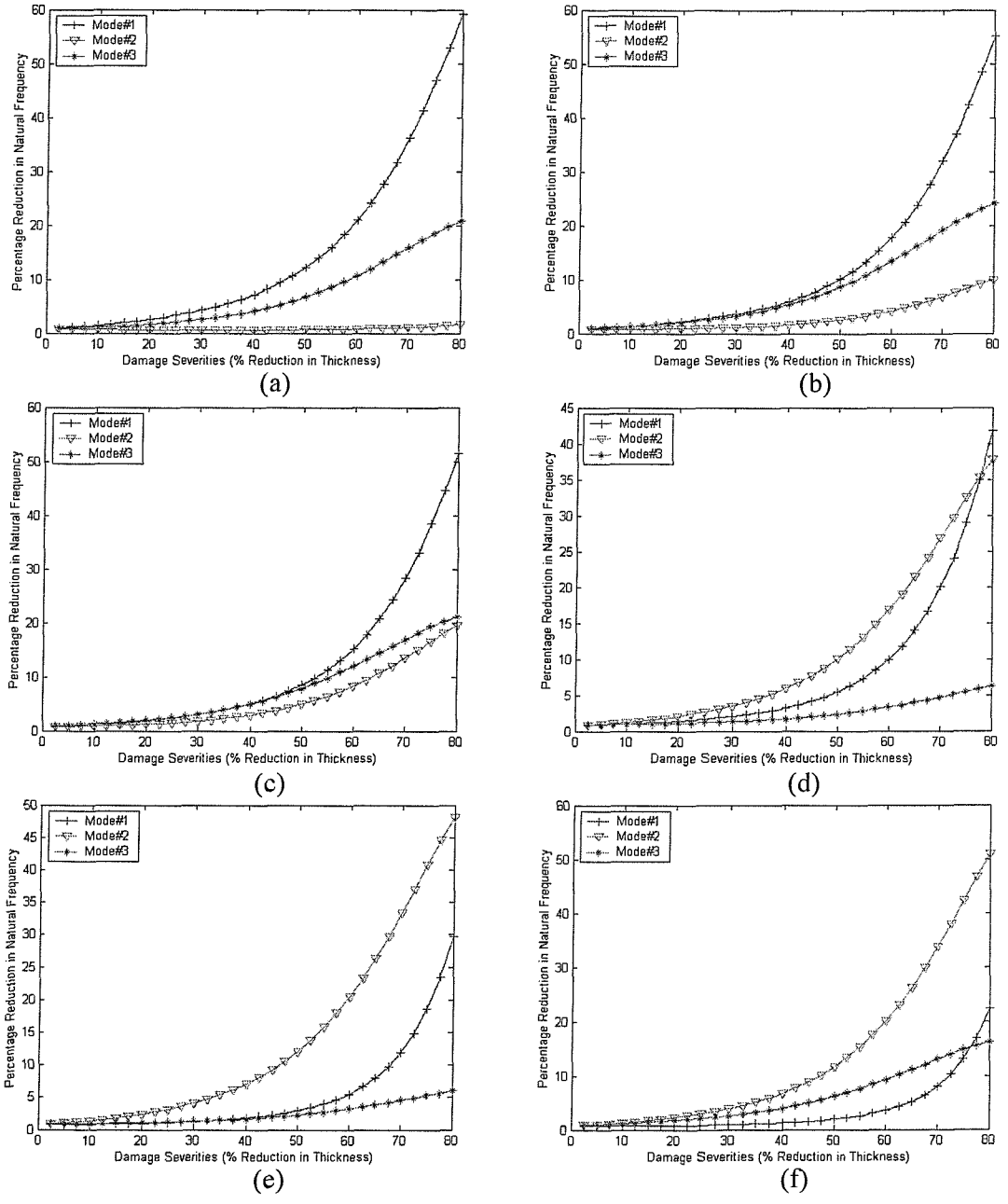

Fig. 8.2 (continued over)

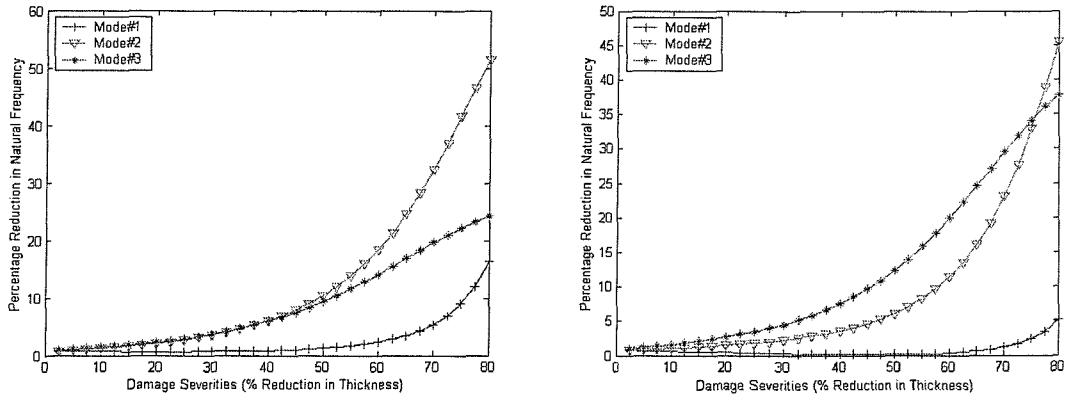

Figure 8.2 Percentage reduction in natural frequencies for different damage locations: Damage located at (a) 0.24*L* (b) 0.3*L* (c) 0.34*L* (d) 0.44*L* (e) 0.54*L* (f) 0.6*L* (g) 0.64*L* (h) 0.74*L*

8.4 Experimental Study

To validate the numerical method proposed for quantification and localisation of the damage in Chapter 7, an experimental study was carried out on steel beam specimens. Beam specimens, experimental procedure, modal analysis aiming resonant frequencies (**Table 6.4**) and strain mode shapes have been described in detail in section 6.2.3. Therefore, in this section, the strain outputs of eight strain gauges in the first three modes of the intact and damaged beams are obtained by using signal conditioning amplifier under constant frequency excitation at each resonant frequency of interest and shown in **Figs. 8.6-8.11**.

Normalisation over strain histories obtained from seven strain gauges is performed with respect to strain gauge at location 8, which provides reasonable finite amount of strain for all three modes, in order to investigate the relative change in damaged beam curvatures at eight different locations with respect to intact ones. **Figures 8.12** and **8.13** show normalised strain mode shapes of intact and damaged beams respectively. Since the additional features extracted from vibration-based analysis are the maximum absolute differences in normalised strain mode shapes between the intact and the damaged beams, **Fig. 8.14** is obtained from **Figs. 8.12** and **8.13** and used as an input to ANN for severity and location predictions. The maximum values are also shown in **Fig. 8.14**.

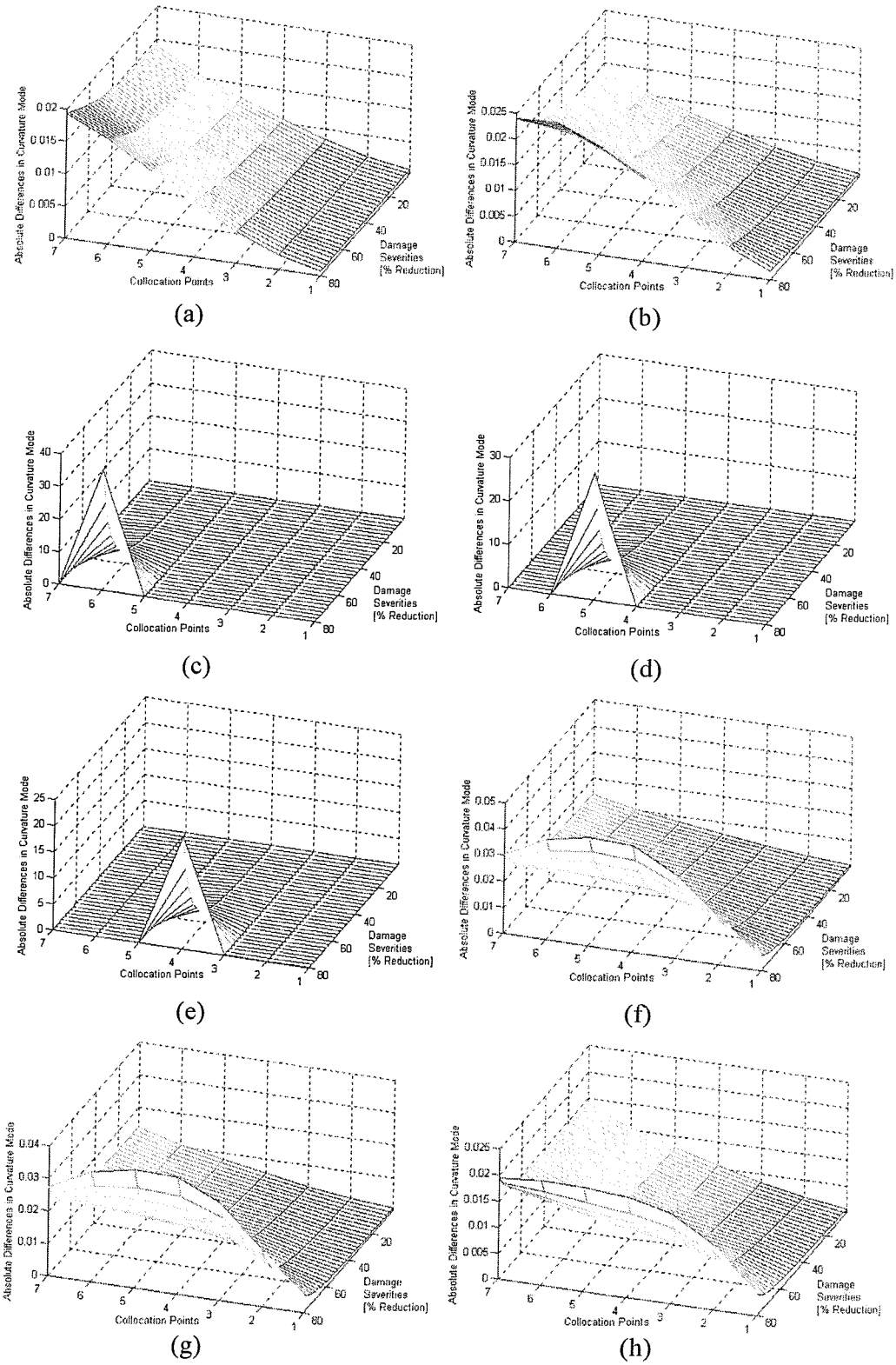

Figure 8.3 Variation of the magnitude of the absolute differences in curvature along the beam with different severities in Mode 1:Damage at (a) $0.24L$ (b) $0.3L$ (c) $0.34L$ (d) $0.44L$ (e) $0.54L$ (f) $0.6L$ (g) $0.64L$ (h) $0.74L$

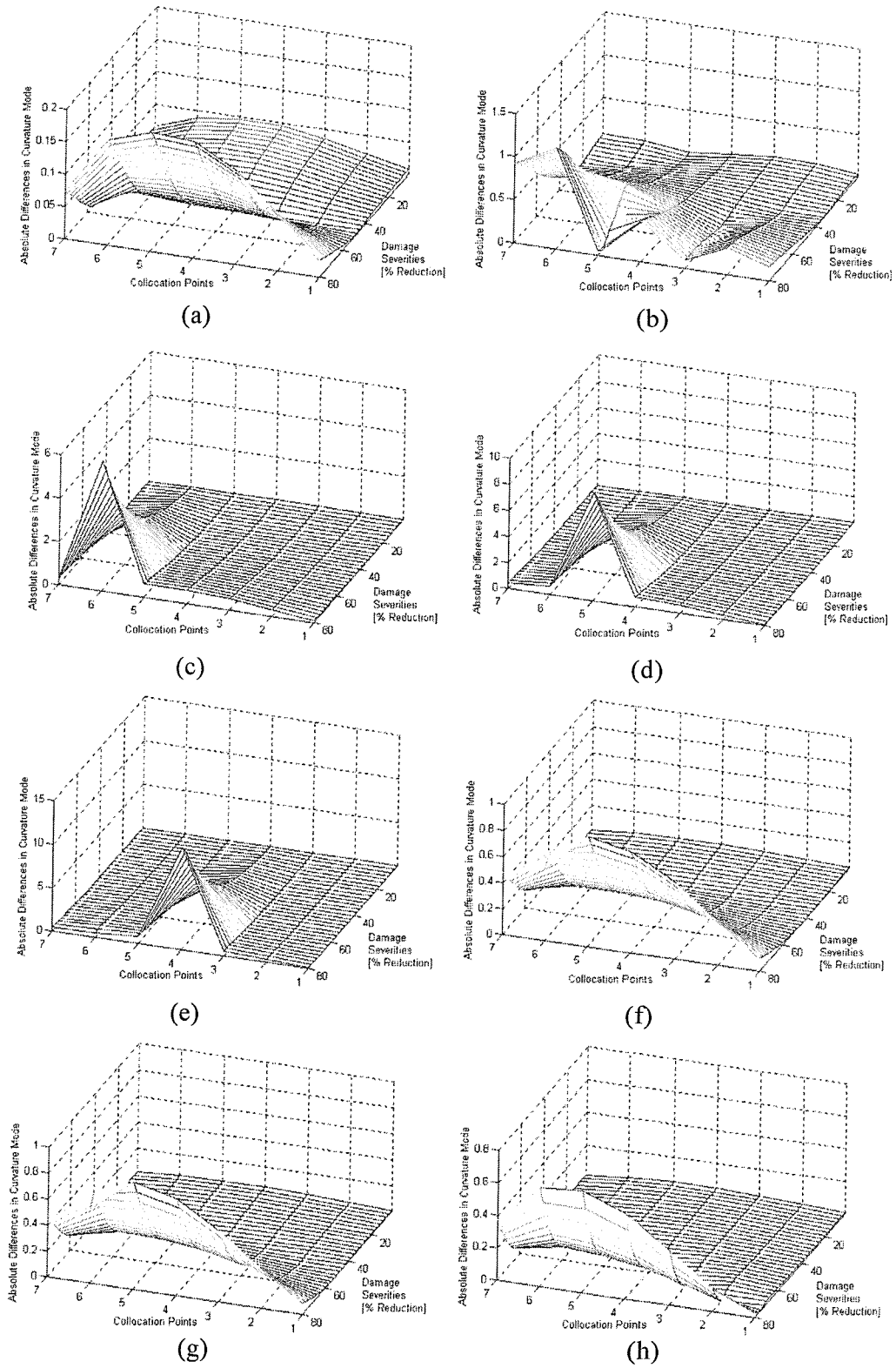

Figure 8.4 Variation of the magnitude of the absolute differences in curvature along the beam with different severities in Mode 2:Damage at (a) $0.24L$ (b) $0.3L$ (c) $0.34L$ (d) $0.44L$ (e) $0.54L$ (f) $0.6L$ (g) $0.64L$ (h) $0.74L$

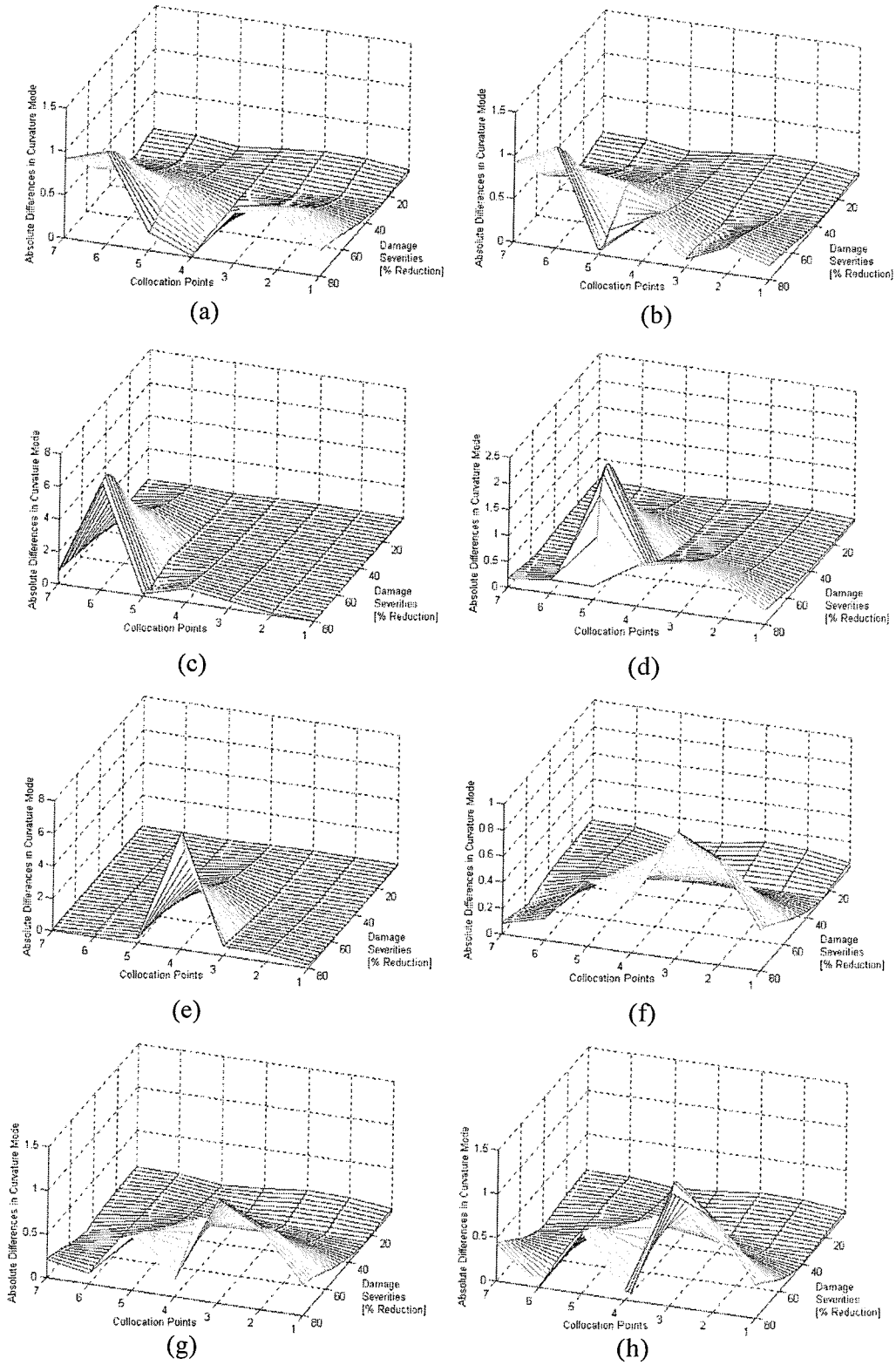

Figure 8.5 Variation of the magnitude of the absolute differences in curvature along the beam with different severities in Mode 3:Damage at (a) 0.24L (b) 0.3L (c) 0.34L (d) 0.44L (e) 0.54L (f) 0.6L (g) 0.64L (h) 0.74L

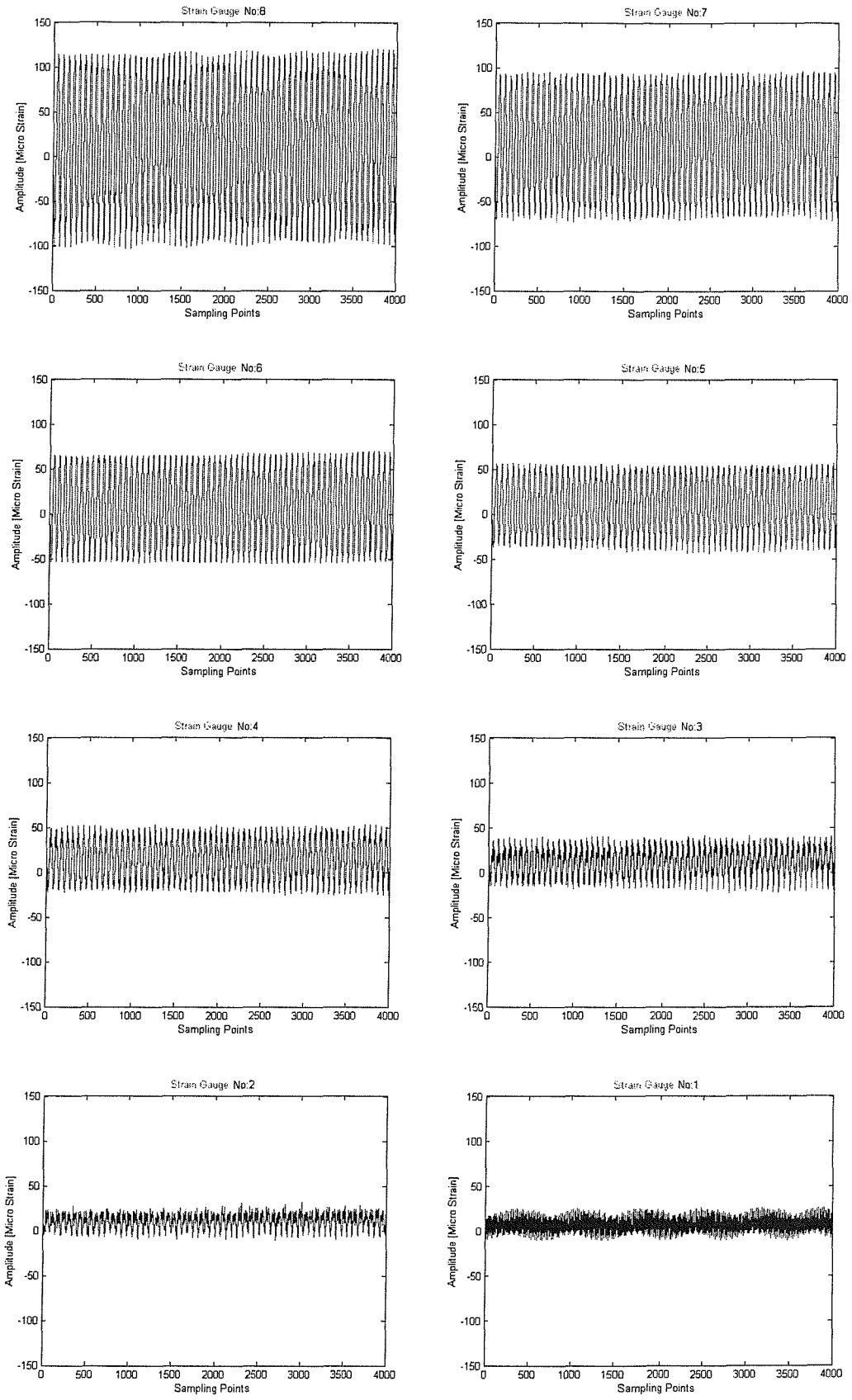

Figure 8.6 Strain output of eight strain gauges in the first mode (Intact Beam)

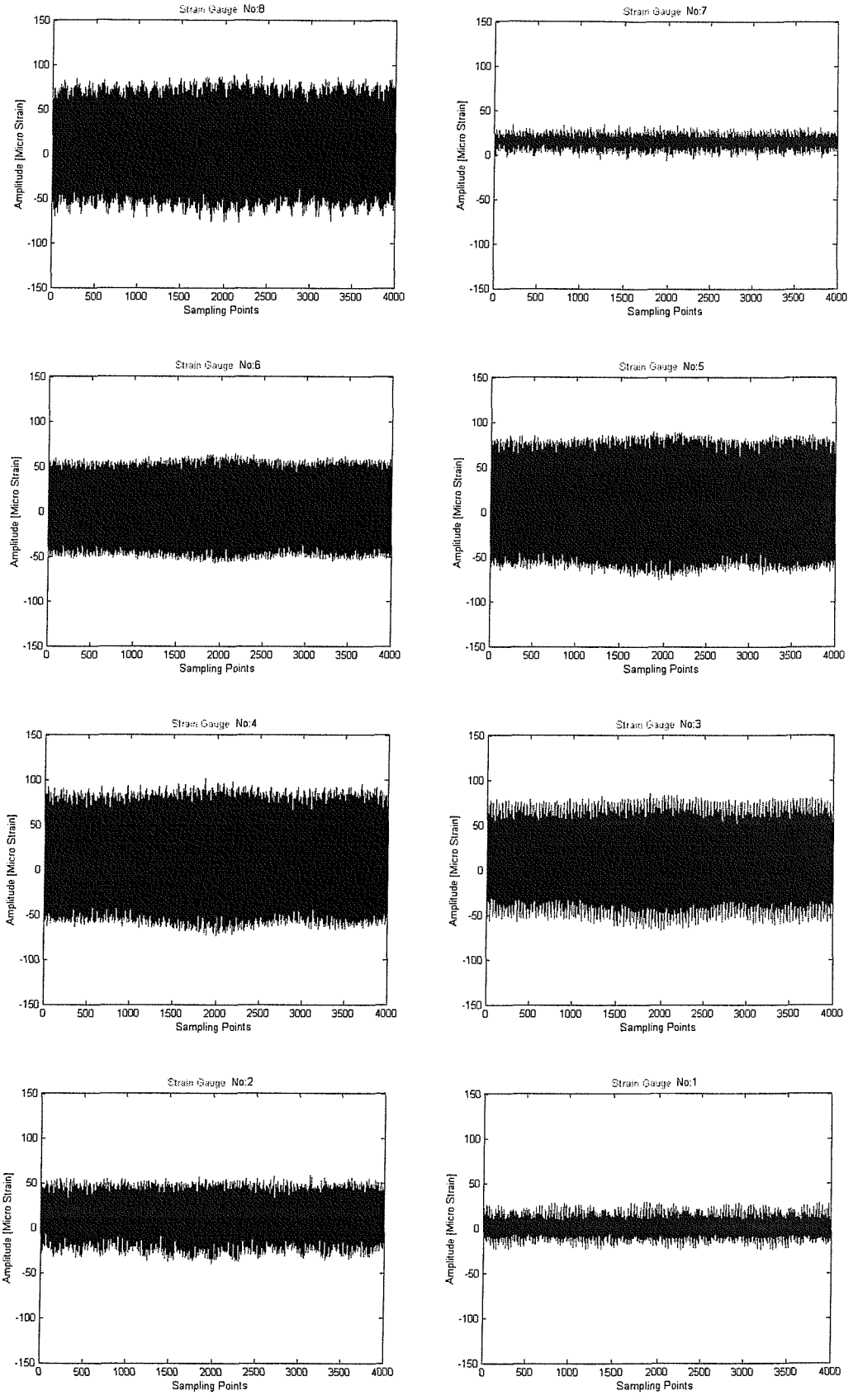

Figure 8.7 Strain output of eight strain gauges in the second mode (Intact Beam)

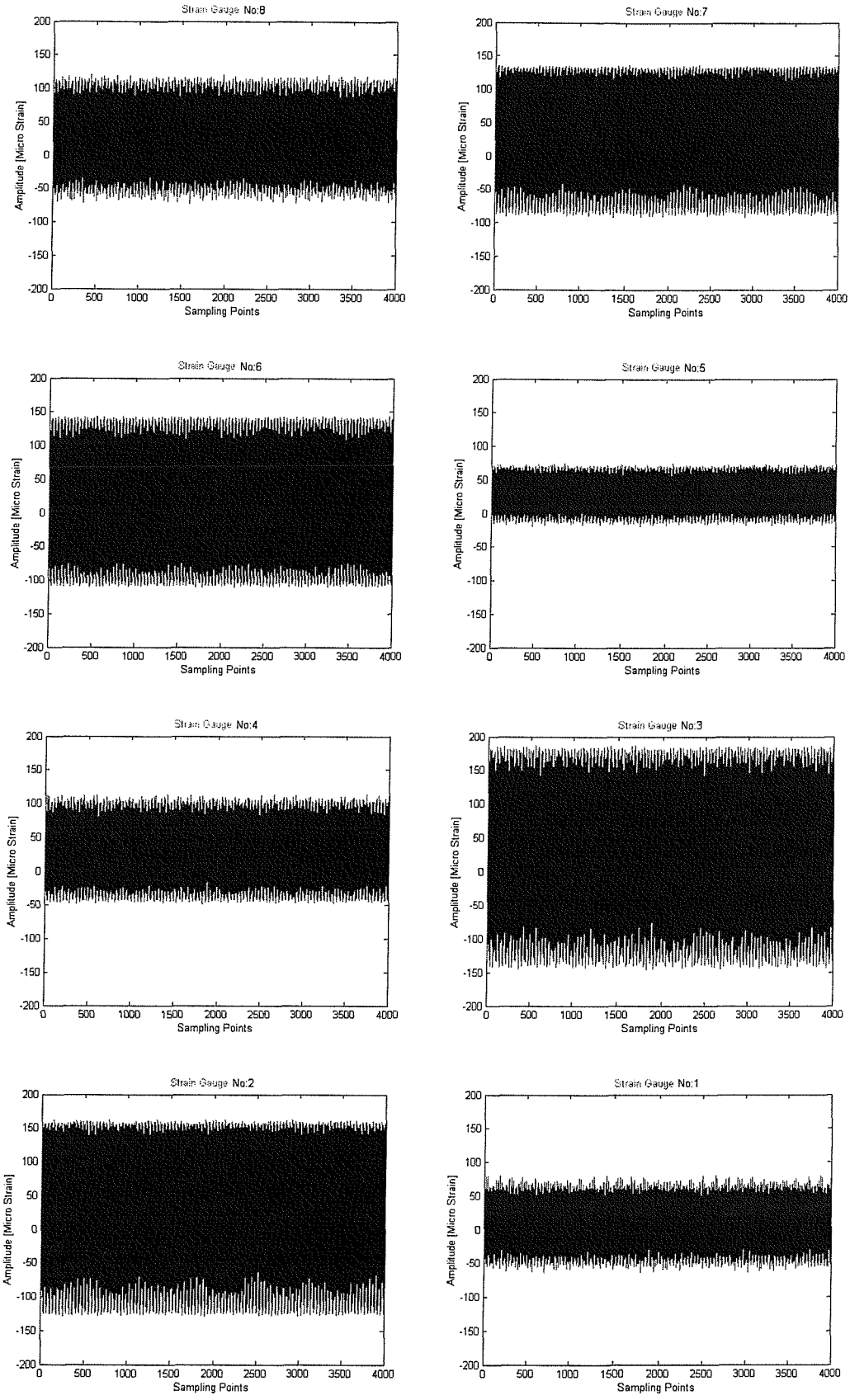

Figure 8.8 Strain output of eight strain gauges in the third mode (Intact Beam)

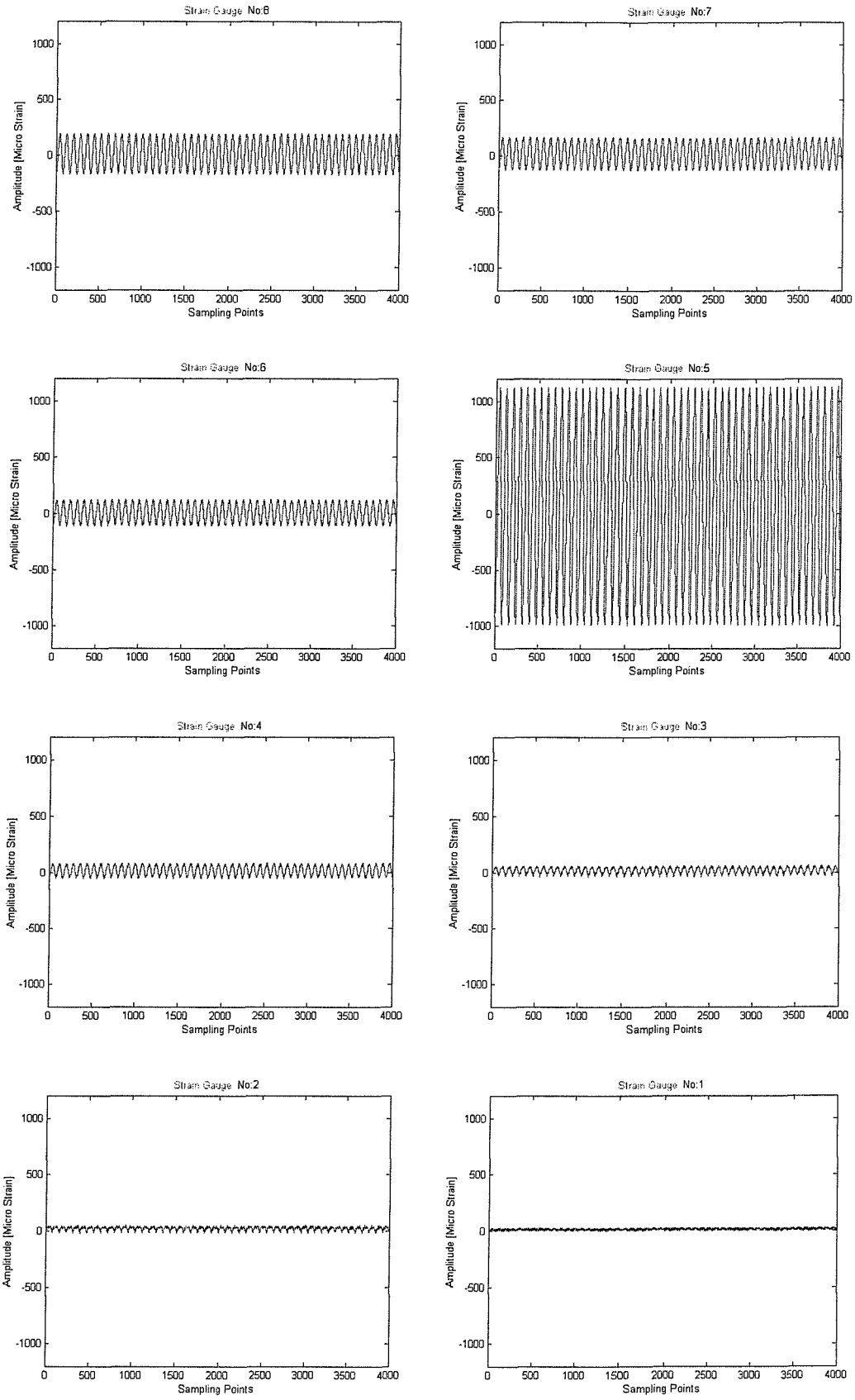

Figure 8.9 Strain output of eight strain gauges in the first mode (Damaged Beam)

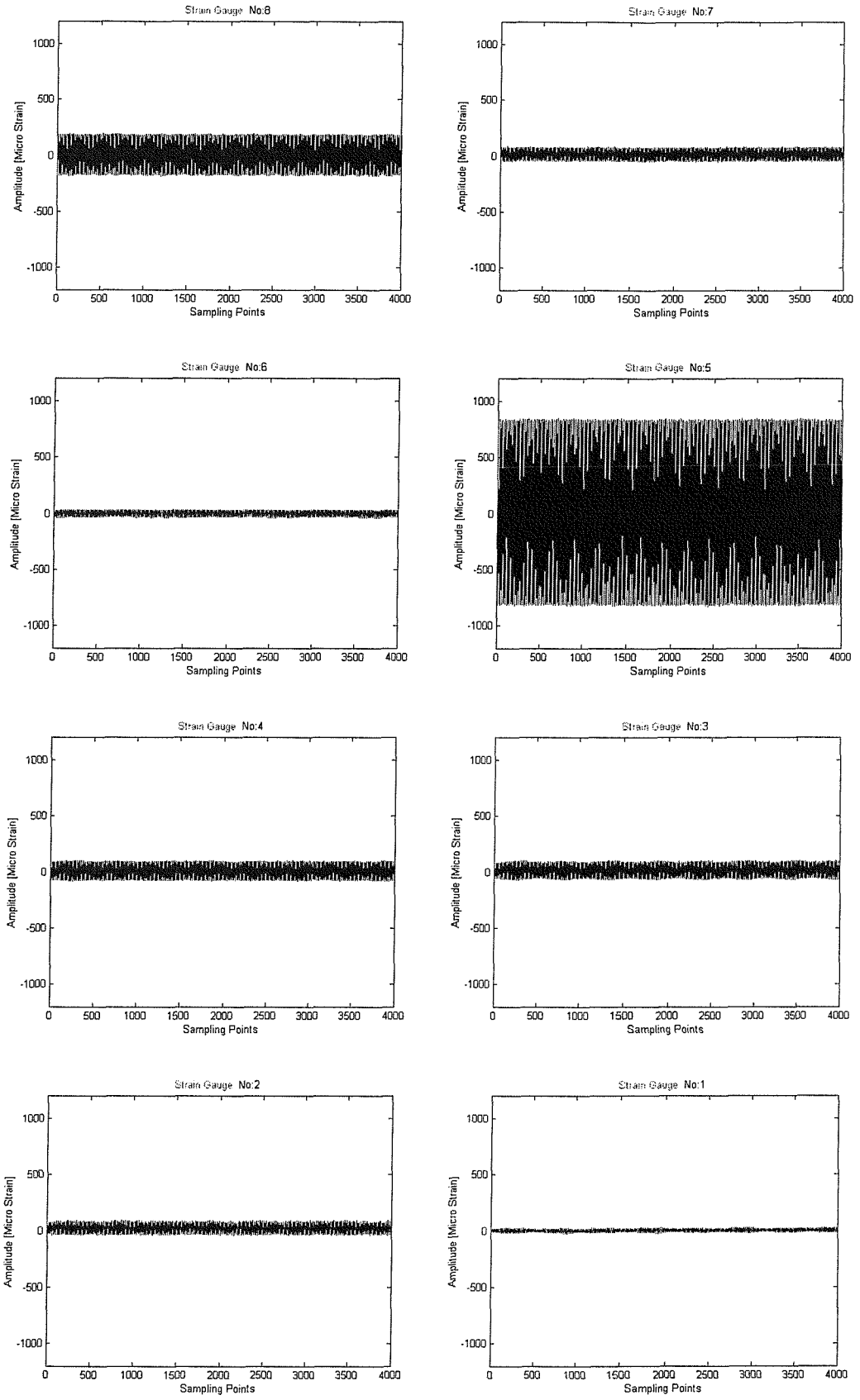

Figure 8.10 Strain output of eight strain gauges in the second mode (Damaged Beam)

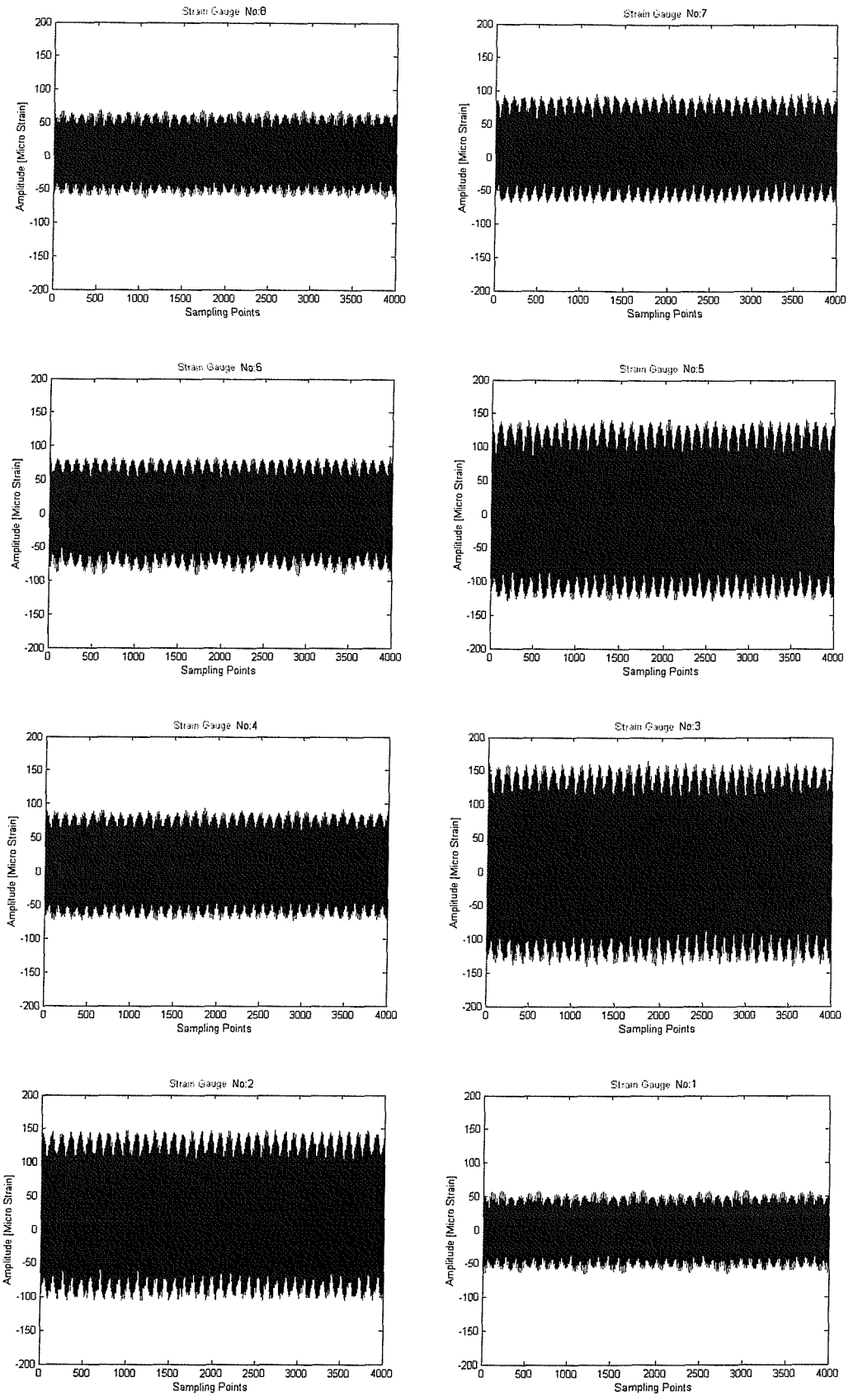

Figure 8.11 Strain output of eight strain gauges in the third mode (Damaged Beam)

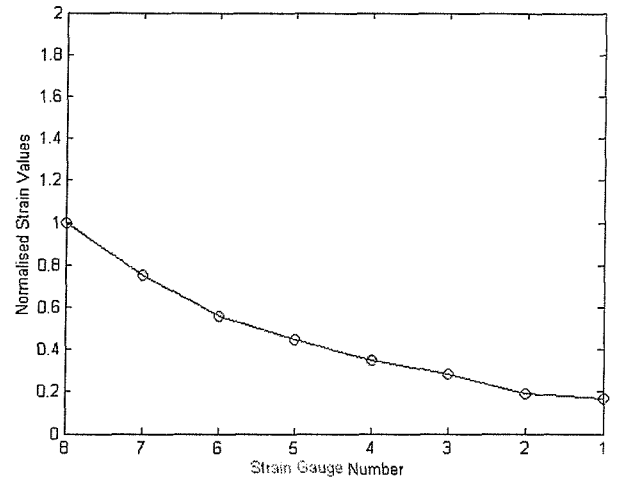

(a)

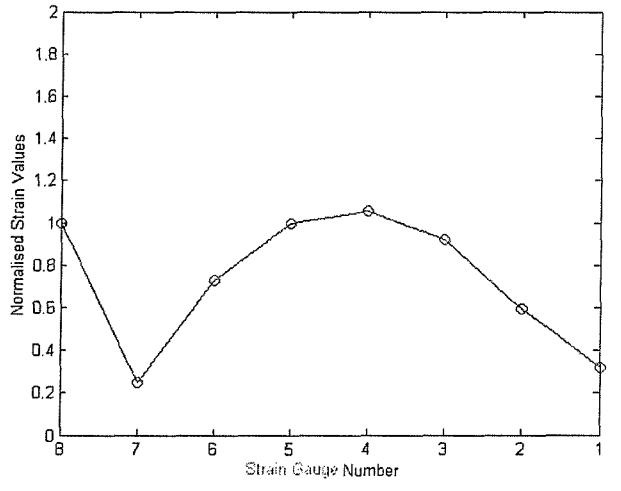

(b)

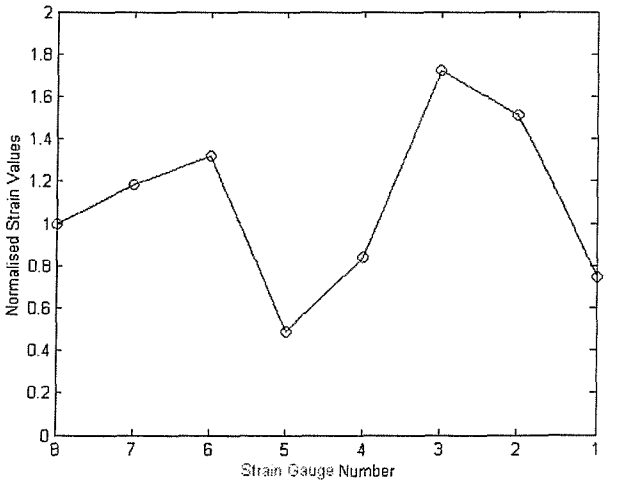

(c)

Figure 8.12 Normalised experimental strain mode shapes of intact beam

(a) Mode 1 (b) Mode 2 (c) Mode 3

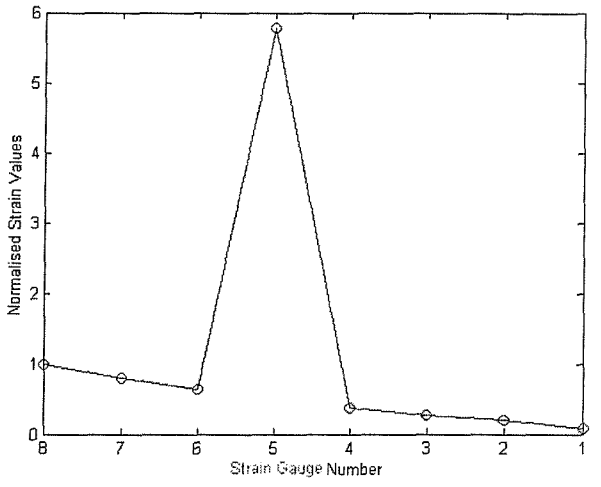

(a)

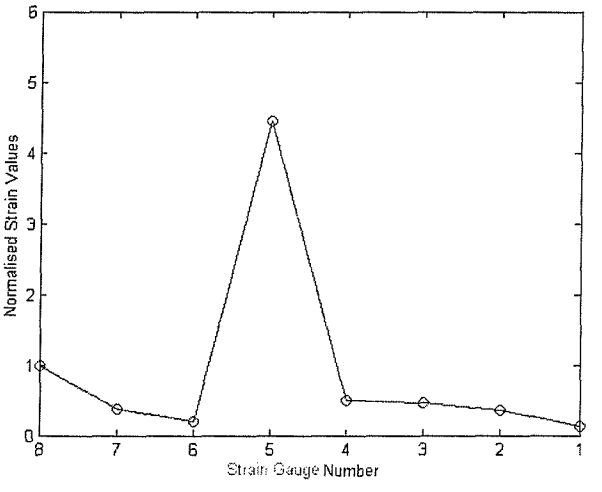

(b)

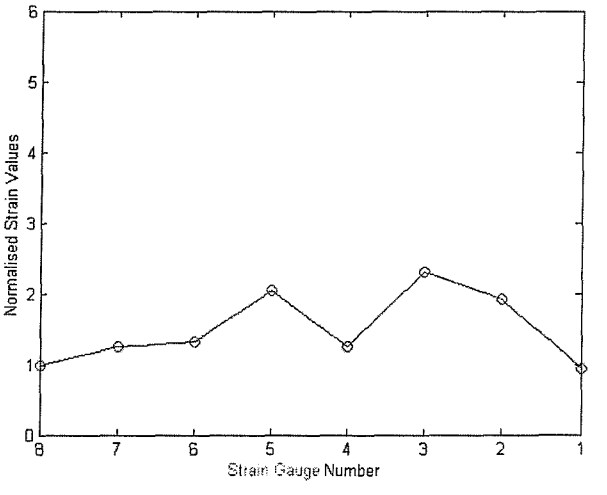

(c)

Figure 8.13 Normalised experimental strain mode shapes of damaged beam

(a) Mode 1 (b) Mode 2 (c) Mode 3

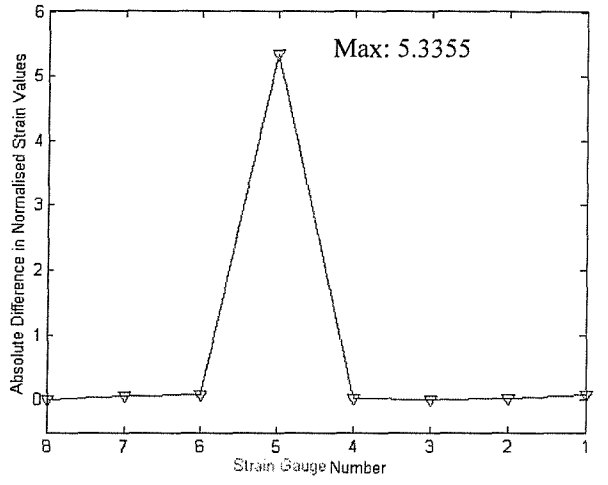

(a)

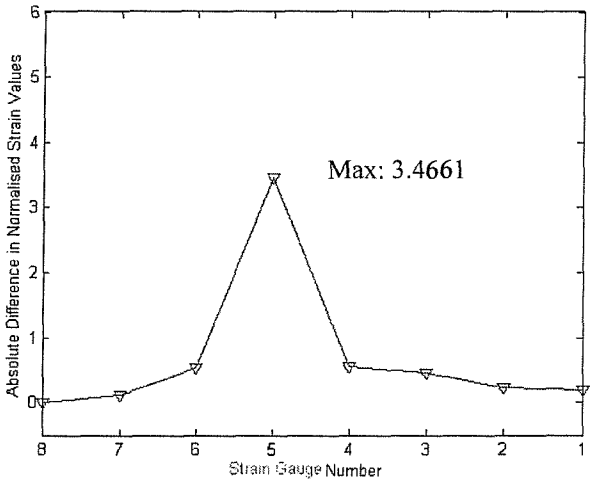

(b)

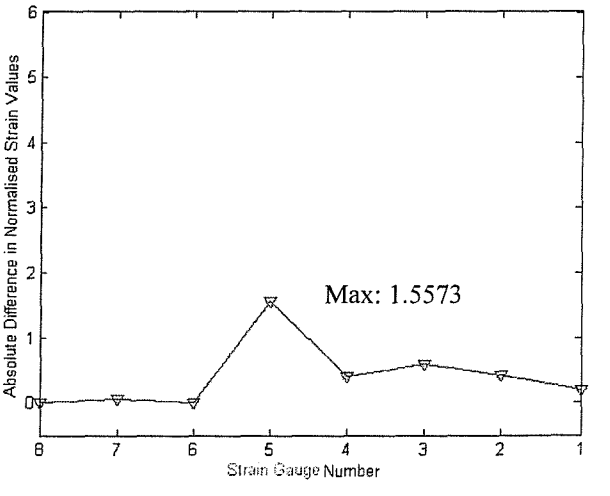

(c)

Figure 8.14 Absolute differences in experimental strain mode shapes between the intact and damaged beams (a) Mode 1 (b) Mode 2 (c) Mode 3

8.5 Application of ANNs

8.5.1 Design, Training and Validation of ANNs

The ANNs used for the verification are selected from **Table 7.2** and tabulated in **Table 8.4** showing different combinations of input and output pairs. In this analysis, 480 different damage scenarios are generated by using 32 different reductions in thickness of the selected elements at 15 different locations throughout the beam. 450 input-output pairs are given to the ANN for training and the rest of the input-output pairs are used to check the generalisation of the learning during the validation process in noise-free case. An artificial random noise has been added (Eq. 7.4) to noise-free data (normalised frequency and maximum differences in curvature mode shape data) in order to simulate the experimental uncertainties numerically. In data with noise case, 50 copies of normalised natural frequencies (when RNF is an input) and 25 copies of normalised natural frequencies, maximum absolute differences in curvature mode shapes and the location corresponding to maximum absolute difference in curvature mode shape (when MADC&LOC and RNF&MADC&LOC are as inputs) are obtained and artificial noise has been added on each copy with different histories. **Table 7.3** shows different percentages of noise combinations added to normalised frequency and maximum absolute differences in curvature mode shape data. Since totally 480 different damage scenarios are used in the analyses, in case of RNF, 22500 and 1500 entries are introduced for training and validation respectively. Similarly, 11250 and 750 entries are used for training and validation of both MADC&LOC and RNF&MADC&LOC.

Table 8.4 ANNs used in the verification analyses

	Input	Output	Architecture
1.	RNF	DS	3:6:1
2.	MADC	DL	3:6:1
3.	MADC&LOC	DL	6:9:1
4.	MADC&LOC	DS&DL	6:12:2
5.	RNF&MADC&LOC	DS&DL	9:18:2

8.5.2 Predictions of ANNs

In this section, the severity and location predictions for noise-free case (**Figs. 8.15-8.19**) are shown in detail by considering the training, validation sets and the variation in mean square error with increasing number of epochs. In the prediction related graphs, the circle denotes the prediction for the case when the experimental damage is the input and dotted lines lying on both sides of the centre line indicate a 5% deviation from the target value.

The training performance of the first ANN (RNF-DS) can be seen in **Fig. 8.15a** considering the trend in mean square error values during training. **Figure 8.15b** shows the prediction of this ANN regarding the severity of the damage.

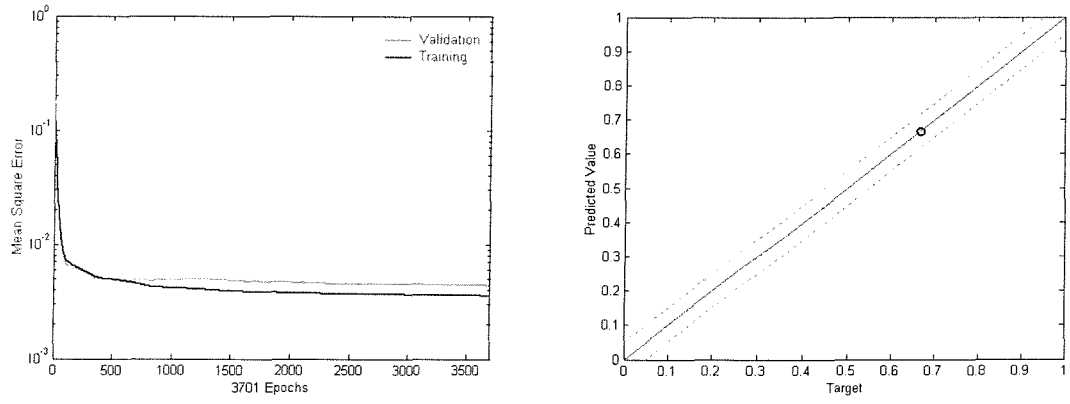

(a) (b)

Figure 8.15 ANN results for severity prediction (Input: RNF, Output: DS)
(a) Mean square error with number of epochs (b) Severity prediction

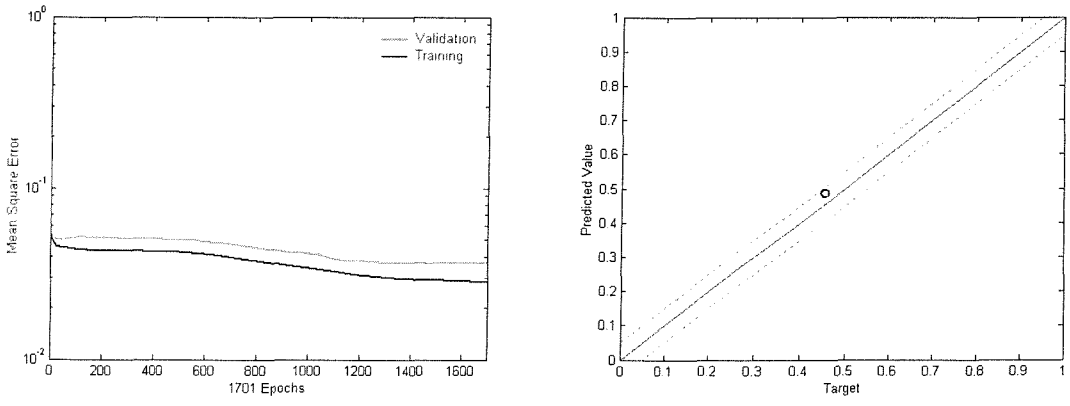

(a) (b)

Figure 8.16 ANN results for location prediction (Input: MADC, Output: DL)
(a) Mean square error with number of epochs (b) Location prediction

In the second and third ANNs, the location of the damage is predicted by using two different input data, which are MADC (**Fig. 8.16**) and MADC&LOC (**Fig. 8.17**) respectively. It can be seen from **Figs. 8.16** and **8.17** that better generalisation (**Fig. 8.17a**) and prediction (**Fig. 8.17b**) are achieved by providing the location information.

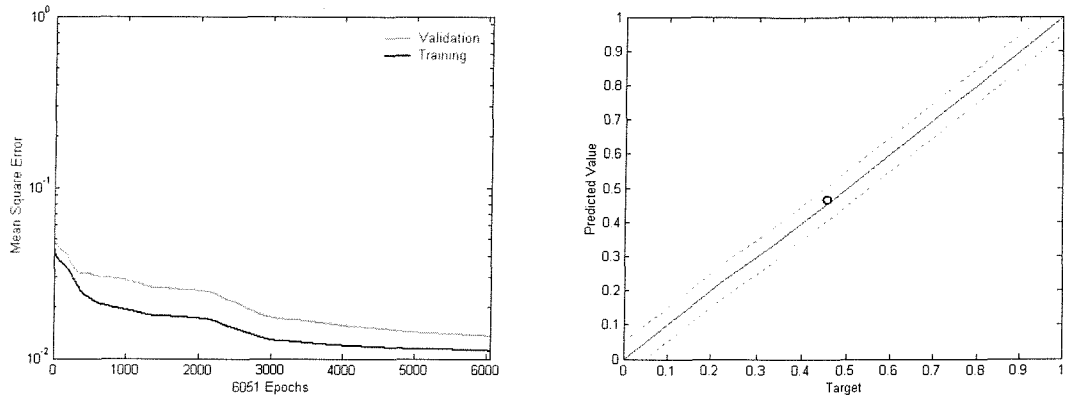

(a) (b)

Figure 8.17 ANN results for location prediction (Input: MADC&LOC, Output: DL)
(a) Mean square error with number of epochs (b) Location prediction

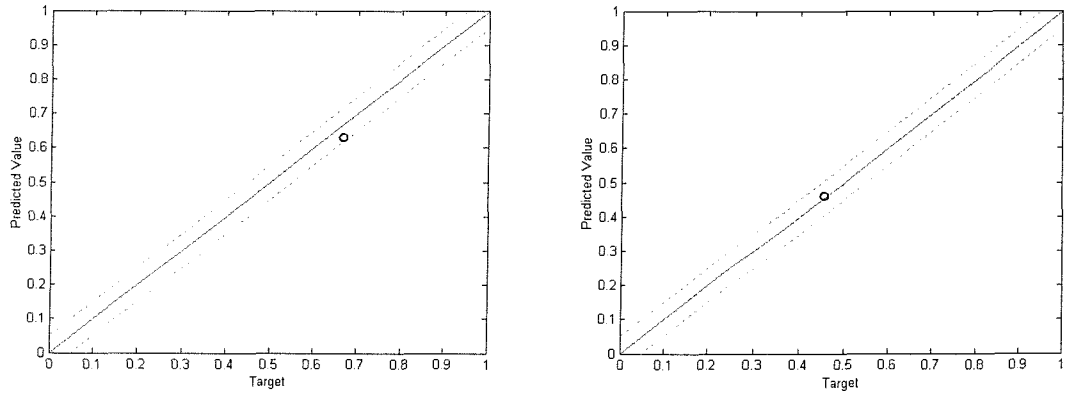

(a) (b)

Figure 8.18 ANN results for severity and location prediction (Input: MADC&LOC)
(a) Severity prediction (Output: DS) (b) Location prediction (Output: DL)

Since the input features, the maximum absolute differences in strain mode shapes between the intact and the damaged beams and their locations, are good indicators for location prediction of the damage, next test run is performed by using these features as an input for both severity (**Fig. 8.18a**) and location (**Fig. 8.18b**) predictions. In the final test run, the severity (**Fig.**

19a) and location (**Fig. 19b**) of the damage are predicted by introducing inputs namely, reduction in natural frequencies, maximum absolute differences in curvature mode shape between the intact and the damaged beams and their corresponding locations along the beams from the first three natural modes.

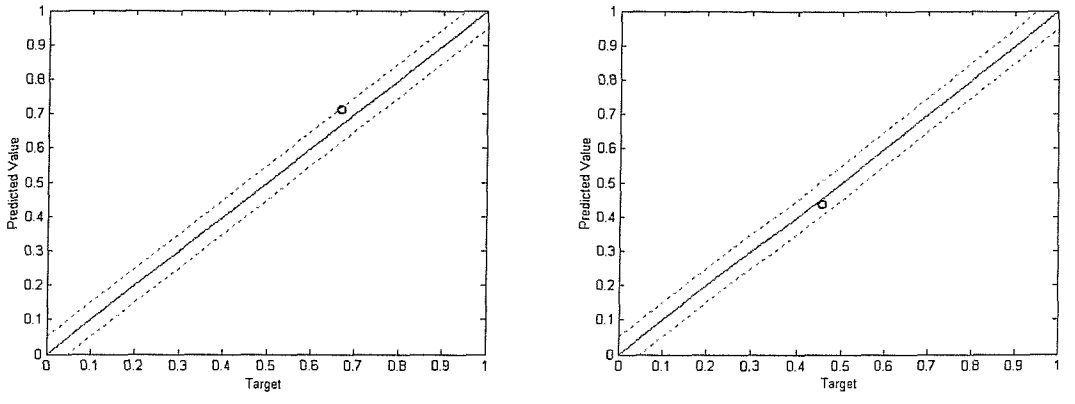

(a) (b)

Figure 8.19 ANN results for severity and location prediction (Input: RNF&MADC&LOC)
(a) Severity prediction (Output: DS) (b) Location prediction (Output: DL)

The results for noise-free (**Table 8.5**) and for additional artificial noise (**Table 8.6**) cases are tabulated for performance comparison. It can be concluded from **Table 8.6** that more accurate results are obtained in location predictions (MADC&LOC-DL) for the damage than severity predictions (RNF-DS), although the noise levels are comparably higher than the ones used on RNF data. When the gradually increased noise combinations applied to the normalised frequency and maximum absolute differences in curvature mode shape are used in the prediction of both severity and location of the damage, better estimations (i.e. deviation within 3%) are achieved in location predictions compared to severity at each levels of artificial noise.

Table 8.5 Predictions of ANNs (Noise-free case)

Input	Output	Target		Prediction		% Deviation*	
RNF	DS	0.6667		0.6653		0.14	
MADC	DL	0.4556		0.4866		-3.10	
MADC&LOC	DL	0.4556		0.4656		-1.00	
MADC&LOC	DS&DL	0.6667	0.4556	0.6291	0.4610	3.76	-0.54
RNF&MADC&LOC	DS&DL	0.6667	0.4556	0.7123	0.4375	-4.56	1.81

*Deviation = [Target – Prediction]

Table 8.6 Predictions of ANNs (Additional artificial noise case)

Input (Noise %)	Output	Target		Prediction		% Deviation*	
RNF (0.5%)	DS	0.6667		0.6541		1.26	
RNF (1%)	DS	0.6667		0.6908		-2.41	
RNF (2%)	DS	0.6667		0.7157		-4.90	
MADC&LOC (1%)	DL	0.4556		0.4613		-0.57	
MADC&LOC (3%)	DL	0.4556		0.4471		0.85	
MADC&LOC (5%)	DL	0.4556		0.4142		4.14	
RNF&MADC&LOC (0.5% & 1%)	DS&DL	0.6667	0.4556	0.7162	0.4319	-4.95	2.37
RNF&MADC&LOC (1% & 3%)	DS&DL	0.6667	0.4556	0.7836	0.4712	-11.69	-1.56
RNF&MADC&LOC (2% & 5%)	DS&DL	0.6667	0.4556	0.8057	0.4507	-13.90	0.49

*Deviation = [Target – Prediction]

8.6 Conclusions

An experimentally validated damage detection algorithm using features extracted from vibration-based analysis data as input to ANNs for location and severity prediction of damage in a steel beam structure was presented. Different damage scenarios have been created by reducing the local thickness of the selected elements at different locations and simulated vibration responses have been introduced to ANNs with and without artificial noise during the training. The sensitivity analysis has also been performed on extracted features by using different vibration modes considering the effect of damage location and severity before introducing them to ANNs. In this study, the test data (i.e. resonant frequencies and strain mode shapes) has been obtained from the intact and damaged steel beam with a local damage of 2mm deep (66.67% reduction in thickness) and 10mm wide slot at 205mm ($0.4556L$) away from the fixed end by using an accelerometer mounted at the tip and eight surface-bonded distributed electrical strain gauges along the centre line. It can be concluded from the ANN predictions that the better accuracy has been achieved in severity predictions than the location ones in noise-free case. On the other hand, introducing an artificial noise on noise-free data has adversely affected the severity predictions although the results are still accurate for the location predictions obtained from each ANN used in the verification by using an experimental data.

Chapter Nine SANDWICH BEAM STRUCTURE

9.1 Introduction

Because of light-weight, high strength, easy fabrication, long term durability and excellent corrosion resistance, GFRP sandwich structures with foam core are widely used in marine and offshore structures. However, internal defects and damage (details in Chapter 4, section 4.3) may be difficult to observe by visual inspection, thus making prevention of serious damage difficult. This can dramatically affect the overall strength and stiffness of these structures and might lead a complete failure. One of the primary issues here is to show the feasibility of improvement in the reliability of composite sandwich structures by monitoring their internal strain conditions. Therefore, this chapter presents the fabrication of sandwich beam structures with embedded FBG strain sensors, vibration-based analysis performed on these structures and ANN predictions for quantification and localisation of the damage.

The static analysis (details in Appendix B) performed on a sandwich beam specimen shows that embedded FBG strain sensors provide accurate local strain information. On the other hand, the strain measurements performed under dynamic excitation with multiple gratings are limited due to the restrictions of the fibre optic Bragg grating interrogation system (FBGIS) (details in Appendix A).

The limitations of the interrogation system can be summarised as follows:

- When the system is used with single fibre Bragg grating, it allows measurements up to approximately 1 kHz sampling frequency. Since the sampling frequency should be at least two times higher than the highest frequency of interest (i.e. cut-off frequency), the interrogation system can be used with single fibre Bragg grating in order to obtain dynamic strain history up to 500Hz.

- The system supports multiple continuous strain measurements in real-time up to eight fibre Bragg gratings. The measurement range of the system is also dependent on the

number of Bragg gratings used. The higher number of Bragg gratings used in a single optical fibre, the lower the scanning rate of the interrogation system. Another factor that plays an important role in dynamic measurements is the number of sampling points used to track the reflective peak of a particular FBG strain sensor. In order to obtain better accuracy, the sampling points per peak should be increased. This has the effect of decreasing the scanning frequency. Working with lower scanning frequency limits the ability to identify the higher frequencies of interest and makes it difficult to identify the higher strain mode shapes from multiple FBG strain sensors as the system can provide strain measurements from 8 gratings up to 150Hz. The further details regarding scanning frequency of multiple Bragg gratings are given in Appendix A.

- Experimental observations show that the faster the scanning frequency, the more noise is introduced into the measured strain data from the interrogation system.

- Before performing any dynamic tests, the laser source needs to be left for a certain period of time to settle to constant operating temperature. A warm-up sequence also needs to be performed. These two factors are very important as they compensate the drift in strain measurement.

9.2 Material and Geometrical Properties of Sandwich Beam

9.2.1 Core Material

Linear polymer foam (Core-Cell® A500) **[9-1]** is used during the manufacturing of sandwich beam specimens. This type of foam core provides excellent stiffness and structural integrity under dynamic loading with low weight. Core-Cell is non-friable, tough and rigid core that has high impact strength and high shear elongation. This core material is also suitable for resin infusion with vacuum bagging technique. The foam core used in the analysis has following material properties (details in Appendix E):

$$E_{core} = 131.13 \times 10^6 \text{ Pa}, \quad \rho_{core} = 144.8 \text{ kg/m}^3, \quad \nu_{core} = 0.32 \text{ (assumed)}.$$

9.2.2 Skin Material

9.2.2.1 *Matrix*

The material properties of the resin system are not very high compared to most metals but when it is combined with reinforcing fibres such as glass, exceptional properties can be obtained. The epoxy system (Prime 20 epoxy infusion system **[9-2]**) provides excellent material properties from ambient temperature cures (i.e. lab environment) and moderate temperature postcures (50°C). Epoxy resins bond well to the Core-Cell foam with mechanical bond only as there is no chemical interaction. One of the most advantageous properties of the epoxy is its low shrinkage during cure that minimises internal stresses. Epoxy resins have also good water and chemical resistance providing high electrical insulation. During the manufacturing, standard hardener **[9-2]** with mix ratio of 100:25 by weight is used. The densities of the resin (before and after cure) and the density of the hardener are as follows:

$$\rho_{\text{resin-before cure}} = 1.127 \text{ g/cm}^3, \quad \rho_{\text{resin-after cure}} = 1.148 \text{ g/cm}^3,$$

$$\rho_{\text{hardener}} = 0.983 \text{ g/cm}^3.$$

9.2.2.2 *Fibre Reinforcement*

The reinforcing fibre (UT-E500 **[9-2]**) used during the sandwich structure construction is the unidirectional (UD) glass fibre. Since orthotropic material properties are needed for FEA of laminated composites, some of the material properties are approximated from the values widely used in the literature. The following combined material properties (i.e. fibre and resin) of the glass-fibre are used during the analysis.

$$E_1 = 33.18 \times 10^9 \text{ Pa}, \quad E_2 = E_3 = 5.69 \times 10^9 \text{ Pa},$$

$$G_{12} = G_{13} = 2.91 \times 10^9 \text{ Pa}, \quad G_{23} = 1.17 \times 10^9 \text{ Pa (assumed)}$$

$$\nu_{12} = \nu_{13} = \nu_{23} = 0.267, \quad \rho_{\text{skin}} = 2031.26 \text{ kg/m}^3 \quad \text{(details in Appendix E).}$$

9.2.3 Geometrical Properties

The sandwich beam structure (450mm x 40.5mm x 14.6mm) used during the analysis has four equal layers of UD glass fibre with layer orientation of $[0°/90°]_s$ and total thickness of 1.3mm on each side of 12mm thick linear polymer foam core. **Figure 9.1** shows the schematic view of the layer orientation of GFRP sandwich structure.

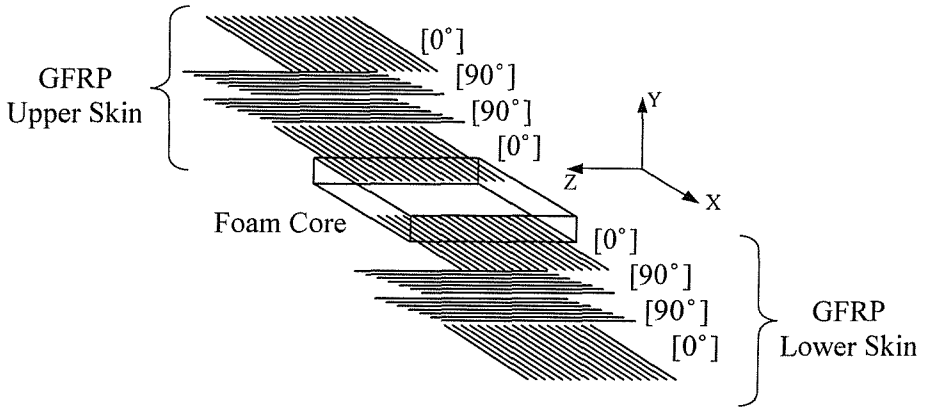

Figure 9.1 Schematic view of the layer orientation of GFRP sandwich structure

9.3 Experimental Analysis

9.3.1 Fabrication of the Sandwich Beam Specimens with Embedded FOSs

In this section, the procedure for the integration of sensor network (i.e. optical fibre with various number of FBG strain sensors) into GFRP sandwich composite structure is described in detail considering bonding, location (Appendix F) and alignment issues of the sensors. FOSs are embedded between the core and laminated skin during manufacturing. The main aim of embedding FOSs at this particular location is owed to the fact that there is a high tendency of separation (i.e. debonding) between the GFRP laminated skin and foam core in sandwich structures under transverse vibration. Considering the layer orientation of the GFRP laminated skin ($[0/90]_s$), which is made up of four equal layers of UD glass fibre material, the optical fibres are positioned on the upper surface of the core and parallel to 0° glass fibre on the skin. This configuration minimises the size of the local resin-rich region **[9-3, 9-4]**, which typically surrounds the embedded optical fibres and degrades the strength of the structure. As resin infusion technique by vacuum bagging is used during the manufacturing of sandwich specimens, it is an important issue to keep the fibre in its original position when the resin

infuses into the vacuum bag. During infusion, the whole material is in liquid resin that might easily dislocate the position of the optical fibre. Therefore, in order to keep the optical fibre in its original aligned position and not to create any impurities within the structure, an epoxy resin is used to pre-bond the optical fibre sensor to the core at particular selected points shown in **Fig. 9.2**. Since the FOS is thin and transparent, the path of the FOS is indicated in **Fig. 9.2**.

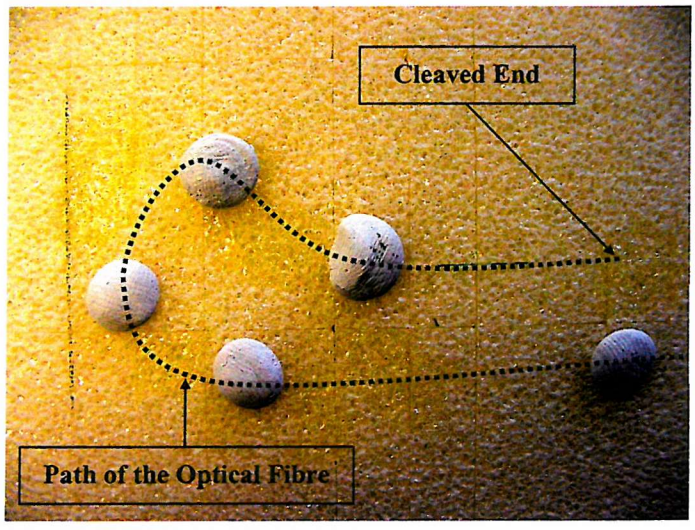

Figure 9.2 Pre-bonded optical fibre

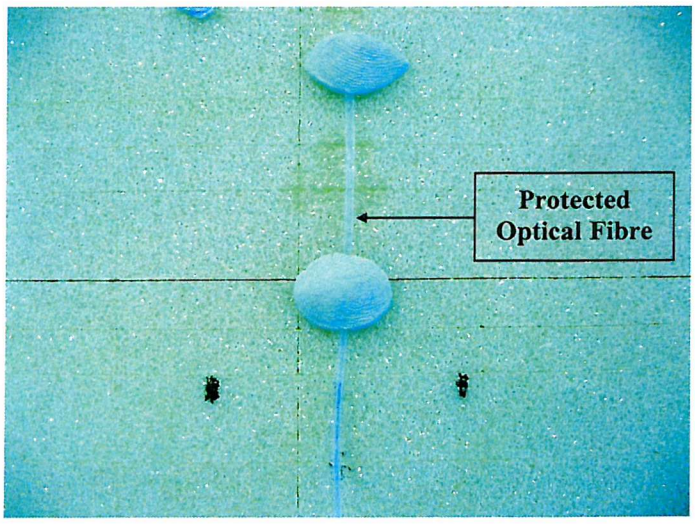

Figure 9.3 Thin plastic tube for the protection of FOS

After solving the alignment problem of the FOS, the second issue is to avoid potential back reflection from the cleaved end that pollutes the reflected Bragg wavelengths. Therefore, a curved-form (**Fig. 9.2**) is created near the cleaved end of the optical fibre to reduce the intensity of the back-reflected light significantly. The optical fibre embedded into the structure is very

delicate and fragile that extra covers (a thin plastic tube, **Fig. 9.3**) are used to take the sensor out through the thickness of the sandwich beam specimen and to give it a bit more flexibility. Since the main aim is to manufacture a GFRP skin sandwich beam specimen, pre-bonded FOS is covered with another four layers of UD glass fibre (**Fig. 9.4**). By using non-sticking film bags, the rest of the optical fibre at the exposed end, which is used to connect the sensors to the interrogation system, is also sealed and shown in **Fig. 9.5**.

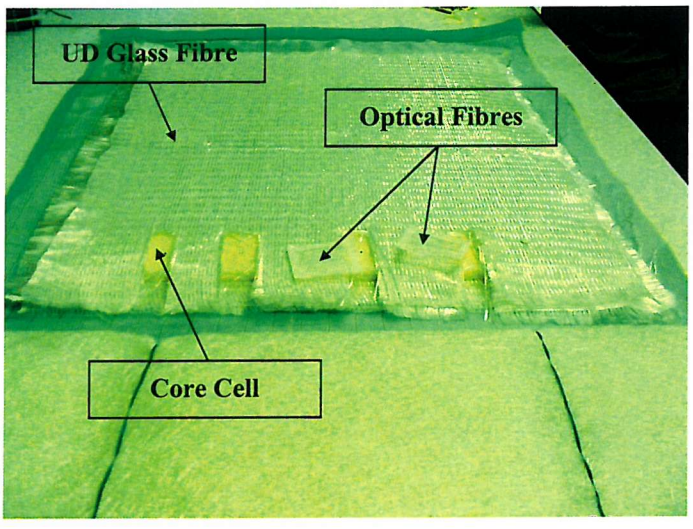

Figure 9.4 Embedded optical fibres coming out from material

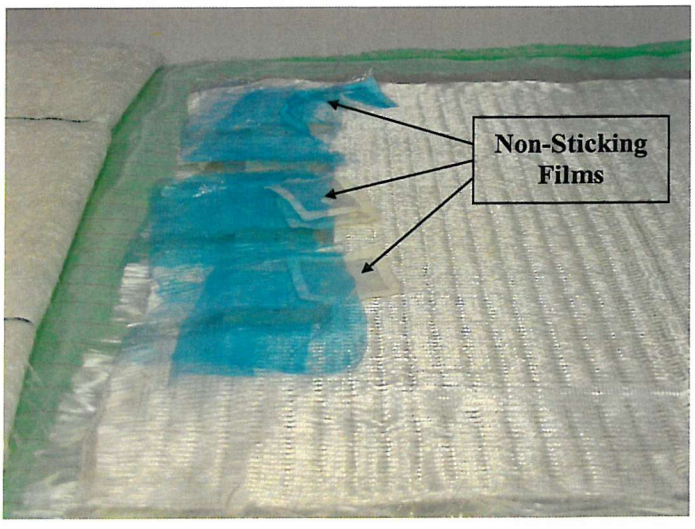

Figure 9.5 Optical fibres sealed in non-sticking film

After taking out the FOS from the layer between core and UD glass fibre, the whole panel (**Fig. 9.6**) is sealed by using sealant tape, covered with vacuum bagging film and then the resin is infused. After infusion, the panel is left for curing at room temperature for approximately 15

hours. Finally, the beam specimen is cut by using diamond-coated saw. One of the sandwich beam specimens manufactured by using the method explained above is shown in **Fig. 9.7**.

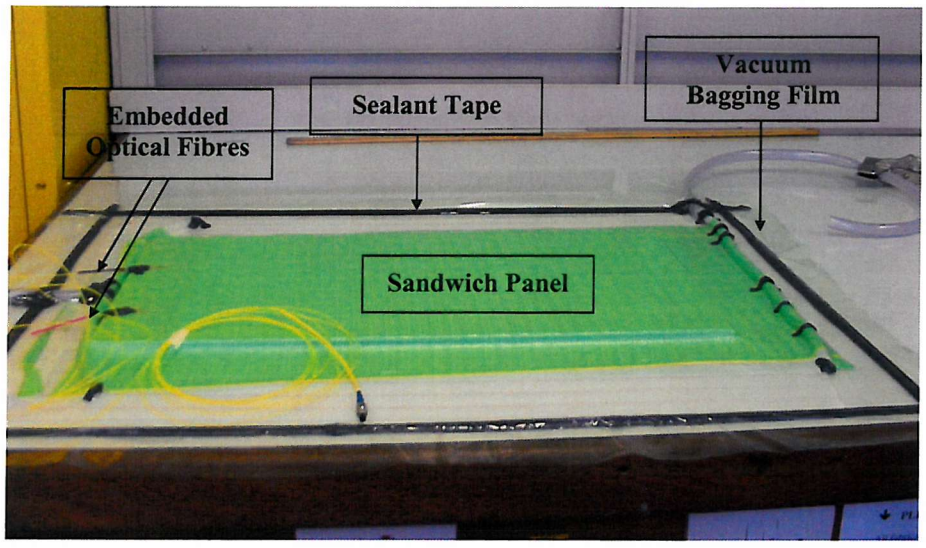

Figure 9.6 Sandwich panel under vacuum bag

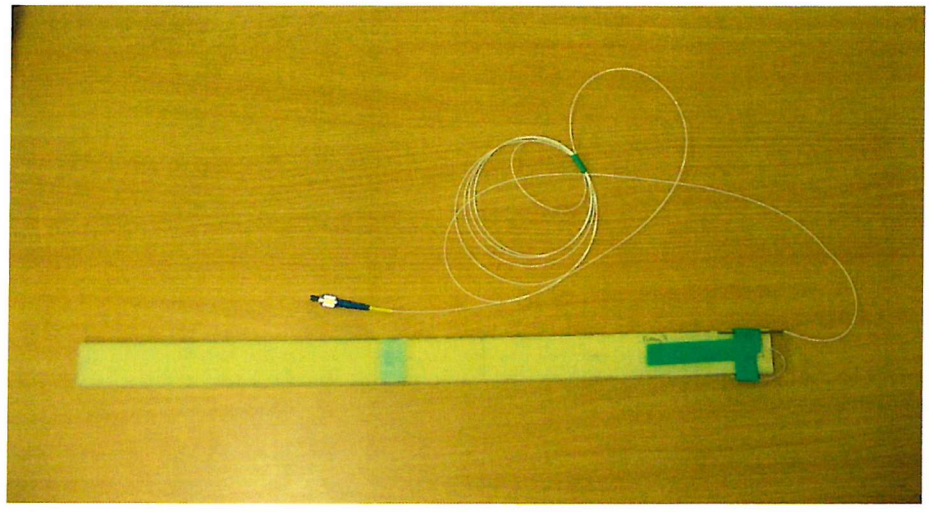

Figure 9.7 Sandwich beam specimen with embedded FOS

9.3.2 Curing Effect on FOS

The change in positions of the peaks (i.e. the reflectivity) of the wavelengths is monitored before and after the curing process in order to investigate the effects of curing on strain measurements. **Figures 9.8** and **9.9** show the curing effect on two different fibres having six Bragg gratings embedded into sandwich structure.

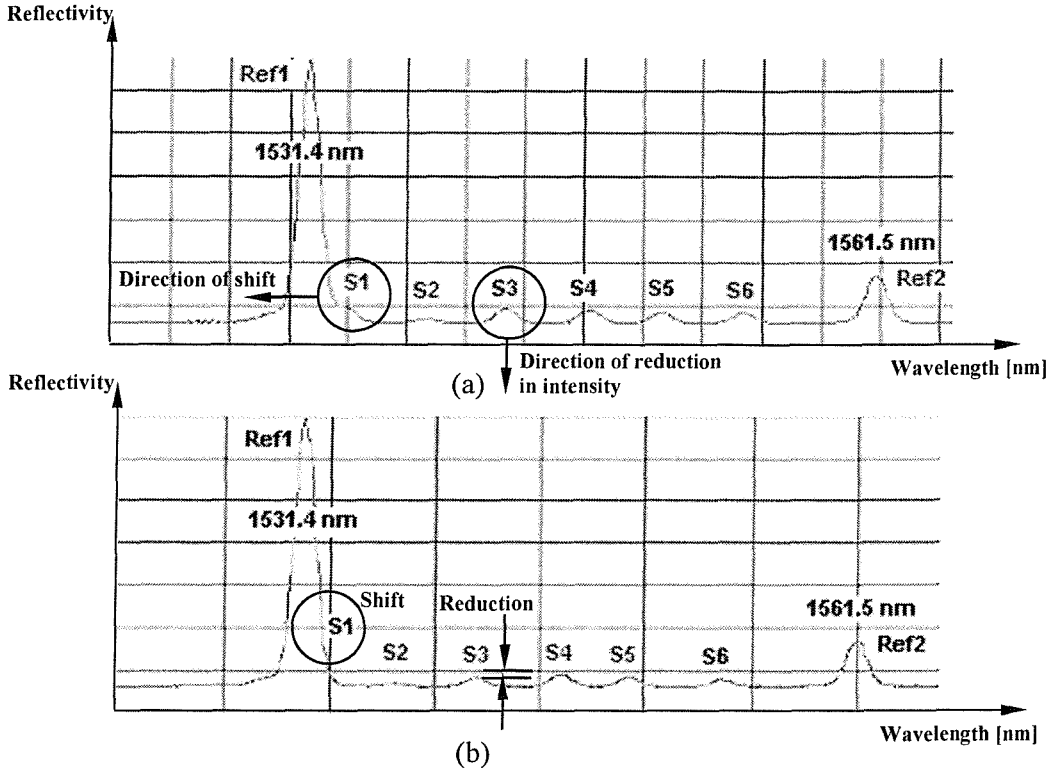

Figure 9.8 Curing effect on Fibre No:1 (a) before curing (b) after curing

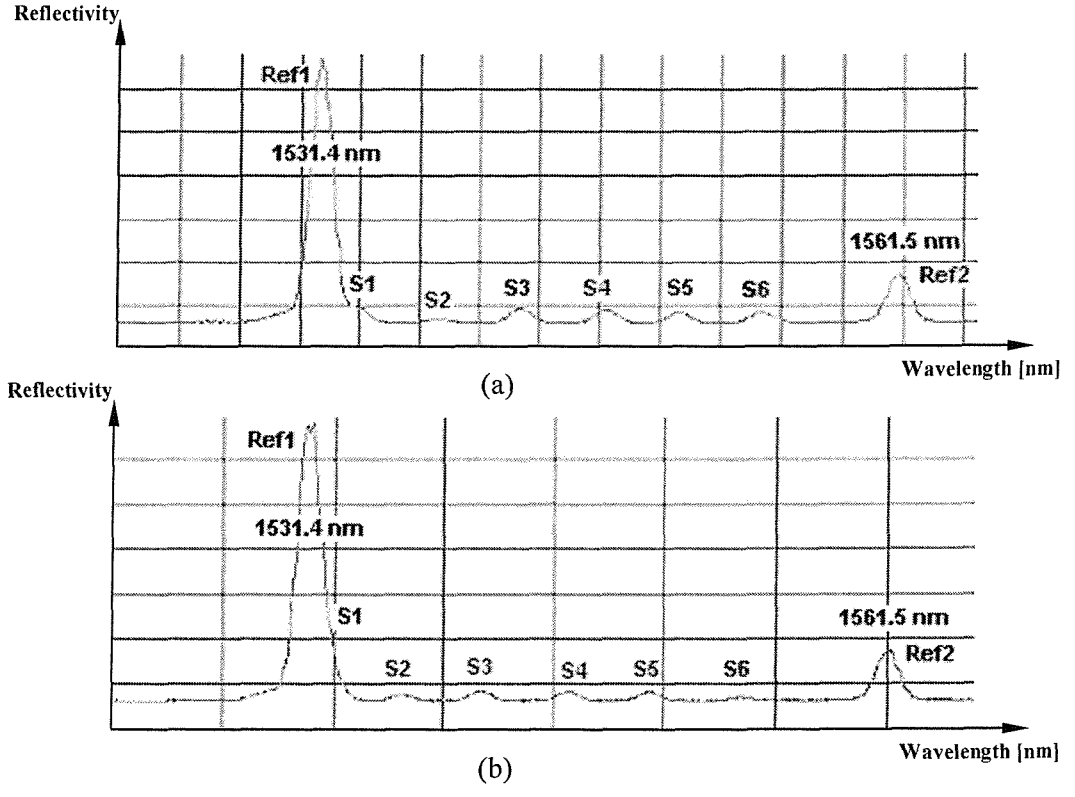

Figure 9.9 Curing effect on Fibre No:2 (a) before curing (b) after curing

It can be concluded from the **Figs. 9.8** and **9.9** that the effect of curing on sensors leads the peak of the Bragg wavelengths to shift to lower values and to decrease their intensities since the curing of the resin creates a residual stress over and around the optical fibre. As the Bragg wavelength of the first sensor (S1) has shifted a value that almost overlaps with one of the reference gratings (Ref1), the measurements from this particular sensor cannot be obtained. Thus, one of the important issues is to write the gratings in such a way that they are spaced in wavelength domain both from each other and from the reference gratings in order to avoid overlapping.

9.3.3 Introducing of Damage

During the manufacturing process, a Teflon tape is inserted between the foam core and the GFRP skin along the length of the sandwich beam. In order to create two different damage extents, the length of the Teflon tape is increased from 30mm to 40mm by keeping its width constant as 40.5mm that is equal to width of the specimen. By removing the upper surface of the skin and the Teflon tape, the final form of the damaged sandwich test specimen is obtained. **Table 9.1** shows the location and the extent of the damage introduced to sandwich beam specimens. The locations are measured from the fixed end to the centre of the damage.

Table 9.1 Extent and location of the damage

Damage Number	Extent [mm]	Location [mm]
1	30	70
2	30	300
3	40	170
4	40	200

9.3.4 Frequency Measurements

The first three resonant frequencies of the intact and four damaged beams are obtained under random excitation in the range of 10Hz to 710Hz. **Figures 9.10** to **9.12** show peak-to-peak response of the accelerometer attached to surface of the intact and selected damaged beams (i.e. beams with damage number 1 and 2 in **Table 9.1**). Intact, damaged and corresponding normalised resonant frequencies of these cantilever sandwich specimens are also tabulated in

Table 9.2. An extensive modal analysis performed on sandwich beam specimen is given in Appendix B.

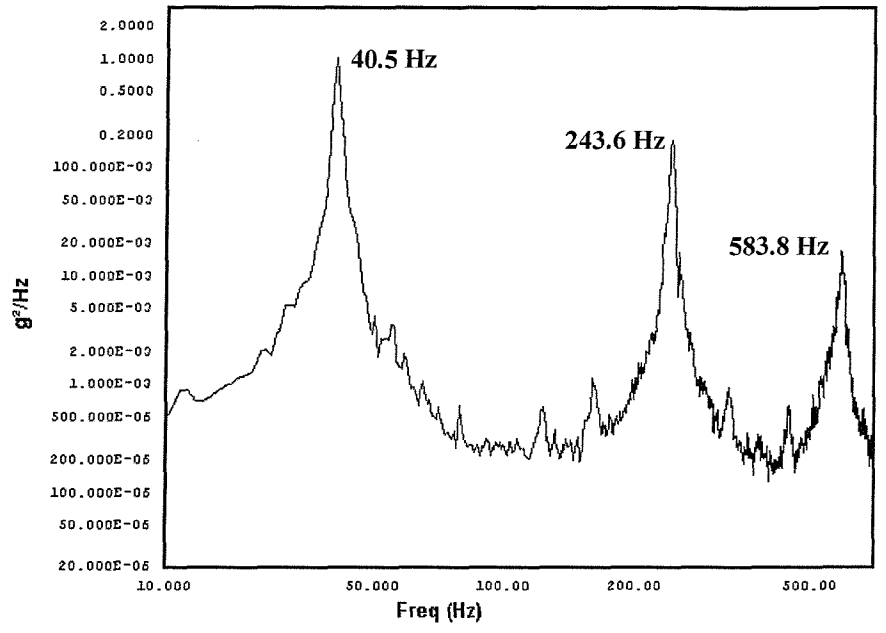

Figure 9.10 Frequency response of intact sandwich beam

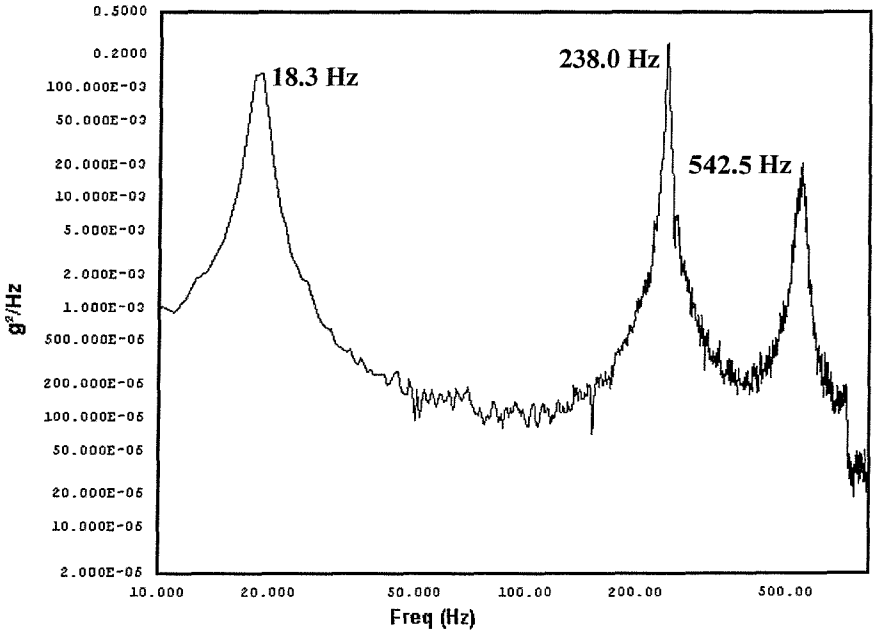

Figure 9.11 Frequency response of damaged sandwich beam
(Damage located at 70mm with an extent of 30mm)

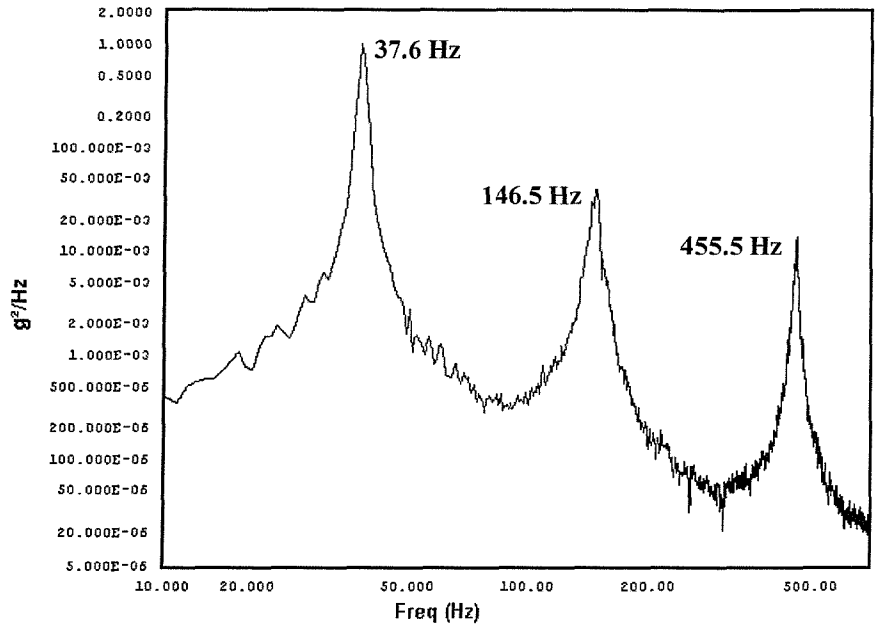

Figure 9.12 Frequency response of damaged sandwich beam
(Damage located at 300mm with an extent of 30mm)

Table 9.2 First three resonant frequencies [Hz] (Experimental)

Mode No	Intact Beam	Damaged Beam		$\frac{f_{damaged}}{f_{intact}}$	
		Damage at 70mm	Damage at 300mm	Damage at 70mm	Damage at 300mm
1st Bending	40.5	18.3	37.6	0.4518	0.9284
2nd Bending	243.6	238.0	146.5	0.9770	0.6014
3rd Bending	583.8	542.5	455.5	0.9293	0.7802

9.4 Finite Element Modelling and Analysis

Three dimensional higher order solid elements (SOLID95 for core and SOLID191for GFRP laminated skin) are selected to model the sandwich beam. In order to validate the model (i.e. combination of SOLID95 and SOLID191) with the results from **[G-1, G-2]**, FEA is performed with graphite/epoxy-aluminium sandwich plate (details in Appendix G). Having decided the element types, boundary condition effect on FEM of sandwich beam is also

investigated (details in Appendix H). The final form of the sandwich beam model can be seen in **Fig. 9.13**.

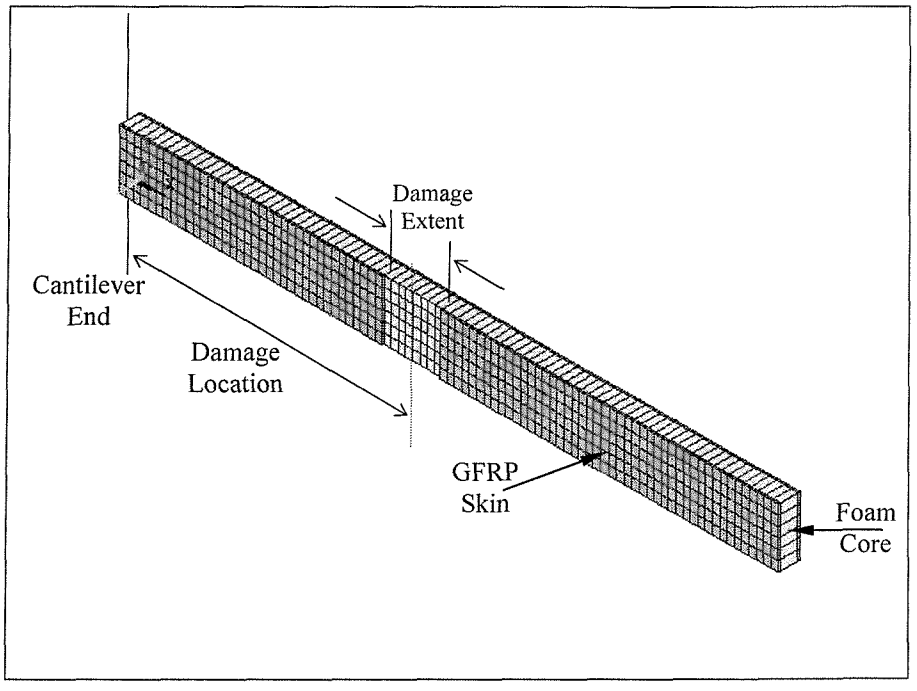

Figure 9.13 Finite element model of sandwich beam (isometric view)

The model has 90 and 6 element divisions along the length and the width respectively and it has one element through the thickness in both upper and lower skin and the foam core. The FEM has 1620 elements (i.e. 1080 SOLID191 and 540 SOLID95 elements) with 9163 nodes. This mesh density is used for all further simulations in order not to increase the computational time as the results obtained from two other models having different mesh densities (i.e. 3240 elements with 18253 nodes and 4320 elements with 21413 nodes) provided less than 0.1 per cent difference in the computed natural frequencies.

9.4.1 Modelling of Damage

The damage is modelled by removing the elements located at the upper surface with different extents (**Fig. 9.13**). In finite element modelling, 5 different damage severities (i.e. 10, 20, 30, 40 and 50mm extent) are simulated at 26 different locations (i.e. locations away from fixed end between 50mm and 300mm by increment of 10mm) along the beam. Therefore, 130 different damage scenarios are created on different models. **Figures 9.14a** to **b** show FEM of

two different damaged beams. The damage samples in **Figs. 9.14a** and **b** have the damage extent of 30mm and they are 70mm and 300 mm away from cantilever end respectively.

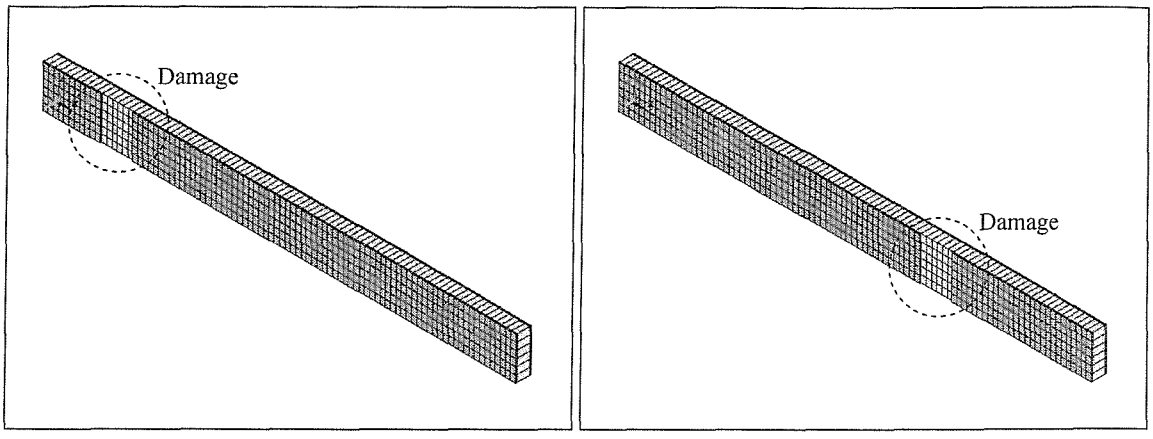

(a) (b)

Figure 9.14 Finite element models of damaged beams
(a) Damage located at 70mm (b) Damage located at 300mm

9.4.2 Finite Element Frequency Analysis

The natural frequencies of intact beam and damaged (130 damage cases) are obtained from the first three vertical bending modes. The damaged natural frequencies are normalised with respect to the intact ones in order to consider the effect of frequency reduction due to damage. The first three natural frequencies of intact and two selected damaged beams obtained from FEA are tabulated in **Table 9.3**.

Table 9.3 Natural frequencies details [Hz] (FEA)

Mode No	Intact Beam	Damaged Beam		$\frac{f_{damaged}}{f_{intact}}$	
		Damage at 70mm	Damage at 300mm	Damage at 70mm	Damage at 300mm
1st Bending	46.95	21.16	43.62	0.4507	0.9291
2nd Bending	251.12	243.75	160.12	0.9707	0.6376
3rd Bending	591.90	573.15	457.69	0.9683	0.7733

As it can be seen from **Tables 9.2** and **9.3** that the experimentally obtained reductions in resonant frequencies from the first three modes show strong agreement (i.e. less than 4% deviation) with the ones obtained from FEA for two different damage located at 70mm and 300mm with an extent of 30mm.

9.4.3 Sensitivity Analysis on Changes in Frequency

Since 5 different damage extents at 26 different damage locations are not enough to create a complete training input set for ANNs, damage scenarios are extended by interpolating (i.e. linear interpolation) the normalised natural frequencies for the damage extents between 10mm and 50mm by an increment of 1mm which gives 41 different damage extents at 26 different damage locations along the beam. Finally, the normalised natural frequencies from 1066 damage cases are obtained from the first three vertical bending modes and their variations are shown in **Fig. 9.15**.

9.5 ANN Predictions

Reduction in natural frequencies is given as input feature to three different ANNs (**Table 9.4**) to predict the severity and the location of the damage. 1000 and 66 input-output pairs are introduced to ANNs in the training and the validation runs respectively. In the first training run (RNF-DS), the mean square error (**Fig. 16a**) is reduced to a value of $1.85 \cdot 10^{-4}$ after 5000 epochs. The corresponding regression plot of this run can be seen in **Fig. 16b**. The second ANN training run (RNF-DL) is for the location prediction of the damage. **Figures 9.17a** and **b** show training and validation performance of this ANN with increasing epochs (i.e. mean square error value of $7.50 \cdot 10^{-5}$ after 5000 epochs) and the corresponding regression plot respectively. The final run aims to train the designed ANN (RNF-DS&DL) for both damage quantification and localisation. Since the feature (RNF) does not provide enough information related to both damage severity and location at the same time in single ANN, the mean square error value (**Fig. 9.18a**) reaches to a value of $3.95 \cdot 10^{-4}$ after 5000 epochs that is the highest among the others. **Figure 9.18b** and **c** show regression plots for damage severity and location respectively for this particular ANN run. The value, R, in the regression plots is the correlation coefficient between the outputs (i.e. predicted values) and targets and it shows the measure of how well the variation in the output is explained by targets. That means, the closer to value of 1, the better the fit and the correlation it indicates.

Table 9.4 ANNs used in the damage prediction of sandwich beam

Input	Output	Architecture
1. RNF	DS	3:6:1
2. RNF	DL	3:6:1
3. RNF	DS&DL	3:8:2

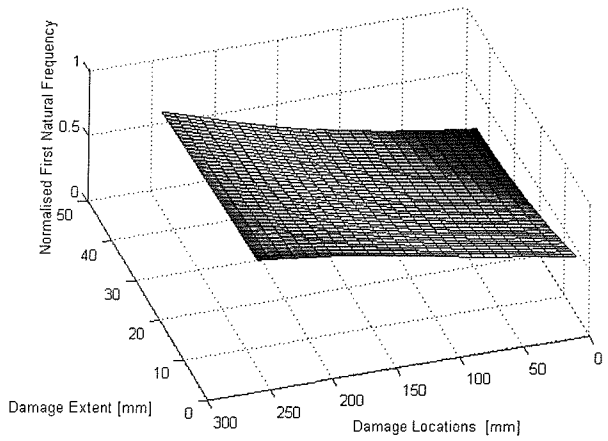

(a)

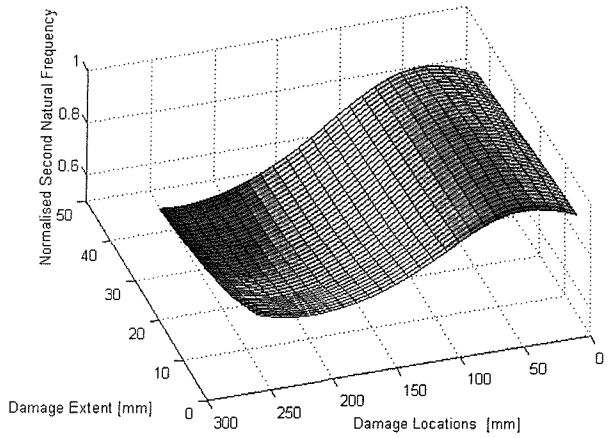

(b)

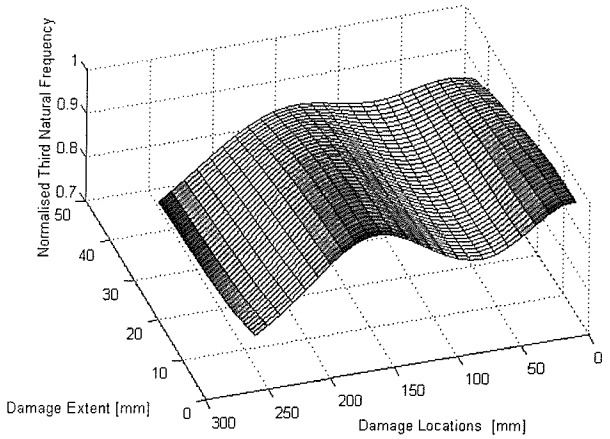

(c)

Figure 9.15 Variation of normalised natural frequencies

(a) Mode 1 (b) Mode 2 (c) Mode 3

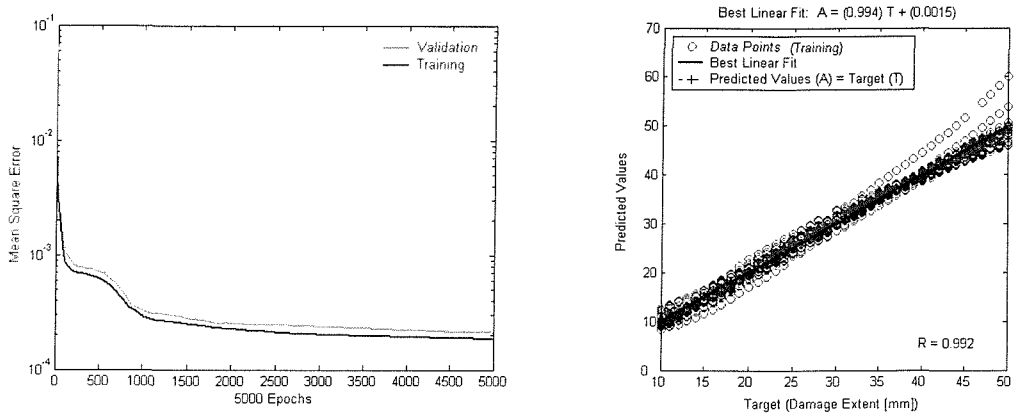

(a) (b)

Figure 9.16 Training and validation of ANN (Input: RNF, Output: DS)

(a) Mean square error with number of epochs (b) Regression plot

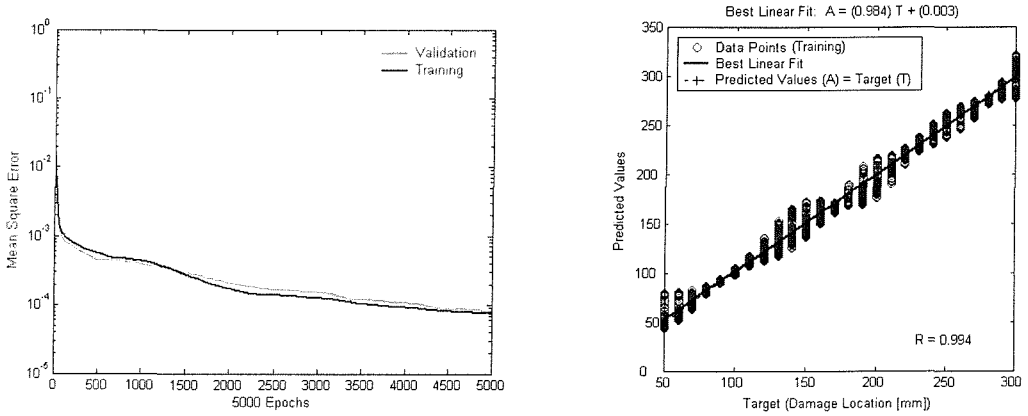

(a) (b)

Figure 9.17 Training and validation of ANN (Input: RNF, Output: DL)

(a) Mean square error with number of epochs (b) Regression plot

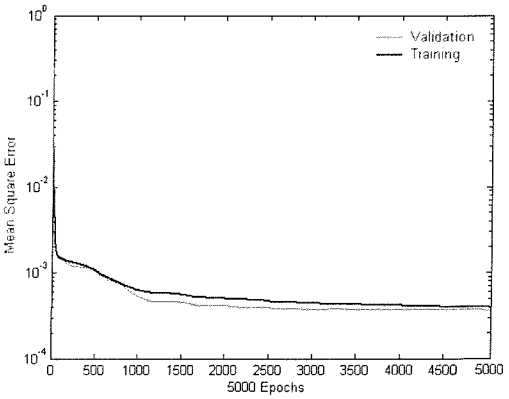

(a)

Fig. 9.18 (continued over)

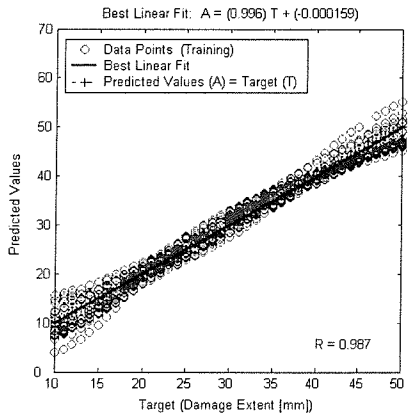

(b)

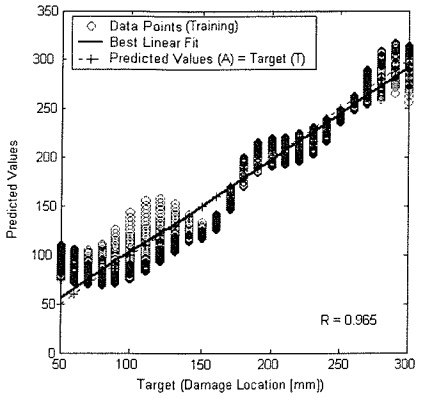

(c)

Figure 9.18 Training and validation of ANN (Input: RNF, Output: DS&DL)

(a) Mean square error with number of epochs

(b) Regression plot for damage severity (c) Regression plot for damage location

Having completed the training of ANNs, experimentally obtained data is introduced in order to predict damage size (extent) and its location along the sandwich beam specimens. All the test results of these ANNs are tabulated in **Table 9.5**.

Table 9.5 Damage size and location predictions

		Experimental Damage [TARGETS]		ANN Test Results [PREDICTIONS]*	
INPUT	OUTPUT	Size [mm]	Location [mm]	Size [mm]	Location [mm]
RNF	DS	30	70	36.8 (22.7)	-
RNF	DS	30	300	32.5 (8.3)	-
RNF	DL	30	70	-	75.4 (7.7)
RNF	DL	30	300	-	303.7 (1.2)
RNF	DS&DL	30	70	35.3 (17.7)	93.2 (33.1)
RNF	DS&DL	30	300	38.6 (28.7)	292.1 (2.6)
RNF	DS	40	170	42.9 (7.3)	-
RNF	DS	40	200	42.0 (5.0)	-
RNF	DL	40	170	-	189.2 (11.3)
RNF	DL	40	200	-	227.0 (13.5)
RNF	DS&DL	40	170	40.6 (1.5)	159.7 (6.0)
RNF	DS&DL	40	200	42.5 (6.2)	218.8 (9.4)

*Numbers in parentheses denote % deviation from target values

9.6 Conclusions

In this chapter, the fabrication of sandwich beam structures with embedded FBG strain sensors was presented with the results of the dynamic analyses performed on them. Results were considered in the context of predictions regarding quantification and localisation of the damage. Since creating an accurate FEM is one of the most important issues in model-dependent vibration-based analysis for damage identification, the dynamic analysis results for the sandwich test specimens were compared to those obtained from FEA. The comparative data shown in **Tables 9.2** and **9.3** clearly validated the numerical models.

Following the validation of the numerical study, experimental dynamic analyses were carried out on sandwich test specimens with embedded FBG strain sensors. It can be concluded from the analyses (details in Appendices A and B) that the FBGIS used in the experimental study provided accurate dynamic and static strain measurements from limited number of FBG strain sensors. However, the frequency domain of experimental interest was predetermined by the geometrical dimensions of the sandwich beams. For the intact and damaged beams investigated in this study, the frequency range was between 18Hz and 600Hz. (**Figs. 9.10 - 9.12**). Since the highest frequency of interest is approximately 600Hz, a superior FBGIS that supports dynamic strain measurements from multiple FBGs to a minimum 1.2kHz sampling frequency is required in order to investigate the first three strain modes shapes of the sandwich test specimens. Therefore, experimental reduction in frequency information obtained from intact and damaged sandwich beams was introduced to numerically trained ANNs in order to predict extent and location of the damage (**Table 9.5**).

It can be seen from the **Figs. 9.16** and **9.17** that lower MSE (i.e. $7.50 \cdot 10^{-5}$) and higher R (i.e. 0.994) values were obtained in the location predictions. This indicates that a better generalisation was achieved in localisation than quantification of the damage during the training and validation of the ANNs. When experimentally obtained frequency data was introduced to ANN for severity prediction (i.e. RNF-DS), the predicted values showed slight overestimation for both damage sizes of 30mm and 40mm. On the other hand, the ANN trained for damage location prediction (i.e. RNF-DL) provided more accurate estimation for the location of the 30mm damage size rather than that of the 40mm one. This is contrary to the observation in Chapter 7 where this combination (i.e. RNF-DL) did not provide good prediction for damage location. However, one should note that the extent of damage in the sandwich beam is different.

Final test run (RNF-DS&DL, **Fig. 9.18**) was performed for both severity and location estimation of the damage. As it can be seen from **Table 9.5**, although the ANN predicted the

size of the damage quite accurately, under and over estimations were observed in damage location predictions. Despite the numerous factors that affect the accuracy of the vibration-based analysis performed on intact and damaged sandwich beams (details in Appendix I), the damage location and severity predictions obtained from the ANNs are close to target values with acceptable deviations.

PART D

CLOSURE

Chapter Ten DISCUSSION

10.1 Achievements

In this thesis, damage identification in beam-like structures has been performed by using vibration-based analysis and artificial neural networks. The term "damage identification" is used here to indicate the use of measured vibration-based structural response in detecting changes in the condition of the structure. These changes are assumed to vary due to the extent and the location of the damage occurring in the structure. Thus, one of the main challenges in damage identification based on response measurements is to locate and quantify the damage from the limited number of locations monitored by sensors (Chapter 3).

The most important conclusions of this work are summarised and *its new contributions are highlighted* in the following paragraphs.

The first part of the study concentrated on finite element modelling and analyses of intact and damaged cantilever beams since the accurate finite element model is essential for vibration-based damage assessment methods using model-dependent approach. As one of the objectives of the present work is to identify damage in structures from changes in their vibration responses, damaged beam models have been generated through local stiffness or thickness changes at different locations with various severities from intact models (i.e. control structures). After performing dynamic analyses, which provide natural frequencies, displacements and curvature mode shapes by using previously generated damage scenarios, sensitivity analyses have been performed in order to investigate the effects of varying locations and extents of damage on eigenparameters.

Having obtained vibration-based analysis patterns mentioned above, damage prediction indicators (i.e. features) have been selected. The first feature used in the damage identification analyses was reduction in natural frequencies (i.e. RNF) due to damage. Depending on the location of the damage, different modes of the beam could be affected to different extents by making the problem non-unique. Therefore, the study focused on the effect of multiple modes

by considering the first three natural modes of the beams in the analyses. It can be concluded from the sensitivity analyses performed on beams having different extents of damage at different locations along the span of the beams that the percentage reduction in natural frequencies increase with the increasing severity of the damage. Additionally, considering a particular mode of vibration, when damage is located at or close to higher curvature point, the percentage reduction in natural frequency due to damage is considerably higher than the one observed when the damage is located at or near to one of the nodal points of that curvature mode shape.

As eigenfrequencies are a global property of a structure, absolute differences between curvature mode shapes of the intact and the damaged beams have also been investigated to provide extra information in the prediction of the location of the damage. It is found from the sensitivity analyses that, by and large, the maximum values of the absolute differences in curvature modes occur near damage location. Thus, the maximum values of the absolute differences in curvature mode shapes (i.e. MADC) and their spatial location along the beam (i.e. LOC) have also been used for localisation and quantification of the damage together with reduction in natural frequencies. The main reason for choosing only the maximum values of the absolute differences in curvature mode shapes is to keep number of vibration-based analysis features as low as possible and yet obtain a high accuracy in the location and severity predictions by improving the damage assessment method.

In literature (Chapter 2), local and global patterns (i.e. curvature mode shapes and natural frequencies, **Table 2.2** and **7.5**) obtained either from numerical or experimental vibration analyses data have been used in ANN applications as input in the damage detection of beam structures. However, there is no particular study found in the literature dealing with composite structures regarding different combinations of the features extracted from vibration analysis data and using them as input to ANN to investigate the severity and location of the damage. Therefore, based on the results of sensitivity analyses performed on intact and damaged composite beams, *the damage sensitive features (i.e. RNF, MADC and LOC) from vibration-based data obtained from the first three modes have been introduced to ANNs* **[7-1]**. Since the aim of these analyses (Chapter 7) has been to investigate the effectiveness of these features and their different combinations in the damage identification process as training set to ANNs, normalised geometrical and dimensionless elastic properties of FRP laminated composite structures have been used in the finite element analysis.

The ANNs designed and used during the analyses are multi-layer feedforward neural networks with backpropagation learning. These types of ANNs are also called pattern associator and frequently used for classification and prediction purposes. Initially, fifteen different neural networks with single hidden layer have been designed for the prediction of severity (as a single output), location (as a single output) and both severity and location in single neural network having two outputs. Before introducing this vibration data to ANNs, a pre-processing has also been performed in order to arrange the data in such a way that ANNs can use them directly as input-output pairs. The first step in pre-processing is the normalisation of input and output pairs. After normalisation, it is necessary to add artificial noise to noise-free input data at some percentages to check the generalisation of the neural network and to simulate the experimental uncertainties.

The detailed analysis considering the performance of multi-hidden-layer ANNs has also been examined and compared with the one having a single hidden layer. The analyses performed on two-hidden-layer ANNs have been shown in Appendix D. Considering the computational time issue and the general fact that an ANN with single hidden layer can be trained to solve pattern recognition problems, single hidden layer ANNs have been selected and used throughout the analyses. As the number of neurons in the input and the output layers have been restricted with the data introduced to ANNs during the training, only the number of neurons in the hidden layer could be adjusted to optimise the performance of the designed ANNs. Thus, different ANN architectures have been tested. Based on this, a particular group of network configurations has been selected to use in further simulations as they have provided the best estimations for both localisation and quantification of the damage. The number of epochs has also been adjusted in such a way that the best convergence in MSE could be achieved during the training and validation of the ANNs.

As mentioned earlier, it is important to provide vibration signatures from multiple modes to solve the non-unique and inverse damage detection problem. Hence, *the effects of multiple vibration modes on the predictions of ANNs* have also been investigated. The noise-free features extracted from each individual mode of vibration have been introduced to single-hidden-layer ANNs. Four different ANNs (RNF, MADC, MADC&LOC and RNF&MADC&LOC as input features) have been selected for training. By comparing their performance, it can be concluded that generalisation and accuracy in predictions improved as the number of features increased through the addition of higher modes. Full details of this particular analysis can be found in Appendix C.

The results obtained from ANN predictions performed on laminated composite beams regarding damage severity and location indicated that neural networks with single output (i.e. either location (DL) or severity (DS)) operated more accurately than neural networks with combined outputs (i.e. both severity and location (DS&DL)). The level of artificial noise on input data also affected the predictions and accurate results have been obtained in the localisation of the damage as compared to damage quantification when the increased level of noise-polluted data has been introduced to ANNs. Finally, it can be concluded from the predictions of the ANNs that the vibration-based patterns, extracted features, effect of noise on these features, architecture and training of the ANNs are the most important factors played an important role in the accuracy of the structural damage assessment method. The numerical analyses results of the present study **[7-2]** could serve as a benchmark for future investigators in selecting ANN as a damage detection tool.

Having gained an extensive knowledge about the damage detection by vibration-based analysis via ANN on numerically generated data with artificial damage scenarios, experimental analysis has been dealt with both intact and damaged isotropic beam specimens with distributed surface bonded strain gauges (Chapter 6). First, structural responses of steel beams have been obtained by using miniature accelerometer under both frequency sweep and random excitation. Then, constant frequency excitation was applied at each resonant frequency of interest to obtain dynamic strain mode shapes at these particular frequencies. The experimental vibration data agreed well with the numerically obtained results for isotropic beams especially for intact case. However, the experimental results obtained from the damaged steel beam showed some variations at the damage location regarding the dynamic strain data. The possible reasons for this deviation could be from the method used in the calculations of curvature modes, the way of modelling of the structural damage and from the other source of errors involved during the experimental analysis. *The damage detection algorithm that uses combination of global and local vibration-based analysis data as input to ANNs for location and severity prediction of the damage in isotropic beam structures via distributed surface bonded electrical strain gauges has also been validated experimentally* **[8-1]**. The predictions of the ANNs regarding the damage severity and location provided reasonable accuracy, albeit for one test case only (Chapter 8).

In the final part of the experimental study (Chapter 9), *GFRP sandwich beam structures with embedded FOSs have been manufactured via resin infusion technique by vacuum bagging.* Considering their advantages (**Table 2.5**) on conventional electrical strain gauges, FOS with multiple Bragg gratings have been selected and used to monitor internal static and dynamic strain in sandwich beam structures. The GFRP sandwich structure used throughout the analyses

has polymer foam core covered with four equal layers of uni-directional glass fibre with layer orientation of $[0/90]_s$ on each side. FOSs have been embedded between core and laminated skin during the manufacturing. The main reason of embedding FOSs at this particular location is owed to the fact that there is a high tendency of separation between the GFRP laminated skin and foam core in sandwich structures under transverse vibration as this is the interface where two different materials meet. By positioning FOS parallel to 0° glass fibre on the skin, the size of the local resin-rich region surrounding the embedded FOS has been minimised.

After embedding optical fibres, the effect of curing on FBG strain sensors has also been investigated by monitoring the changes in positions of the peaks (i.e. the reflectivity) of the wavelengths. It was observed from the cure monitoring that the peak of the Bragg wavelengths shifted to lower values and their intensities decreased as the curing of the resin created residual stresses over and around the optical fibres. As the Bragg wavelength of the first sensor overlapped with one of the reference gratings, the measurements from this particular sensor could not be obtained. Thus, the FBGs should be written in a way that they are spaced in wavelength domain both from each other and from the reference gratings in order to avoid overlapping.

Having manufactured the sandwich beam specimens, analyses have been performed to investigate the capabilities of the FBGIS and the effectiveness of the FBG sensors on static and dynamic strain measurements. The static analysis (Appendix B) performed on GFRP sandwich beams showed that embedded FBG strain sensors have provided accurate local strain. On the other hand, dynamic strain history (Appendix A) obtained from multiple FBG strain sensors is restricted with the capabilities of the FBGIS. Hence, experimental validation of the damage detection algorithm on GFRP sandwich beam-like structures has been achieved by introducing reduction in natural frequency information to ANNs. The ANNs trained for the damage identification with FEA data have been tested by using an experimental input and accurate location and severity estimations have been obtained with acceptable deviations from the desired target values.

A list of publications arising from this research is given in Appendix J.

10.2 Future Work

The following suggestions are made for future research:

- Generalisation of the proposed algorithm to two-dimensional structures with sensor optimisation

As one-dimensional beam-like structures were used throughout the study, the work can be expanded by generalising and applying the algorithm to two-dimensional plates or shell structures. This requires a strain sensor network that can provide double curvature information under dynamic loading conditions. This brings the necessity of optimisation in number of sensors and their locations. The key point in selection and use of sensors for structural health monitoring is to install them in such a way that the dynamic mechanical characteristics of the host structure are not significantly modified. Therefore, the optimisation procedure is one of the crucial stages in the design of health monitoring system and it plays an important role from the final design and maintenance point of view.

- Inclusion of horizontal bending and torsion modes in the analysis

This thesis addressed the application of the vibration-based damage identification method by using only the vertical bending modes of vibration of the beam-like structures. Depending on the behaviour of the damage, different types of vibration modes might provide additional information in the detection, localisation and quantification of the damage when they are introduced as input feature to ANNs.

- Inclusion of multiple damage scenarios

The damage identification method proposed here considers single damage case. The further research requires the investigation of more damage sensitive features from multiple damage scenarios as there is always a possibility of having more than one damage in the structure.

- Investigation of the residual life of a structure

Since distributed strain information was obtained and served as one of the damage sensitive features, it can also be used to obtain stress information that might be combined with various fracture mechanics criteria and fatigue analysis in the determination of the remaining life of the structure. Depending on the type and the loading condition, structural health monitoring and

damage detection methods can be improved to investigate higher levels of damage assessment such as Level#4 (Section 1.1).

- Application of the technique to real structures

As the damage detection technique used in this study was applied to small-scale models and test specimens in controlled laboratory environment with artificially introduced damage, there is a need to implement the technique to real aeronautical, civil, marine and off-shore structures having complex shape and boundary conditions with unknown environmental and operational conditions in their service life.

Chapter Eleven CONCLUDING REMARKS

A damage identification technique using model-dependent vibration-based analyses has been developed and employed in quantification and localisation of damage in beam-like structures. The approach adopted is based on the use of measured vibration data from accelerometers, surface bonded strain gauges and embedded fibre Bragg grating (FBG) strain sensors to identify different extents of damage at various locations along the structures via artificial neural networks (ANNs).

Finite element models of steel, fibre reinforced plastic (FRP) laminated composites, and foam-core sandwich beam-like structures were produced and modal analyses were performed on models with artificially generated damage scenarios in order to obtain input-output data sets for training of ANNs. A group of features providing both global and local damage information were extracted and introduced to ANNs with different combination in the form of normalised relative changes between healthy and damaged structures. As one of the aims of the technique adopted here was to test the efficacy of selected vibration signatures, ANNs were chosen as information-processing algorithms for the solution of this non-unique and inverse pattern recognition problem. The results of the numerical simulations showed that both selected features and the level of artificial noise added to them are very important from the generalisation and robustness point of view of the designed ANNs.

As sensors used for vibration measurements become increasingly inexpensive, a structure can be densely populated with them, making damage easier to quantify and localise by providing more information. Hence, experiments were performed by using surface bonded strain gauges and embedded FBG strain sensors in beam-like structures to collect information about the condition of the host structure and to estimate location and severity of damage with numerically trained ANNs. It has been observed from the experimental work of damage detection that there is strong correspondence between the selected features and the ANNs predictions regarding the location and severity of damage.

It can also be concluded from the proposed approach that better localisation of damage was achieved without compromising the accuracy in damage quantification predictions. Finally, the study proved that a combination of global and local vibration-based damage sensitive features measured from beam-like sensory structures used as input to ANNs from multiple modes is very effective in identifying damage patterns.

REFERENCES

CHAPTER 1: Introduction

[1-1] **Matthews, F.L.** Damage in fibre-reinforced plastics; its nature, consequences and detection. *Proceeding of the International Conference on Damage Assessment of Structures (DAMAS99)* 1999, 1-15.

[1-2] **Doebling, S.W., Farrar, C.R., Prime, M.B.** and **Shevitz, D.W.** Damage identification and health monitoring of structural and mechanical systems from changes in their vibration characteristics: a literature review. 1996, Tech. Rep. No: LA-13070-MS. (Los Alamos National Laboratory)

CHAPTER 2: Literature Review

[2-1] ETL 1110-2-548 *Composite materials for civil engineering structures*, 1997 (Publications of the Headquarters, United States Army Corps of Engineers, Engineer Technical Letters, Civil Works: 8.2-8.5)

[2-2] **Salawu, O.S.** Detection of structural damage through changes in frequency: A review. *Engineering Structures*, 1997, **19**(9), 718-723.

[2-3] **Zou, Y., Tong, L.** and **Steven, G.P.** Vibration-based model-dependent damage (delamination) identification and health monitoring for composite structures-A review. *Journal of Sound and Vibration*, 2000, **230**(2), 357-378.

[2-4] **Sohn, H., Farrar, C.R., Hemez, F.M., Czarnecki, J.J., Shunk, D.D., Stinemates, D.W.,** and **Nadler, B.R.** A review of structural health monitoring literature: 1996-2001, 2002, Tech. Rep. No: LA-13070-MS-updated version. (Los Alamos National Laboratory)

[2-5] **Farrar, C.R., Duffey T.A., Doebling, S.W.** and **Nix, D.A.** A statistical pattern recognition paradigm for vibration-based structural health monitoring. *Structural Health Monitoring 2000, Proceeding of the Second International Workshop on Structural Health Monitoring*, 1999, 764-773.

[2-6] **Doebling, S.W., Farrar, C.R.** and **Prime, M.B.** A summary review of vibration-based damage identification methods. *The Shock and Vibration Digest*, 1998, **20**(2), 91-105.

[2-7] **Cawley, P.** and **Adams, R.D.** The location of defects in structures from measurements of natural frequencies. *Journal of Strain Analysis*, 1979, **14**(2), 49-57.

[2-8] **Inada, T., Shimamura, Y., Todoroki, A., Kobayashi, H.,** and **Nakamura, H.** Damage identification method for smart composite cantilever beams with piezoelectric materials. *Structural Health Monitoring 2000, Proceeding of the Second International Workshop on Structural Health Monitoring*, 1999, 986-994.

[2-9] **Zak, A., Krawczuk, M.,** and **Ostachowichz, W.** Vibration analysis of composite plate with closing delamination. *Structural Health Monitoring 2000, Proceeding of the Second International Workshop on Structural Health Monitoring*, 1999, 1019-1028.

[2-10] **Diaz Valdes, S.H.** and **Soutis, C.** Delamination detection in composite laminates from variations of their modal characteristics. *Journal of Sound and Vibration*, 1996, **228**(1), 1-9.

[2-11] **Lakshmi, K.** and **Jebaraj, C.** Sensitivity analysis of local/global modal parameters for identification of a crack in a beam. *Journal of Sound and Vibration*, 1999, **228**(5), 977-994.

[2-12] **Hu, N., Wang, X., Fukunaga, H., Yao, Z.H., Zhang, H.X.,** and **Wu, Z.S.** Damage assessment of structures using modal test data. *International Journal of Solids and Structures,* 2001, **38**(18), 3111-3126.

[2-13] **Ren, W.X.** and **Roeck De G.** Structural damage identification using modal data. I: Simulation verification. *Journal of Structural Engineering*, 2002, **128**(1), 87-95.

[2-14] **Ren, W.X.** and **Roeck De G.** Structural damage identification using modal data. II: Test verification. *Journal of Structural Engineering*, 2002, **128**(1), 96-104.

[2-15] **Ahmadian, H., Mottershead, J.E. and Friswell, M.I.** Damage detection from substructure modes, *Proceedings of ISMA21, 1996 International Conference on Noise and Vibration Engineering*, 1996, Volume II, 983-991.

[2-16] **Friswell, M.I., Penny, J.E.T.** and **Garvey, S.D.** A combined genetic and eigensensitivity algorithm for the location of damage in structures. *In Proceeding of Identification in Engineering Systems*, 1996, 357-367.

[2-17] **Fox, C.H.J.** The location of defects in structures: A comparison of the use of natural frequency and mode shape data. *Proceeding of the International Modal Analysis Conference*, 1992, **10**(1), 522-528.

[2-18] **Pandey, A. K., Biswas, M.,** and **Samman, M.M.** Damage detection from changes in curvature mode shapes. *Journal of Sound and Vibration*, 1991, **145**(2), 321-332.

[2-19] **Yuen, M.M.F.** A numerical study of the eigenparameters of a damaged cantilever. *Journal of Sound and Vibration*, 1985, **103**(3), 301-310.

[2-20] **Ratcliffe, C.P.** Damage detection using a modified Laplacian operator on mode shape data. *Journal of Sound and Vibration*, 1997, **204**(3), 505-517.

[2-21] **Ho, Y.K.** and **Ewins, D.J.** Numerical evaluation of the damage index. *Structural Health Monitoring 2000, Proceeding of the Second International Workshop on Structural Health Monitoring*, 1999, 995-1011.

[2-22] **Pai, P.F.** and **Young, L.G.** Damage detection of beams using operational deflection shapes. *International Journal of Solids and Structures*, 2001, **38**(18), 3161-3192.

[2-23] **Pai, P.F.** and **Jin, S.** Locating structural damage by detecting boundary effects. *Journal of Sound and Vibration*, 2000, **231**(4), 1079-1110.

[2-24] **Cornwell, P., Doebling, S.W.** and **Farrar, C.R.** Application of the strain energy damage detection method to plate-like structures. *Journal of Sound and Vibration*, 1999, **224**(2), 359-374.

[2-25] **Wahab, M.M.A.** and **Roeck, D.D.** Damage detection in bridges using modal curvatures: application to a real damage scenario. *Journal of Sound and Vibration*, 1999, **226**(2), 217-235.

[2-26] **Waldron, K., Ghoshal, A., Schulz, M.J., Sundaresan, M.J., Ferguson, F., Pai, P.F.** and **Chung, J.H.** Damage detection using finite element and laser operational deflection shapes. *Finite Elements in Analysis and Design*, 2002, **38**(3), 193-226.

[2-27] **Jian, X.H., Tzou, H.S., Lissenden C.J., and Penn, L.S.** Damage detection by piezoelectric patches in a free vibration method. *Journal of Composite Materials*, 1997, **31**(4), 345-359.

[2-28] **Lee, U.** and **Shin, J.** A frequency response function-based structural damage identification method. *Computers & Structures*, 2002, **80**(2), 117-132.

[2-29] **Sampaio, R.P.C., Maia, N.M.M.,** and **Silva, J.M.M.** Damage detection using the frequency-response-function curvature method. *Journal of Sound and Vibration*, 1999, **226**(5), 1029-1042.

[2-30] **Castellini, P.** and **Revel, G.M.** Damage detection by laser vibration measurement. *15th World Conference on Non-Destructive Testing*, 2000, *15th WCNDT*, Roma2000.

[2-31] **Sanders, D.R., Kim, Y.I.** and **Stubbs, N.** Nondestructive evaluation of damage in composite structures using modal parameters. *Experimental Mechanics*, 1992, **32**(3), 240-251.

[2-32] **Fukunaga, H., Hu, N.** and **Chang, F.K.** Structural damage identification using piezoelectric sensors. *International Journal of Solids and Structures*, 2002, **39**(2), 393-418.

[2-33] **Kessler, S.S., Spearing, S.M., Atalla, M.J., Cesnik, C.E.S.** and **Soutis, C.** Damage detection in composite materials using frequency response methods. *Composites Part B: Engineering,* 2002, **33**(1), 87-95.

[2-34] **Staszewski, W.J.** Intelligent signal processing for damage detection in composite materials. *Composite science and technology,* 2002, **62**(7-8), 941-950

[2-35] **Wu, Y.J., Shi, X.Z.,** and **Zhuang, T.G.** Fusion of wavelet packets and neural network in detection of composites. *AIAA Journal*, 2000, **38**(6), 1063-1069.

[2-36] **Okafor, A.C.** and **Dutta, A.** Structural damage detection in beams by wavelet transforms. *Smart Materials and Structures*, 2000, **9**(6), 906-917.

[2-37] **Lopes, V. Jr., Muller-Slany, H.H., Brunzel, F.,** and **Inman, D.J.** Damage detection in structures by electrical impedance and optimisation technique. *Proceeding of the IUTAM Symposium–Smart Structures and Structronic Systems,* 2000, Magdeburg-Germany.

[2-38] **Lopes, V. Jr., Turra, A.E., Muller-Slany, H.H., Brunzel, F.,** and **Inman, D.J.** A new methodology of damage detection by electrical impedance and optimisation technique. *Diname 2001*, Florinapolis-Brazil.

[2-39] **Waszczyszyn, Z.** and **Ziemianski, L.** Neural networks in mechanics of structures and materials - New results and prospects of applications. *European Conference on Computational Mechanics*, 1999, Munchen-Germany

[2-40] **Worden, K.** and **Tomlinson, G.R.** Damage location and quantification using neural networks. *In Engineering Integrity Assessment,* 1994, 11-31. (J. H. Edwards, J. Kerr and P. Stanley Eds.)

[2-41] **Worden, K.** and **Burrows, A.P.** Optimal sensor placement for fault detection. *Engineering Structures,* 2001, **23**(8), 885-901.

[2-42] **Mukherjee, A.** and **Ravindra, V.** A fuzzy-neuro health monitoring tool transient vibration response, *Proceedings of VETEMAC-1*, 2000, Bangalore-India

[2-43] **Zang, C.** and **Imregun, M.** Structural damage detection using artificial neural networks and measured frf data reduced via principal component projection. *Journal of Sound and Vibration*, 2000, **242**(5), 813-827.

[2-44] **Zapico, J.L., Worden, K.** and **Molina, F.J.** Vibration-based damage assessment in steel frames using neural networks. *Smart Materials and Structures*, 2001, **10**(3), 553-559.

[2-45] **Xu, Y.G., Liu, G.R., Wu, Z.P.** and **Huang, X.M.** Adaptive multilayer perceptron networks for detection of cracks in anisotropic laminated plates. *International Journal of Solids and Structures*, 2001, **38**(32-33), 5625-5645.

[2-46] **Ball, A.D.** and **Worden, K.** Vibration signal conditioning using neural networks. *In Proceedings of 5th International Congress on Condition Monitoring and Diagnostic Engineering Management*, 1992, 412-417.

[2-47] **Worden, K.** and **Ball, A.D.** Modal analysis-based condition assessment of structures using neural networks. *In Proceedings of 6th International Congress on Condition Monitoring and Diagnostic Engineering Management*, 1994,139-146.

[2-48] **Worden, K., Patsias, S.** and **Staszewski, W. J.** Damage detection in machines using neural networks. *Proceedings of ISMA 23*, 1998, Vol. 1, 91-98.

[2-49] **Worden, K., Ball, A.D.,** and **Tomlinson, G.R.** Fault location in structures using neural networks. *Proceeding of 75th Meeting of the AGARD Structures and Materials Panel on Smart Structures for Aircraft and Spacecraft*, 1992, 19.1-19.19.

[2-50] **Sensburg, O., Worden, K.** and **Tomlinson, G.R.** Detection and location of structural damage using dynamic test data. *In Proceedings of the 19th ICAS Congress/AIAA Aircraft Systems Conference*, 1994, 2834-2844.

[2-51] **Kudva, J.N., Munir, N.** and **Tan, P.W.** Damage detection in smart structures using neural networks and finite-element analyses. *Smart Materials and Structures*, 1992, **1**(2), 108-112.

[2-52] **Islam, A.S.** and **Craig, K.C.** Damage detection in composite structures using piezoelectric materials. *Smart Materials and Structures*, 1994, **3**(2), 318-328.

[2-53] **Okafor, A.C., Chandrashekhara, K.** and **Jiang, Y.P.** Delamination prediction in composite beams with built-in piezoelectric devices using modal analysis and neural network. *Smart Materials and Structures*, 1996, **5**(2), 338-347.

[2-54] **Roberts, S.M, Kusiak, J., Liu, Y.L., Forcellese, A.,** and **Withers, P.J.** Prediction of damage evolution in forged aluminium metal matrix composites using neural network approach. *Journal of Materials Processing Technology*, 1998, **80-81**, 507-512.

[2-55] **Yun, C.B.** and **Bahng, E.Y.** Substructural identification using neural networks. *Computers and Structures*, 2000, **77**(1), 41-52.

[2-56] **Pandey, P.C.** and **Barai, S.V.** Multilayer perceptron in damage detection of bridge structures. *Computers & Structures,* 1995, **54**(4), 597-608.

[2-57] **Barai, S.V.** and **Pandey, P.C.** Performance of the generalized delta rule in structural damage detection. *Engng. Applic. Artif. Intell.*, 1995, **8**(2), 211-221.

[2-58] **Seo, D.C.** and **Lee, J.J.** Damage detection of CFRP laminates using electrical resistance measurement and neural network. *Composite Structures,* 1999, **47**, 525-530.

[2-59] **Chiu, W.K., Galea, S.C., Koss, L.L.** and **Rajic, N.** Damage detection in bonded repairs using piezoceramics. *Smart Materials and Structures*, 2000, **9**(4), 466-475.

[2-60] **Chattopadhyay, A., Nam, C.** and **Kim, Y.** Damage detection and vibration control of a deleminated smart composite plate. *Advanced Composite Letters*, 2000, **9**(1), 7-15.

[2-61] **Wang, C.S.** and **Chang, F.K.** Built-in diagnostics for impact damage identification of composite structures. *Structural Health Monitoring 2000, Proceeding of the Second International Workshop on Structural Health Monitoring*, 1999, 612-621.

[2-62] **Ogisu, T., Nomuro, M., Kikukawa, H.,** and **Takeda, N.** Development of health monitoring system using embedded SMA foils in CFRP laminates. *Structural Health Monitoring 2000, Proceeding of the Second International Workshop on Structural Health Monitoring*, 1999, 317-326.

[2-63] **Sunar, M.** and **Rao, S.S.** Distributed modeling and actuator location for piezoelectric control systems. *AIAA Journal*, **34**(10). Technical Notes 2209-2211.

[2-64] **Kang, Y.K., Park, H.C., Hwang, W.** and **Han, K.S.** Optimum placement of piezoelectric sensor/actuator for vibration control of laminated beams. *AIAA Journal*, 1996, **34**(9), 1921-1926.

[2-65] **Burke, S.E.** and **Hubbard, Jr. J.E.** Active vibration control of a simply supported beam using a spatially distributed actuator. *IEEE Control System Magazine*, August 1987, 25-30.

[2-66] **Devasia, S., Meressi, T., Paden, B.** and **Bayo, E.** Piezoelectric actuator design for vibration suppression: placement and sizing. *Journal of Guidance, Control and Dynamics*, 1993, **16**(5), 859-864.

[2-67] **Bai, M.R.** and **Lin, G.M.** The development of a DSP-based active small amplitude vibration control system for flexible beams by using the LQG algorithms and intelligent materials. *Journal of Sound and Vibration*, 1996, **198**(4), 411-427.

[2-68] **Okabe, Y., Yashiro, S., Kosaka, T.** and **Takeda, N.** Detection of transverse cracks in CFRP composites using embedded fiber Bragg grating sensors. *Smart Materials and Structures*, 2000, **9**(6), 832-838.

[2-69] **Green, A.K., Zaidman, M., Shafir, E., Tur, M.** and **Gali, S.** Infrastructure development for incorporating fibre-optic sensors in composite materials. *Smart Materials and Structures*, 2000, **9**(3), 316-321.

[2-70] **Dakai, L., Mingshun, H., Baoqi, T.,** and **Hao, Q.** Research on some problems about optic fiber embedded in carbon fiber smart structure. *Structural Health Monitoring 2000, Proceeding of the Second International Workshop on Structural Health Monitoring*, 1999, 680-689.

[2-71] **Johnson, G.A., Pran, K., Wang, G., Havsgard, G.B.,** and **Vohra, S.T.** Structural monitoring of a composite hull air cushion catamaran with a multi-channel fiber Bragg grating sensor system. *Structural Health Monitoring 2000, Proceeding of the Second International Workshop on Structural Health Monitoring*, 1999, 190-198.

[2-72] **Rippert, L., Wevers, M.,** and **Huffel, S.V.** Optical fibres for in situ monitoring the damage development in composites. *15th World Conference on Non-Destructive Testing*, 2000, *15th WCNDT*, Roma2000.

[2-73] **Han, L., Voloshin, A.,** and **Coulter, J.** Application of the integrating fiber optic sensor for vibration monitoring. *Smart Materials and Structures*, 1995, **4**(2), 100-105.

[2-74] **Bhatia, V., Schmid, C.A., Murphy, K.A., Claus, R.O., Tran, T.A., Greene, J.A.,** and **Miller, M.S.** Optical fibre sensing technique for edge-induced and internal delamination detection in composites. *Smart Materials and Structures*, 1995, **4**(3), 164-169.

[2-75] **Davis, M.A., Kersey, A.D., Sirkis, J.,** and **Friebele, E.J.** Shape and vibration mode sensing using a fiber optic Bragg grating array. *Smart Materials and Structures*, 1996, **5**(6), 759-765.

CHAPTER 4: Theoretical Modelling

[4-1] **Herakovich, C.T.** *Mechanics of fibrous composites*, 1998 (John Wiley & Sons, Inc.)

[4-2] **Daniel, I.M.** and **Ishai, O.** *Engineering mechanics of composite materials*, 1994 (Oxford University Press)

[4-3] **Morley, J.G.** *High -performance fibre composites*, 1987 (Academic Press Limited, London)

[4-4] **Zenkert, D.** *An introduction to sandwich construction*, 1995 (EMAS Publishing)

[4-5] **Vinson, J.R** and **Sierakowski, R.L.** *The behavior of structures composed of composite materials*, 1987 (Martinus Nijhoff Publishers)

[4-6] **Chia, C.Y.** *Nonlinear analysis of plates*, 1980 (McGraw-Hill, Inc.)

[4-7] **Ochoa, O.O.** and **Reddy, J.N.** *Finite element analysis of composite laminates*, 1992 (Kluwer Academic Publishers)

[4-8] **Leissa, A.W.** The free vibration of rectangular plates. *Journal of Sound and Vibration*, 1973, **31**(3), 257-293.

[4-9] **Reddy, J.N.** Free vibration of anisotropic, angle-ply laminated plates including transverse shear deformation by the finite element method. *Journal of Sound and Vibration*, 1979, **66**(4), 565-576.

[4-10] **Mizusawa T.** Vibration of rectangular Mindlin plates by the spline strip method. *Journal of Sound and Vibration*, 1979, **163**(2), 193-205.

[4-11] **Reddy, J.N.** and **Phan, N.D.** Stability and vibration of isotropic, orthotropic and laminated plates according to a higher-order shear deformation theory. *Journal of Sound and Vibration*, 1985, **98**(2), 157-170.

[4-12] **Kant, T.** and **Mallikarjuna** Vibrations of unsymmetrically laminated plates analyzed by using a higher order theory with a C^0 finite element formulation. *Journal of Sound and Vibration*, 1989, **134**(1), 1-16.

[4-13] **Reddy, J.N.** and **Khdeir, A.A.** Buckling and vibration of laminated composite plates using various plate theories. *AIAA Journal*, 1989, **27**(12), 1808-1817.

[4-14] **Nosier, A., Kapania, R.K. and Reddy, J.N** Free vibration analysis of laminated plates using a layerwise theory. *AIAA Journal*, 1993, **31**(12), 2335-2346.

[4-15] **Nayak, A.K.** *On dynamic analysis of laminated composite and sandwich plates by using finite element method*, 2002, PhD Thesis, University of Southampton.

[4-16] **Chao, C.C. And Chern, Y.C.** Comparison of natural frequencies of laminates by 3-d theory, part I: Rectangular plates. *Journal of Sound and Vibration*, 2000, **230**(5), 985-1007.

[4-17] **Noor, A. K.** Free vibrations of multilayered composite plates. *AIAA Journal*, 1973, **11**(7), 1038-1039.

[4-18] **Fan, J.** and **Ye, J.** An exact solution for the statics and dynamics of laminated thick plates with orthotropic layers. *International Journal of Solids Structures*, 1990, **26**(5/6), 655-662.

[4-19] **Vinson, J.R.** *The behavior of thin walled structures: Beams, plates and shells*, 1989 (Kluwer Academic Publishers)

[4-20] **Blevins, R.D.** *Formulas for natural frequency and mode shape*, 1979 (Robert E. Krieger Publishing Co., Inc.)

[4-21] **Rao, S.S.** *Mechanical vibrations*, 1986 (Addison-Wesley Publishing Company)

[4-22] **Cartmell, M.** *Introduction to linear, parametric and nonlinear vibrations*, 1990 (Chapman and Hall)

[4-23] **Schalkoff, R.J.** *Pattern Recognition: Statistical, structural and neural approaches*, 1992 (John Wiley & Sons, Inc.)

[4-24] **Beale, R.** and **Jackson, T.** *Neural computing: an introduction*, 1990 (The Institute of Physics)

[4-25] **Hassoun, M.H.** *Fundamentals of artificial neural networks*, 1995 (The M.I.T. Press)

[4-26] **Mehrotra, K., Mohan, K. C., and Ranka, S.** *Elements of artificial neural networks*, 1997 (The M.I.T Press)

[4-27] **Wasserman, P.D.** *Neura l computing – Theory and practice*, 1989 (Van Nostrand Reinhold, NY)

[4-28] **Patterson, D.W.** *Artificial neural networks: Theory and applications*, 1996 (Prentice Hall)

[4-29] **Bishop, C.M.** *Neural networks for pattern recognition*, 1995 (Clarendon Press)

CHAPTER 5: Experimental Design

[5-1] Ling Dynamic Systems (LDS) *System manual*, V830 Vibration Test Systems, (Manual Number 805341, Edition 1, Amendment 18)

[5-2] Ling Dynamic Systems (LDS) *Installation and operating manual*, Digital Vibration Controller DVC48, (Manual Number 805511, Edition 1, Amendment 3)

[5-3] **Cunningham, P.R.** and **White, R.G.** A new measurement technique for the estimation of core shear strain in closed sandwich structures. *Composite Structures*, 2001, **51**, 319-334.

[5-4] **Rao, Y.J.** In-fibre Bragg grating sensors. *Meas. Sci. Technol.*, 1997, **8**, 355-375

[5-5] **Collacott, R.A.** *Vibration monitoring and diagnosis*, 1979 (The Pitman Press, Bath)

[5-6] ENDEVCO, *Instrumentation catalog* (ENDEVCO® Corporation, USA)

[5-7] ICP® Accelerometer, *Installation and operating manual*, PCB Piezotronics Vibration Division

[5-8] Strain Gage, *Calibration Data*, (Tokyo Sokki Kenkyujo Co., Ltd.)

[5-9] **Brian, C.** and **Dakin, J.** *Optical fiber sensors: Component and subsystems, Volume three*, 1996 (Artech House, Inc.)

[5-10] **Dakin, J.** and **Brian, C.** *Optical fiber sensors: Applications, analysis and future trends, Volume four*, 1997 (Artech House, Inc.)

[5-11] ENDEVCO, *Model 28981A-Modal hammer set-manual* (ENDEVCO® Corporation)

CHAPTER 6: Isotropic Beam Structure

[6-1] ANSYS®, *User Manual*, 2002 (ANSYS, Inc.)

[6-2] ANSYS Help System, *Elements manual*, 2002 (ANSYS, Inc.)

[6-3] **Nashif, A.D., Jones, D.I.G.** and **Henderson, J.P.** *Vibration damping*, 1985 (John Wiley & Sons, Inc.)

[6-4] **Ewins, D.J.** *Modal testing: Theory and practice,* 1984 (2nd Edition, John Wiley & Sons, Inc.)

[6-5] **Connell, Mc.** *Vibration testing – Theory and practice,* 1995 (John Wiley & Sons, Inc.)

[6-6] MATLAB®, *Reference guide*, 1992 (The Math Works, Inc.)

CHAPTER 7: Laminated Composite Beam Structure

[7-1] **Sahin, M.** and **Shenoi, R.A.** Damage detection in FRP laminated beams using neural networks. *First European Workshop on Structural Health Monitoring, Proceeding of the First European Workshop*, Ecole Normale Superieure, Cachan (Paris), July 10-12, 2002, 726-733.

[7-2] **Sahin, M.** and **Shenoi, R.A.** Vibration-based damage identification in beam-like composite laminates by using artificial neural networks. *IMechE Part C, Journal of Mechanical Engineering Science*, 2003, **217**(6), 661-676.

[7-3] **Mallikarjuna** and **Kant, T.** Free vibration of symmetrically laminated plates using higher-order theory with finite element technique. *International Journal for Numerical Methods in Engineering,* 1989, **28**, 1875-1889.

[7-4] **Reddy, J.N.** and **Phan, N.D.** Stability and vibration of isotropic and laminated plates according to higher-order shear theory. *Journal of Sound and Vibration*, 1985, **98**, 157-170.

[7-5] **Demuth, H.** and **Beale, M.** *Neural network toolbox*, User's guide, Version 4, 2000, (The Math Works, Inc.)

CHAPTER 8: Experimental Validation of the Method

[8-1] **Sahin, M.** and **Shenoi, R.A.** Quantification and localisation of damage in beam-like structures by using artificial neural networks with experimental validation. *Engineering Structures*, 2003, **25**(14), 1785–1802.

CHAPTER 9: Sandwich Beam Structure

[9-1] Technical Data Sheet, ATC Chemical Corporation, www.atc-chem.com, 5.9.2003

[9-2] Product Information, SP Systems Composite Engineering Materials, http://www.spsystems.com/prodinfo.htm, 5.9.2003

[9-3] **Mall, S., Dosedel, S.B.**, and **Holl, M.W.** The performance of graphite-epoxy composite with embedded optical fibers under compression. *Smart Materials and Structures*, 1996, **5**(2), 209-215.

[9-4] **Greene, J.A., Tran, T.U., Bhatia, V., Gunther, M.F., Wang, A., Murphy, K.A.** and **Claus, O.** Optical fiber sensing technique for impact detection and location in composites and metal specimens. *Smart Materials and Structures*, 1995, **4**(2), 93-99.

APPENDICES

[B-1] **Hammond, J.K.** *Introduction to signal processing* (Lecture Notes), 2000, ISVR, University of Southampton.

[B-2] **Randall, R.B.** *Frequency analysis, B&K*, 1987 (C. Tech., B. A.)

[B-3] **Newland, D.E.** *An introduction to random vibrations and spectral analysis*, 1975 (Longman)

[E-1] **Smith, C.S.** *Design of marine structures in composite materials*, 1990, (Spon Press)

[G-1] **Crawley, E.F.** The natural modes of Graphite/epoxy cantilever plates and shells. *Journal of Composite Materials*, 1979, **13,** 195-205.

[G-2] **Nayak, A.K., Shenoi, R.A.** and **Moy, S.S.J.** Transient response of composite sandwich plates, *Composite Structures*, 2004, **64**(3-4), 249-267.

[G-3] **Crawley, E.F.** and **Dugundji, J.** Frequency determination and non-dimensionalization for composite cantilever plates, *Journal of Sound and Vibration*, 1980, **72**(1), 1-10.

[I-1] **Baird, D.C.** *Experimentation: An introduction to measurement theory and experiment design*, 1995 (Prentice-Hall, Inc.)

[I-2] **Meyer, S.L.** *Data analysis for scientists and engineers*, 1975 (John Wiley&Sons, Inc.)

APPENDICES

Appendix A FIBRE OPTIC BRAGG GRATING INTERROGATION SYSTEM

One of the important factor plays an important role during the dynamic strain measurements is the determination of the scanning frequency for the fibre optic Bragg grating interrogation system (FBGIS) so that it could scan multiple FBG sensors fast enough to capture high frequency excitation. Therefore, the intention of this appendix is to provide the dynamic strain measurement results obtained from sandwich cantilever beam and in this way to verify the dynamic measurement capabilities of the interrogation system and show its' limitations.

The sandwich beam used in the experiment has a length of 450mm and a width of 40.5mm with a total thickness of 14.6mm, which includes a core thickness of 12mm and a laminated skin thickness of 1.3mm on either side of the core. The laminated skin consists of four equal layers with a layer orientation of $[0/90]_s$. FBG sensors were embedded between the core and the upper laminated skin at 30mm, 70mm, 130mm and 170mm from the root in order to monitor dynamic strain along the beam. The cantilever sandwich beam is vibrated by random excitation and following strain histories (**Fig. A.1**) are recorded from the embedded FBG sensors individually. Then, FFT of the strain histories are calculated and shown in **Fig. A.2**. Sensors are numbered starting from the one closer to cantilever end of the beam.

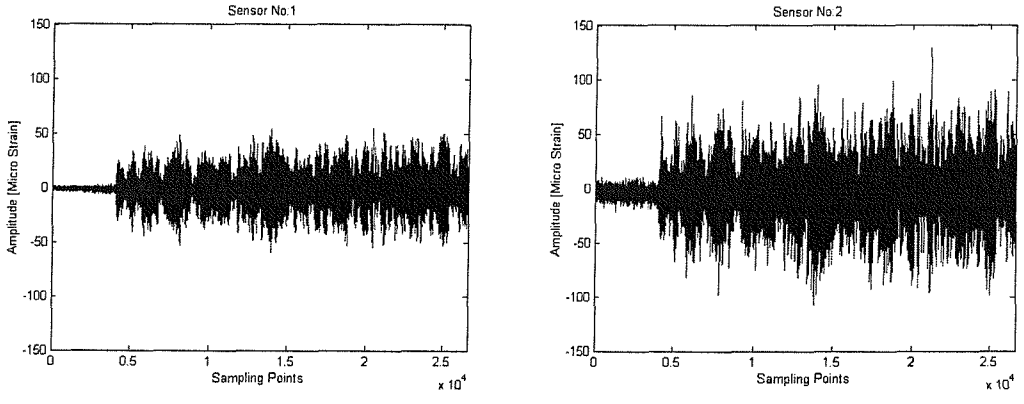

Fig. A.1 (continued over)

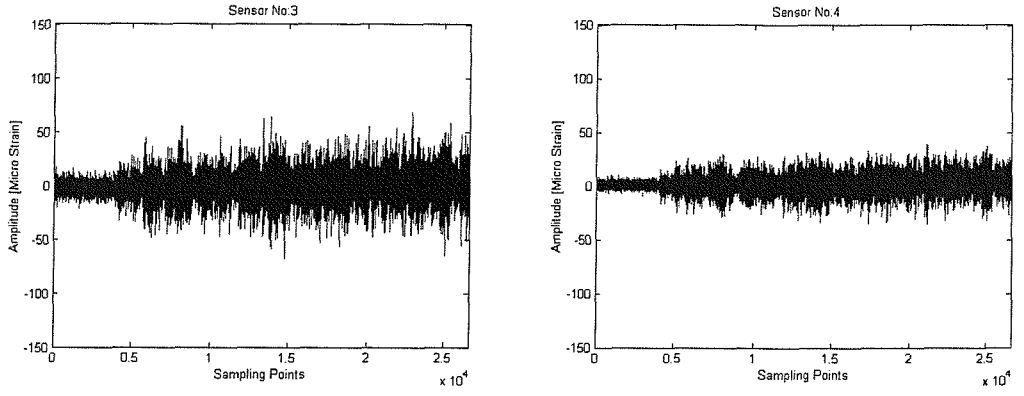

Figure A.1 Strain histories of four sensors.

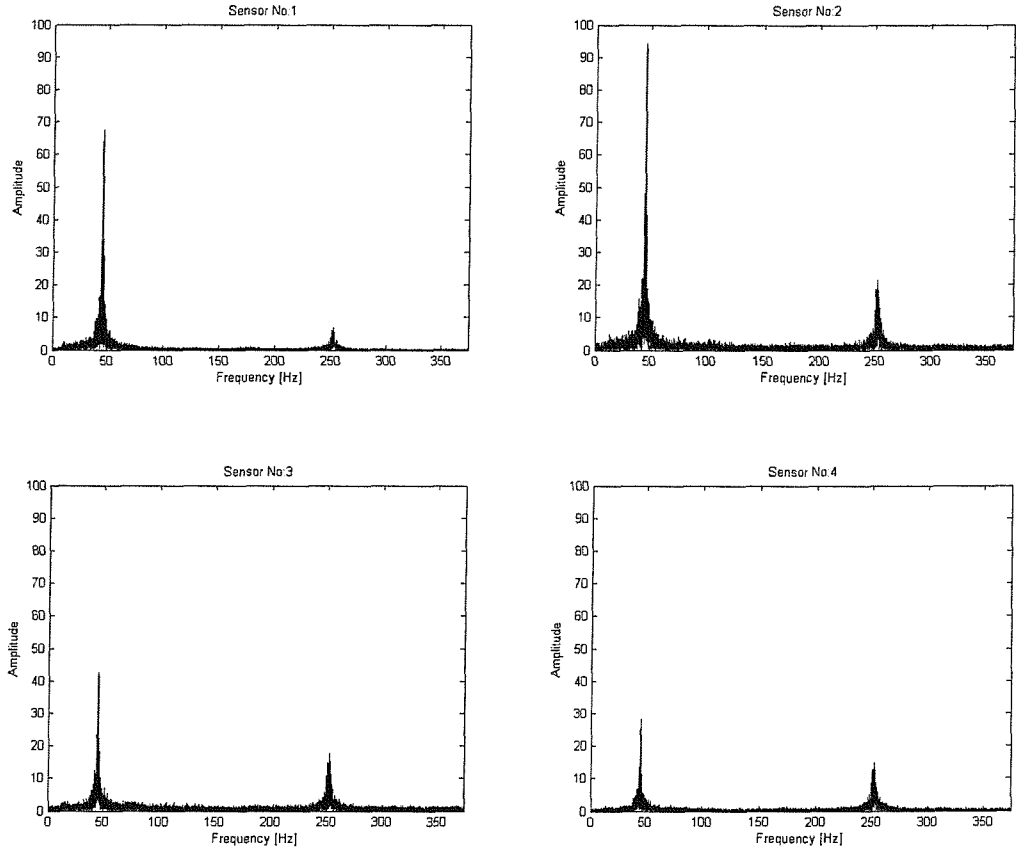

Figure A.2 Frequency spectrum of four sensors.

The frequency response (**Fig. A.3**) of the specimen under random excitation is also obtained from an accelerometer mounted near root of the beam. The numbers near each peak response indicate experimentally obtained resonant frequencies.

It can be seen from the **Fig. A.2** that the scanning rate of the FBGIS is capable of capturing the frequency content accurately from individual FBG strain sensors at excitation level just over 250Hz as the frequencies corresponding to maximum amplitude values match with the resonant frequencies obtained from the accelerometer (**Fig. A.3**). Therefore the interrogation system can be used for further experimental analysis aiming to measure dynamic strain from limited number of FBG strain sensors embedded into sandwich beam structure.

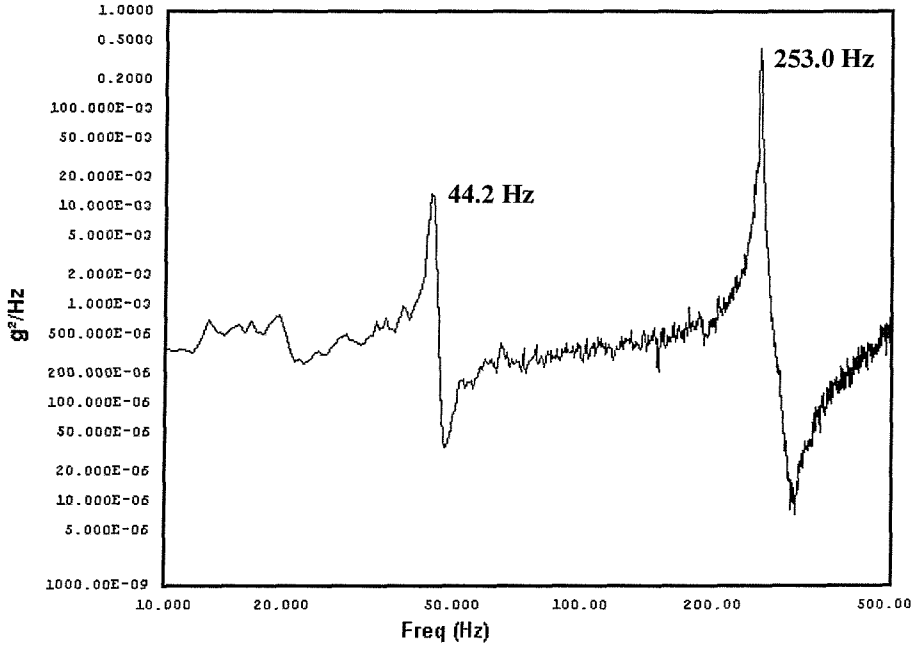

Figure A.3 Frequency response of a sandwich beam.

The following calculations show the steps followed to calculate the scanning frequency for the FBGIS with eight FBG strain sensors.

Scanning frequency for one point [Hz]: $f = \dfrac{(2 \cdot 10^9)}{[dioclk \times (36 + blanks)]}$

where;

dioclk [ns] = The digital clock set in the interrogation system = 500 (optimum)

blanks = The buffer spacing = 128 (optimum)

$$f = \frac{(2 \cdot 10^9)}{[500 \times (36+128)]} = 24.39 \cdot 10^3 \text{ Hz}$$

Scanning period for one point [s]: $t = \frac{1}{f}$

$$t = \frac{1}{24.39 \cdot 10^3} = 4.1 \cdot 10^{-5} \text{ s}$$

Scanning period for n number of FBG sensors [s]: $t_{\text{n sensors}} = 2 \cdot (n_t) \cdot (samppts) \cdot (dithpts) \cdot t$

where;

n = number of FBG sensors = 8

n_t = total number of FBG sensors including 2 reference gratings = n+2 = 10

samppts = the number of sampling points used to track the reflective peak of a particular Bragg grating = 2 (optimum)

dithpts = dither points to track the changes in the centre wavelength = 2

Scanning period for eight FBG sensors: $t_{8\,\text{sensors}} = 2 \cdot (10) \cdot (2) \cdot (2) \cdot 4.1 \cdot 10^{-5} = 3.28 \cdot 10^{-3}$ s

Scanning frequency for n number of FBG sensors [Hz]: $f_{\text{n sensors}} = \frac{1}{t_{\text{n sensors}}}$

Scanning frequency for eight FBG sensors: $f_{8\,\text{sensors}} = \frac{1}{3.28 \cdot 10^{-3}} = 304.878$ Hz

As the sampling frequency should be at least two times higher than the highest frequency of interest, interrogation system can be used with eight FBG strain sensors to obtain dynamic strain up to 150Hz that is much lower than the second resonant frequency of the sandwich beam specimen.

Appendix B MODAL AND STATIC STRAIN ANALYSIS OF SANDWICH BEAM SPECIMEN

In modal analysis part, the resonant frequencies of cantilever sandwich beam (450mm x 40.5mm x 14.6mm) are investigated by applying impact and frequency sweep type excitations and the corresponding response of the beam is monitored by using piezoelectric accelerometer. In static strain analysis part, the local strain value is obtained from an electrical resistance strain gauge and FBG strain sensors. Finally, both experimentally obtained dynamic and static analysis results are compared to FEA ones.

B.1 Modal Analysis

B.1.1 Estimation of Frequency Response Function

The mathematical basis of frequency analysis **[B-1, B-2, B-3, 6-4, 6-5]** is the Fourier Transform taking different forms that depends on the type of signal analysed. In this analysis, since the signal is discrete in both time and frequency domains, Discrete Fourier Transform (DFT) is used. Lets $g(t_n)$ be a sampled time function (or sequence), the forward transform of this signal is expressed as;

$$G(f_k) = \frac{1}{N}\sum_{n=0}^{N-1} g(t_n) e^{-j\frac{2\pi nk}{N}} \tag{B.1}$$

where N is the number of time samples (or frequency components) and $\frac{1}{N}$ is the simple scaling factor. In discrete Fourier transform, to obtain N number of frequency components, N^2 complex multiplication must be done. On the other hand, another calculation procedure, which is called as Fast Fourier Transform (FFT), provides the same result with a number of complex multiplications of the order $N\log_2 N$. This means, FFT algorithm reduces the computation time

drastically. The discretisation of the originally continuous time history can cause a phenomenon called aliasing where a high frequency signal is sampled and takes on the appearance of a lower frequency. To avoid aliasing, a sampling rate, f_s, which is given by $f_s = \frac{1}{\Delta t}$, can be chosen in such a way that it is at least two times greater than the cut-off (highest frequency of interest) frequency. Therefore, the upper frequency limit of a digital signal called Nyquist frequency (or folding frequency) is half of the sampling frequency and taken as 5000 Hz. Since, the first three bending natural frequencies are lower than 5 kHz, this value can be accepted as a cut-off frequency. Here Δt is the time interval and the reciprocal of the total time (t) gives the analysis resolution. All the values used during the analysis are tabulated in **Table B.1**.

Table B.1 Parameters used during the analysis

Parameters	Value
Time interval, Δt	0.0001 s
Total time, T	3 s
Total data recorded, N	30000
Sampling frequency, f_s	10000 Hz
Nyquist Frequency, $f_{c/o}$	5000 Hz
Analysis resolution, Δf	0.333 Hz

In dual-channel frequency analysis, there are two signals and for each signal the time function is transformed by using FFT algorithm to a complex spectrum. The squared amplitudes of a number of such instantaneous spectra are averaged in an averaging buffer to give the "auto-spectrum" for that particular signal (Eqs. B.2 and B.3). If the instantaneous spectra of both channels are used then "cross-spectrum" can be obtained by using equation (B.4). Another important parameter called coherence, the ratio of the square of the magnitude of the averaged cross-spectrum between the force and the response to the product of the averaged autospectra of the force and the response, gives a measure of the degree of the linear dependency between the two signals as a function of frequency (Eq. B.5).

$$S_{xx}(f) = \lim_{T\to\infty} E\frac{|X_T(f)|^2}{T} \tag{B.2}$$

$$S_{yy}(f) = \lim_{T\to\infty} E\frac{|Y_T(f)|^2}{T} \tag{B.3}$$

$$S_{xy}(f) = \lim_{T\to\infty} E\frac{\left|X_T^*(f)Y_T(f)\right|}{T} \tag{B.4}$$

$$0 \le \gamma_{xy}^2(f) = \frac{|S_{xy}(f)|^2}{S_{xx}(f).S_{yy}(f)} \le 1 \tag{B.5}$$

Uncorrelated Data ◄——— ———► Correlated Data

After obtaining cross- and auto-spectrums, the normalisation of the cross-spectrum with input and output auto-spectrum, $H_1(f)$ (Eq. B.6) and $H_2(f)$ (Eq. B.7) type estimators can be obtained respectively. On the other hand, $H_v(f)$ type estimator is based upon the concept of total least squares that is shown to be the maximum likelihood estimator for frequency response function $H(f)$ of a linear time-invariant system (Eq. B.8).

$$H_1(f) = \frac{S_{xy}(f)}{S_{xx}(f)} \tag{B.6}$$

$$H_2(f) = \frac{S_{yy}(f)}{S_{xy}^*(f)} \tag{B.7}$$

$$H_v(f) = \frac{S_{yy}(f) - \kappa(f)S_{xx}(f) + \sqrt{\Psi(f)}}{2S_{yx}(f)} \tag{B.8a}$$

$$\Psi(f) = \left[S_{xx}(f)\cdot\kappa(f) - S_{yy}(f)\right]^2 + 4\left|S_{xy}(f)\right|^2\cdot\kappa(f) \tag{B.8b}$$

$$\kappa(f) = \frac{S_{yy\_noise}(f)}{S_{xx\_noise}(f)} \tag{B.8c}$$

Figure B.1 shows the schematic representation of obtaining frequency response function estimators.

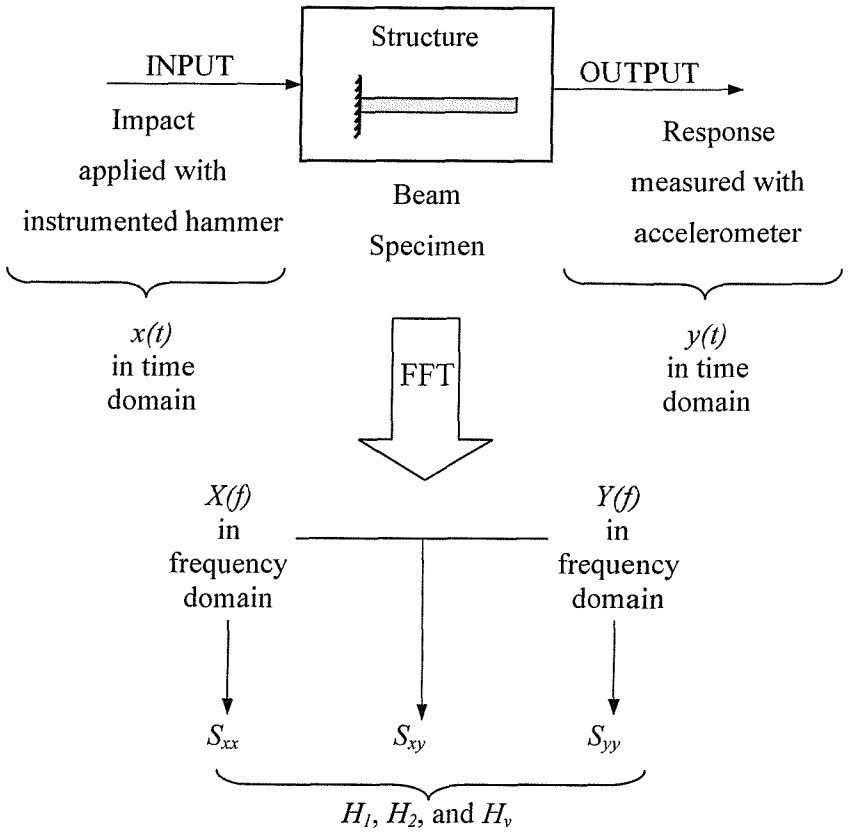

Figure B.1 Schematic representation of calculating the frequency response function estimators

B.1.2 Experimental Resonant Frequencies from Estimators

The first three vertical and two horizontal bending resonant frequencies are obtained by using impact hammer and monitoring the response from a piezoelectric accelerometer mounted to tip of the beam. **Figures B-2** and **B-3** show force and acceleration time histories, calculated estimators and coherence in the estimation of vertical and horizontal resonant frequencies of the cantilever sandwich beam respectively. **Table B.2** presents these resonant frequencies in a tabulated form.

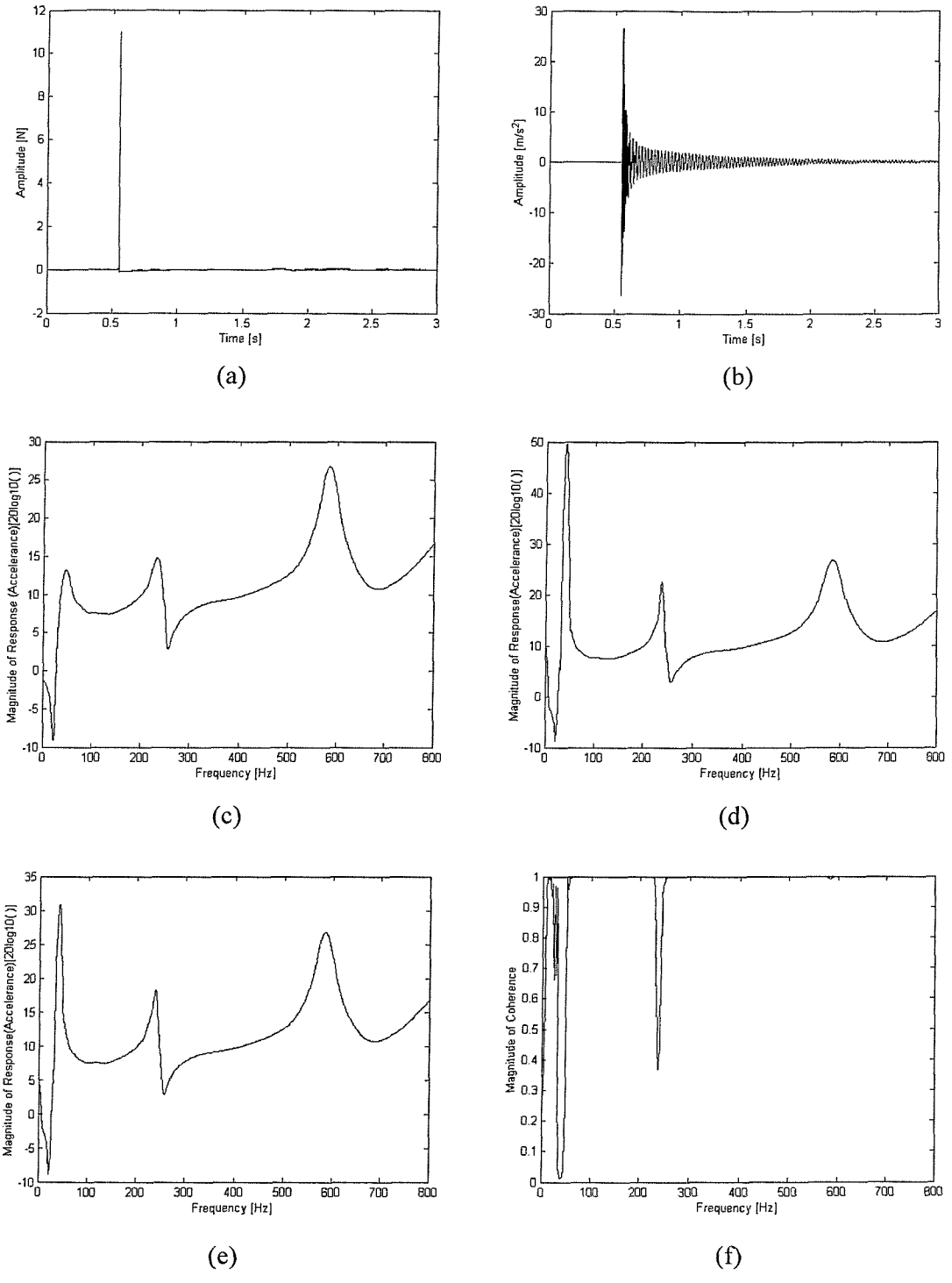

Figure B.2 Vertical bending resonant frequency estimation

(a) Force time history (b) Acceleration time history

(c) H_1 estimator (d) H_2 estimator (e) H_v estimator (f) Coherence

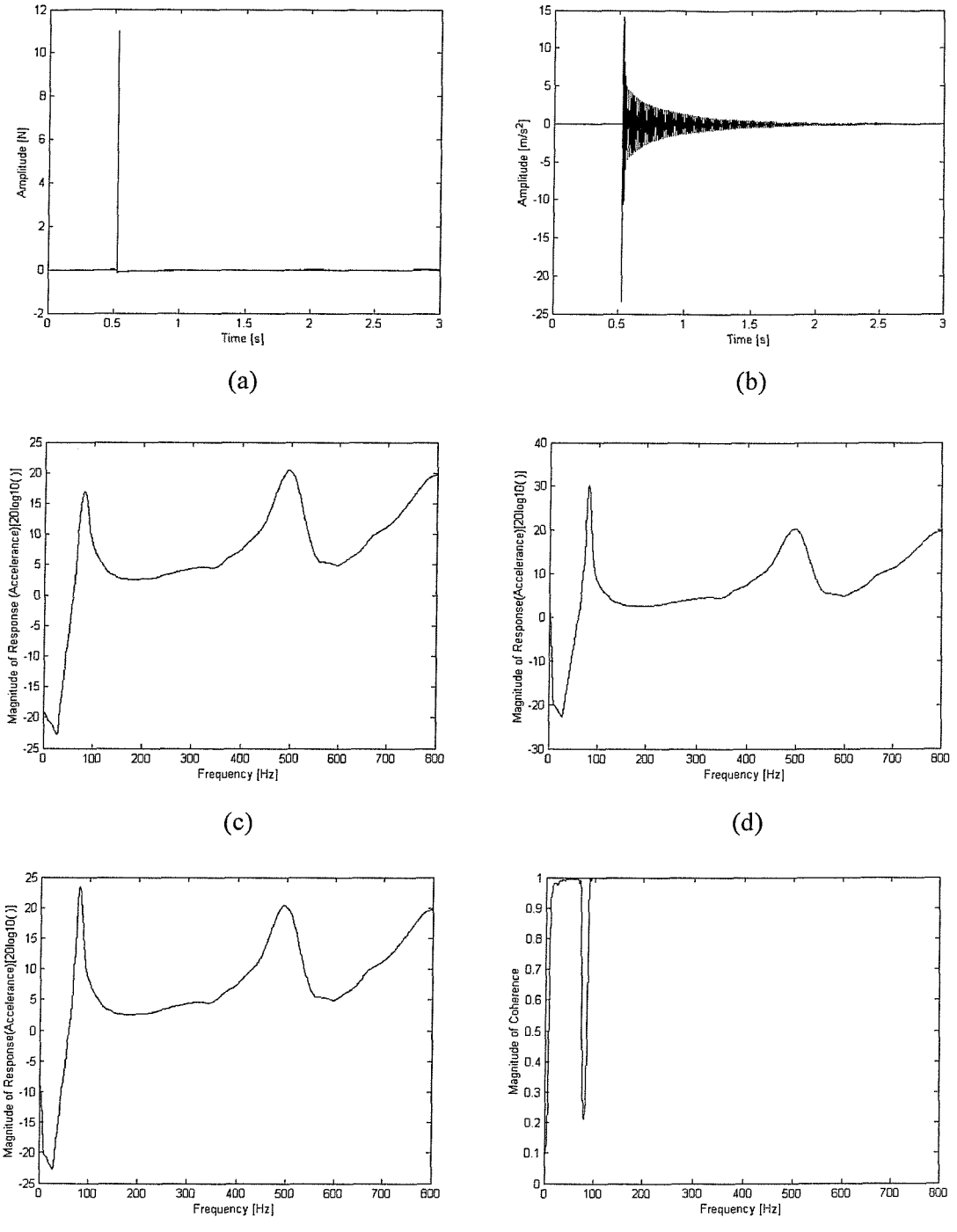

Figure B.3 Horizontal bending resonant frequency estimation

(a) Force time history (b) Acceleration time history

(c) H_1 estimator (d) H_2 estimator (e) H_v estimator (f) Coherence

Table B.2 Resonant frequencies from estimators

Mode No	Resonant Frequencies [Hz]
1st Vertical Bending	41.0
1st Horizontal Bending	80.0
2nd Vertical Bending	238.0
2nd Horizontal Bending	496.0
3rd Vertical Bending	584.0

B.1.3 Experimental Resonant Frequencies from Frequency Sweep

In the second part of the modal analysis, resonant frequencies are estimated by sweeping the frequency via electro-dynamic shaker in the frequency range of 10Hz to 810Hz (for the first three vertical bending resonant frequencies), 5Hz to 125Hz (for the first horizontal bending resonant frequency) and 185Hz to 515Hz (for the second horizontal bending resonant frequency). The corresponding frequency responses are shown in **Figs. B.4** to **B.6** and the resonant frequencies are tabulated in **Table B.3**.

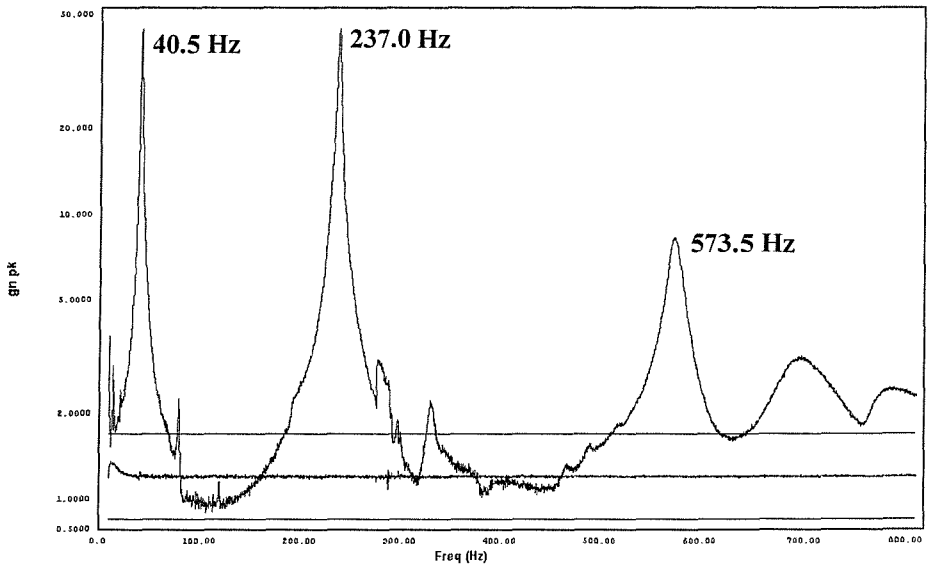

Figure B.4 Vertical frequency response of sandwich beam (10 Hz to 810 Hz)

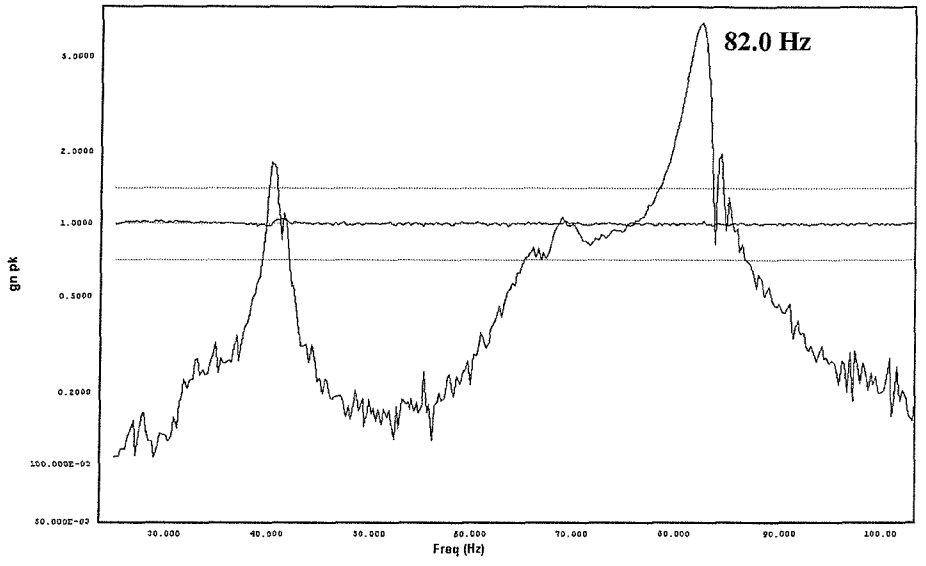

Figure B.5 Horizontal frequency response of sandwich beam (5 Hz to 125 Hz)

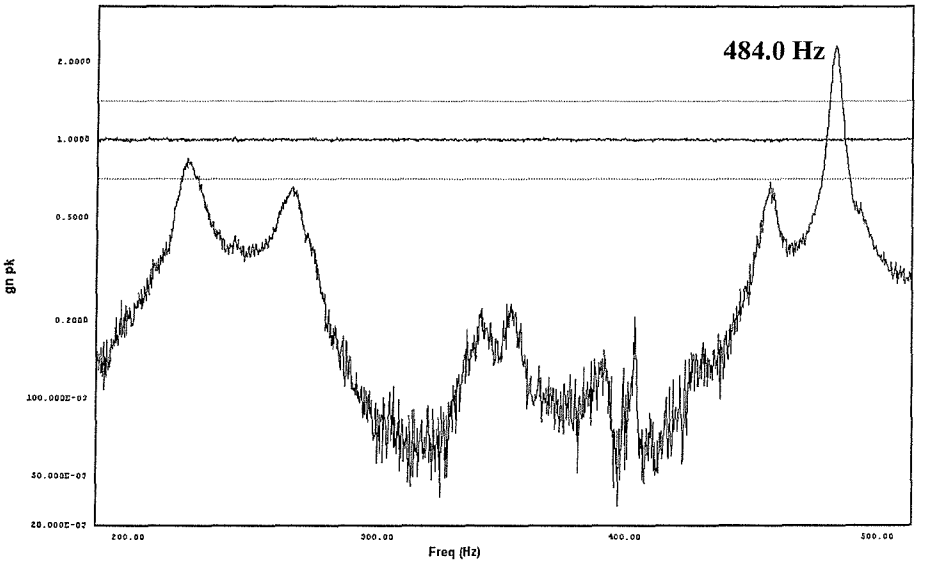

Figure B.6 Horizontal frequency response of sandwich beam (185 Hz to 515 Hz)

Table B.3 Resonant frequencies from frequency sweep

Mode No	Resonant Frequencies [Hz]
1st Vertical Bending	40.5
1st Horizontal Bending	82.0
2nd Vertical Bending	237.0
2nd Horizontal Bending	484.0
3rd Vertical Bending	573.5

B.1.4 Natural Frequencies from FEA

The normal mode dynamic analysis is performed on FEM of cantilever sandwich beam. The details about the modelling of the beam, geometrical and material properties, selection of element type and boundary condition effect are given in Appendices E, G and H. The first six natural frequencies obtained from FEA are tabulated in **Table B.4**.

Table B.4 Natural frequencies from FEA

Mode No	Natural Frequencies [Hz]
1st Vertical Bending	45.865
1st Horizontal Bending	82.840
2nd Vertical Bending	249.901
Torsion	275.161
2nd Horizontal Bending	484.809
3rd Vertical Bending	591.268

In order to investigate the effect of the 4-gram piezoelectric accelerometer mounted at the tip of the beam, a concentrated mass is modelled by using MASS21 type of element in the FEM. The natural frequencies of the sandwich beam with the existence of concentrated mass are given in a tabulated form in **Table B.5**.

Table B.5 Natural frequencies from FEA with 4-gram mass

Mode No	Natural Frequencies [Hz]
1st Vertical Bending	43.390
1st Horizontal Bending	78.315
2nd Vertical Bending	239.483
Torsion	272.704
2nd Horizontal Bending	464.032
3rd Vertical Bending	570.669

B.2 Static Strain Analysis

B.2.1 Measurements by Strain Gauge

In order to verify FEM of the sandwich beam, the static strain analysis is performed by bonding a strain gauge to upper surface of the structure on the centre line at location of 100mm away from the root. A static load of 1000-gram is applied from the tip of the beam. A single element electrical resistance gauge (FLA 3-23) with gauge length of 3mm, nominal resistance of 120 Ω ± 0.3 and a gauge factor of 2.15 is used to measure the strain on the surface of the beam. The strain gauge and the beam structure can be seen in **Fig. B.7**. The local strain is calculated by using equations (5.1) and (5.2) as:

$$\varepsilon_{x=100\,\mathrm{mm}|_{\,\mathrm{experimental}}} = 295.81\,\mu\varepsilon$$

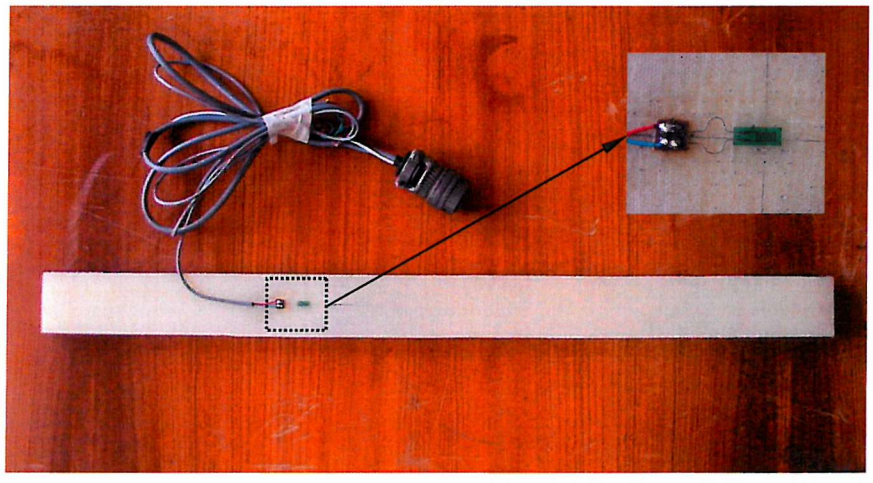

Figure B.7 Sandwich beam with surface bonded electrical strain gauge

Same FEM used in dynamic analysis is chosen for the analysis of the static strain under 9.81N point force in negative Z direction creating a tension on the upper surface of the cantilever sandwich beam. **Figure B.8** shows the beam model and strain distribution along the beam length. The nodal strain in X direction at location of 100mm away from the root of the beam is also obtained for the sake of comparison as this is the location where the strain gauge is bonded to the test specimen.

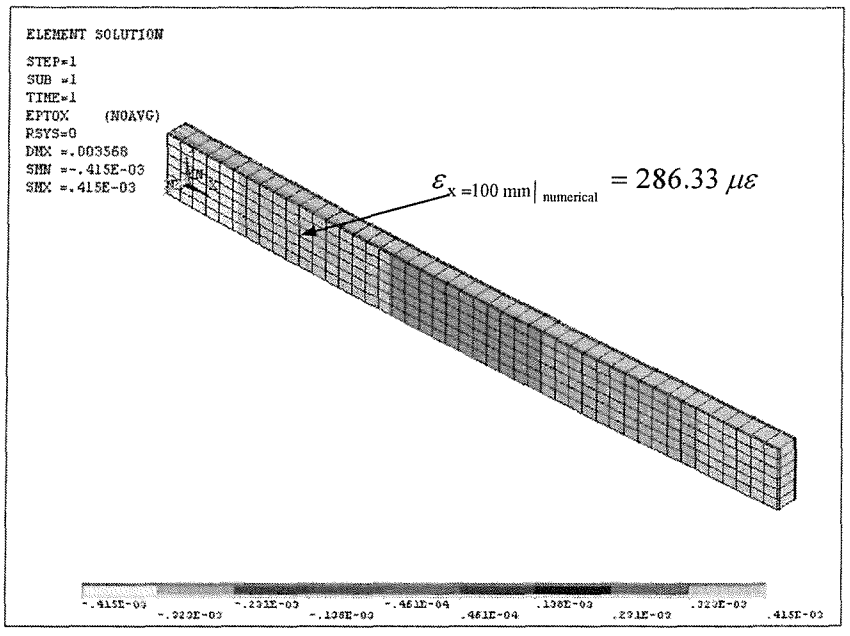

Figure B.8 Strain distribution along the sandwich beam

The difference between experimental and numerical local strain (i.e. 9.48 $\mu\varepsilon$) is due to the estimated material properties in FEM, misalignment of the electrical strain gauge from the centre line of the beam and the adhesive bonding between the electrical strain gauge and the surface of the beam.

B.2.2 Measurements by FBG Strain Sensors

An analysis was carried out to establish the ability and accuracy of the FBGIS to measure strain under static loading conditions. It involved setting up a cantilever sandwich beam containing six FBG strain sensors located between the core and GFRP laminated skin at 30mm, 70mm, 130mm, 170mm, 210mm and 260mm from the cantilever end. A number of weights were applied to the tip of the beam in order to obtain its static curvature shape and the resulting strain was measured using the FBGIS. **Figure B.9a** shows a comparison of the measured normalised strain, with respect to the first sensor measurement, under four different static loads (i.e. 1kg, 1.1kg, 1.2kg and 1.3kg) with the results obtained from FEA simulation of a similar sandwich beam.

It can be seen from **Fig. B.9a** that the FBG sensors exhibit the same behaviour under different loading conditions proving the repeatability of the measurement process within the elastic deformation range of the beam. Even though the FBG measurements do not exactly

match with the linear profile of the FEA result, the measurements are evenly distributed around it. A linear regression analysis is also performed on the FBG results (**Fig. B.9b**) and it indicates a close match with the profile of the FEA analysis.

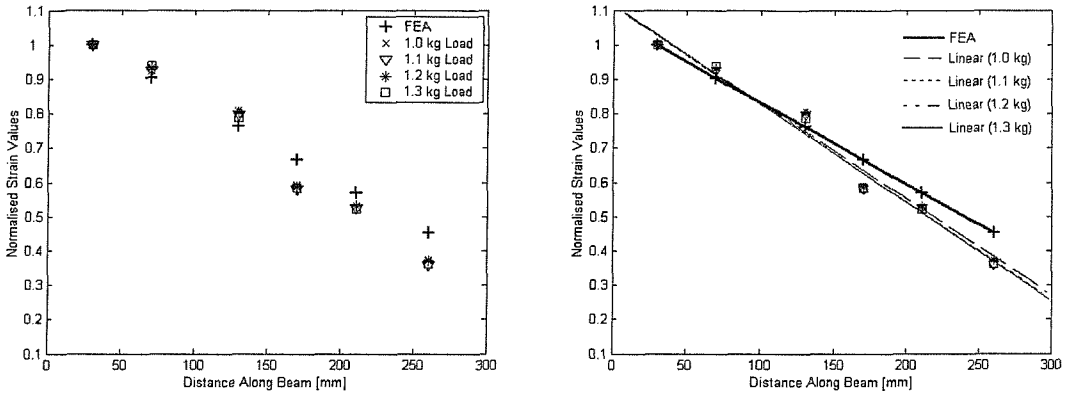

(a) (b)

Figure B.9 Comparison of FBG strain sensor measurements with FEA
(a) Normalised strain values for different static load (b) Linear regression curves

The slight deviation from the ideal FEA profile can be the result of many factors. Primarily it can be attributed to the manufacturing process. This involves initial bonding of the fibre containing the FBG sensors to the core creating resin rich area before the final infusion process takes place. Therefore, when the final manufacturing step is taken and the resin is infused, some areas of the optical fibre come into contact with the GFRP skin and some areas come into contact with the foam core. Consequently, this type of coupling is not represented in the FEM as it assumes perfect coupling between the GFRP skin and the core. Hence, there would be a discrepancy between the measured FBG strain sensor results and the FEA ones.

Appendix C EFFECTS OF MULTIPLE MODES ON PREDICTIONS OF ARTIFICIAL NEURAL NETWORKS

The aim of this appendix is to present the effects of multiple modes on predictions of ANNs. The features extracted from individual modes of vibration are introduced to single hidden layer ANNs that have been trained and tested by using noise-free data sets in Chapter 7, section 7.5.1. **Table C.1** shows the tabulated form of the ANNs used during the analysis.

Table C.1 ANN architectures and input-output pairs

	Input	Output	Architecture	Epoch
1.	RNF (1^{st} Mode only)	DS	1:6:1	2000
2.	RNF (1^{st} and 2^{nd} Modes)	DS	2:6:1	2000
3.	RNF (1^{st}, 2^{nd} and 3^{rd} Modes)	DS	3:6:1	2000
4.	MADC (1^{st} Mode only)	DL	1:6:1	2000
5.	MADC (1^{st} and 2^{nd} Modes)	DL	2:6:1	2000
6.	MADC (1^{st}, 2^{nd} and 3^{rd} Modes)	DL	3:6:1	2000
7.	MADC&LOC (1^{st} Mode only)	DL	2:9:1	2000
8.	MADC&LOC (1^{st} and 2^{nd} Modes)	DL	4:9:1	2000
9.	MADC&LOC (1^{st}, 2^{nd} and 3^{rd} Modes)	DL	6:9:1	2000
10.	RNF&MADC&LOC (1^{st} Mode only)	DS&DL	3:18:2	4000
11.	RNF&MADC&LOC (1^{st} and 2^{nd} Modes)	DS&DL	6:18:2	4000
12.	RNF&MADC&LOC (1^{st}, 2^{nd} and 3^{rd} Modes)	DS&DL	9:18:2	4000

As it can be seen from **Table C.1** that mainly four ANNs are trained. In order to make the comparison easy in the generalisation of ANNs, the number of epochs are kept constant (i.e. 2000) when RNF, MADC and MADC&LOC are introduced as input features. Since RNF&MADC&LOC (10^{th}, 11^{th} and 12^{th} ANNs in **Table C.1**) has large number of input data compared to other ANNs, number of epoch is set to 4000 for these three networks. **Figures C.1-12** show severity and location predictions of ANNs with different input and output pairs.

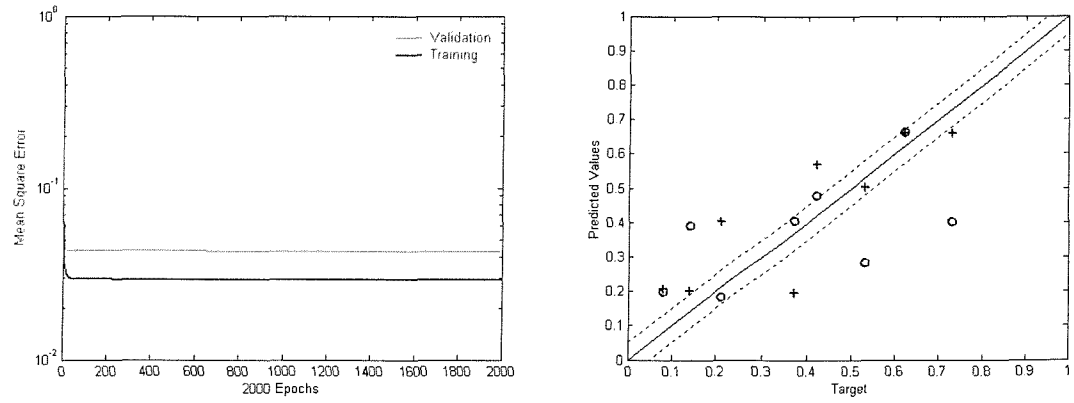

(a) (b)

Figure C.1 ANN results for severity predictions. Input: RNF (1st Mode only) and Output: DS (a) Mean square error with number of epochs (b) Severity predictions

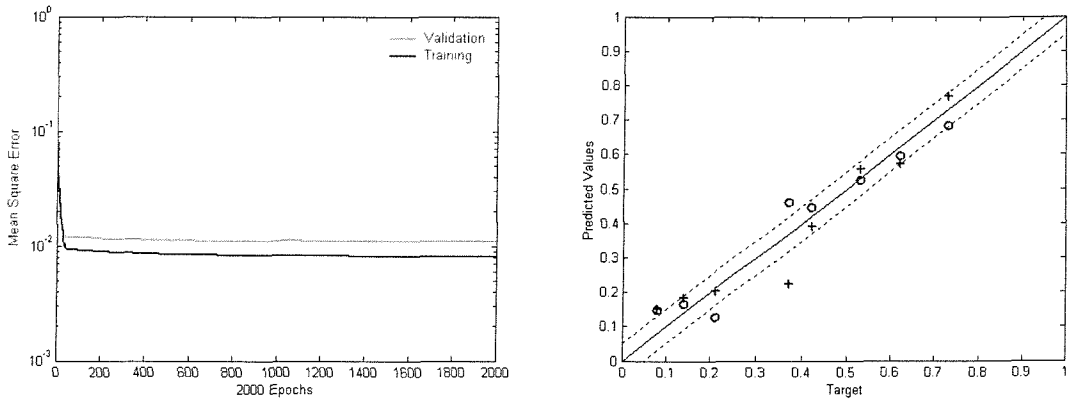

(a) (b)

Figure C.2 ANN results for severity predictions. Input: RNF (1st and 2nd Modes) and Output: DS (a) Mean square error with number of epochs (b) Severity predictions

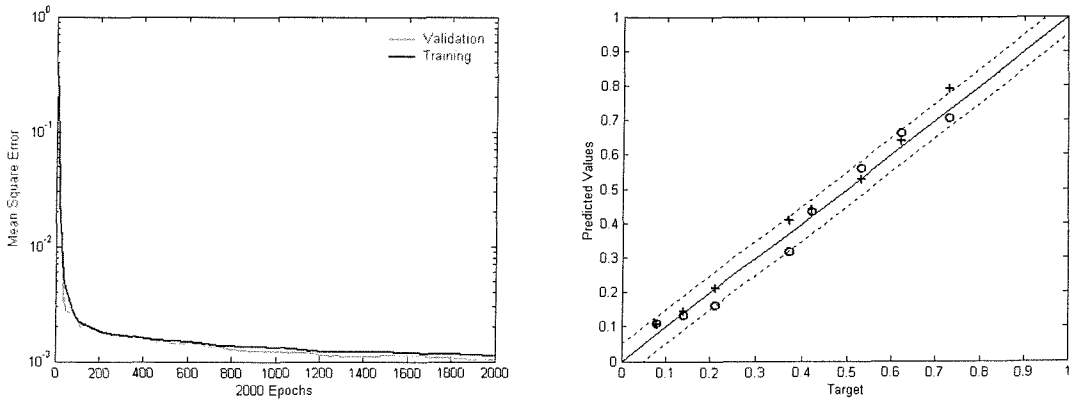

(a) (b)

Figure C.3 ANN results for severity predictions. Input: RNF (1st, 2nd and 3rd Modes) and Output: DS (a) Mean square error with number of epochs (b) Severity predictions

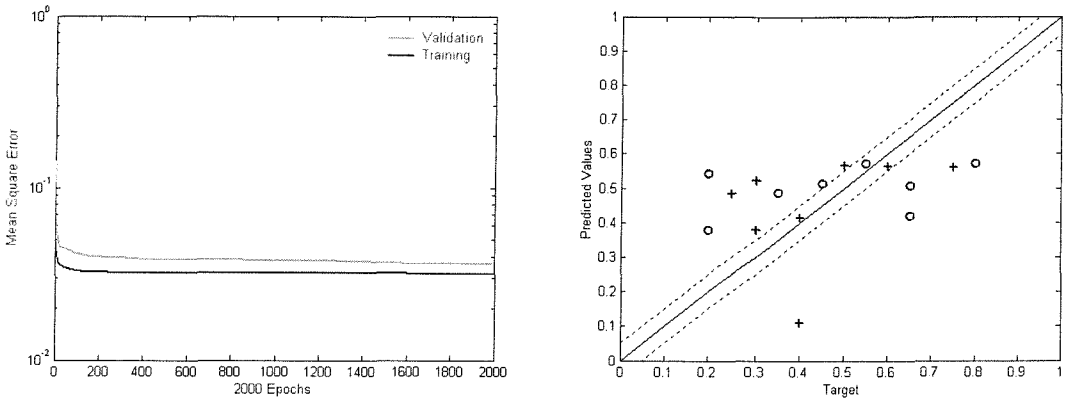

(a) (b)

Figure C.4 ANN results for location predictions. Input: MADC (1st Mode only) and Output: DL (a) Mean square error with number of epochs (b) Location predictions

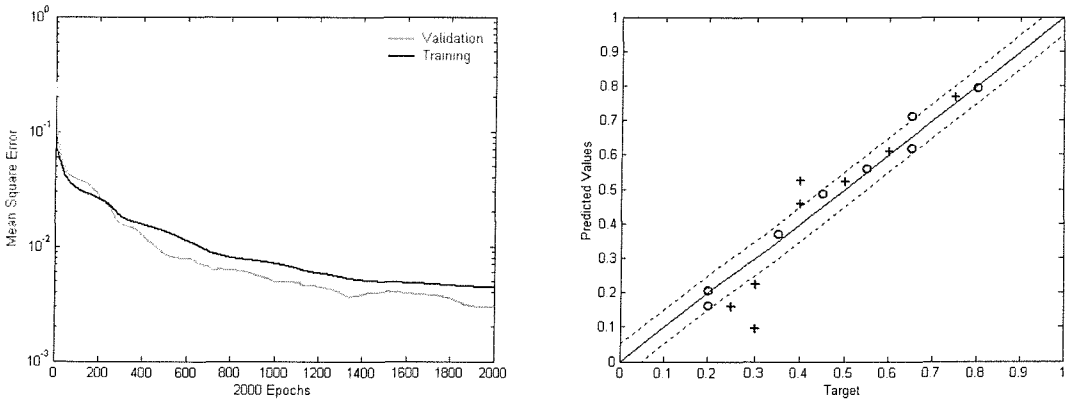

(a) (b)

Figure C.5 ANN results for location predictions. Input: MADC (1st and 2nd Modes) and Output: DL (a) Mean square error with number of epochs (b) Location predictions

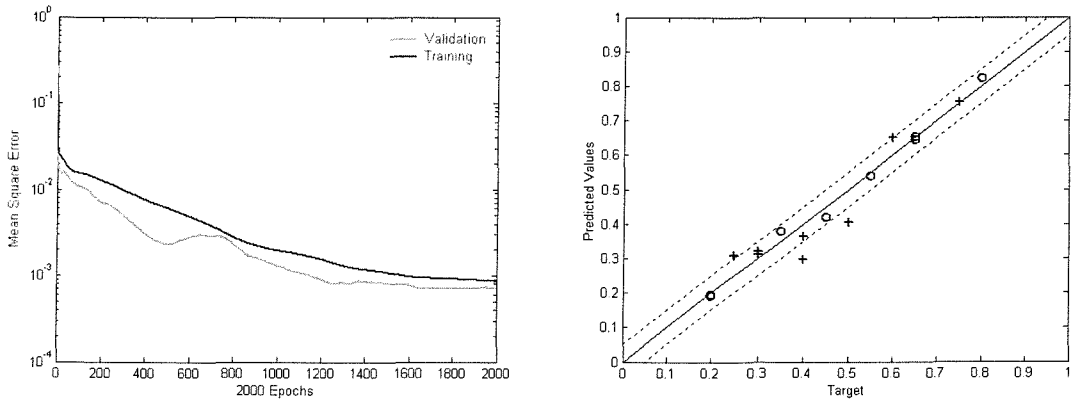

(a) (b)

Figure C.6 ANN results for location predictions. Input: MADC (1st, 2nd and 3rd Modes) and Output: DL (a) Mean square error with number of epochs (b) Location predictions

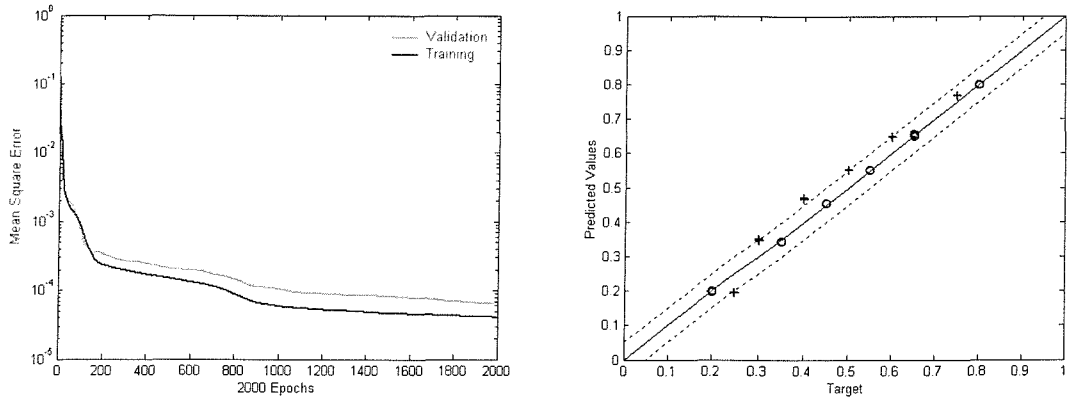

(a) (b)

Figure C.7 ANN results for location predictions. Input: MADC&LOC (1st Mode only) and Output: DL (a) Mean square error with number of epochs (b) Location predictions

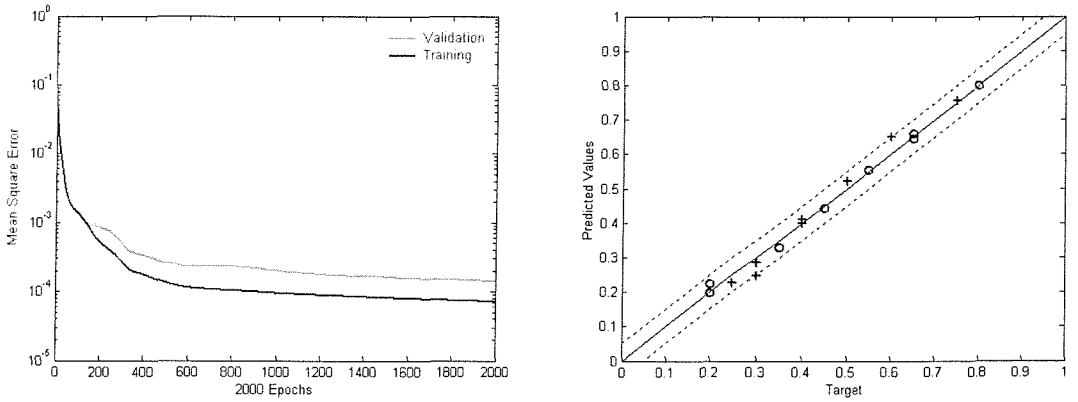

(a) (b)

Figure C.8 ANN results for location predictions. Input: MADC&LOC (1st and 2nd Modes) and Output: DL (a) Mean square error with number of epochs (b) Location predictions

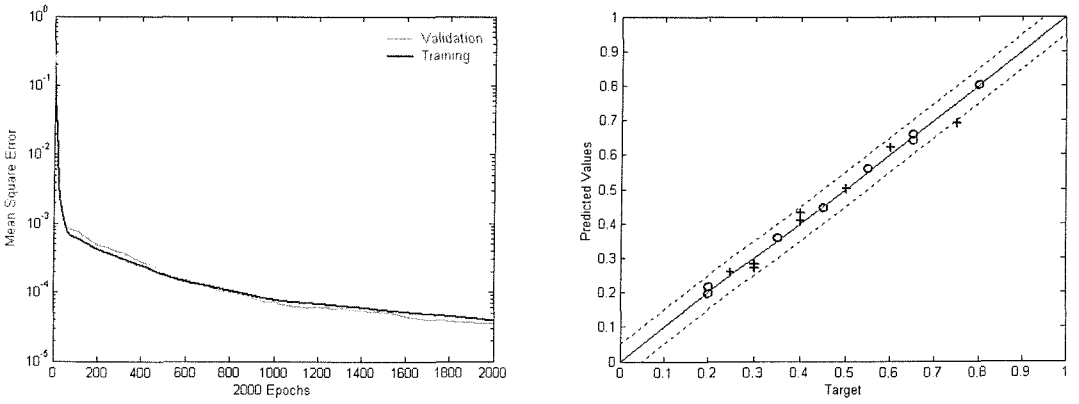

(a) (b)

Figure C.9 ANN results for location predictions. Input: MADC&LOC (1st, 2nd and 3rd Modes) and Output: DL (a) Mean square error with number of epochs (b) Location predictions

In the first set of training and test runs (ANNs No:1, 2 and 3 in **Table C.1**), RNF, which is obtained from 1st mode, combination of 1st and 2nd modes and all three modes, was used input feature for DS prediction. As it can be seen from **Figs. C.1** to **C.3**, the predictions are in acceptable 5% deviation range from the target values when multiple modes are introduced. Moreover, a continuous decrease was achieved in MSE value (2000 number of epochs) from single mode input to all three modes (**Figs. C.1a-3a**).

The second set of training and test runs (ANNs No:4, 5 and 6 in **Table C.1**) was performed by using maximum absolute differences in curvature (MADC) mode shape data. Since the input data (i.e. information from 1st mode only) was not enough for complete generalisation, the predictions regarding DL showed large variation from the target values. MSE reached to an approximate value of $3.2 \cdot 10^{-2}$ after 2000 epochs (**Fig. C.4a**).

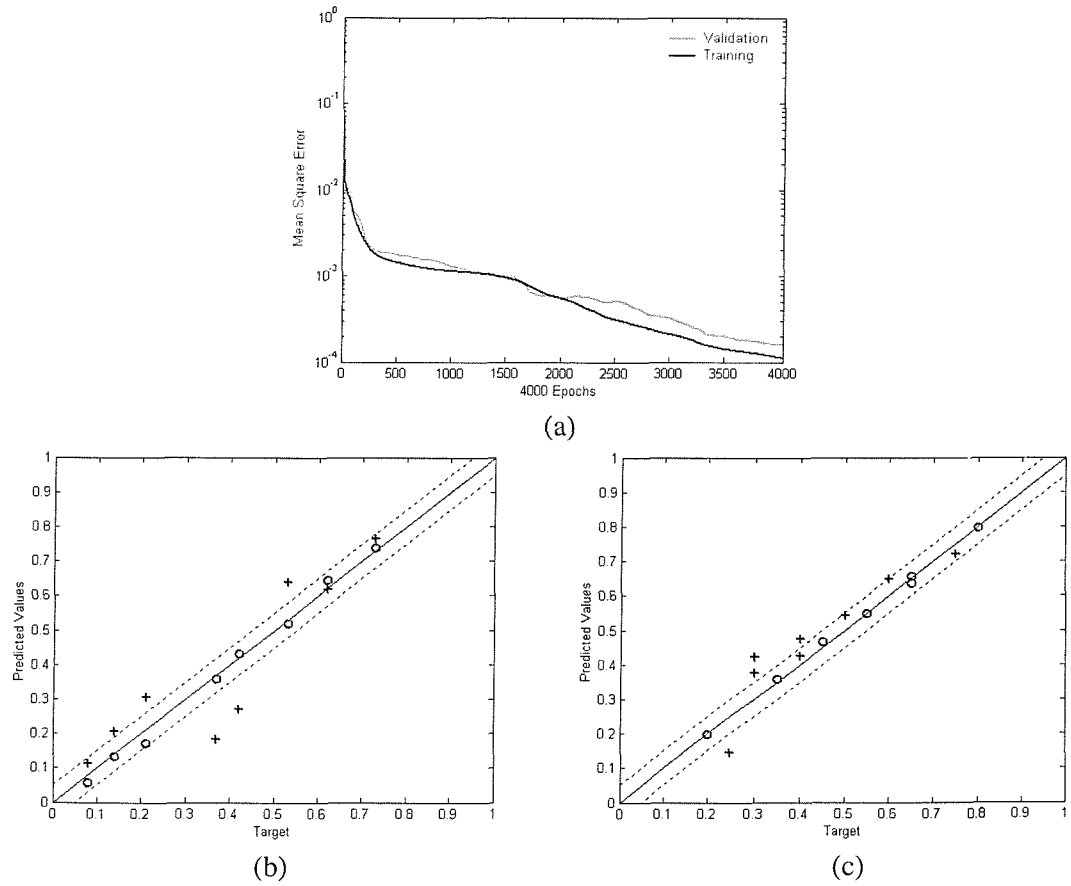

Figure C.10 ANN results for location and severity prediction. Input:RNF&MADC&LOC (1st Mode only) and Output: DS&DL (a) Mean square error with number of epochs (b) Severity predictions (c) Location predictions

Introducing of MADC obtained from both 1st and 2nd modes improved generalisation (**Fig. C.5b**) by pulling MSE down to $4.4 \cdot 10^{-3}$ (**Fig. C.5a**). Finally, MADC from all three modes of vibration was used as input for DL predictions and MSE converged to its lowest value of $8.6 \cdot 10^{-4}$ as it can be seen from **Fig. C.6a**. The corresponding DL predictions are shown in **Fig. C.6b**.

The improvement in DL predictions was achieved by addition of location information to MADC. That means, MADC&LOC was used in the third set of training and test runs (ANNs No:7, 8 and 9 in **Table C.1**). MSE values were reduced to 10^{-4} (**Figs. C.7a-9a**) and almost all predictions laid within 5% limit by providing better generalisation compared to the ones obtained from ANNs No:4, 5 and 6 in **Table C.1**.

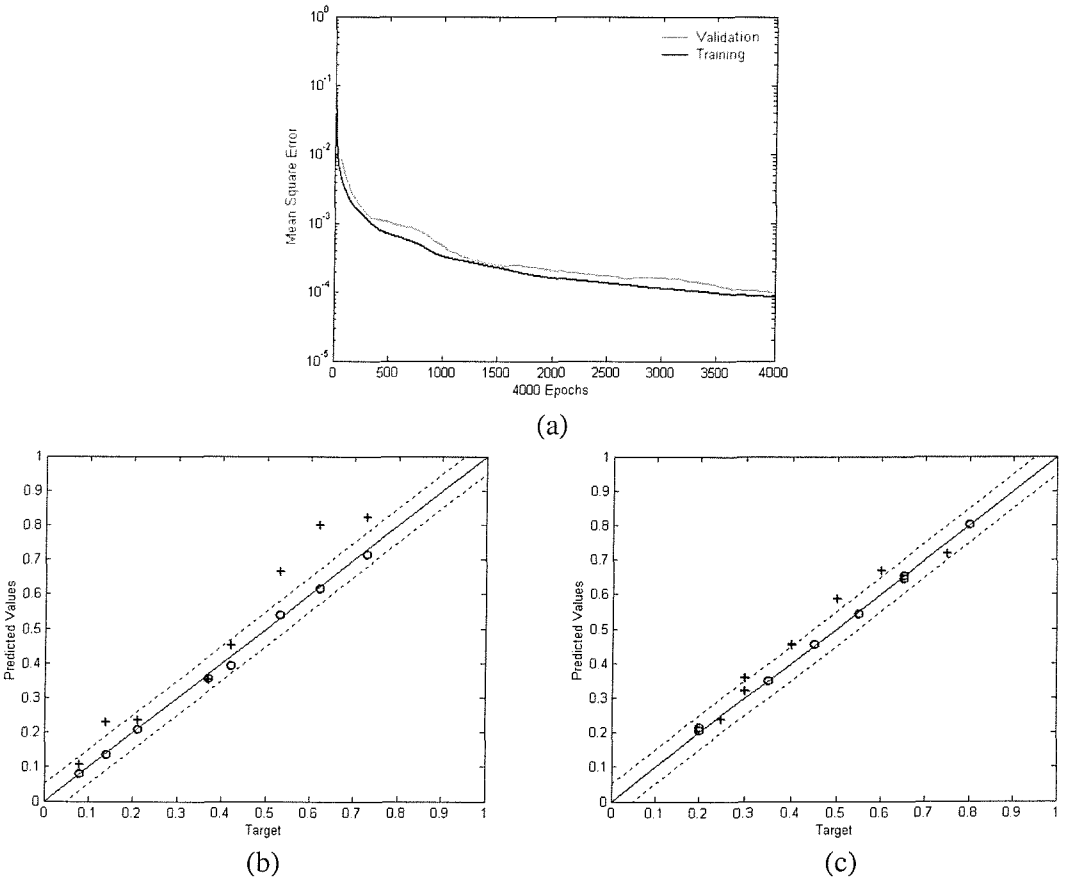

Figure C.11 ANN results for location and severity predictions. Input:RNF&MADC&LOC (1st and 2nd Modes) and Output: DS&DL (a) Mean square error with number of epochs (b) Severity predictions (c) Location predictions

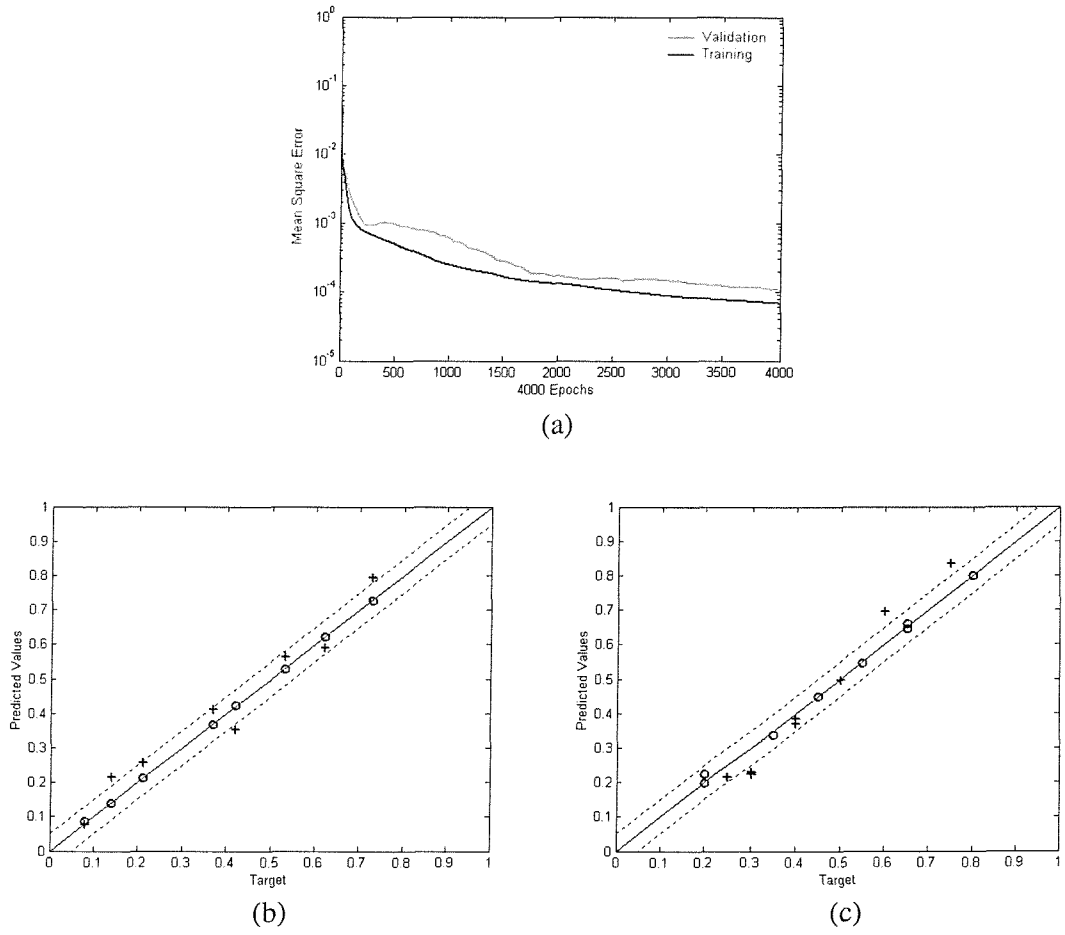

Figure C.12 ANN results for location and severity predictions. Input:RNF&MADC&LOC (1st, 2nd and 3rd Modes) and Output: DS&DL (a) Mean square error with number of epochs (b) Severity predictions (c) Location predictions

The final set of networks (ANNs No:10, 11 and 12 in **Table C.1**) involved in training and test runs used RNF&MADC&LOC as input parameter for both DS and DL predictions. In this case, there are slight over and under estimations in DS predictions (**Figs. C.10b-12b**) which were improved by including higher modes. Considering DL predictions, the outputs are closer to target values with acceptable deviations (**Figs. C.10c-12c**).

Appendix D DESIGN OF ARTIFICIAL NEURAL NETWORK ARCHITECTURE

The aim of this section is to present a comparative study performed on ANNs that have different number of hidden layers with different number of neuron combinations in each hidden layer. During the analysis, ANNs with two hidden layers are designed, tested for damage detection and their predictions are compared with each other and the ANNs with single hidden layer used in Chapter7, section 7.5.1. All ANNs in this section trained by using noise-free data sets. **Figures D.1** and **D.2** show the schematic view of one and two-layer ANNs designed by using MATLAB® Neural Network Toolbox **[7-5]** respectively.

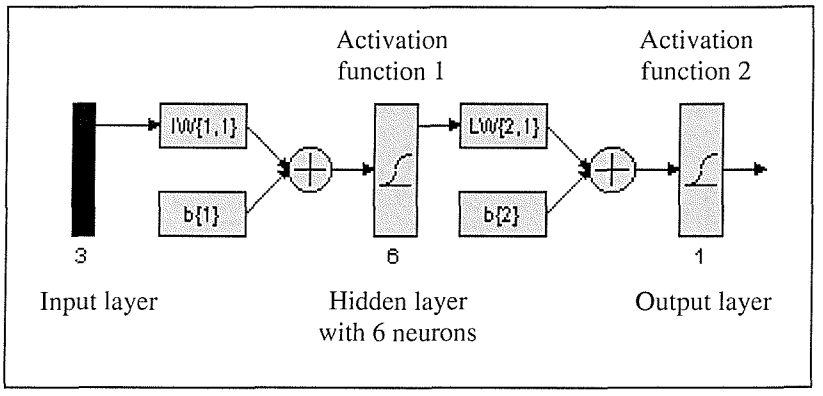

Figure D.1 ANN with single hidden layer (Architecture 3:6:1)

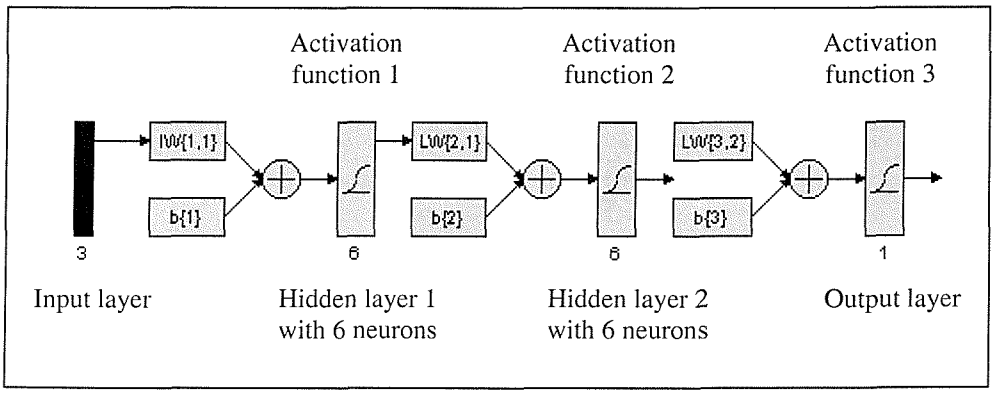

Figure D.2 ANN with two hidden layers (Architecture 3:6:6:1)

The detail information about the input-output (**Table 7.2**) and the test (**Table 7.4**) data sets are already given in Chapter 7, sections 7.4 and 7.5. Only the ANNs showed best performance during the training are selected for two-hidden-layer architecture applications. All ANNs used during the analysis are tabulated in **Table D.1**.

Table D.1 ANN architectures with two hidden layers

	Input	Output	Architecture	Number of Epoch
1.	RNF	DS	3:6:6:1	10000
2.	RNF	DS	3:6:6:1	2001
3.	RNF	DS	3:6:3:1	10000
4.	RNF	DS	3:6:3:1	3150
5.	MADC&LOC	DL	6:9:9:1	10000
6.	MADC&LOC	DL	6:9:9:1	1351
7.	MADC&LOC	DL	6:9:6:1	10000
8.	MADC&LOC	DL	6:9:6:1	1001
9.	RNF&MADC&LOC	DS&DL	9:18:18:2	10000
10.	RNF&MADC&LOC	DS&DL	9:18:18:2	2401
11.	RNF&MADC&LOC	DS&DL	9:18:9:2	10000
12.	RNF&MADC&LOC	DS&DL	9:18:9:2	3201

The first four ANNs use reduction in natural frequency (RNF) as an input for the damage severity (DS) predictions. The performance of these ANNs during the training process and their severity predictions can be seen from **Figs. D.3** to **D.6**.

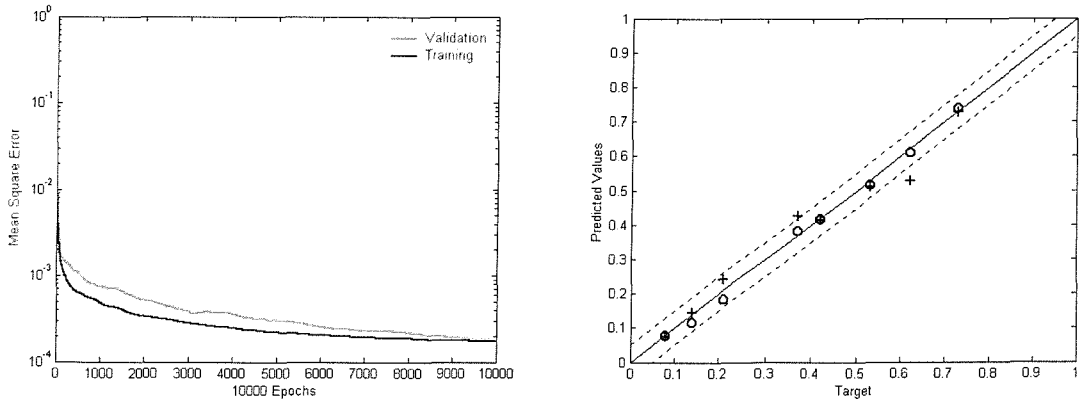

(a) (b)

Figure D.3 ANN (3:6:6:1) results for severity predictions (Input:RNF, Output:DS)
(a) Mean square error with 10000 number of epochs (b) Severity predictions

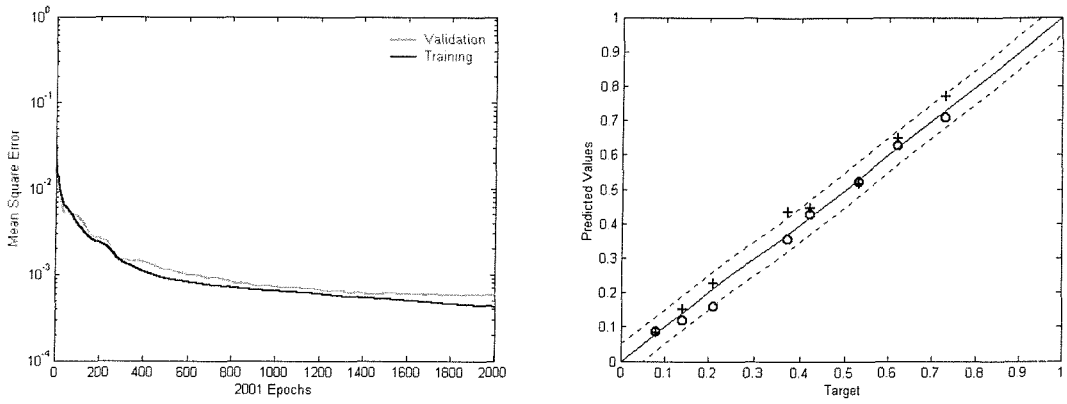

(a) (b)

Figure D.4 ANN (3:6:6:1) results for severity predictions (Input:RNF, Output:DS)
(a) Mean square error with 2001 number of epochs (b) Severity predictions

It can be concluded from **Figs. D.3** and **D.4** that early stopping (i.e. 2001 epochs) in the training provides acceptable accuracy in the predictions (1st and 2nd ANNs in **Table D.1**) when RNF-DS is used with two-hidden-layer ANN that has equal number of neurons in each hidden layer. When the number of neurons in the second hidden layer is reduced to half (3rd and 4th ANNs in **Table D.1**), the predictions of the ANN trained for higher number of epochs are better than that of the one trained up to 3151 number of epochs. **Figures D.5** and **D.6** show the prediction results of these ANNs respectively.

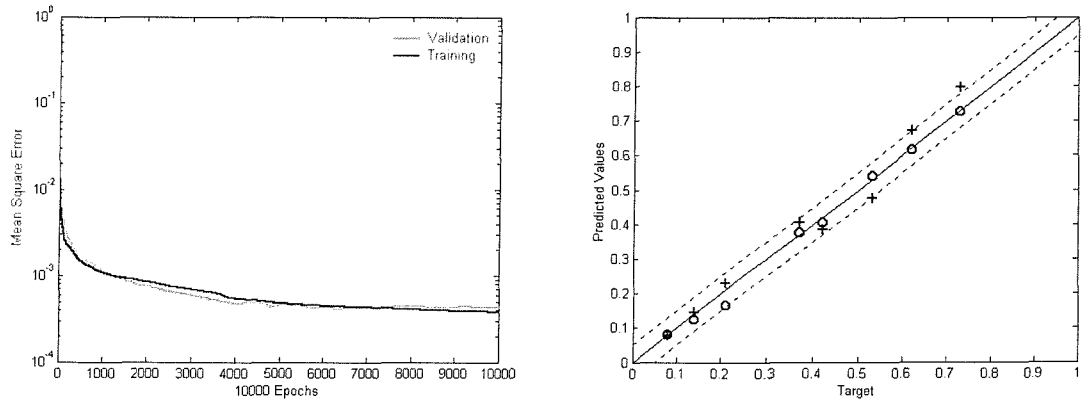

(a) (b)

Figure D.5 ANN (3:6:3:1) results for severity predictions (Input:RNF, Output:DS)
(a) Mean square error with 10000 number of epochs (b) Severity predictions

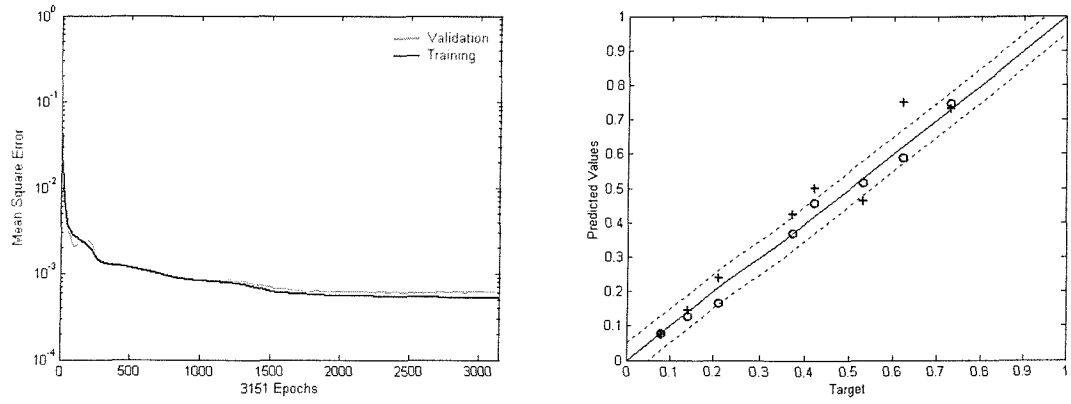

(a) (b)

Figure D.6 ANN (3:6:3:1) results for severity predictions (Input:RNF, Output:DS)
(a) Mean square error with 3151 number of epochs (b) Severity predictions

Second group of ANNs are the ones used maximum absolute differences in curvature mode shapes and their corresponding locations along the beam as input for the location detection of the damage. It can easily be seen from the **Figs. D.7a** and **D.8a** that MSE values drop to values around 10^{-6}. This shows that the input features introduced to ANN are directly related to the output set, which is location of the damage. Same sensitivity analyses regarding the number of neurons in the hidden layer and the number of epochs during the training are also performed on these two-hidden-layer ANNs (5^{th}, 6^{th}, 7^{th} and 8^{th} ANNs in **Table D.1**). Prediction results are shown in **Figs. D.7b-10b**.

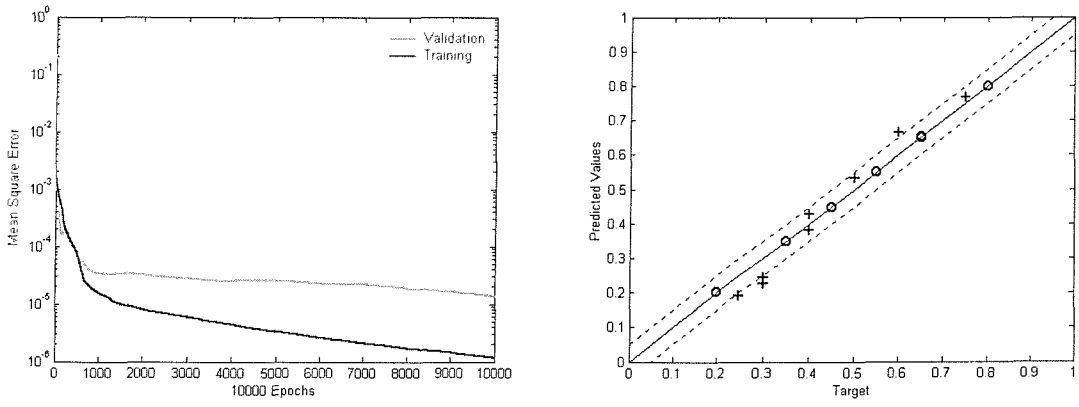

(a) (b)

Figure D.7 ANN (6:9:9:1) results for severity predictions (Input:MADC&LOC, Output:DL)
(a) Mean square error with 10000 number of epochs (b) Location predictions

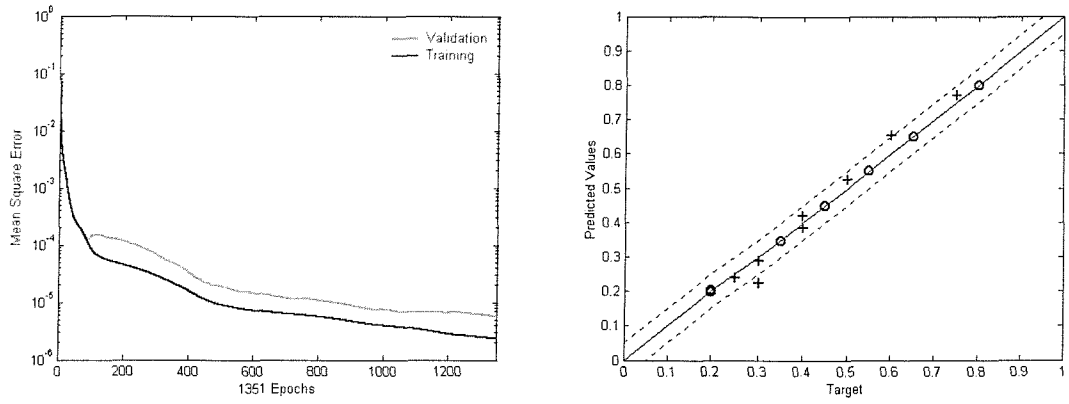

(a) (b)

Figure D.8 ANN (6:9:9:1) results for severity predictions (Input:MADC&LOC, Output:DL)
(a) Mean square error with 1351 number of epochs (b) Location predictions

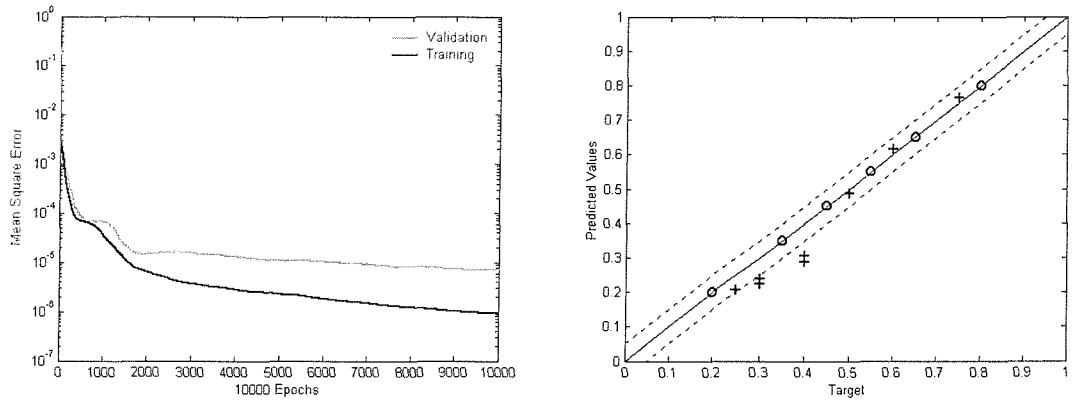

(a) (b)

Figure D.9 ANN (6:9:6:1) results for severity predictions (Input:MADC&LOC, Output:DL)
(a) Mean square error with 10000 number of epochs (b) Location predictions

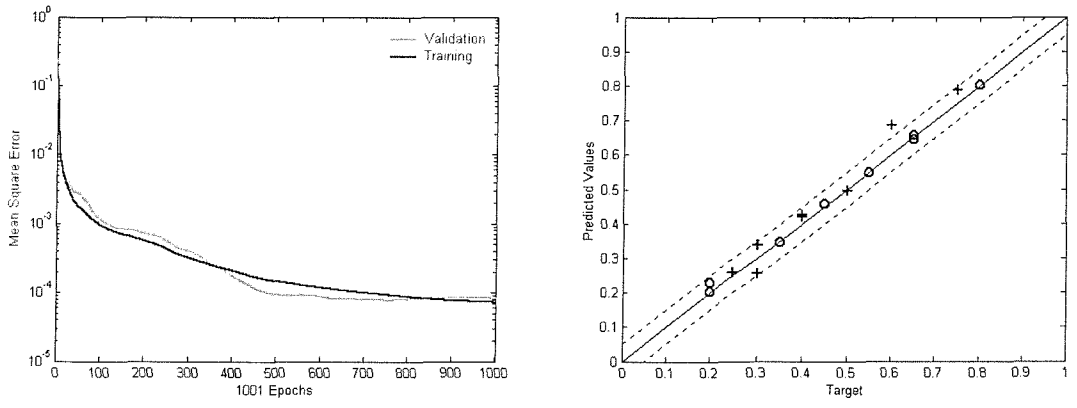

(a) (b)

Figure D.10 ANN (6:9:6:1) results for severity predictions (Input:MADC&LOC, Output:DL)
(a) Mean square error with 1001 number of epochs (b) Location predictions

The final group of ANNs (9th, 10th, 11th and 12th ANN in **Table D.1**) are trained by using all combined inputs namely; reduction in natural frequencies, maximum absolute differences in curvature mode shape and their corresponding locations along the beam from the first three natural modes for the detection of damage location and severity at the same time. The severity and location predictions of the two-hidden-layer ANNs that have 18 neurons in each hidden layer can be seen from **Figs. D.11** and **D.12**. Although there are couple of over and under estimations in the localisation of the damage, ANNs that are trained up to 10000 and 2401 number of epochs provide better accuracy as compared to quantification of the damage.

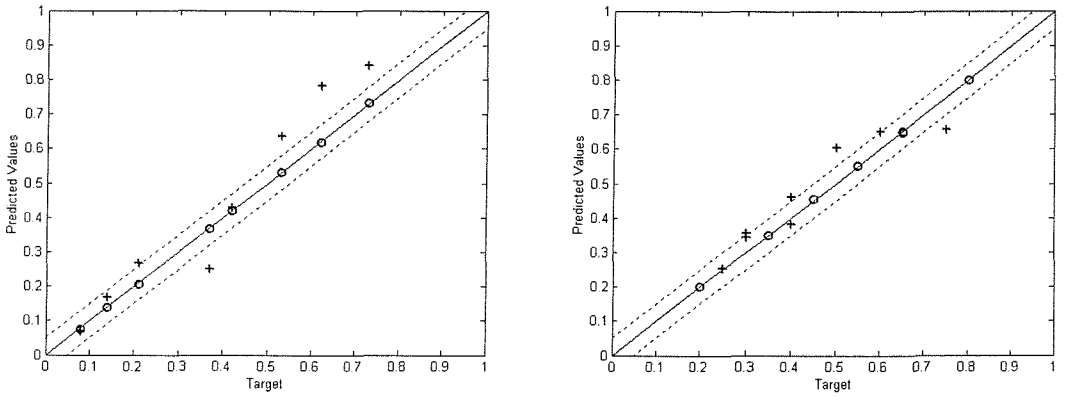

(a) (b)

Figure D.11 ANN (9:18:18:2) results with 10000 number of epochs (Input:RNF&MADC&LOC, Output: DS&DL) (a) Severity predictions (b) Location predictions

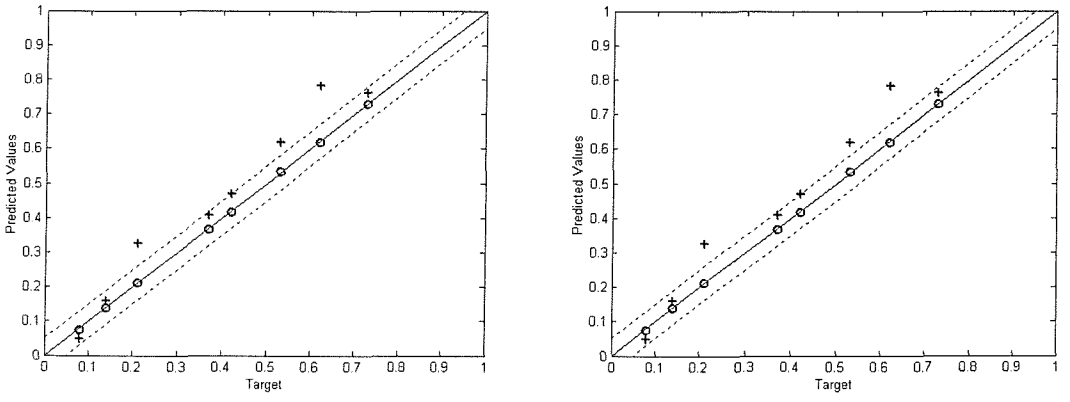

(a) (b)

Figure D.12 ANN (9:18:18:2) results with 2401 number of epochs (Input:RNF&MADC&LOC, Output: DS&DL) (a) Severity predictions (b) Location predictions

In the second part of the analysis, ANNs that use same data set (i.e. RNF&MADC&LOC) as input are redesigned by reducing the number of neurons in the second hidden layer from 18 to 9. It can be seen from **Figs. D.13** and **D.14** that the predictions of these two ANNs (11^{th} and 12^{th} ANNs in **Table D.1**) regarding the severity and location of the damage are as accurate as the 9^{th} and 10^{th} ANNs in **Table D.1**.

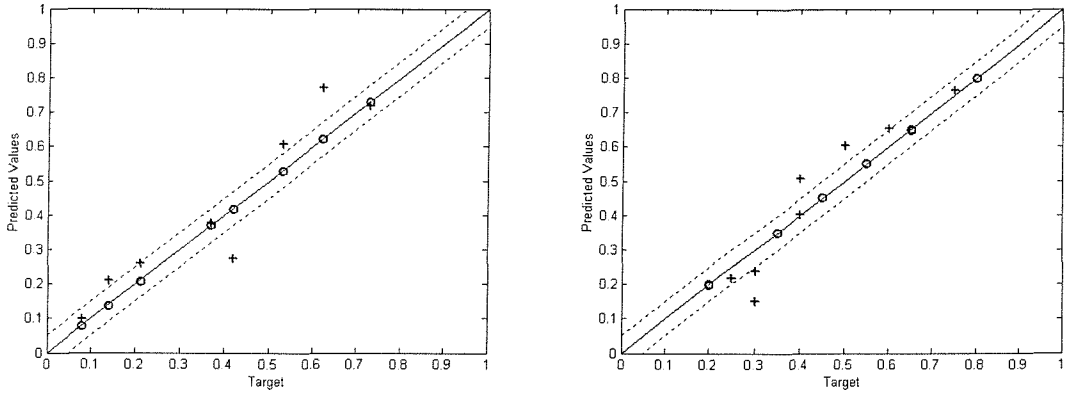

(a) (b)

Figure D.13 ANN (9:18:9:2) results with 10000 number of epochs (Input:RNF&MADC&LOC, Output: DS&DL) (a) Severity predictions (b) Location predictions

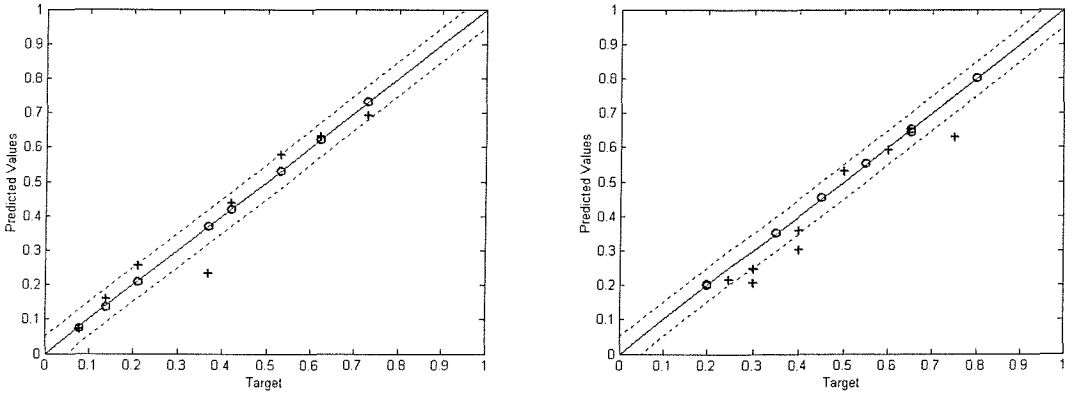

(a) (b)

Figure D.14 ANN (9:18:9:2) results with 3201 number of epochs (Input:RNF&MADC&LOC, Output: DS&DL) (a) Severity predictions (b) Location predictions

Finally all predictions obtained from different ANNs with two hidden layers are compared with the ones with single hidden layer (**Figs. 7.6**, **7.10** and **7.11** in Chapter 7, section 7.5.1).

The following conclusions can be drawn from this analysis:

- The performance (i.e. change in MSE value with increasing epochs) of the ANNs used in the analysis is in the range of 10^{-6} and 10^{-3} with slight differences. This means that generalisation is almost achieved in all ANNs considering the trend in MSE during the training and validation process.

- Providing more input-output data sets for the training may improve the generalisation of these two-hidden-layer ANNs.

- The difference in MSE value between the validation and training performance curves after certain number of epochs plays an important role in the generalisation and the predictions for the damage identification.

- Considering the computation time issue and the general fact that single hidden layer ANNs can be trained to approximate any functions arbitrarily well and be also used to solve pattern recognition problems, the ANNs with single hidden layer are selected and used for further applications in the analysis (Chapter 7, 8 and 9).

Appendix E DETERMINATION OF MATERIAL PROPERTIES OF SANDWICH STRUCTURE

E.1 Skin Density Estimation (Burn-off Test)

Since the density of the skin is one of the most important parameters affecting the dynamic characteristics of the sandwich structure, fibre volume ratio, which can be used for more accurate density estimation, is determined by performing a burn-off test. The four-layer ([0°/90°/90°/0°]) GFRP laminae sample (60mm × 40mm × 1.53mm) selected for the test has been kept in the muffle furnace at the temperature of 650°C for 3 hours.

Total mass of the sample laminae: $m_{\text{composite}} = m_{\text{fibre+matrix}} = 5.87$ g

Volume of the sample laminae: $V_{\text{composite}} = 6 \times 4 \times 0.153 = 3.672\ \text{cm}^3$

Mass of the glass fibre after burn-off: $m_{\text{fibre}} = 4.31$ g

Mass of the matrix: $m_{\text{matrix}} = m_{\text{composite}} - m_{\text{fibre}} = 1.56$ g

Density of the matrix: $\rho_{\text{resin-after cure}} = 1.148\ \text{g/cm}^3$

Volume of the matrix: $V_{\text{matrix}} = \dfrac{m_{\text{matrix}}}{\rho_{\text{resin-after cure}}} = \dfrac{1.56}{1.148} = 1.35889\ \text{cm}^3$

Volume fraction of the matrix: $k_{\text{matrix}} = \dfrac{V_{\text{matrix}}}{V_{\text{composite}}} = \dfrac{1.35889}{3.672} = 0.37$

Volume fraction of the fibre: $k_{\text{fibre}} = 1 - k_{\text{matrix}} = 1 - 0.37 = 0.63$

Density of the Glass Fibre **[E-1]**: $\rho_{\text{fibre}} = 2.55\ \text{g/cm}^3$

Density of the GFRP skin: $\rho_{\text{skin}} = k_{\text{fibre}} \times \rho_{\text{fibre}} + k_{\text{matrix}} \times \rho_{\text{matrix}}$

$= 0.63 \times 2.55 + 0.37 \times 1.148 = 2.03126\ \text{g/cm}^3$

E.2 Core Density and Modulus of Elasticity Estimation

During the analysis double-cut core cell, which has two cuts 0° and 90° made on each side intersecting in the centre, is used. Since the pre-cuts are filled with resin during the infusion, the core density increases drastically after curing. The effect of the cured resin is investigated and the density of the core is modified accordingly. **Figures E.1** and **E.2** show the core material before and after resin infusion. The effect of the infused resin can be seen from **Fig. E.2**.

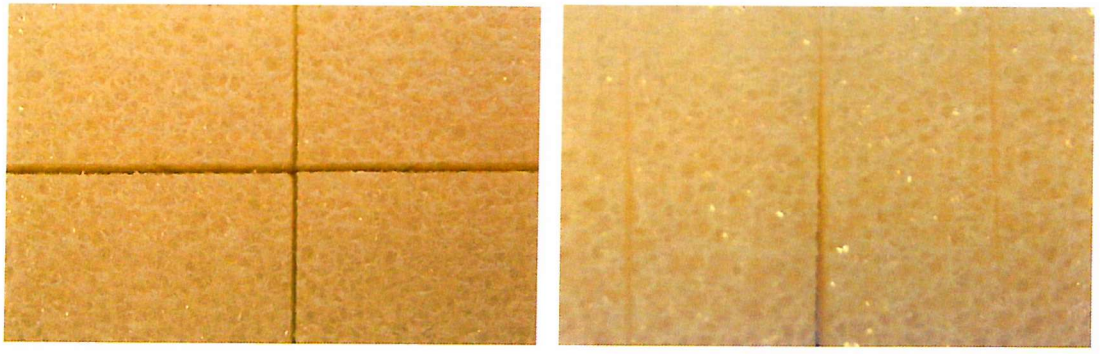

(a) (b)

Figure E.1 Core material before resin infusion (a) Top view (b) Side view

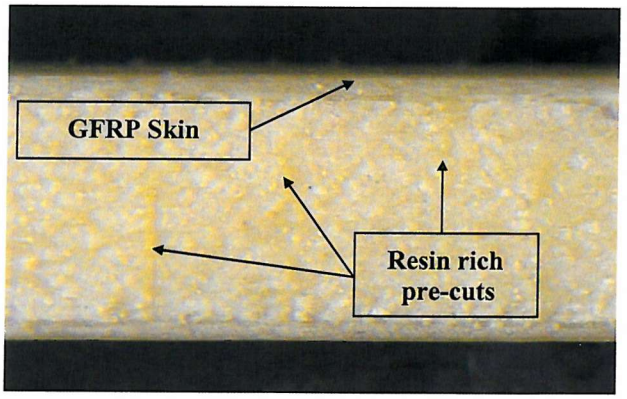

Figure E.2 Core material after resin infusion (Side view)

As the core material has 2% of air bubble and 3% of pre-cuts in volume, 5% of the core is assumed to be filled with resin in total after infusion process. Hence, the modified density of the core can be calculated as follows;

Density of the core:
$$\rho_{\text{core}} = \rho_{\text{core-manufacturer}} \times 0.95 + \rho_{\text{resin-after cure}} \times 0.05$$
$$= 0.092 \times 0.95 + 1.148 \times 0.05 = 0.1448 \text{ g/cm}^3$$

The modulus of elasticity of the core is also calculated by assuming a 20% increase in its value **[9-1]** due to pre-cuts filled with resin after infusion.

Modulus of elasticity of the core:
$$E_{\text{core}} = E_{\text{core-manufacturer}} \times 1.2 = 109.28 \times 1.2 = 131.13 \text{ MPa}.$$

Appendix F DETERMINATION OF SENSOR LOCATIONS IN BEAM-LIKE STRUCTURES

Determination of sensor locations plays an important role in maximum sensing of strain along the beam structure. The approach used in the analysis is to find the locations corresponding to maximum and zero curvature (i.e. nodal points) along the beam. Since strain is directly related to curvature (i.e. second spatial derivative of the displacement mode shape), modal analysis is used to find the locations of the sensors. The analysis is performed on 450mm long cantilever beam shown in **Fig. F.1**.

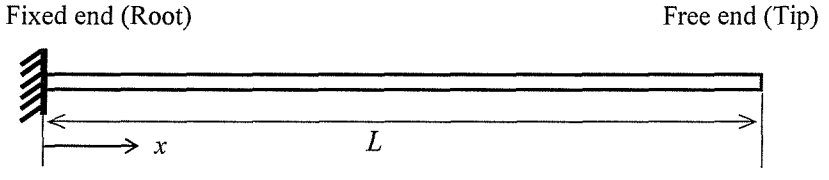

Figure F.1 Cantilever beam

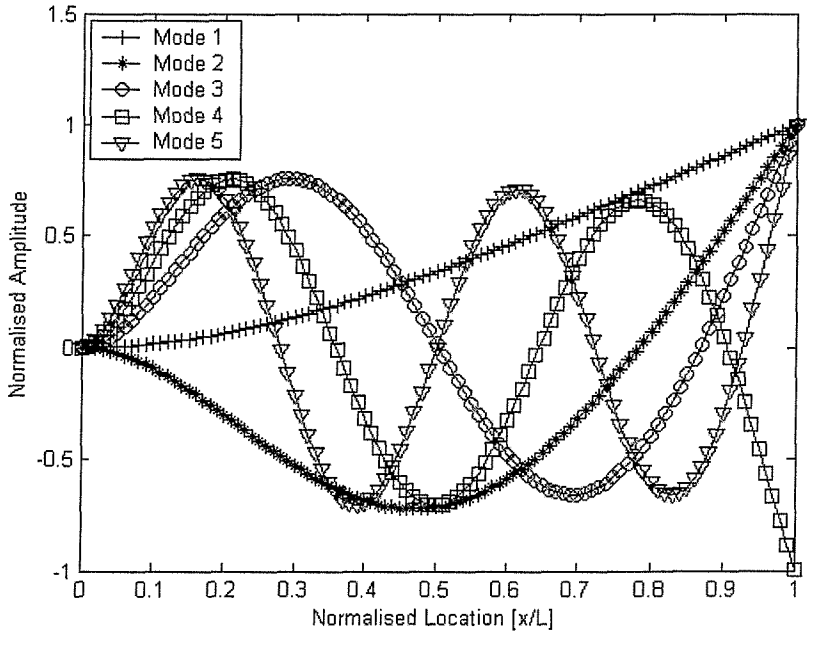

Figure F.2 First five normalised displacement mode shapes of the fixed-free beam

First of all, normalised displacement mode shapes (**Fig. F.2**) are obtained and used in the calculation of the curvature modes (**Fig. F.3**) in the first five natural modes of cantilever beam. Since both positive and negative curvatures are equally effective in the dynamic analysis, the absolute values of the curvature modes are plotted in **Fig. F.4** in order to find the maximum and nodal curvature locations.

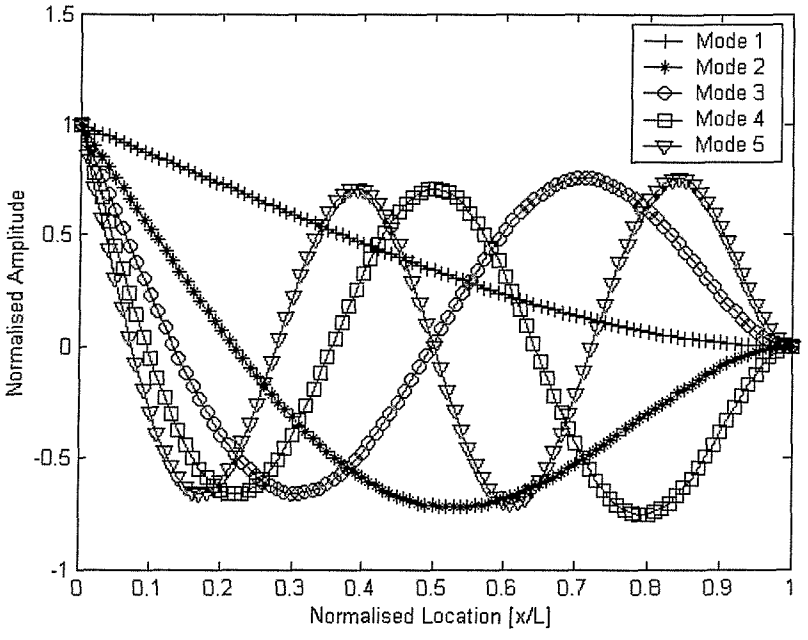

Figure F.3 First five normalised curvature mode shapes of the fixed-free beam

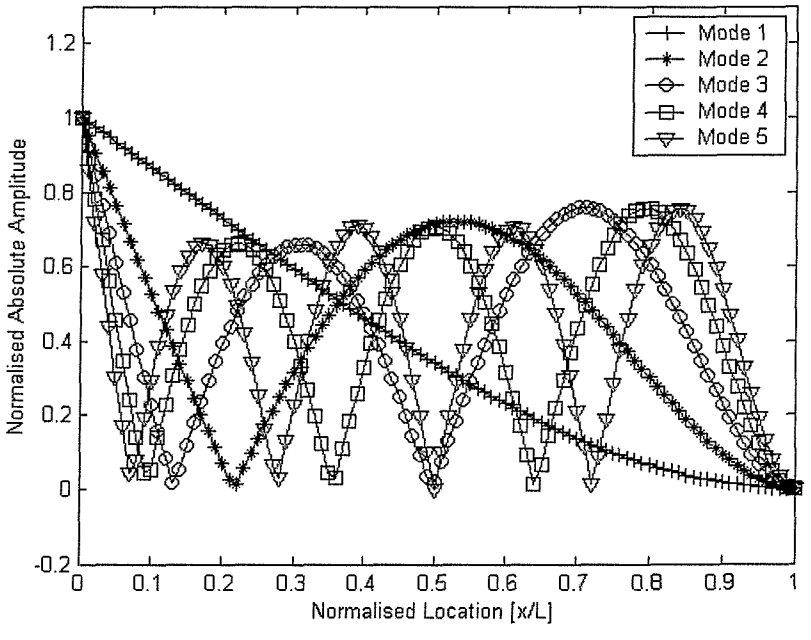

Figure F.4 First five absolute curvature mode shapes of the fixed-free beam

These locations are also tabulated in **Table F.1** considering the first five bending modes of the beam.

Table F.1 Maximum and nodal curvature locations

Mode No	Maximum Curvature Location [*x/L*]	Curvature Node Location [*x/L*]
1st Bending	0	-
2nd Bending	0, 0.52	0.21
3rd Bending	0, 0.30, 0.70	0.13, 0.49
4th Bending	0, 0.22, 0.50, 0.80	0.09, 0.35, 0.65
5th Bending	0, 0.18, 0.38, 0.62, 0.84	0.07, 0.27, 0.50, 0.72

Another important point in determination of the location of the sensors is to find spatial locations along the span of the beam in such a way that they provide enough sensitivity for different modes of vibration. This is especially important when frequency sweep excitation is applied. Thus, the first five absolute curvature mode shapes are added to each other and the envelope in **Fig. F.5** is obtained.

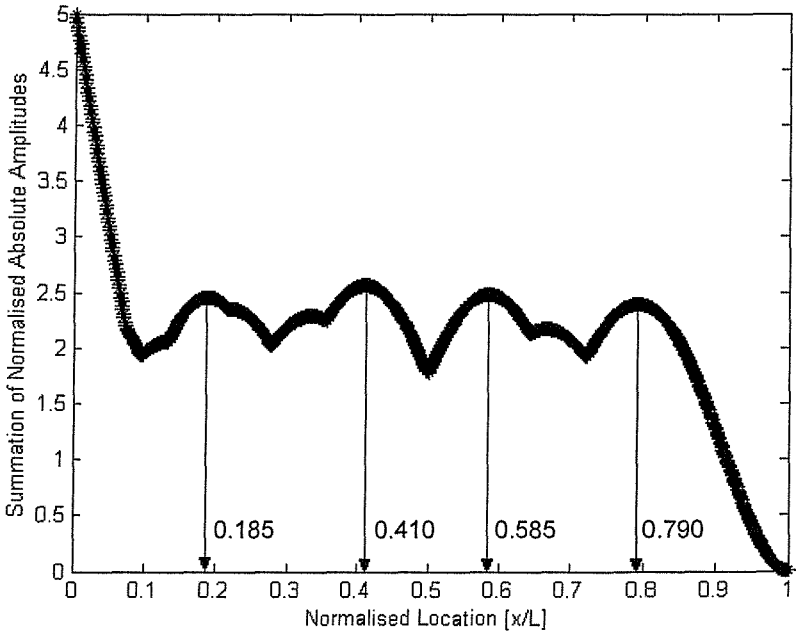

Figure F.5 Summation of absolute curvature mode shapes of the fixed-free beam

The normalised locations (such as 0.185, 0.410, 0.585 and 0.790) corresponding to peak points where the amplitude of the summation of the curvature modes are considerably high can be seen from the **Fig. F.5**. Finally, the locations of the fibre optic sensors are decided and tabulated in **Table F.2** with their actual locations along the beam and their corresponding most sensitive mode(s) by using the data in **Fig F.4** and **Table F.1**.

Table F.2 Location of the sensors and most sensitive corresponding mode(s)

Normalised Location [x/L]	Actual Location [mm]	Most Sensitive Mode
0.0333	15	1^{st}, 2^{nd}, 3^{rd}, 4^{th}, 5^{th}
0.1777	80	5^{th}, 4^{th}
0.3000	135	3^{rd}
0.3777	170	5^{th}, 3^{rd}
0.5000	225	2^{nd}
0.6000	270	5^{th}, 2^{nd}
0.7000	315	3^{rd}
0.8111	365	4^{th}, 5^{th}

Appendix G SELECTION OF ELEMENT TYPE FOR MODELLING OF SANDWICH STRUCTURE

Free vibration analysis of rectangular plate with cantilever edge is performed by using a package program, ANSYS 6.1®, to select the most suitable type of element(s) for modelling of composite sandwich structure. The graphite/epoxy–aluminium sandwich plate (0.152m x 0.076m x 0.00204m) **[G-1, G-2, G-3]** with eight plies of graphite/epoxy placed symmetrically about a sheet of aluminium (2024-T3) is used during the FEA. The material properties of the graphite/epoxy face with a nominal ply thickness of 0.13mm and the 1mm thick aluminium core are as follows:

Orthotropic material properties of graphite/epoxy:

$E_1 = 128.0$ GPa, $E_2 = E_3 = 11.0$ GPa, $G_{12} = G_{13} = 4.48$ GPa, $G_{23} = 1.53$ GPa,

$\nu_{12} = \nu_{13} = \nu_{23} = 0.25$, $\rho = 1500\ \text{kg/m}^3$

Isotropic material properties of aluminium:

$E = 68.9$ GPa, $\nu = 0.30$, $\rho = 2770\ \text{kg/m}^3$

The first five modes **[G-3]** of vibration of the sandwich plate are obtained by using different types of elements with various mesh densities. The results are tabulated in each section and summarised at the end.

G.1 Shell Element (SHELL99) for Configurations of $[0_4/\text{Al}]_s$, $[0/\pm 45/90/\text{Al}]_s$ and $[\pm 45/\mp 45/\text{Al}]_s$

The advantage of using SHELL99 is that 6 DOF per node (i.e. 3 translational and 3 rotational) allows modelling of cantilever boundary condition more realistically. On the other hand, damage can only be modelled by reducing the thickness or stiffness of the particular layer

of interest, which is not suitable for debonding or delamination modelling applications. Additionally, inter laminar strain output is not available in this type of element. **Figure G.1** shows FEM of the cantilever sandwich plate meshed by SHELL99.

The first five natural frequencies of sandwich plate with SHELL99 (8 x 4 mesh density):

$[0_4/Al]_s$ Configuration:

$$f_1 = 108.0\,Hz,\quad f_2 = 226.7\,Hz,\quad f_3 = 674.3\,Hz,\quad f_4 = 877.2\,Hz,\quad f_5 = 1147.9\,Hz$$

$[0/\pm 45/90/Al]_s$ Configuration:

$$f_1 = 80.5\,Hz,\quad f_2 = 310.2\,Hz,\quad f_3 = 500.8\,Hz,\quad f_4 = 1022.2\,Hz,\quad f_5 = 1398.6\,Hz$$

$[\pm 45/\mp 45/Al]_s$ Configuration:

$$f_1 = 58.0\,Hz,\quad f_2 = 351.7\,Hz,\quad f_3 = 374.6\,Hz,\quad f_4 = 1015.8\,Hz,\quad f_5 = 1169.7\,Hz$$

The corresponding mode shapes are shown in **Figs. G.4 – G.6**.

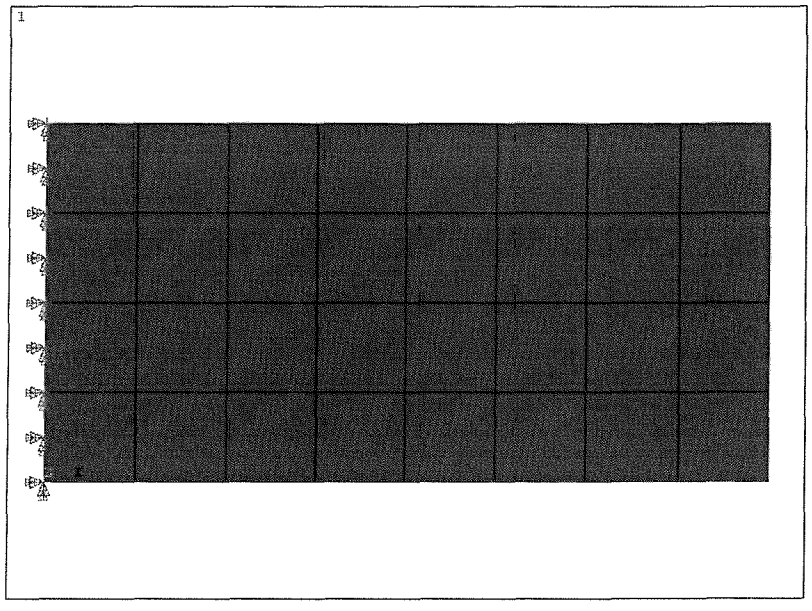

Figure G.1 Finite element model of cantilever sandwich plate
(SHELL99, 8 x 4 mesh density, top view)

G.2 Solid Elements (SOLID46 and SOLID191) for $[0_4/Al]_s$ Configuration

G.2.1 Modelling with SOLID46

By using SOLID46 (an 8-node brick element), damage can be modelled not only by changing the geometry but also by reducing the stiffness of the particular layer of interest. One of the disadvantages of SOLID46 is that 3 DOF per node (i.e. translational DOF only) makes modelling of boundary condition (fixed-end) inaccurate. Moreover, inter laminar strain output is not available if one solid element is used through the thickness.

The first five natural frequencies of sandwich plate with SOLID46:

a) Mesh density of 8 x 4 x 1*

$f_1 = 108.3$ Hz, $f_2 = 239.7$ Hz, $f_3 = 700.3$ Hz, $f_4 = 994.8$ Hz, $f_5 = 1275.8$ Hz

b) Mesh density of 40 x 20 x 1*

$f_1 = 108.0$ Hz, $f_2 = 226.6$ Hz, $f_3 = 674.6$ Hz, $f_4 = 876.9$ Hz, $f_5 = 1145.8$ Hz

G.2.2 Modelling with SOLID191

SOLID191 has an additional centre node on each edge of the 3-D solid element. This provides more number of nodes by keeping the number of elements constant compared to the model created by using SOLID46. **Figure G.2** shows FEM of the cantilever sandwich plate meshed by solid elements.

The first five natural frequencies of sandwich plate with SOLID191:

a) Mesh density of 8 x 1 x 1*

$f_1 = 108.3$ Hz, $f_2 = 227.2$ Hz, $f_3 = 676.4$ Hz, $f_4 = 880.1$ Hz, $f_5 = 1152.1$ Hz

b) Mesh density of 40 x 20 x 1*

$f_1 = 108.1$ Hz, $f_2 = 226.6$ Hz, $f_3 = 675.2$ Hz, $f_4 = 877.8$ Hz, $f_5 = 1146.7$ Hz

* One solid element through the thickness

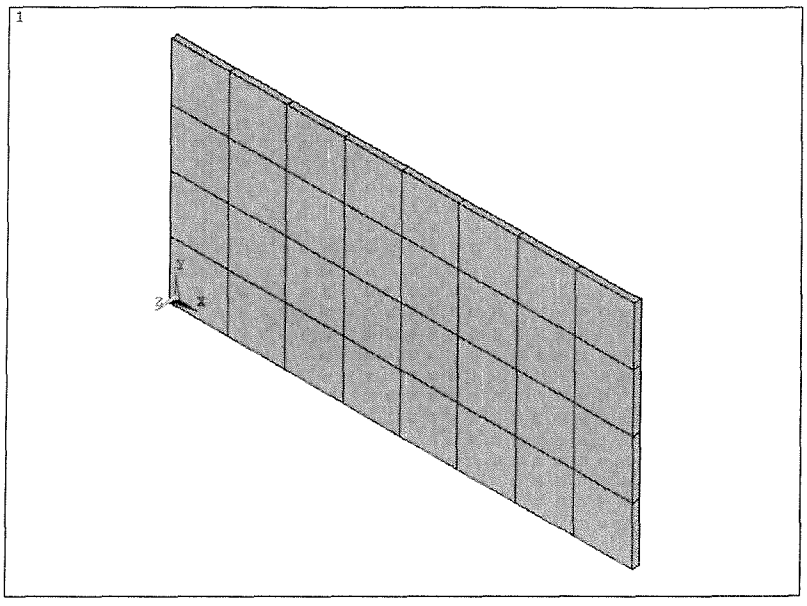

Figure G.2 Finite element model of cantilever sandwich plate
(Solid elements, 8 x 4 x 1 mesh density, isometric view)

G.3 Mixed Solid Elements (SOLID45 for core and SOLID46 for face modelling)

Since both solid elements have the same number of nodes at each face of the element (i.e. 4 nodes), SOLID45 with isotropic material properties can be used in the modelling of core together with layered orthotropic solid element, SOLID46, which is chosen to model graphite/epoxy face of the sandwich plate. The model has three different blocks stacked on top of each other: One block for each face with four layers of lamina and another block at the centre for the modelling of isotropic core. The layer configuration is defined layer-by-layer from bottom to top. The bottom layer is designated as the first layer, and additional layers are stacked from bottom to top in the positive normal direction of the element coordinate system. **Figure G.3** shows FEM of the cantilever sandwich plate meshed by mixed solid elements.

G.3.1 $[0_4/Al]_s$ Configuration

a) Mesh density of 8 x 4 x 3

$f_1 = 108.4$ Hz, $f_2 = 250.2$ Hz, $f_3 = 702.2$ Hz, $f_4 = 1079.3$ Hz, $f_5 = 1390.3$ Hz

b) Mesh density of 40 x 20 x 3

$$f_1 = 108.1\,\text{Hz},\quad f_2 = 227.2\,\text{Hz},\quad f_3 = 675.6\,\text{Hz},\quad f_4 = 880.1\,\text{Hz},\quad f_5 = 1147.2\,\text{Hz}$$

Since the core is almost twice as thick as the faces, 2 and 1-element division are used for the core and the each face respectively for better accuracy in case (c).

c) Mesh density of 40 x 20 x 4

$$f_1 = 108.1\,\text{Hz},\quad f_2 = 227.2\,\text{Hz},\quad f_3 = 675.7\,\text{Hz},\quad f_4 = 880.2\,\text{Hz},\quad f_5 = 1147.3\,\text{Hz}$$

Then, mesh density in thickness direction is increased by using 4 and 1-element division for the core and the each face respectively. In addition to this, the element division is also doubled along the length and width of the plate. The results of this particular model is as follows:

d) Mesh density of 80 x 40 x 6

$$f_1 = 108.0\,\text{Hz},\quad f_2 = 226.8\,\text{Hz},\quad f_3 = 674.8\,\text{Hz},\quad f_4 = 878.2\,\text{Hz},\quad f_5 = 1143.5\,\text{Hz}$$

Further analyses are performed by using two different layer orientations of the faces of the sandwich plate.

G.3.2 $[0/\pm 45/90/Al]_s$ Configuration

a) Mesh density of 8 x 4 x 3

$$f_1 = 81.5\,\text{Hz},\quad f_2 = 338.1\,\text{Hz},\quad f_3 = 524.1\,\text{Hz},\quad f_4 = 1215.0\,\text{Hz},\quad f_5 = 1571.5\,\text{Hz}$$

b) Mesh density of 40 x 20 x 3

$$f_1 = 80.6\,\text{Hz},\quad f_2 = 310.6\,\text{Hz},\quad f_3 = 500.9\,\text{Hz},\quad f_4 = 1024.2\,\text{Hz},\quad f_5 = 1398.7\,\text{Hz}$$

G.3.3 $[\pm 45/\mp 45/Al]_s$ Configuration

a) Mesh density of 8 x 4 x 3

$$f_1 = 61.2\,\text{Hz},\quad f_2 = 379.3\,\text{Hz},\quad f_3 = 406.5\,\text{Hz},\quad f_4 = 11825.0\,\text{Hz},\quad f_5 = 1375.7\,\text{Hz}$$

b) Mesh density of 40 x 20 x 3

$$f_1 = 58.0\,\text{Hz},\quad f_2 = 352.0\,\text{Hz},\quad f_3 = 374.7\,\text{Hz},\quad f_4 = 1017.9\,\text{Hz},\quad f_5 = 1170.8\,\text{Hz}$$

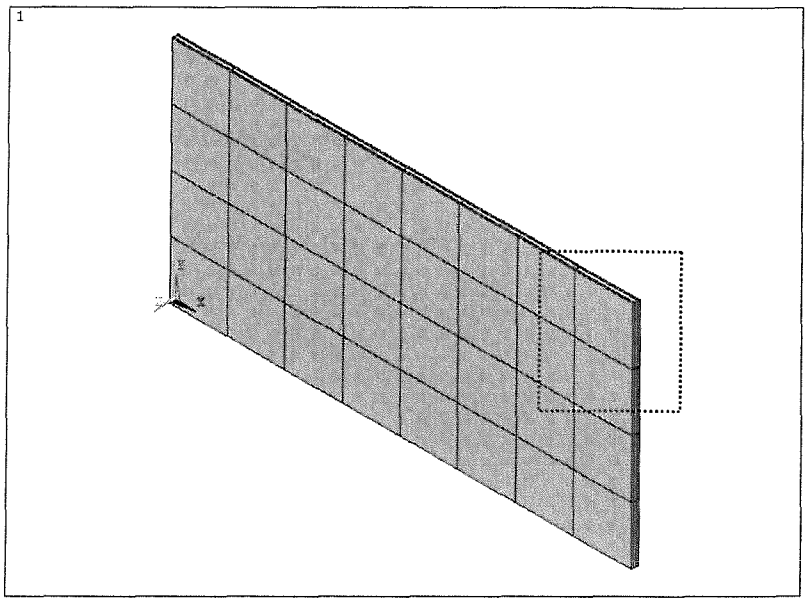

(a)

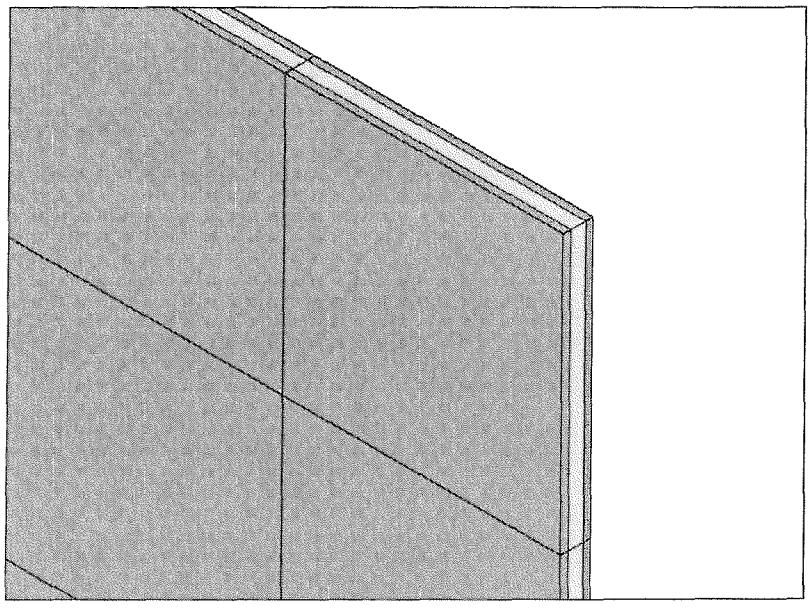

(b)

Figure G.3 Finite element model of cantilever sandwich plate
(Mixed solid elements, 8 x 4 x 3 mesh density) (a) Isometric view (b) Zoom view

G.4 Mixed Solid Elements (SOLID95 for core and SOLID191 for face modelling)

This section presents the first five natural frequencies of the sandwich plate obtained from FEM using higher order 3-D solid elements (SOLID95 and SOLID191). The way of creating the mesh is same as the one described in Section G.3 for the element types of SOLID45 and SOLID46.

G.4.1 $[0_4/Al]_s$ Configuration

a) Mesh density of 8 x 4 x 3

$f_1 = 108.3$ Hz, $f_2 = 227.9$ Hz, $f_3 = 681.0$ Hz, $f_4 = 887.1$ Hz, $f_5 = 1171.6$ Hz

b) Mesh density of 16 x 8 x 3

$f_1 = 108.1$ Hz, $f_2 = 227.0$ Hz, $f_3 = 675.3$ Hz, $f_4 = 878.8$ Hz, $f_5 = 1147.5$ Hz

G.4.2 $[0/\pm 45/90/Al]_s$ Configuration

a) Mesh density of 8 x 4 x 3

$f_1 = 80.9$ Hz, $f_2 = 312.2$ Hz, $f_3 = 506.2$ Hz, $f_4 = 1034.9$ Hz, $f_5 = 1435.5$ Hz

b) Mesh density of 16 x 8 x 3

$f_1 = 80.6$ Hz, $f_2 = 309.8$ Hz, $f_3 = 501.0$ Hz, $f_4 = 1021.4$ Hz, $f_5 = 1396.7$ Hz

G.4.3 $[\pm 45/\mp 45/Al]_s$ Configuration

a) Mesh density of 8 x 4 x 3

$f_1 = 58.9$ Hz, $f_2 = 358.8$ Hz, $f_3 = 378.5$ Hz, $f_4 = 1060.0$ Hz, $f_5 = 1190.5$ Hz

b) Mesh density of 16 x 8 x 3

$f_1 = 58.1$ Hz, $f_2 = 352.3$ Hz, $f_3 = 374.4$ Hz, $f_4 = 1018.2$ Hz, $f_5 = 1169.4$ Hz

G.5 Summary and Comparison of the Results

Finally, all case studies performed by using different element types with various mesh densities on sandwich plate that has different layer orientations for the graphite/epoxy faces are summarised in **Table G.1**.

Table G.1 Comparison of the first five natural frequencies of the sandwich plate [Hz]

Mode No	Experiment **[G-1]**	FEM **[G-1]**	FEM 4-node (8 x 4) **[G-2]**	FEM 9-node (8 x 4) **[G-2]**	Present SHELL99 (8 x 4)	Present SOLID45 &SOLID46 (40 x 20 x 3)	Present SOLID95 &SOLID191 (16 x 8 x 3)
				$[0_4/Al]_s$			
1	101.7	108.8	107.9	108.2	108.0	108.1	108.1
2	229.0	228.8	227.6	227.3	226.7	227.2	227.0
3	631.9	680.2	681.3	675.0	674.3	675.6	675.3
4	865.0	885.6	887.3	879.6	877.2	880.1	878.8
5	1129.0	1168.0	1168.8	1147.4	1147.9	1147.2	1147.5
				$[0/\pm 45/90/Al]_s$			
1	75.9	81.16	80.6	80.0	80.5	80.6	80.6
2	302.0	313.8	312.6	311.9	310.2	310.6	309.8
3	469.6	505.1	505.4	501.0	500.8	500.9	501.0
4	983.0	1035.0	1037.3	1028.3	1022.2	1024.2	1021.4
5	1306.0	1438.0	1435.4	1399.8	1398.6	1398.7	1396.7
				$[\pm 45/\mp 45/Al]_s$			
1	58.3	58.5	58.2	57.9	58.0	58.0	58.1
2	351.6	354.7	356.6	352.8	351.7	352.0	352.3
3	358.0	379.6	378.3	377.4	374.6	374.7	374.4
4	1006.0	1029.0	1047.6	1020.6	1015.8	1017.9	1018.2
5	1113.0	1187.0	1189.7	1179.2	1169.7	1170.8	1169.4

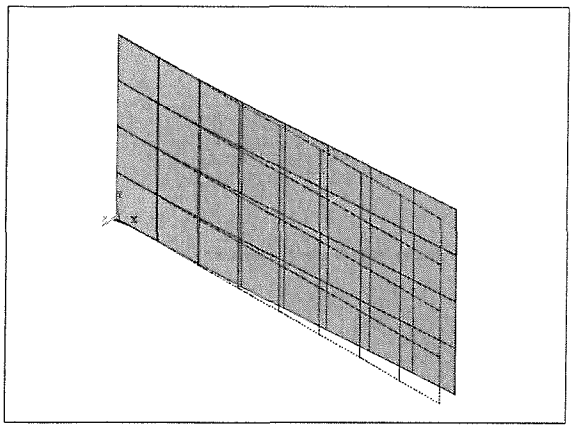

(a) Natural Frequency of 108.0 Hz

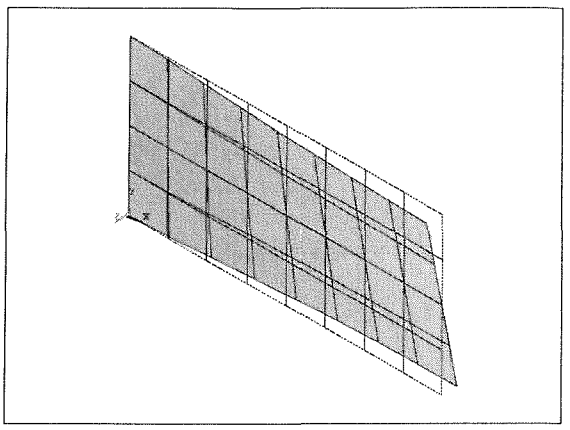

(b) Natural Frequency of 226.7 Hz

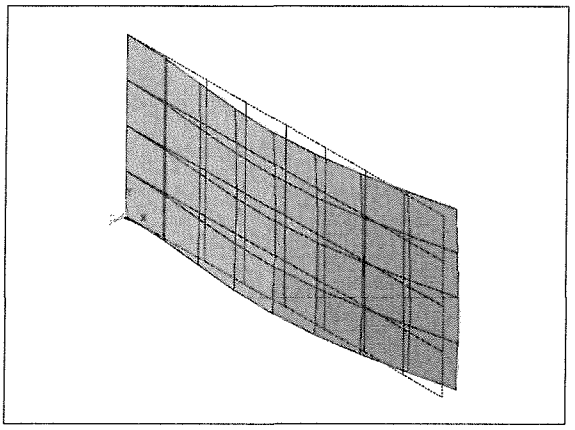

(c) Natural Frequency of 674.3 Hz

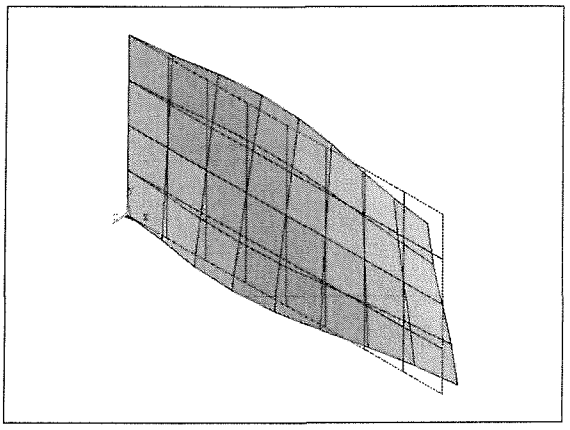

(d) Natural Frequency of 877.2 Hz

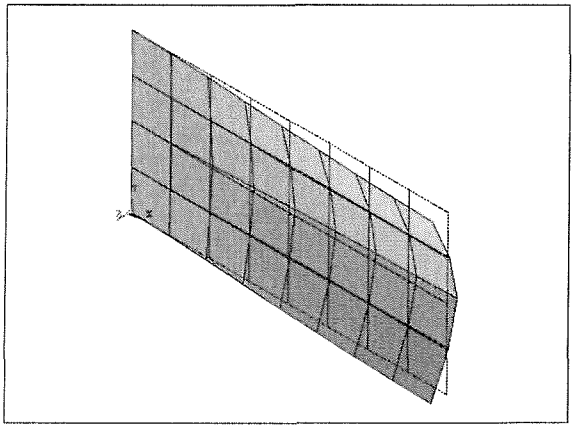

(e) Natural Frequency of 1147.9 Hz

Figure G.4 The first five mode shapes of cantilever plate modelled by SHELL99 ($[0_4/Al]_s$ configuration)

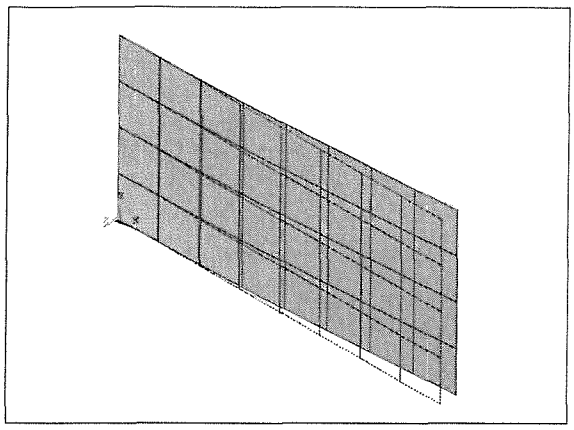

(a) Natural Frequency of 80.5 Hz

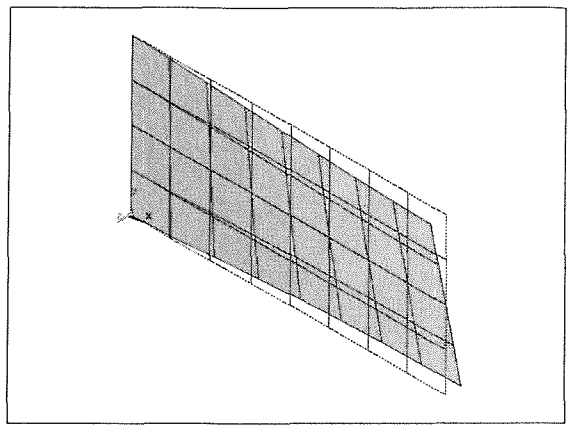

(b) Natural Frequency of 310.2 Hz

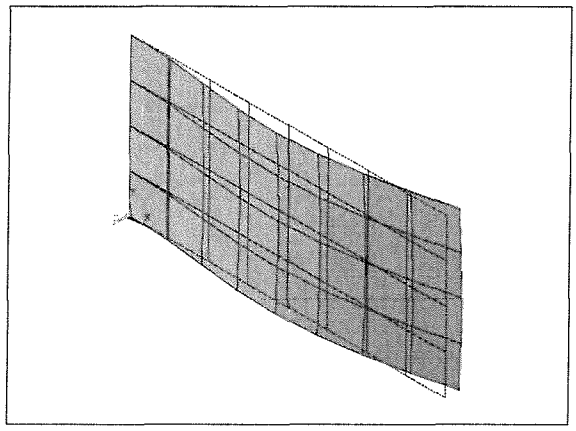

(c) Natural Frequency of 500.8 Hz

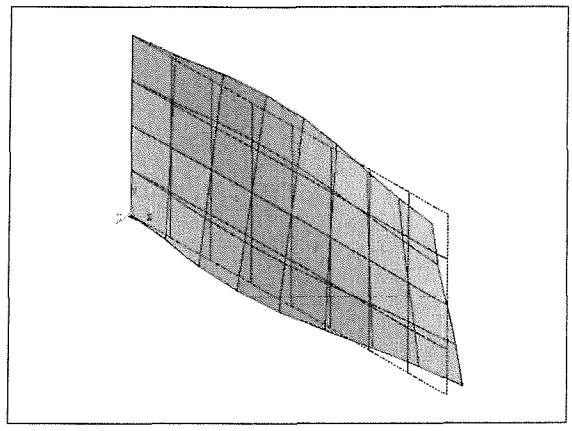

(d) Natural Frequency of 1022.2 Hz

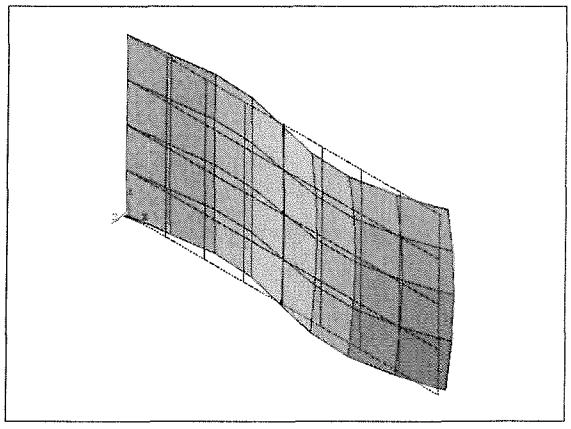

(e) Natural Frequency of 1398.6 Hz

Figure G.5 The first five mode shapes of cantilever plate modelled by SHELL99 ($[0/\pm 45/90/Al]_s$ configuration)

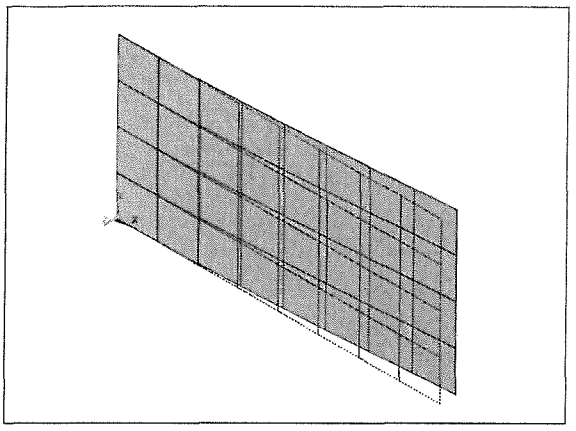

(a) Natural Frequency of 58.0 Hz

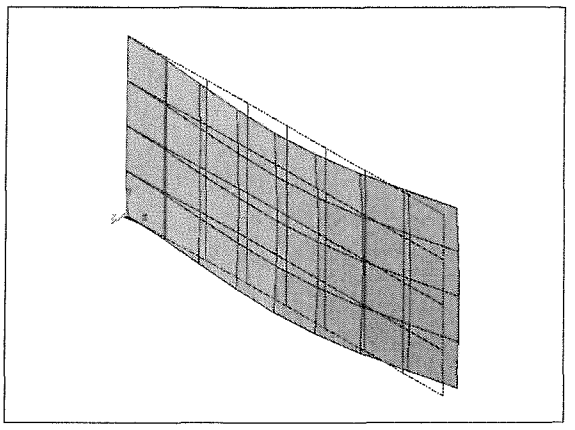

(b) Natural Frequency of 351.7 Hz

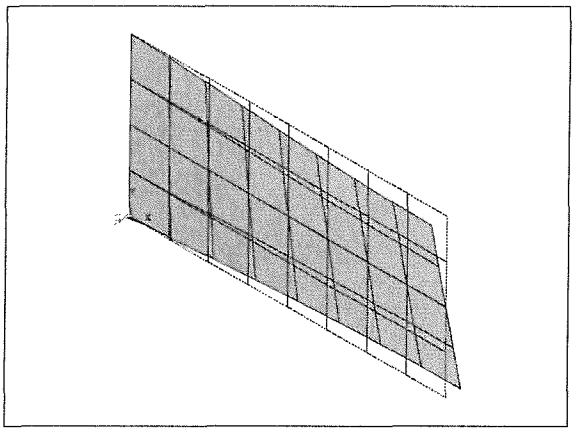

(c) Natural Frequency of 374.6 Hz

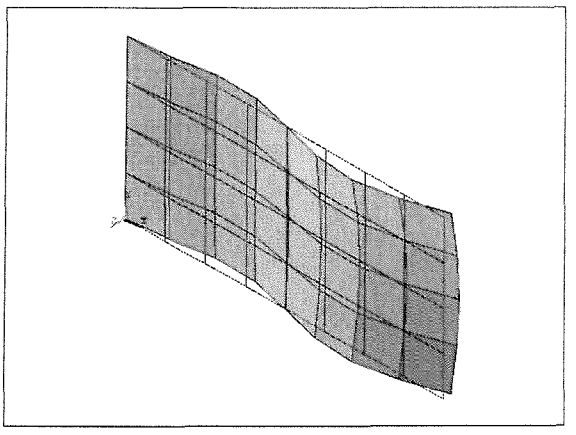

(d) Natural Frequency of 1015.8 Hz

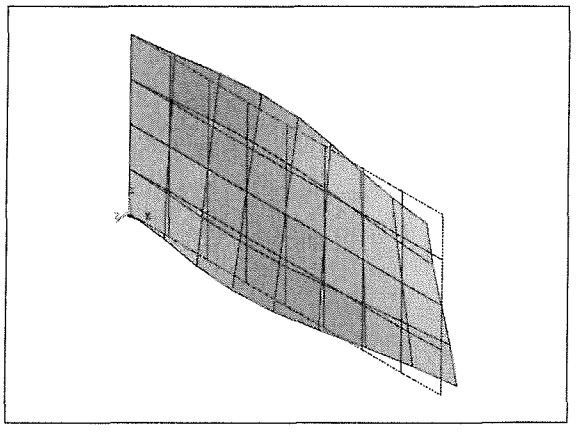

(e) Natural Frequency of 1169.7 Hz

Figure G.6 The first five mode shapes of cantilever plate modelled by SHELL99 ($[\pm 45/\mp 45/\mathrm{Al}]_s$ configuration)

The following conclusions can be drawn from **Table G.1**:

- The results obtained from models meshed with mixed solid elements provide acceptable accuracy.

- Since solid elements are quite stiff compared to 6-DOF shell elements, finer mesh densities are used in the modelling with solid elements.

- In normal mode dynamic analysis, combination of SOLID95 and SOLID191 provides same accuracy with that of SOLID45 and SOLID46 although the mesh density used in SOLID45&SOLID46 model is much finer than the one used in model with SOLID95&SOLID191 elements.

- Since the results obtained from models with solid elements converge to ones obtained from models with SHELL99, it can be concluded that the required mesh densities are achieved in solid element models.

- The cantilever boundary condition is modelled by using two different types of element, shell and solid, which have 6-DOF and 3-DOF respectively. Acceptable results are obtained from each model.

Finally, combination of SOLID95 and SOLID191 is selected for meshing of sandwich beam for further analysis.

Appendix H BOUNDARY CONDITION EFFECT ON FEM OF SANDWICH BEAM

In this section, the effect of the boundary condition on FEM of the sandwich beam structure used in Chapter 9 is investigated. Since core to face thickness ratio of the sandwich beam is approximately 9.23 which gives a total thickness of 14.6mm, the modelling of the cantilever boundary condition requires extra attention in order to simulate experimental fixing condition realistically. **Figure H.1** shows sandwich beam specimen mounted to steel clamp.

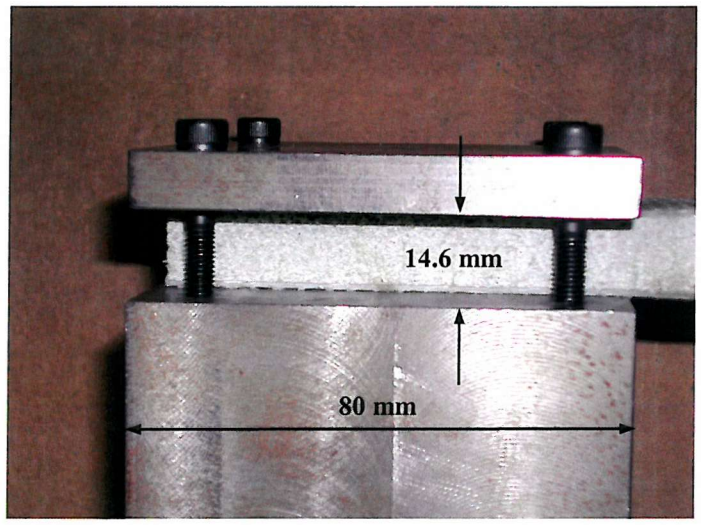

Figure H.1 Steel clamp and sandwich beam specimen

It can be seen from the **Fig. H.1** that the left-end of the specimen is free and only the upper and the lower surfaces are touching to steel clamp. Therefore, three different FEMs with various boundary conditions are used to simulate this experimental clamp. **Figures H.2** to **H.4** show these boundary conditions which are namely:

- Boundary Condition No:1 (BC #1): Fully clamped at the root, i.e. all DOFs are equal to zero at location where X = 0

- Boundary Condition No:2 (BC #2): Fixed at the upper and lower edge, i.e. all DOFs are equal to zero at location where X = 0 & Z = 0 and X = 0 & Z = beam total thickness

- Boundary Condition No:3 (BC #3): Fixed at the upper and lower surface, i.e. all DOFs are equal to zero at location where X = 0 & Z = 0 and X = 0 & Z = beam total thickness and $0 \leq Y \leq 80$mm. Another beam (530mm x 40.5mm x 14.6mm), which is 80mm longer than the ones used in BC #2 and BC #3, is modelled in order to define this particular boundary condition.

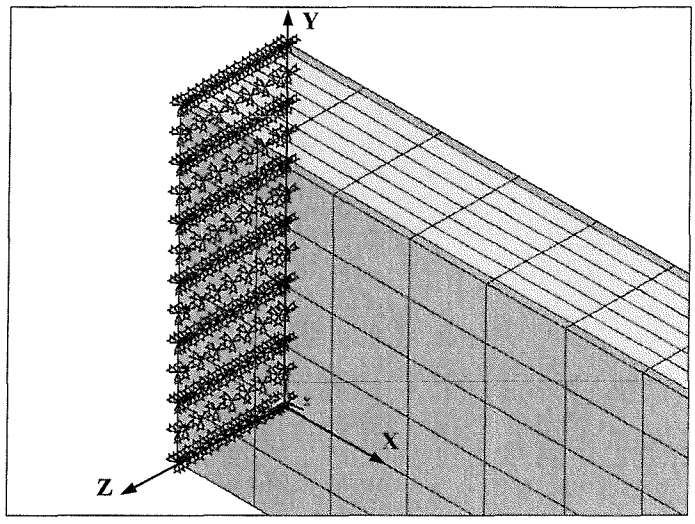

Figure H.2 Boundary condition No:1 (Isometric zoom view)

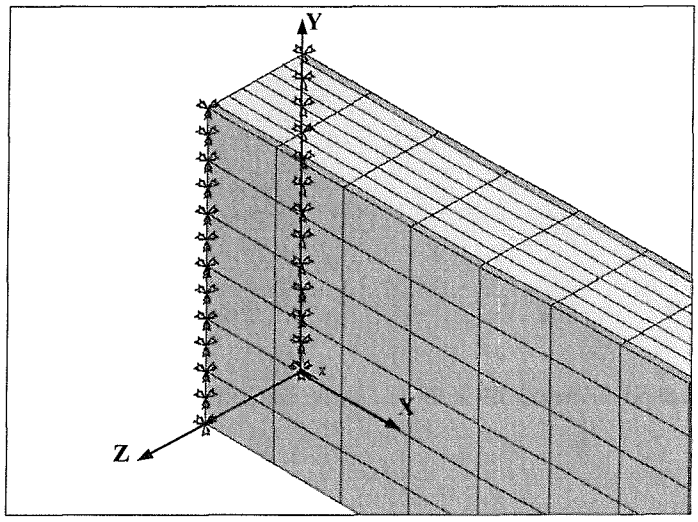

Figure H.3 Boundary condition No:2 (Isometric zoom view)

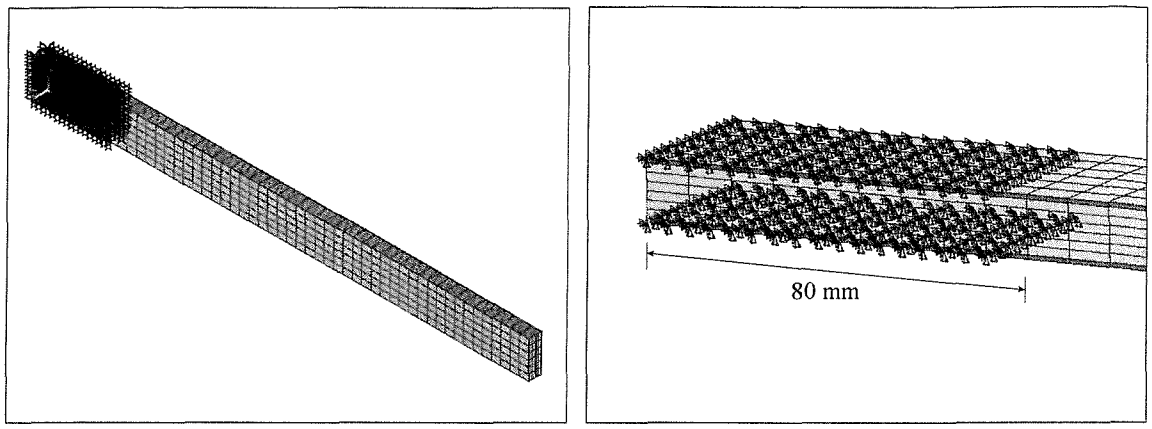

(a) (b)

Figure H.4 Boundary condition No:3 (a) Isometric view (b) Side zoom view

Normal mode dynamic analysis is performed on these three different FEMs to find the first three bending natural frequencies. The analysis results are summarised in **Table H.1**.

Table H.1 First three natural frequencies of sandwich beam

	Natural Frequency [Hz]		
Mode No	BC #1	BC #2	BC #3
1st Bending	46.944	45.865	46.741
2nd Bending	251.109	249.901	250.826
3rd Bending	591.850	591.268	591.567

It can be seen from **Table H.1** that the first three bending natural frequencies of models with various boundary conditions are quite close to each other. Since the model with BC #3 has 1888 more nodes and 384 more elements than the other two models (BC #1 and BC #2), it is not practical to use this model (BC #3) as it increases the computational time gradually. Model with BC #2 is selected for further analysis since it allows internal nodes at the root to move freely as it is in experimental clamp.

Appendix I ERROR ANALYSIS

In this section, errors and uncertainties **[I-1, I-2]** inherent in the measurement of the parameters that are used during the static and dynamic analysis of beam-like structures are investigated. The main assumptions made during these analyses and the other source of errors are outlined in order to identify dominant errors, and hence to provide a guide to improve the experimental work.

I.1 Precision of the Measurements

It is a fact that all measured values cannot be exact. The uncertainty in the measurement can arise either from limitations of the instruments or from statistical fluctuations in the quantity being measured. The main aim is to estimate the level of this uncertainty (so-called "absolute uncertainty"). Another quantity called "relative uncertainty" is the precision of the measurement (I.1) and shows the effect (or significance) of the absolute uncertainty.

$$\text{Relative Uncertainty (Precision)} = \frac{\text{Absolute Uncertainty}}{\text{Measured Value}} \tag{I.1}$$

Since one of the sandwich specimen used in the experimental analysis has dimensions of $450.0\text{mm} \times 40.5\text{mm} \times 14.60\text{mm}$, the following precision can be obtained from each measurements:

- Ruler [0-500mm $\pm$ 0.5mm]: Used to measure the length of the specimen.

$$\text{Precision of the measurement along the width} = \frac{\pm 0.5}{450.0} = \pm 1.1 \cdot 10^{-3} = 0.11\,\%$$

- Vernier Caliper [0-150mm $\pm$ 0.1mm]: Used to measure the width of the specimen.

$$\text{Precision of the measurement along the width} = \frac{\pm 0.1}{40.5} = \pm 2.5 \cdot 10^{-3} = 0.25\,\%$$

- Micrometer [0-25mm ± 0.01mm]: Used to measure the thickness of the specimen.

$$\text{Precision of the measurement along the thickness} = \frac{\pm 0.01}{14.60} = \pm 6.85 \cdot 10^{-4} = 0.0685\,\%$$

- Balance (Digital Display) [0-1500g ± 0.01g]: Used to weigh the glass fibre used in burn-off test (Section E.1).

Mass of the glass fibre after burn-off: $m_{\text{fibre}} = 4.31\,\text{g}$

$$\text{Precision of the measurement in weigth of the fibre} = \frac{\pm 0.01}{4.31} = \pm 2.32 \cdot 10^{-3} = 0.232\,\%$$

After measuring three dimensions (60mm × 40mm × 1.53mm) and the mass of the specimen (i.e. the one used in burn-off test), the precision in density calculation can be obtained as follows:

Precision of the density of GFRP laminae sample

$$\cong \%\Delta\text{Length} + \%\Delta\text{Width} + \%\Delta\text{Thickness} + \%\Delta\text{Mass}$$

$$\cong \frac{\pm 0.5}{60.0} \times 100 + \frac{\pm 0.5}{40.0} \times 100 + \frac{\pm 0.01}{1.53} \times 100 + 0.232$$

$$\cong 2.97\,\%$$

- Voltmeter (Digital Display) [0-1000V ± 0.01V]: Used to measure the output voltage coming from signal conditioning unit. During the calibration, excitation level was set to 2 V (i.e. calibration voltage) that is equivalent to $1000\,\mu\varepsilon$. Therefore, every ± 0.01V change causes $\pm 10\,\mu\varepsilon$ change in strain reading. The measured strain values also depend on the gauge factor, resistance of the strain gauge used in the analysis, calibration resistor and the voltage reading from loaded strain gauge (Section 5.2.2).

I.2 Main Assumptions and Other Source of Errors

The errors in the measurement can be either reading errors depending on the finest scale division or the calibration errors that are systematic errors (i.e. accuracy) coming from measurement devices. The other type of error associated with a directly measured quantity is

called the "reading error" and for a digital instrument, it is ± one-half of the last digit. The objective of a good experiment is to minimise both the errors of precision and accuracy in order to obtain accurate results that can be used to verify the numerical model. Here are the main assumptions made and the other source of errors involved during the experimental and numerical analysis.

I.2.1 Experimental Analysis

- The size of the intact and that of the damaged beams were assumed equal.

- The width and the thickness of the beams were assumed uniform along the length.

- Although surface roughness of the GFRP sandwich beam specimen and adhesive used to bond strain gauges affected the measured strain, perfect bonding (i.e. good structural coupling) was assumed between strain gauges and the host structure.

- The strain gauges bonded on the surface of beams and the embedded FOSs were assumed to be aligned and located along the centre line of the specimens (i.e. no misalignment).

- Although temperature of the laboratory was assumed constant, a slight change in strain was observed when strain gauges were used during the dynamic strain measurements. This was due to heat transfer between electro-dynamic shaker and the surface-bonded strain gauges. This change was considerable low (i.e. insignificant) when embedded FOSs were used during dynamic analysis.

- The electromagnetic interference between surface-bonded strain gauges and electro-dynamic shaker affected dynamic strain measurements by causing random fluctuations. Since FOSs are insensitive to electromagnetic field, more accurate results were obtained compared to surface-bonded strain gauges.

- Torque-wrench was used to tighten the bolts holding the specimen in the clamp in order to reduce the boundary condition effect when different specimens were used for frequency analysis. The soft core of the sandwich specimen made the use of torque-wrench quite difficult.

➢ Since it was difficult to control the input force given to electro-dynamic shaker during low-frequency forced vibration applications, an extra noise was introduced to system.

➢ The weight and the location of 4-gram piezoelectric-accelerometer affected the resonant frequency measurements. This effect is investigated by changing the location of the accelerometer along the span of the beam and by performing random vibration analysis to find the first three resonant frequencies. Accelerometer is bonded on the upper surface of the sandwich beam at 10 different normalised locations from 0.1 to 1 (i.e. tip of the beam) with $0.1L$ increment. The variations in these resonant frequencies are shown in **Figs. I.1** to **I.3** for the intact and the damaged sandwich beam having 40mm-length damage located at 200 mm away from fixed-end.

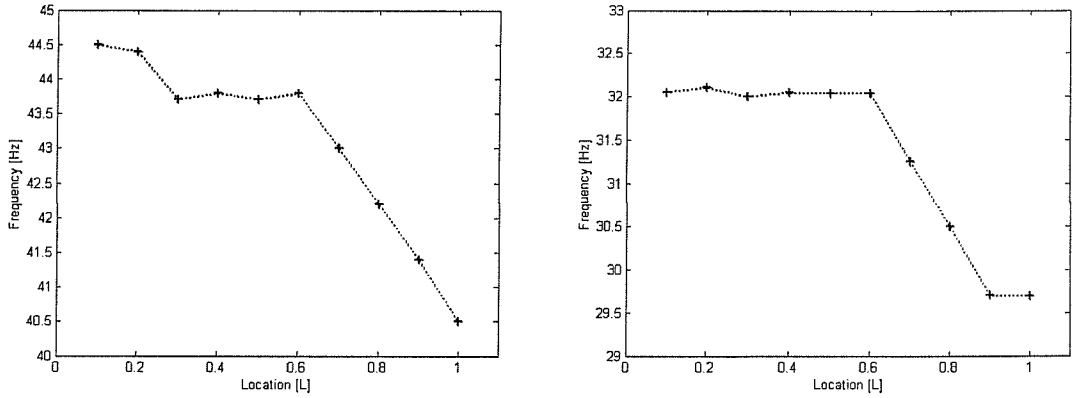

Figure I.1 Variation in the first resonant frequency due to accelerometer location
(a) Intact Beam (b) Damaged Beam

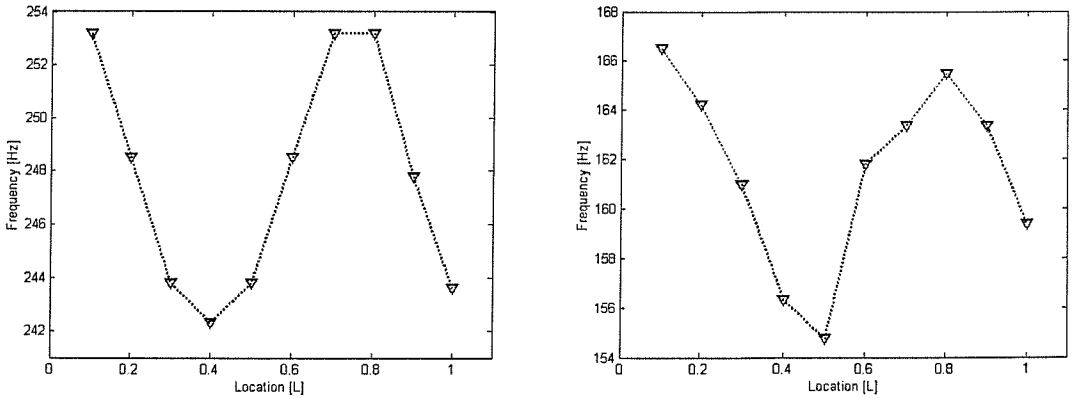

Figure I.2 Variation in the second resonant frequency due to accelerometer location
(a) Intact Beam (b) Damaged Beam

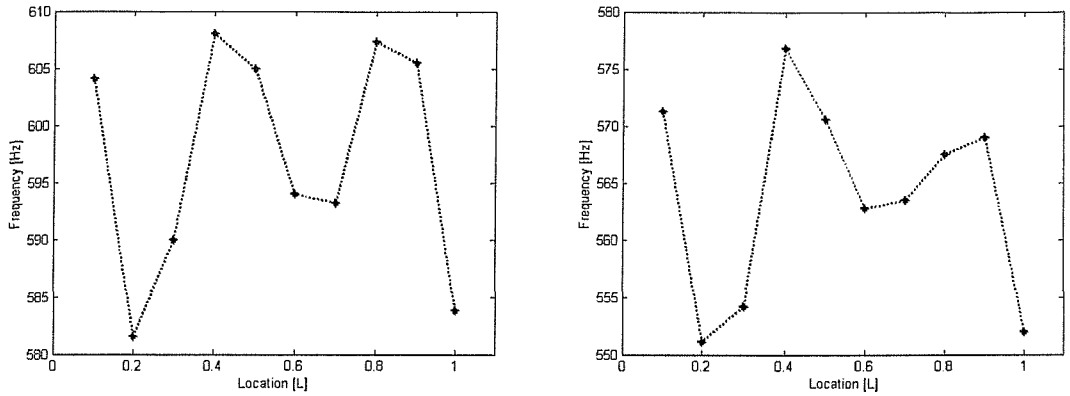

Figure I.3 Variation in the third resonant frequency due to accelerometer location (a) Intact Beam (b) Damaged Beam

As it can be seen from **Figs. I.1** to **I.3** that each frequency of interest (i.e. in each mode) varies within certain range. The effect of this variation can be reduced by normalising the resonant frequencies of the damaged beam with respect to that of the intact one and it is shown in **Fig. I.4**.

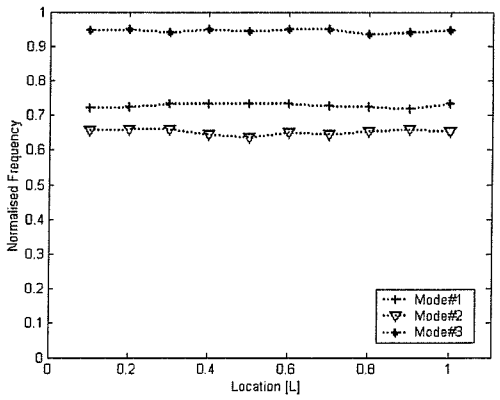

Figure I.4 Normalised resonant frequencies in the first three modes

I.2.2 Numerical Analysis (FEA)

➢ Some of the material properties were assumed by approximating the values taken from statistics.

➢ Equal thickness was assumed for individual layers of GFRP laminae in FEM.

- Debonding was modelled by removing selected elements from the upper surface of GFRP sandwich beam structure in FEA in order to simulate the damage.

- There is also a rounding-off error that is more effective in successive calculations during the numerical analysis.

Appendix J LIST OF PUBLICATIONS

J.1 Journal Papers

Sahin, M. and **Shenoi, R.A.** Vibration-based damage identification in beam-like composite laminates by using artificial neural networks. *Proceedings of the IMechE, Part C, Journal of Mechanical Engineering Science*, 2003, **217**(6), 661-676.

Sahin, M. and **Shenoi, R.A.** Quantification and localisation of damage in beam-like structures by using artificial neural networks with experimental validation. *Engineering Structures*, 2003, **25**(14), 1785-1802.

Dawood, T.A., Shenoi, R. A., Veres, S.M., and Sahin, M. Damage characterisation in FRP sandwich beams using the Lipschitz exponent estimated using a complex Gaussian wavelet. *Journal of Intelligent Material Systems and Structures* (under review)

J.2 Conference Papers

Sahin, M. and **Shenoi, R.A.** Damage detection in FRP laminated beams using neural networks. *First European Workshop on Structural Health Monitoring, Proceeding of the First European Workshop*, Ecole Normale Superieure, Cachan (Paris), July 10-12, 2002, 726-733.

Dawood, T.A., Shenoi, R. A., Veres, S.M., Sahin, M. and **Gunning, M.J.** Damage detection in a sandwich composite beam using wavelet transforms. *Smart Structures and Materials 2003: Modeling, Signal Processing, and Control, Proceedings of SPIE.* 3-6 March 2003, San Diego, California, USA. Vol. 5049, 706-717.

Dawood, T.A., Shenoi, R. A., Veres, S.M., and **Sahin, M.** Low level damage characterisation in FRP sandwich beams using the Lipschitz exponent (Accepted for *Second European Workshop on Structural Health Monitoring*)

Dawood, T.A., Shenoi, R. A., Veres, S.M., Sahin, M. and **Gunning, M.J.** Damage characterisation in FRP sandwich beams using a wavelet based multifractal approach (Accepted for *Second European Workshop on Structural Health Monitoring*)